PHYSIK-DEPARTMENT
TECHNISCHE UNIVERSITÄT MÜNCHEN

Coupled core-crust-magnetosphere oscillations of magnetars

Dissertation
von

Michael Gabler

MAX-PLANCK-INSTITUT FÜR ASTROPHYSIK

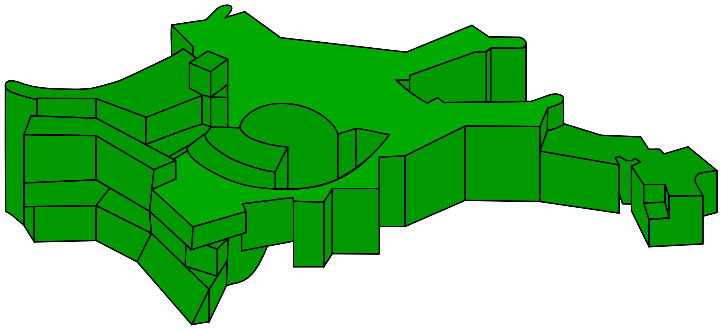

Technische Universität München
Max-Planck-Institut für Astrophysik

Coupled core-crust-magnetosphere oscillations of magnetars

Michael Gabler

Vollständiger Abdruck der von der Fakultät für Physik der Technischen Universität München zur Erlangung des akademischen Grades eines

Doktors der Naturwissenschaften (Dr. rer. nat.)

genehmigten Dissertation.

Vorsitzender: Univ.-Prof. Dr. L. Oberauer

Prüfer der Dissertation:

1. Priv.-Doz. Dr. E. Müller
2. Univ.-Prof. Dr. A. Ibarra

Die Dissertation wurde am 06.10.2011 bei der Technischen Universität München eingereicht und durch die Fakultät für Physik am 22.11.2011 angenommen.

Contents

Conventions

- The signature of the metric is $(-+++)$.
- Einstein's sum convention applies whenever a lower and upper index are equal.
- Latin indices run from 1 to 3, Greek indices run from 0 to 3. The 0-component is the time component.
- Partial (co-variant) derivatives $\frac{\partial B}{\partial \alpha}$ $(\nabla_\mu B^\mu)$ are often abbreviated by $B_{,\alpha}$ $(B^\mu_{;\mu})$
- vectors and tensors are written in bold font

Units

Throughout this work, we use natural units $c = 1$ and $G = 1$. This implies that

$$1 \text{ s} = 2.9979 \cdot 10^{10} \text{ cm}\,,$$
$$1 \text{ g} = 7.4237 \cdot 10^{-29} \text{ cm}\,.$$

In consequence, the units of the density and pressure, commonly measured in g/cm^3 and $dyn/cm^2 = g/(cm \cdot s^2)$, are

$$1 \text{ km}^{-2} = 1.3477 \cdot 10^{18} \frac{\text{g}}{\text{cm}^3}\,,$$
$$1 \text{ km}^{-2} = 1.2106 \cdot 10^{30} \frac{\text{g}}{\text{cm s}^2}\,.$$

For better illustration we present some of the properties of the sun in these units:

$$M_\odot = 1.4766 \text{ km}\,,$$
$$R_\odot = 6.960 \cdot 10^5 \text{ km}\,,$$

and some typical values for neutron stars

$$M_{NS} = 2 \text{ km}\,,$$
$$R_{NS} = 10 \text{ km}\,.$$

We use the Heaviside-Lorentz magnetic field units, i.e. the stress-energy tensor $T^{\mu\nu}$ is given by

$$T^{\mu\nu} = F^{\mu\alpha} F^\nu_{\ \alpha} - \frac{1}{4} g^{\mu\nu} F_{\alpha\beta} F^{\alpha\beta}\,,$$

where $F^{\alpha\beta}$ is the electromagnetic tensor.

1 Introduction

There are only few if any objects in modern physics which have such fascinating properties like neutron stars. They have masses between 1 and 2 solar masses (see Lattimer and Prakash, 2005; Demorest et al., 2010, for observations) compressed by their own gravity to almost perfect spheres with radii of about 8 to 15 km. Theoretical models predict densities in the core of neutron stars which exceed the nuclear saturation density $\rho_0 = 2.8 \times 10^{14}\,\mathrm{g/cm^3}$ by a factor of a few. These stars are so compact that general relativistic effects are important to describe their properties. Some pulsars, i.e. neutron stars emitting pulsed electromagnetic radiation, are rotating almost 1000 times per second (millisecond pulsars), and the strongest magnets ever discovered are neutron stars. While usual neutron stars have magnetic field strengths of the order $10^{12} - 10^{13}\,\mathrm{G}$, a subclass is believed to have fields as strong as $\sim 10^{15}\,\mathrm{G}$. For comparison the natural magnetic field of the earth is of the order 1 G, that of strong sun spots 4000 G, and the strongest man-made fields during explosions are about $10^7\,\mathrm{G}$. The highly magnetized neutron stars are called magnetars.

All the interesting physics related to the ultra high densities and the ultra strong magnetic fields makes neutron stars an ideal space laboratory to test the laws of physics under conditions humans will never be able to achieve on earth.

The interior structure of neutron stars is widely unknown. The simplest models assume pure baryonic matter with leptons, i.e. mainly neutrons with a small fraction of protons and electrons. Other models require significant fractions of muons, pions and/or kaons. Since the density in the core of neutron stars is supposed to exceed nuclear density by a factor of a few, it is not guaranteed that the matter inside neutron stars can be described with exclusively hadronic matter. Quantum chromodynamics (QCD) predicts the presence of phases containing deconfined quarks in a quark-gluon plasma. Additional properties like superfluidity of the neutrons, superconductivity of protons or color-superconductivity of quarks are heavily discussed. The aim of all different models is to provide a relation between density and pressure, the equation of state (EoS). The EoS defines the structure of neutron stars, i.e. it can be used to construct equilibrium models of these stars. Comparing these theoretical models with observations, allows one to constrain the EoS (Lattimer and Prakash, 2007; Özel and Psaltis, 2009; Steiner et al., 2010). This task of constraining the EoS by observed properties is called an inverse problem. With a better understanding of the EoS of neutron stars scientist could also draw conclusions on the interaction of the fundamental particles.

The influence of the EoS on the structure of a neutron star is often illustrated in the mass-radius diagram (see Fig. 1.1, Demorest et al. (2010)), where the allowed neutron

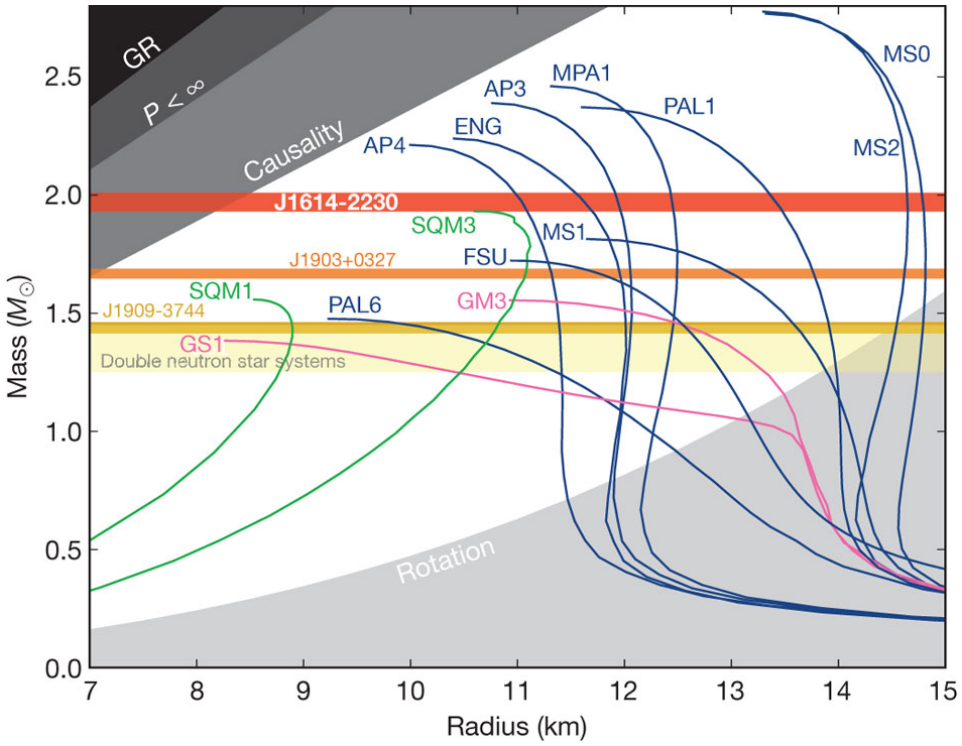

Figure 1.1: Mass-radius relation for neutron stars with different EoS. Green lines represent models with strange quark matter, magenta lines models with exotic hadronic matter like kaons or pions, and blue lines give models with "normal" hadronic matter. Horizontal bands give the range of observed masses with error bars. Courtesy: Demorest et al. (2010)

star models are given. These models are obtained by providing a central density and integrating the Tolman-Oppenheimer-Volkoff equations (Tolman, 1939; Oppenheimer and Volkoff, 1939). The TOV equations give the equilibrium structure of spherically symmetric objects in General Relativity, if an EoS is provided. The solution is completely defined by the central density. Different EoS give different mass-radius relations. Therefore, a simultaneous measurement of the mass and the radius of a neutron star could distinguish between different EoS, and thus constrain the number of models significantly. However, the determination of both properties is very difficult, and the error bars on each measurement are large, such that up to day no strong constraints on the EoS could be obtained. Some promising approaches to obtain the mass are the use of Kepler's laws (see Lattimer and Prakash, 2005, and references therein) or the Shapiro delay (Demorest et al., 2010) for neutron stars in binaries. The second method (Shapiro delay) is based on the relativistic time delay of an electromagnetic wave passing through a gravitational potential. For neutron stars with accretion disks the association of observed kHz quasi-periodic oscillations (QPOs) with the rotation period of the inner edge of the disk, and hence with the innermost stable circular orbit (ISCO) gives a mass estimate, because the ISCO is a function of the latter (see van der Klis, 2006, for a review on different

mode	name	driven by	frequency
p	pressure	pressure	$\sim$ kHz
g	gravity	buoyancy	$\sim$ 10 Hz
f	fundamental	pressure	$\sim$ kHz
w	gravitational wave	gravitational-radiation-reaction	$\sim$ kHz
s	spheroidal shear	shear in crust	$\sim$ kHz
	superfluid	superfluid interior	$\sim$ 10 kHz
t	toroidal shear	shear in crust	10 . . . 1000 Hz
i	interfacial		$\sim$ 100 Hz
r	rotational	Coriolis force	$\sim$rotation period
a	Alfvén	magnetic field	$\sim$magnetic field

Table 1.1: Selection of oscillation modes, their restoring force and expected frequencies. (McDermott et al., 1988; Stergioulas, 1998; Kokkotas and Schmidt, 1999)

models for kHz QPOs). Methods to obtain radii are based on estimates of the surface of the photosphere of thermally emitting neutron stars or the surface of thermonuclear explosions of accreted matter on the surface. In some objects the two properties may be obtained simultaneously, e.g. during explosions with photospheric radius expansion (van Paradijs and Lewin, 1987; Özel et al., 2009), which give estimates of the Eddington flux and the emitting area. The Eddington flux is defined as the radiation flux, whose outward pressure balances the inwards directed gravitational attraction. Alternatively the observation of absorption lines, which may be red-shifted ($\sim$M/R) and broadened ($\sim$M/R^2) by thermal motion, could provide an estimate of mass and radius (Paerels, 1997). In Fig. 1.1 some constraints on the mass-radius relation of neutron stars are given. The upper shaded regions are forbidden due to theoretical limits, as causality or the appearance of infinite pressure in the models. The lower shaded region is forbidden due to the mass shedding limit for the fastest spinning pulsar observed. Horizontal bands give present mass measurements with the corresponding error bars. The highest measured mass of about 2 solar masses excludes a number of models for the EoS, i.e. models of strange quark stars (SQM1, SQM3) and stars with exotic hadronic matter like pions or kaons (GS1, GM3) are ruled out. For details see Demorest et al. (2010).

In this thesis we follow another idea of obtaining information about the structure of neutron stars, and hence the EoS. In analogy to seismology on earth, scientists have been very successful to obtain information about the structure of the sun from solar oscillations with helioseismology. It is thus natural that astronomers are working to extend the methods towards asteroseismology, and to study oscillations of neutron stars in order to extract information about their interior configuration. The idea thereby is to obtain the EoS by comparing observed frequencies of neutron star oscillations with the corresponding theoretical models based on a particular EoS. The oscillation spectrum of neutron stars consists of different families of modes, which can be defined by their restoring force.

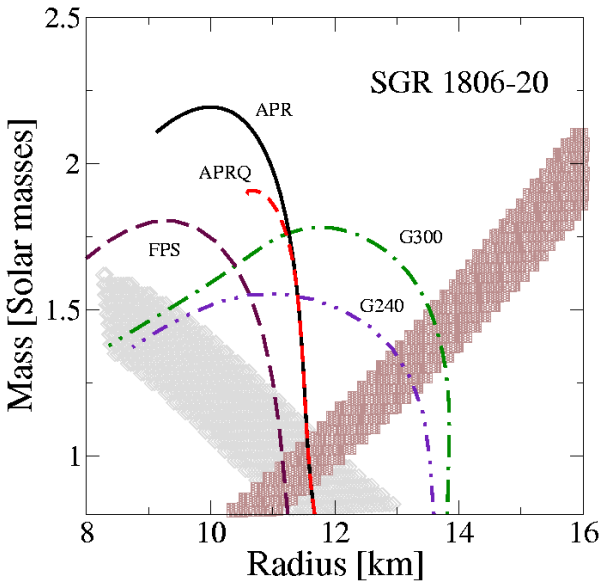

Figure 1.2: Illustration of magnetar seismology with the mass-radius relation for neutron stars with different EoS. Dashed regions give constraints from torsional shear modes of the crust of neutron stars. These constraints have to be fulfilled simultaneously, and hence EoS G300 and G240 are ruled out in this example. Courtesy: Samuelsson and Andersson (2007).

The most important oscillation modes of neutron stars are given in Table 1.1.

An idea how neutron star seismology could work was presented in Samuelsson and Andersson (2007). Different crustal shear modes depend differently on the radius and the mass of the neutron star (see Section 3.2 for details). This can be used to constrain different QPOs as is illustrated in Fig. 1.2. In this mass-radius diagram the constraints originating from the different modes are indicated by the dashed regions. Since both constraints have to be fulfilled, only EoS which produce models with masses and radii in the overlap region are allowed. This is a toy example, because the presented constraints are derived from very simplified models. Nevertheless the principles apply in general, and a similar ansatz can be used to constrain the EoS with more realistic models of the oscillations.

There has been tremendous progress in understanding and modeling the physics of neutron stars. A large number of models, accounting for different microphysical parameters (i.e. different EoS), have been calculated, and the models of neutron star oscillations include ever more detailed physics, but still we are only at the beginning to disclose their properties. Very recently observations begin to constrain the state of the matter in neutron stars. Shternin et al. (2011) and Page et al. (2011) show that the observed decrease of the surface temperature of the neutron star in the Cassiopeia A supernova remnant can be explained with current models only if superfluid neutrons and superconducting protons are present in the core of this neutron star.

A direct way of observing of neutron star oscillations is through the detection of grav-

itational waves from these objects. The advantage of gravitational waves is that they do not originate from the photosphere where the electromagnetic radiation is emitted. Therefore, gravitational waves carry information about the interior of the star where they are created. Perfectly spherical objects do not emit gravitational waves even when oscillating radially, because they do not change the gravitational potential outside their own radii. The lowest order waves in gravity are thus caused by quadrupolar deformations. Therefore, the most promising wave sources from compact stars are rotating neutron stars. Two possible scenarios are the presence of asymmetries like mountains, which emit gravitational waves when rotating, or these stars may develop instabilities like the CFS-instability (Chandrasekhar, 1970; Friedman and Schutz, 1978). Under certain circumstances this mechanism drives the fundamental oscillation mode unstable with respect to emission of gravitational waves.

An alternative source of gravitational waves are explosions like the bursts caused by magnetic reconnection in magnetars. During these very energetic events, oscillations of the star may be excited, which couple to gravitational waves. However, not even the next generation of gravitational wave detectors will provide sufficient sensitivity for a detection of these waves. A merger of binary neutron stars or a neutron star - black hole binary results in much stronger gravitational wave signals, but in this case the wave carries less information about the interior structure of a neutron star. The first detection of a gravitational wave is only expected within the next few years, and the detection of a signal originating from a neutron star may take even more time. However, once the window to the detection of gravitational waves is open it will boost our observational data, and thus increase our understanding of neutron stars significantly.

For the time being we are limited to the information provided by electromagnetic radiation. Fortunately, there exists already data which is interpreted as being related to oscillations of neutron stars. During a giant outburst of a so-called *soft gamma-ray repeater* (SGR) Israel et al. (2005) found a number of quasi-periodic oscillations. In this thesis we discuss a possible origin of these oscillations, i.e. magneto-elastic oscillations of a magnetar, and investigate how the QPOs may influence the gamma-ray signal.

1.1 SGR - observations

SGRs are believed to be one subclass of the magnetar family. They are characterized by recurrent bursting activity in hard X-rays/soft γ-rays. The first identified burst of a SGR dates back to 1979 (Mazets et al., 1979). Initially these events have been associated with gamma-ray bursts. Therefore, they have been termed soft gamma-ray repeater, although their emission occurs mainly in the hard X-ray band. It was only a couple of weeks after the first detection of a bursting SGR when on March 5th, 1979 a giant explosion on SGR 0526-66 launched huge amounts of gamma rays that saturated all detectors on that time X-ray space telescopes. This was one of only three giant flares of SGRs detected up to date. A short list of confirmed SGRs and some of their properties are given in Table 1.2. Remarkable features of all SGRs are their young ages ($<$few$\times 10^4$ years), and

Name	Period [s]	B [10^{14} G]	distance [kpc]	bursts	giant burst
SGR 1806-20	7.6	24	9	✓	✓
SGR 0526-66	8.1	5.6	50	✓	✓
SGR 1900+14	5.2	7.0	12-15	✓	✓
SGR 1627-41	2.6	2.2	11	✓	
SGR 0501+4516	5.8	1.9	?	✓	
SGR 0418+5729	9.1	< 0.075	?	✓	
SGR 1833-0832	7.6	1.8	?	✓	

Table 1.2: List of confirmed SGRs and their periods, estimated surface magnetic fields inferred from dipole radiation, distances, and bursting activity. (credit: http://www.physics.mcgill.ca/~pulsar/magnetar/main.html)

very narrow rotation period P range of 2-10 s. Normal pulsars have a much wider range of periods between ~ 1 ms to ~ 10 s. The reason is probably that magnetars spin down very efficiently on a short time scale, and they become dim when the magnetic field has decayed sufficiently, which is expected to occur on time scales of 10^4 years. One can use the spin down $\dot{P}$ of the rotation period to estimate the magnetic field of a star by assuming dipolar electromagnetic radiation: $B[\mathrm{G}] = 3.2 \times 10^{19} \left(P\dot{P}\right)^{1/2}$. The corresponding values of the SGRs are given in Table 1.2.

The second group of magnetars are anomalous X-ray pulsars. These AXPs have very similar properties as the SGRs, but show less if any bursting activity. In the following we concentrate on SGRs.

For recent reviews on the following observational aspects of magnetars see Mereghetti (2008) or Rea and Esposito (2011).

Persistent emission

Magnetars emit on average an energy of about few$\times 10^{35}$ erg/s. The main radiation from SGRs is in the X-ray band. Generally the signal can be divided into two contributions, one at energies < 10 keV and one > 20 keV. The soft part is usually fitted with a black body of ~ 0.5 keV plus a non-thermal contribution in form of a power law with a quadratic dependence on the frequency (photon index ~ 2). The hard X-ray spectra may carry a significant amount of the total energy of the radiation, and is usually fitted with power laws. The optical and infrared emission of all magnetars is very faint if detectable at all (Mignani, 2011), and transient radio emission has been found only directly after giant flares.

Bursts

The characteristic property of SGRs is the presence of recurring periods of active bursting. Depending on the source a few up to hundreds of bursts with luminosities of up to $\sim 10^{42}$ erg/s have been observed. The typical duration is of the order of 0.01 to 1

burster	SGR 0526-66	SGR 1900+14	SGR 1806-20
date	March 5, 1979	August 27, 1998	December 27, 2004
duration (initial spike) [s]	0.25	0.35	0.5
peak luminosity [erg/s]	3.6×10^{44}	$> 8.4 \times 10^{44}$	>several$\times 10^{46}$
duration (tail) [s]	200	400	380
isotropic energy (tail) [ergs]	3.6×10^{44}	1.2×10^{44}	1.3×10^{44}
black body fit (tail) [keV]	30	20	15-30
observed QPO frequencies[Hz]	43	28, 53, 84, 155	18, 26, 30, 92, 150, 625, 1840 (17, 21, 36, 59, 116)[1] [84, 103, 648][2]

Table 1.3: Properties of the three observed giant flares of SGRs: date, duration, peak luminosity, temperature of possible black body fit, and QPO frequencies. The main part of this table can be found in Mereghetti (2008). Recently detected QPOs are provided by (1) Hambaryan et al. (2011) and (2) El-Mezeini and Ibrahim (2010).

s, thereby obeying log-normal distribution[1] peaking at 0.1 s. The waiting time between successive bursts is also distributed log-normally. The spectra of the outburst can be described by double humped curves which can be tentatively fitted with two black body spectra in the range of 2-4 keV and 8-12 keV, respectively (see for example Feroci et al., 2004). However, there is no conclusive physical interpretation for this particular choice of the fit.

Some authors divide further into normal and intermediate bursts. The latter are much brighter, but also much rarer than the former ones. These intermediate bursts have properties in between the normal bursts and the giant flares. They last quite long ($\lesssim 40$ s), show pulsations at the rotation period, but do not show any initial spike like the giant flares have. With more and more data available, the bursts seem to span a continuum of intensities such that a division into normal and intermediate bursts appears to be artificial. However, a conclusive model to explain all bursting activity has not emerged yet.

Giant flares

Giant flares are very rare events which are much more energetic explosions ($> 1000\times$) on the SGRs than normal bursts. Up to date only three of these events have been observed. Their main properties are summarized in Table 1.3, where we also give the observed QPOs which are discussed in more detail in Section 1.4. All giant flares show very similar rise times of about ~ 0.3 s of the initial hard spike, which has a characteristic temperature of hundreds of keV. The long lasting pulsating tails of the flares persist all for about

[1] A log-normal distribution is a probability distribution of a random variable whose logarithm is normally distributed.

$\sim 400\,\mathrm{s}$. The luminosity of the neutron star during the initial spike (10^{44}-$10^{47}\,\mathrm{erg/s}$) is so huge, that most instruments which detected the giant flares have been saturated when the signal arrived. This makes it very difficult to obtain reliable information about the peak flux, and the shape of the light curve at this phase of the flare. The spectra of the decaying tails are generally softer, and show a complicated pulse profile. Despite the large differences in the luminosity of the initial spikes ($10^{44} \ldots 10^{46}\,\mathrm{erg/s}$), all observed tails have similar energies of $\sim 10^{44}\,\mathrm{ergs}$. The corresponding luminosity is much brighter than the Eddington limit predicts. However, the latter limit assumes a balance between the force of the outward radiation pressure and magnetic confinement. The ultra-strong magnetic field suppresses the interaction between the radiation and the plasma, i.e. the electron cross section of one polarization state is reduced below ($\sim 10^{-4}$) the Thompson cross section, such that more photons are able to escape without blowing the overlying matter away.

1.2 Magnetars - theoretical model

The estimation of the magnetic field with the dipole-radiation model gives values of the surface magnetic field strength of 10^{14}-$10^{15}\,\mathrm{G}$ (see Table 1.2). Initially not many scientists were convinced that such strong fields, exceeding that of normal pulsars by orders of magnitude, exist. It was not clear how such strong fields, even stronger than the quantum electrodynamics field strength $B_{\mathrm{QED}} = 4.4 \times 10^{13}\,\mathrm{G}$, can be created[2]. The idea of highly magnetized neutron stars became more widely accepted when Duncan and Thompson (1992) explained the formation of magnetars as the consequence of helical dynamo action during a short period after the gravitational collapse had occurred. In the following we will describe in detail the ingredients of the magnetar model. Despite the ultra-strong magnetic fields, the interior structure of magnetars is almost unchanged when compared to ordinary neutron stars. Except for a very thin region close to the surface, the pressure and density inside such compact objects are much larger than the magnetic pressure. However, the region just outside the star will be affected significantly by the magnetic field.

Structure of neutron stars

Like other neutron stars, magnetars can be characterized by a onion skin model, see Fig. 1.3. The outer shells have densities below nuclear density $\rho \leq 2.8 \times 10^{14}\,\mathrm{g/cm^3}$, and consist of ordinary matter like neutrons, protons and electrons. Therefore, theoretical methods developed for nuclear physics under terrestrial conditions can be applied to these parts of the neutron stars. The deeper one looks into the neutron star, the larger the uncertainties of the theoretical models become. For a recent review on the physics of

[2] $B_{\mathrm{QED}} := m_e c^3/e\hbar = m_e c^2/2\mu_B$, where mu_B is the Bohr magneton. B_{QED} is the magnetic field at which the potential magnetic energy of an electron becomes of same order as its rest mass energy. Above this magnetic field quantum electrodynamic effects as for example photon splitting become important.

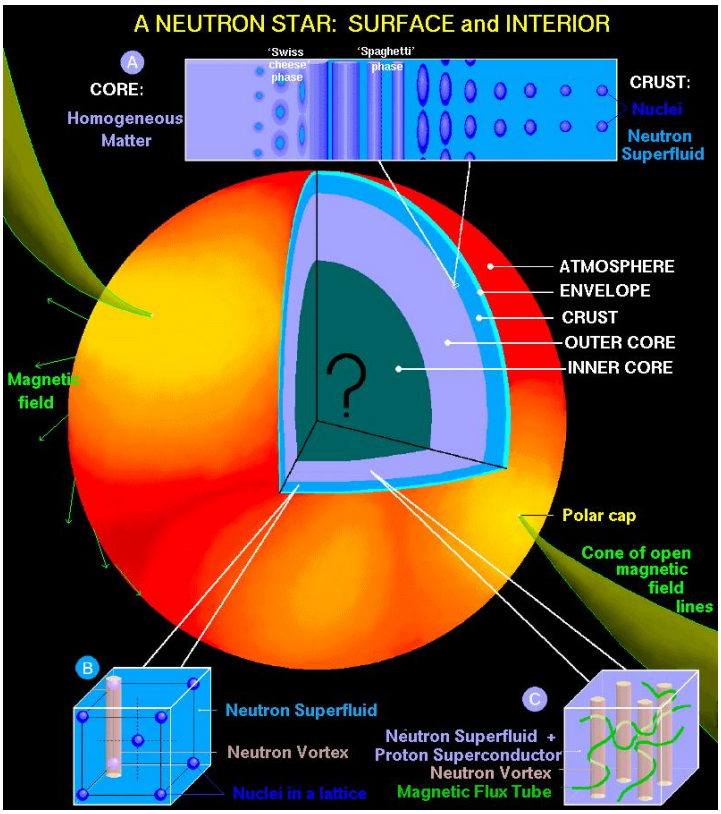

Figure 1.3: Illustration of a neutron star's interior structure. Courtesy: Page and Reddy (2006)

neutron star crusts see Chamel and Haensel (2008). The outermost layer, the envelope (thickness $< 100\,\mathrm{m}$), is formed by light nuclei reaching up to iron. In the outer part of the crust (thickness $\sim 300\,\mathrm{m}$) the nuclei are organized in form of a body-centered, cubic Coulomb lattice (mainly iron ^{56}Fe). At $10^6\,\mathrm{g/cm^3}$ electrons become degenerate and contribute very efficiently to the electric and thermal conductivity. Starting at densities above $10^7\,\mathrm{g/cm^3}$ the nuclei become more and more neutron rich by electron capture when going deeper into the neutron star. With increasing density one reaches a threshold at about $4 \times 10^{11}\,\mathrm{g/cm^3}$, where it becomes energetically favorable for neutrons to drip out of the nuclei, and to move around freely. This is called *neutron drip* and defines the interface between outer and inner crust (thickness$\sim 1\,\mathrm{km}$). Under the conditions in the inner crust, neutrons are expected to form a superfluid.

The transition between the lattice structure in the solid crust and homogeneous matter in the liquid core occurs at around $\gtrsim 10^{14}\,\mathrm{g/cm^3}$. This transition is not abrupt and can be described by a continuous change of the lattice in terms of *pasta phases*. At low densities the nucleons form a meatball like structure. With increasing density they get compressed and form spaghetti like fibers, which in turn merge to lasagna like sheets. At even higher densities the anti-structures of the pasta phases form, where the pasta-like structures are formed by tubes or holes. The final pasta phase is the "anti-meatball" or

"Swiss cheese" structure.

In the outer core (thickness$\sim$ 3 km) the protons drip out and are expected to form a superconductor. There are predominantly neutrons with smaller fractions of protons and electrons present. The main pressure contribution comes from free neutrons (the outer crust is dominated by electron degeneracy pressure). The composition of the inner core (radius$\sim$ 5 km) is heavily debated and very exotic particles might be able to form. Different models are for example traditional neutron stars (neutrons, protons, electron, muons), stars with pion condensates, nucleon stars with kaon condensates, hyperon stars or quark-hybrid stars with an inner core formed by a quark-gluon plasma. Even strange stars with color-superconducting strange quark matter and very thin crusts cannot be ruled out completely.

Neutron star formation

Neutron stars are the end products of stellar evolution for stars with masses between 8 - 20 solar masses. After having consumed all its hydrogen the star burns subsequently other fuels like helium, carbon, and oxygen. When all elements lighter than nickel-56 are consumed, no material for exothermic fusion is available and the core of the star consists of a mixture of iron group nuclei. If the iron core is heavier than the Chandrasekhar mass limit ($\sim$ 1.4 solar masses), it is not able to balance its self-gravity, and undergoes a gravitational collapse during which the matter in the core is neutronized due to electron capture. The explosion powered by huge amounts ($\sim 10^{53}$ ergs) of gravitational binding energy ejects the surrounding matter. In the case of neutron star formation the gravitational collapse is halted at around nuclear saturation density by the large incompressibility of neutron-rich nuclear matter. The collapsed core is initially very hot ($\sim 10^{11}$ K). If the star is too massive the collapse proceeds towards a black hole. The hot proto-neutron star cools very efficiently by emission of neutrinos within $\sim$ 20 seconds after birth to temperatures less than 10^7 K.

Magnetic fields

Currently there exist two models which may explain the ultra strong magnetic fields observed in magnetars. One possibility are fossil fields of the progenitor stars, which become amplified during the collapse because of conservation of magnetic flux (Braithwaite and Spruit, 2004; Ferrario and Wickramasinghe, 2006). This would imply that magnetars are the final state of very massive stars which additionally have high total magnetic fluxes. In the second scenario the proto-neutron star has to be a fast rotator ($\sim$ 1 ms) in order to allow a helical dynamo to operate (Duncan and Thompson, 1992). This selection effect would naturally provide a bimodal distribution. There are proto-neutron stars which do not rotate sufficiently fast (normal pulsars) and the ones which rotate with periods around $\sim$ 1 ms (magnetars). After the initial phase of fast rotation, the strong magnetic fields in magnetars cause it to subsequently slow down very efficiently by emission of electromagnetic radiation. The magnetic field freezes in

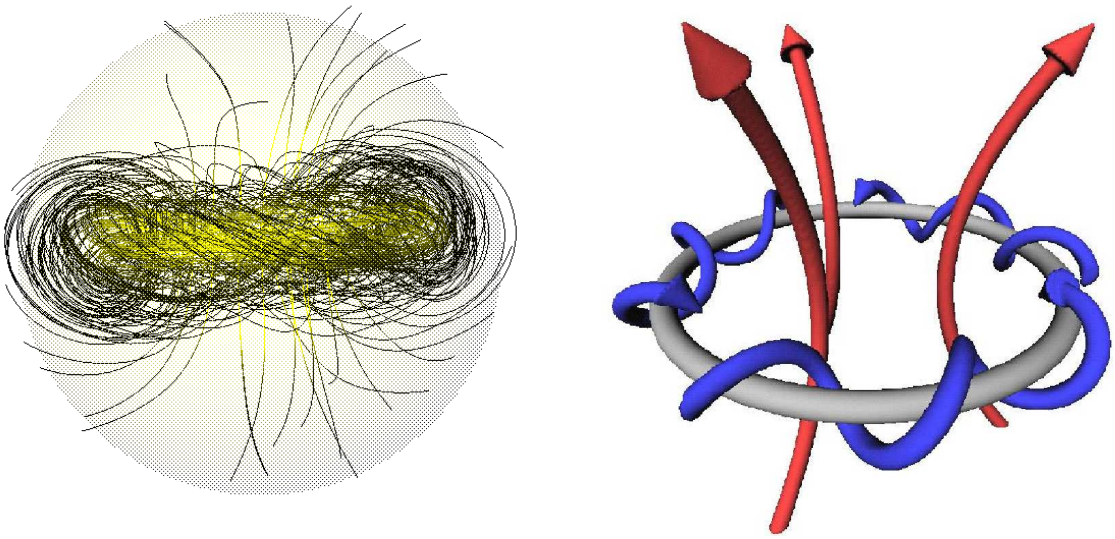

Figure 1.4: *Left panel*: Numerically obtained magnetic field configuration inside a star with toroidal and poloidal magnetic fields. Yellow lines represent strong magnetic field, black weak field. *Right panel*: Schematic illustration of a twisted torus configuration. Courtesy: Braithwaite and Spruit (2004); Braithwaite (2009)

the crust when the latter crystallizes during the cooling of the neutron star. The dynamo model has further observational consequences. First, the supernova is expected to be more energetic than ordinary core collapse events. Second, the resulting neutron star may have received a strong kick during the explosion, because the strong magnetic field is very likely to produce an anisotropic explosion and magnetic winds.

Interior magnetic fields

Due to the inaccessibility of the neutron star's interior, its magnetic field is not well known. However, purely toroidal and purely poloidal configurations are unstable with respect to different instabilities (Markey and Tayler, 1973; Tayler, 1973; Wright, 1973; Flowers and Ruderman, 1977). The most promising structure is thus a mixed field. For an illustration see Fig. 1.4. This configuration has been studied in axisymmetry and with different approaches by Braithwaite and Spruit (2004, 2006); Braithwaite and Nordlund (2006); Braithwaite (2009); Ciolfi et al. (2009), and Lander and Jones (2009). All groups find a poloidal field which looks qualitatively similar to a pure dipole field, and a toroidal component which is concentrated in the region whose field lines close inside the neutron star. However, the ratio of the poloidal to the toroidal field strength has very different values in the different studies. Due to its geometrical form, the configuration found was termed twisted torus.

Very recently three-dimensional magneto-hydrodynamical simulations confirmed a twisted-torus like structure also for relativistic stars (Lasky et al., 2011; Ciolfi et al.,

2011). This configuration is the end state of the numerical evolution, i.e. after reaching a quasi-equilibrium. The numerical results are not very sensitive to the particular form of the initial data. In contrast to the previous work, the obtained structure is no longer axisymmetric.

There is no conclusive theory about the stability of magnetic field configurations in three dimensions. Most of the previous models are obtained with numerical simulations and the analytic work by Ciolfi et al. (2009) lacks a stability analysis of the obtained configurations.

Magnetosphere

The region outside of a neutron star whose dynamics is dominated by a magnetic field is called magnetosphere. In normal pulsars the magnetosphere is filled with plasma. The corresponding electric currents are produced by the rotation of the star, and the density of the charge carriers is called Goldreich-Julian charge density (Goldreich and Julian, 1969).

To explain the persistent emission of magnetars, Thompson et al. (2002) require currents in the magnetosphere. Since the rotation in magnetars is too slow, $P \sim 2 \ldots 10\,\mathrm{s}$, to create sufficient plasma to explain the observations, the currents have to be created by a non-vanishing φ-component of the magnetic field (see below). Such a configuration is often referred to as a twisted dipole. This twist creates a very high voltage between the foot-points of the magnetic field lines in magnetars. Therefore, electrons and even light ions, which are thermally excited above the surface, can be lifted out of the gravitational potential and get accelerated along the magnetic field lines (Thompson et al., 2000). These particles serve as seeds for avalanches of pair creation (Beloborodov and Thompson, 2007), and the magnetosphere is filled with an electron-positron dominated plasma. The charge density in such a magnetar magnetosphere can be orders of magnitude larger than the Goldreich-Julian density. Due to the very strong magnetic fields around magnetars the charge carriers will flow along the magnetic field lines and the corresponding current can be assumed to be force-free, i.e. the Lorentz force vanishes ($\mathbf{J} \times \mathbf{B} = 0$). This holds, because the pressure of the plasma is much smaller than the one from the magnetic field, and the evolution is dominated by the latter. In this case, i.e. if one neglects all pressure and density terms due to particles, the Maxwell equations reduce to $\mathbf{J} \times \mathbf{B} = 0$. The described twist of the magnetic field is gradually dissipated on time scales of years (Beloborodov and Thompson, 2007).

Until very recently the models of the force-free magnetospheric magnetic field were based on a self-similar model for twisted dipoles (Thompson et al., 2002). The possible applications of this model are very limited. It has one free parameter: the twist angle, i.e. the azimuthal angle between the foot-points of the magnetic field lines, which defines the strength of the toroidal magnetic field. The two most extreme configurations of this model result in the magnetic dipole and the magnetic monopole. By changing the twist angle, there is a unique transition between both extremes. However, it is neither possible to describe any configuration which has only localized twist, nor can one specify

the boundary values for the magnetic field and obtain the corresponding configuration in the whole magnetosphere. A generalization of this self-similar model to deformed quadrupolar and higher-order multipoles was given by Pavan et al. (2009).

In a work parallel to ours, Viganò et al. (2011) construct force-free magnetic fields numerically by using the magneto-frictional method. In this approach one defines a fictitious friction force proportional to the Lorentz force, which drives the magnetic field configuration to a force-free equilibrium. This approach was applied very successfully in the context of the physics of the solar corona (Yang et al., 1986; Roumeliotis et al., 1994). The magnetic fields constructed can sustain very large twists, i.e. strong toroidal magnetic field components, and the current in the magnetosphere may have a complicated form. However, the magneto-frictional method used by Viganò et al. (2011) suffers from the fact that only the radial magnetic field at the surface can be specified as a boundary condition, and that the same radial field at the boundary does not give a unique configuration. The latter depends on the initial guess of the magnetic field in the whole domain.

1.3 Emission mechanism

Persistent emission

To power the persistent emission at $\sim 10^{36}\,\mathrm{erg/s}$ observed in magnetars over a time scale of 10^4 years requires a huge energy reservoir. This can be provided by the ultra-strong magnetic field of those stars. For example, a magnetic field of the order of $10^{15}\,\mathrm{G}$ may heat the neutron star by ambipolar diffusion sufficiently to produce the corresponding luminosity (Thompson and Duncan, 1996). Additionally, the currents in a twisted magnetosphere provide a source of heating, when the energetic charge carriers hit the surface.

Current models to explain the different contributions to the emission of quiescent magnetars are based on resonant cyclotron scattering (RCS)[3] of photons emitted from the neutron star surface. The unscattered fraction of the photons gives the observed Planck spectrum at a temperature of about $0.5\,\mathrm{keV}$. The large currents present in a twisted magnetosphere provide a large number of scattering targets for the resonant cyclotron absorption of X-rays. The magnetosphere is has thus large optical depth. The resonant cross section is orders of magnitudes larger than the Thomson cross section, which applies in the case of elastic scattering of electromagnetic radiation by free charged particles. The energy absorbed by the electrons which carry the current is emitted almost immediately due to synchrotron radiation (Lyutikov and Gavriil, 2006). Therefore, we are allowed to treat the whole process of absorption and prompt re-emission as scattering. Lyutikov and Gavriil (2006) show in a 1-dimensional model that the emission is changed due to the RCS in the following way. The transmitted flux is on average Comp-

[3]RCS occurs when an electron is excited into a higher Landau level by a photon of the appropriate energy and the electron re-emits the gained energy by synchrotron radiation. The Landau levels are the quantized energy values an electron in a cyclotron orbit in a magnetic field can occupy.

ton up-scattered, and narrow spectral features produced near the surface, like cyclotron lines, can be erased. This may explain the non-thermal component of the spectrum, and the absence of cyclotron lines in the observations. In subsequent publications (Fernández and Thompson, 2007; Nobili et al., 2008a,b; Rea et al., 2008; Zane et al., 2009; Fernández and Davis, 2011) two different groups applied the RCS model to more realistic axisymmetric neutron star magnetospheres with self-similar twisted dipole configurations of the magnetic field. With their three-dimensional Monte-Carlo simulations they were able to fit the observed spectra with the black body of 0.5 keV and the non-thermal power law component remarkably well. In all these works only ad-hoc configurations of the magnetic field and the corresponding currents were assumed. Beloborodov (2009) started to investigate more realistic current distributions. The RCS model may also provide an explanation for the hard X-ray emission above 20 keV. The corresponding investigations are closely linked to the development of a realistic model for the current distribution.

Normal bursts

The bursting activity probably has its origin in the interior of the neutron star. It is assumed that the magnetic field diffuses through the neutron star (Goldreich and Reisenegger, 1992), and hence strains the crust in which the magnetic field is anchored (Perna and Pons, 2011). At some point the crust (or at least some parts of the crust) can no longer support the stresses and breaks. The corresponding sudden displacement of the foot-points of the magnetospheric field, may launch Alfvén waves into the magnetosphere (Thompson and Duncan, 1995). These waves cascade to smaller scales caused by non-linear damping, and finally create a photon-pair plasma around the excited magnetic field lines. This plasma is trapped by the ultra-strong magnetic field, because the charged particles are forced on trajectories which gyrate along the magnetic field lines and cannot travel perpendicular to the lines (cyclotron motion). The trapped plasma is also called *trapped fireball*, and evaporates due to the emission of soft γ- or hard X-ray radiation.

Giant flares

There exist two promising mechanisms to create a giant flare (Thompson and Duncan, 1995). The first is based on similar physical processes which act in the case of the normal bursts. Alfvén waves are injected into the magnetosphere as consequence of foot-point motions caused by cracking of the crust. However, the reason for the crustal cracking in this case is probably a large scale instability of the magnetic field inside the core of the neutron star. Since the field is anchored in the crust, the rearrangement of the field in the core causes enormous stresses on the latter. These stresses are released subsequently by repeatedly deforming the crust until it cracks. The amount of energy of the corresponding Alfvén waves injected into the magnetosphere is therefore much larger than in the case of normal bursts. Alternatively, the foot-points of the magnetospheric field lines in the crust may evolve smoothly corresponding to the evolution of the internal magnetic field. The twisted magnetosphere expands more and more with increasing

twist. When reaching a certain threshold, the exterior magnetic field configuration becomes energetically unfavored, and a reconnection event takes place. The energy of the twisted field is released in form of a magnetic plasmoid.

The energy emitted during a giant flare is so large, that the magnetic field cannot trap all of it. Therefore, the initial phase of a giant flare is expected to be characterized by a very strong energetic outflow. This is likely to be observed as the initial hard spike in the spectrum. The decaying tail of the giant flare can be interpreted as the remaining fireball, which evaporates on a time scale of minutes by emission of X-rays.

Arguments in favor of the magnetar model

To summarize the theoretical interpretation of SGRs we give the arguments in favor of the magnetar model ($B > 10^{14}\,\mathrm{G}$), which explains most of the observational properties of SGRs.

- At least one SGR (SGR 0526-66) can be associated with a supernova remnant (SNR N49). Therefore, its age can be estimated to be about 3000 years. To spin down a neutron star by dipole radiation on this time-scale to rotation periods of ∼few seconds requires huge magnetic fields.
- The persistent emission of SGRs is about $10^{35}\,\mathrm{erg/s}$. Rotation at periods of a few seconds cannot power this emission during a time of $\sim 10^4$ years.
- The energy reservoir which powers the giant flares, i.e. the magnetic field, has to have sufficient energy.
- The dissipation of the magnetic field is proportional to its field strength. Very strong magnetic fields are required to dissipate sufficient energy to power the bursts and the persistent emission in the short time during which SGRs are active (10^4 years).
- The magnetic field has to be sufficiently strong to trap the large, hot fireball appearing in the magnetosphere during the giant flares.
- The cross section of the X-rays with the particles in the fireball has to be reduced by a sufficiently strong magnetic field to allow for fluxes exceeding the magnetic Eddington limit by orders of magnitudes.
- The short rise time ($\sim 0.2\,\mathrm{s}$) of the giant bursts, which is caused by a large-scale rearrangement of the magnetic field, has to be shorter than the Alfvén wave travel time through the star ($0.2 \gtrsim t_\mathrm{a} \sim B^{-1}$).

Recently, Rea and Esposito (2011) observed SGR like behavior in SGR 0418+5729, which has a estimated dipolar magnetic field of $7.5 \times 10^{12}\,\mathrm{G}$. However, to fit its X-ray spectra Guver et al. (2011) require a strong magnetic field of the order of $10^{14}\,\mathrm{G}$. Higher order multipoles may contribute significantly to the total magnetic field strength, while

the dipolar component responsible for the field strength estimate is very weak. Moreover, Perna and Pons (2011) and Turolla et al. (2011) discuss aged magnetars with low dipolar magnetic field strength $B \lesssim 10^{13}$ G as possible sources of SGR like bursts.

Alternative models

The ultra strong magnetic fields involved in the magnetar model encouraged a lot of work to find alternative scenarios which could explain the observations. The most promising and most consistent alternative considers accretion from a fossil disk. With such a model Alpar (2001) explains the rapid spin-down of the AXPs/SGRs by a so called propeller stage, during which infalling material is expelled in form of winds. When the propeller efficiency decreases during the evolution the star-disk system may reach a point at which the propeller turns off and normal accretion from the disk onto the neutron star sets in. In this phase the quiescent emission of AXPs/SGRs may be powered by the accretion (Chatterjee et al., 2000). Marsden et al. (2001) claimed that the formation of disks around the observed AXPs and SGRs is favored compared to usual pulsars, because AXPs and SGRs are born in regions of dense interstellar medium. This idea was disproved by further observations and by a paper by Duncan (2002).

There are major problems of the disk model to explain all observations related to magnetar candidates. First, there is no unambiguous observation of an infrared excess in the spectra, which should be caused by a disk. Second, to explain the bursting activity and the giant flares of SGRs requires an additional mechanism. While in the magnetar model the ultra strong magnetic field gives a natural explanation (see corresponding subsection in Section 1.3), the disk does not give rise to bursts in simple models. Moreover, the observed QPOs in the giant flare may be explained by oscillations of the neutron star, if there is a coupling through the magnetic field. This coupling is less efficient for weaker magnetic fields as in normal pulsars with a disk.

Another more tentative idea involves massive, fast rotating, and highly magnetized ($B \lesssim 2 \times 10^{11}$ G) white dwarfs (WDs) (Malheiro et al., 2011) instead of magnetars. In this case the rotational energy would be sufficient to explain the quiescent emission and the bursting activity. However, there is the problem to explain the giant flares and their properties which do not fit in this model at all. Moreover, the high energy emission above 10 keV cannot be accommodated.

More exotic models are based on the possibility that pure quark matter is the most stable configuration under the conditions expected in a compact star (Xu et al., 2006; Xu, 2007; Horvath, 2007). The energy emitted during bursts or giant flares in this model could be provided by the gravitational energy during star quakes. Solid quark stars are highly speculative and no further observations have been obtained to support this idea.

1.4 QPOs in Giant flares

The discovery of quasi-periodic oscillations in the decaying tail of the giant flare of SGR 1806-20 in 2004 (Israel et al., 2005) may have been the first detection of neutron

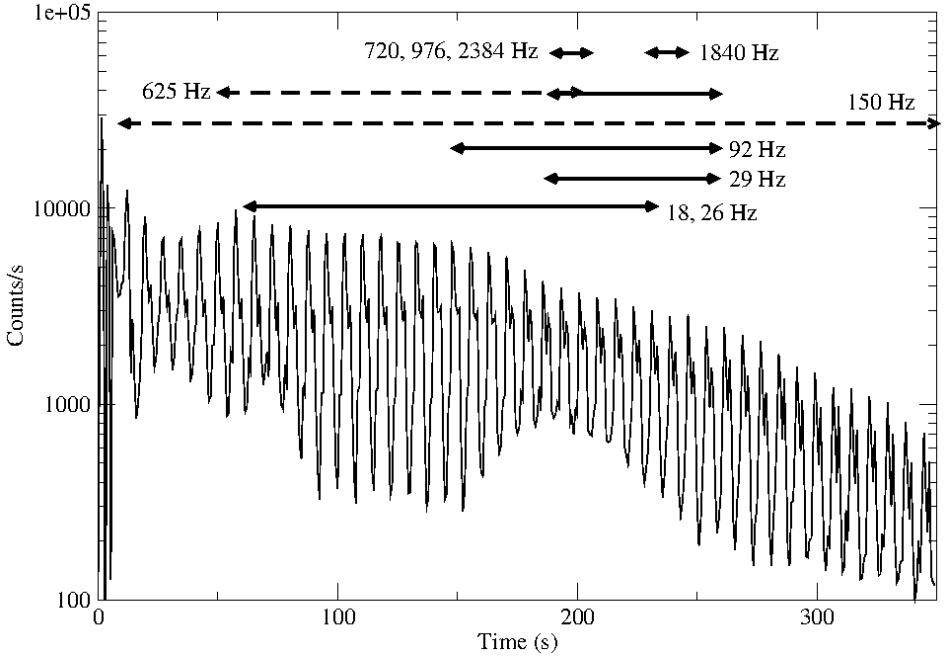

Figure 1.5: Light curve of the giant flare of SGR 1806-20 in 2004. Arrows indicate the presence of long-lasting QPOs. The period of the visible amplitude modulation of the signal coincides with the rotation period. Courtesy: Strohmayer and Watts (2006)

star oscillations. The authors have found signals in the Rossi X-ray Timing Explorer (RXTE) data for this event at 18, 30, and 92.5 Hz which last at least 50 s. Later Watts and Strohmayer (2006) (with Reuven Ramaty High Energy Solar Spectroscope Image - RHESSI) and Strohmayer and Watts (2006) (reanalyzing the RXTE data) confirmed these findings and discovered additional QPOs at 26, 150, 625, and 1840 Hz. In Fig. 1.5, we show the light curve of the 2004 giant flare. The strong modulation with a period of the order of a few seconds reflects the rotation period. The time span during which different QPOs are observed is indicated with arrows. As less observational data were collected during the giant flare of SGR 0526-66 only one QPO at 43 Hz was found by Barat et al. (1983). The search for further evidence of QPOs in the giant flare of SGR 1806-20 led to the discovery of the frequencies at 28, 54, 84, and 155 Hz, respectively (Strohmayer and Watts, 2005). Most of the QPOs last of the order of a few minutes and can be associated to certain intervals in the rotational phase (see Watts and Strohmayer, 2007, for a review). A recent analysis of the RXTE observations by El-Mezeini and Ibrahim (2010) has also revealed QPOs at 84, 103, and 648 Hz in the normal bursts of SGR 1806-20. With a different method, Hambaryan et al. (2011) found new QPOs in the data of the SGR 1806-20 giant burst at frequencies of 16.9, 21.4, 36.4, 59.0, and 116.3 Hz. These are truly fascinating discoveries as the methods employed will allow one to increase the existing observational database and to extend the set of SGR candidates showing QPOs to those magnetars not showing giant flares.

The interpretation of the observed QPOs in terms of oscillations of the magnetar itself seems very promising. If correct, it provides insight into the properties of these objects and constrains the EoS above nuclear matter density. The first step towards such magnetar asteroseismology would be the identification of the modes of the star which have frequencies in the appropriate range, and which could be observable during an outburst. Since the discovery of the QPOs in SGR 1900-16 in 1998 the main focus has been directed towards torsional shear oscillations of the solid crust. Their frequencies lie in the range between 10s of Hz for node-less modes and kHz for $n = 1$ modes, and hence match the observed frequencies cited above (see Duncan, 1998; Strohmayer and Watts, 2005; Piro, 2005; Sotani et al., 2007; Samuelsson and Andersson, 2007; Steiner and Watts, 2009, and references therein). From energetic considerations it is very likely that these oscillations are excited during a SGR outburst (Duncan, 1998). Moreover, torsional shear oscillations couple preferably to the exterior magnetosphere (Blaes et al., 1989), where the emission is supposed to occur in form of a trapped fireball (Thompson and Duncan, 2001). Therefore, these oscillations may naturally influence the γ-ray signal emitted during the flare. However, despite some recent improvements of the models (Steiner and Watts, 2009), the sequence of the frequencies of successive shear modes does not allow for a complete interpretation of all observed QPOs.

Since the publications by Levin (2006) and Glampedakis and Andersson (2006) another possibility has been investigated. These authors show that the crust-core coupling due to the extremely strong magnetic field present in magnetars may have significant impact on the shear oscillations of the crust. It was shown in a simplified toy model that the shear modes can be damped very efficiently into a MHD continuum of Alfvén oscillations existing in the core of the neutron star. This idea stimulated further interest into the direction of magneto-elastic oscillations by ever more sophisticated toy models (Levin, 2007; Lee, 2007, 2008). In particular, Levin (2007) showed that due to the coupling through the crust long-lived QPOs can be produced inside such a Alfvén continuum.

Before studying magneto-elastic oscillations in realistic scenarios it is necessary to understand purely Alfvén oscillations of neutron stars in General Relativity. Studies using general-relativistic MHD models without taking an extended crust into account revealed two families of long-lived QPOs in the continuum formed by Alfvén oscillations of dipolar magnetic field configurations (Sotani et al., 2008b; Cerdá-Durán et al., 2009; Colaiuda et al., 2009). Cerdá-Durán et al. (2009) derived a semi-analytic model based on standing waves in the short-wavelength approximation, which agrees with the MHD numerical results very well, i.e. the frequencies agree within a few per cent for the fundamental and even more accurate for the overtones. The first family of QPOs is related to open field lines close to the symmetry axis of the magnetic field, while the second family can be found in a region of closed field lines near the equator. In this model the members of the first family of QPOs have their maximum amplitudes at the surface of the star and are therefore candidates to explain the observed QPOs (see Section 3.3 for more details). The different overtones have frequency ratios given by integer numbers,

making them very attractive to explain some of the observed frequencies: 30, 92, and 150 Hz in SGR 1806-20. If these Alfvén QPOs could coexist with crustal shear modes, the frequencies of the magnetic QPOs may enrich the spectrum of the crustal modes, and hence be associated to some of the unexplained QPOs observed in SGRs.

Recently a few groups have published results considering magneto-elastic oscillations in improved neutron star models. van Hoven and Levin (2011) extended a non-relativistic toy model and showed that the oscillatory spectrum can be influenced significantly by the physical properties of the model. For example, the presence of an entangled magnetic field allows for the existence of discrete Alfvén modes, or the decoupling of neutrons in the core from Alfvén waves can change the frequencies of the continuum. In Gabler et al. (2011) and Gabler et al. (2010) we presented the first results regarding coupled magneto-elastic oscillations of magnetars in spherically symmetric models obtained with tabulated EoS including an extended solid crust. There we calculated the damping time scale of crustal shear modes when coupled to the Alfvén continuum of the core. This time scale ($\sim 0.01\,\mathrm{s}$) turned out to be orders of magnitude shorter than the time during which the QPOs were observed ($\sim 100\,\mathrm{s}$). We also discussed the influence of the crust on the Alfvén oscillations and the existence of a threshold at which the magneto-elastic QPOs reach the surface with significant amplitudes. In a different approach based on the coupling of a number of linear one dimensional wave equations in the core and a two dimensional wave equation in the crust, Colaiuda and Kokkotas (2011) found a new set of global, discrete Alfvén oscillation. Both van Hoven and Levin (2011) and Colaiuda and Kokkotas (2011) stress the possibility that the frequencies of crustal shear modes may lie between the frequencies of successive continua of the core. In this case the shear modes cannot be damped resonantly, i.e. they could be observed as QPOs. These QPOs are called gap modes.

1.5 Coupled core-crust-magnetosphere oscillations of neutron stars

The aim of this thesis is to study coupled core-crust-magnetosphere oscillations of highly magnetized neutron stars in order to improve the understanding of QPOs observed in the giant flares of SGRs. We extend the analysis of Cerdá-Durán et al. (2009), who studied purely Alfvén oscillations of neutron stars endowed with a dipolar magnetic field. In this thesis we consider the structure of a neutron star as illustrated in Fig. 1.6. In absence of any consensus about the EoS of matter in neutron stars we assume a neutral perfect fluid in the core and a perfect solid in the crust which are described by some selected tabulated EoS. Both regions are penetrated by a magnetic field of the order of 10^{14}-$10^{15}\,\mathrm{G}$, which extends further into the surrounding magnetosphere.

In Chapter 2 we present the theoretical formalism and the numerical tools required to study magneto-elastic oscillations of the neutron star interior. This includes a short introduction to General Relativity, which is the basic framework in which compact objects, like neutron stars, are described. Before giving the final equations describing torsional,

magneto-elastic oscillation of neutron stars, we further introduce the basic properties of general-relativistic magneto-hydrodynamics and relativistic elasticity. Chapter 3 is concerned with the analysis of results of the numerical solution of these equations. As introduction we discuss the uncoupled systems of purely shear and Alfvén oscillations separately. In subsequent sections we present the results of the coupled magneto-elastic oscillations for dipolar fields (Section 3.4) and magnetic fields confined to the crust (Section 3.5).

In our model the QPOs are related to oscillations of the neutron star interior. However, it is commonly assumed that the emission occurs in the magnetosphere. Therefore, we need to find a mechanism which modulates the emission outside of the neutron star. A very promising approach, i.e. resonant cyclotron scattering (RCS) of X-ray photons by the charge carriers of the currents induced by a twisted magnetospheric field, was applied to the quiescent emission of magnetars. In Chapter 5 we follow this idea (Timokhin et al., 2008) and present a Monte-Carlo code able to perform simulations of RCS. The connection to our simulations of the neutron star interior is provided in Chapter 4. By assuming that all processes in the magnetosphere occur on much shorter time scales than in the interior ($t_{\mathrm{magnetosphere}} << t_{\mathrm{interior}}$), we construct a sequence of force-free magnetic field configurations in the magnetosphere which are uniquely determined by the magnetic field at the surface. In this way the QPOs computed in the interior give rise to different magnetic field configurations in the magnetosphere, which in turn change the currents. These currents determine the optical depth with respect to RCS, and hence any modulation of the currents caused by the QPOs is expected to modulate the emission from the fireball.

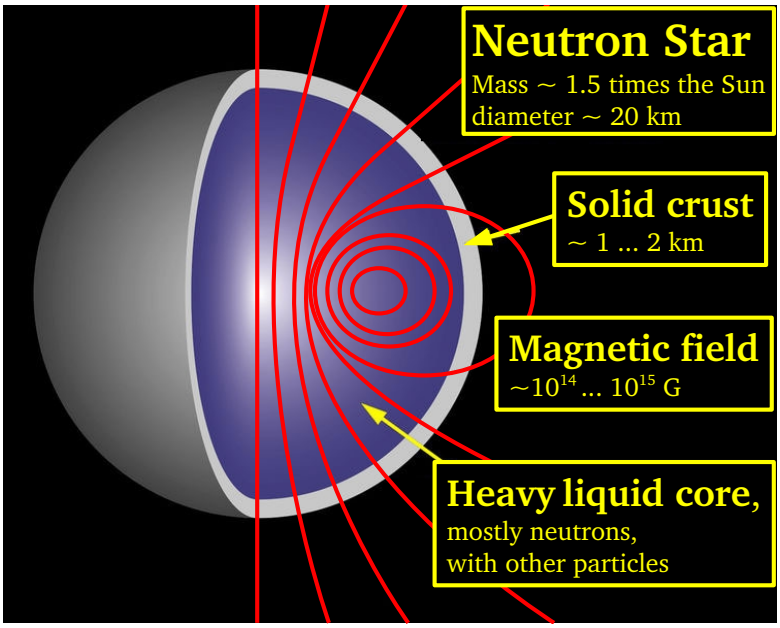

Figure 1.6: Model neutron star with solid crust and fluid core, both penetrated by a ultra-strong magnetic field which extends into the exterior magnetosphere.

2 General-relativistic magneto-hydrodynamics in fluids and solids

This chapter is devoted to derive the theoretical background for the study of our magnetar oscillation model to explain the observed quasi-periodic observations (QPOs) in soft-gamma repeaters. Here, we are interested in a mechanism that could explain the frequencies. When adopting the general consensus that the QPOs are created by or near a strongly magnetized neutron star (Thompson and Duncan, 1995), the most promising source of coherent oscillations over several oscillation periods is the neutron star itself. Currently two competing ideas dominate the discussion in the literature: shear modes of the crust (Duncan, 1998; Strohmayer and Watts, 2005; Piro, 2005; Sotani et al., 2007; Samuelsson and Andersson, 2007; Steiner and Watts, 2009) or Alfvén oscillations of the core (Sotani et al., 2008b; Cerdá-Durán et al., 2009; Colaiuda et al., 2009). To investigate the more general scenario, including a description of both possibilities, one has to cope with oscillations of magnetized neutron stars with an extended, elastic crust. This has been treated approximately with toy models (Levin, 2006; Glampedakis et al., 2006; Levin, 2007; Lee, 2007, 2008). Only very recently more sophisticated models appeared (Gabler et al., 2010; van Hoven and Levin, 2011; Colaiuda and Kokkotas, 2011; Gabler et al., 2011). For compact objects such as neutron stars self-gravity is dynamically important and any description should include General Relativity (GR). Therefore, we first give the equations of General Relativity in the so called "3+1" split, which is appropriate for numerical integration. Second, we show how to describe magneto-fluids in GR, because we can treat the neutron star as such a fluid. In order to include the effects of an elastic crust on top of the fluid neutron star, we make use of the theory of relativistic elasticity. Finally, all ingredients are combined to present the elastic GRMHD equations.

In the last part of this chapter we present the numerical methods we used to evolve the fluid, and we explain how we succeeded to set up the delicate crust-core interface.

2.1 General Relativity in the "3+1" - formalism

2.1.1 Einstein equations

The theory of General Relativity is a geometric description of gravity. The framework is provided by the spacetime, which is understood as the unification of the familiar three-

dimensional space with time. The spacetime is defined as a four-dimensional manifold $\mathcal{M}$ equipped with a rank-2 tensor $g_{\mu\nu}$ called metric: $(\mathcal{M},\ g_{\mu\nu})$. A manifold $\mathcal{M}$ is an abstract mathematical structure, where every point has a neighborhood resembling Euclidean space. The metric enters the line element:

$$ds^2 = g_{\mu\nu} dx^\mu dx^\nu \,, \tag{2.1}$$

which measures distances in $\mathcal{M}$. Here dx^μ are coordinate basis vectors, and Einstein's sum convention applies. $g_{\mu\nu}$ is the central object of GR. It defines a scalar product between vectors, and hence introduces the notion of orthogonality and of measuring lengths. The metric further serves to raise and lower indices of tensors on $\mathcal{M}$.

In curved spacetimes, i.e. spacetimes containing matter, singularities, radiation or other forms of energy, the concept of derivatives has to be generalized. The reason is that if space is curved, basis vectors may differ from one point of the manifold to another like in the case of curvilinear coordinates. Therefore, the usual directional derivative is no longer invariant under transformations. By introducing connections, which describe the change of the basis vectors between two points of the manifold, one can define the co-variant derivative ∇:

$$\nabla_\alpha T^\mu{}_\lambda = T^\mu{}_{\lambda,\alpha} + \Gamma^\mu{}_{\rho\alpha} T^\rho{}_\lambda - \Gamma^\rho{}_{\lambda\alpha} T^\mu{}_\rho \,. \tag{2.2}$$

Here $\Gamma^\mu{}_{\rho\alpha}$ is a particular connection called Christoffel symbol, and ∂_α is the usual partial derivative with respect to the coordinate x^α. The connection $\Gamma^\mu{}_{\rho\alpha}$ has the unique property of generating metric compatible derivatives, i.e. $\nabla_\alpha g^{\alpha\beta} = 0$, and the ∇_α are torsion free. The latter expression means for any vector fields $\mathbf{X}$ and $\mathbf{Y}$ on $\mathcal{M}$ that $\nabla_{\mathbf{X}}\mathbf{Y} - \nabla_{\mathbf{Y}}\mathbf{X} =: [\mathbf{X}, \mathbf{Y}]$, where $[\mathbf{X}, \mathbf{Y}]$ is the Lie bracket for vector fields, and $\nabla_{\mathbf{X}} := X^\mu \nabla_\mu$. The Christoffel symbols are defined by

$$\Gamma^\gamma{}_{\mu\nu} := \frac{1}{2} g^{\gamma\rho} \left(g_{\rho\nu,\mu} + g_{\mu\rho,\nu} - g_{\mu\nu,\rho} \right) . \tag{2.3}$$

With the Christoffel symbols we can write down a tensor, which describes the geometry of the spacetime, the Riemann tensor $R^\alpha{}_{\beta\gamma\delta}$:

$$R^\alpha{}_{\beta\gamma\delta} := \Gamma^\alpha{}_{\delta\beta,\gamma} - \Gamma^\alpha{}_{\gamma\beta,\delta} + \Gamma^\alpha{}_{\gamma\rho}\Gamma^\rho{}_{\delta\beta} - \Gamma^\alpha{}_{\delta\rho}\Gamma^\rho{}_{\gamma\beta} \tag{2.4}$$

It represents the change of a vector field $\mathbf{V}$ while being parallel transported around a closed loop, and can be expressed alternatively as

$$R^\alpha{}_{\beta\gamma\delta} V^\beta = \nabla_\gamma \nabla_\delta V^\alpha - \nabla_\delta \nabla_\gamma V^\alpha \,. \tag{2.5}$$

Parallel transport in this context means that any two vectors which are transported parallel along a smooth path preserve the angle in between them.

The Riemann tensor contains the information of how the spacetime is curved. Two

related expressions are the contractions

$$R_{\mu\nu} := R^{\alpha}{}_{\mu\alpha\nu}\,, \tag{2.6}$$

$$R := R^{\alpha}{}_{\alpha}\,. \tag{2.7}$$

Where $R_{\mu\nu}$ is the Ricci tensor and R is the Ricci scalar. With these two and the stress-energy tensor $T_{\mu\nu}$, which describes the energy and matter contained in the spacetime, we are able to write down the Einstein field equations

$$G_{\mu\nu} := R_{\mu\nu} - \frac{1}{2} g_{\mu\nu} R = 8\pi T_{\mu\nu}\,, \tag{2.8}$$

where $G_{\mu\nu}$ is the Einstein tensor. Expression (2.8) hides all the complexity incorporated in it behind the elegant tensor notation. Explicitly written Eqs. (2.8) consist of a set of ten coupled, non-linear, partial differential equations containing contractions of the Riemann tensor. In general, the latter is a complicated object itself and consists of Christoffel symbols, the metric and its derivatives. Altogether thousands of terms are easily reached. The contraction of the Einstein tensor with the co-variant derivative leads to

$$\nabla_{\nu} G^{\mu\nu} = 0\,, \tag{2.9}$$

This is a direct consequence of the Bianchi identities, which follow from the symmetry of the Riemann tensor. Eqs. (2.9) imply directly local conservation of energy and momentum

$$\nabla_{\nu} G^{\mu\nu} = \nabla_{\nu} T^{\mu\nu} = 0\,. \tag{2.10}$$

In a curved spacetime a straight line is not a priori the shortest connection between two points. A free falling particle or photon, does not follow a straight line in general. This is an important difference between GR and Euclidean geometry. The equivalent to a straight line in a curved manifold is called geodesic. A geodesic is a path, which parallel transports its own tangent vector

$$t^{\mu} := \left(\frac{dx^{\mu}}{d\lambda} \right) \tag{2.11}$$

according to

$$\frac{D}{d\lambda} t^{\mu} := \frac{dx^{\mu}}{d\lambda} \nabla_{\mu} \left(\frac{dx^{\mu}}{d\lambda} \right) = 0\,, \tag{2.12}$$

where λ is the affine parameter describing the curve. With the definition of the co-variant derivative, this can be transformed into the alternative formulation of the geodesic equa-

tion

$$\frac{d^2x^\mu}{d\lambda^2} + \Gamma^\mu{}_{\rho\sigma}\frac{dx^\rho}{d\lambda}\frac{dx^\sigma}{d\lambda} = 0\,. \tag{2.13}$$

Some standard text books covering the topic of General Relativity are: Misner et al. (1973), Wald (1984) and Carroll (2004).

2.1.2 The "3+1" split of General Relativity

The formulation of the theory of relativity in terms of Expression (2.8) is very elegant and very appealing in terms of having a simple expression containing all information. However, for the numerical implementation and to solve any dynamical problem, Eqs. (2.8) are not very useful, because of their intrinsic complexity. Following Lichnerowicz (1944) and Choquet-Bruhat (1952) it is possible to express the Einstein equations in a form more suitable and more intuitive for numerical integration. In their "3+1"-approach the four-dimensional manifold is split into three space dimensions and one time dimension, allowing to write the Einstein equations as a system of partial differential equations. Later, York (1979) proposed a formalism which is widely used until today. Based on the "3+1" split Arnowitt, Deser and Misner developed their famous ADM formalism describing the GR evolution equations in a canonical Hamiltonian formulation (Arnowitt et al., 1962).

In the "3+1" framework the unified four-dimensional manifold $\mathcal{M}$ is decomposed into a set of space-like hypersurfaces Σ_t. These three-dimensional submanifolds are said to be embedded in $\mathcal{M}$. Embedding in the current context is defined as a one-to-one map from the three-dimensional manifold $\hat{\Sigma}$ to its image Σ in $\mathcal{M}$

$$\Phi : \hat{\Sigma} \to \Sigma\,, \tag{2.14}$$

with Φ and Φ^{-1} being continuous. See Figure 2.1 for an illustration. This embedding brings new notions of push-forwards, pull-backs and projections with it. Since Φ carries points from $\hat{\Sigma}$ to $\mathcal{M}$, it trivially describes a curve $\Phi(C)$ in $\mathcal{M}$ based on C in $\hat{\Sigma}$. We have seen that a parametrized curve defines its own tangent vector (Eq. (2.11). Φ defines thus a push-forward Φ_* as a mapping of vectors from $\hat{\Sigma}$ to vectors from $\mathcal{M}$, i.e. $\Phi_* : \mathcal{T}_p(\hat{\Sigma}) \to \mathcal{T}_p(\mathcal{M})$, where $\mathcal{T}_p(\hat{\Sigma})$ ($\mathcal{T}_p(\mathcal{M})$) is the tangent space of $\hat{\Sigma}$ ($\mathcal{M}$). Similarly one can define the pull-back Φ^* of linear forms on $\mathcal{M}$ to $\hat{\Sigma}$ as the map $\Phi^* : \mathcal{T}_p^*(\mathcal{M}) \to \mathcal{T}_p^*(\hat{\Sigma})$. Here $\mathcal{T}_p^*$ is the cotangent space of the corresponding manifold.

These maps introduce new objects on the hypersurface Σ. One very important application of the pull-back operation defines the induced metric γ, which in some context is also called the three-metric or spatial metric:

$$\gamma := \Phi^*\mathbf{g}\,. \tag{2.15}$$

In terms of an appropriate coordinate system $x^\mu = (t, x^i)$, where the scalar field t defines

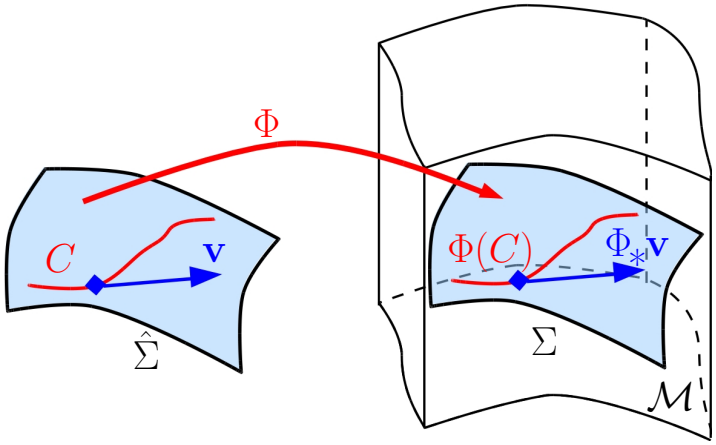

Figure 2.1: Illustration of the embedding of a three-dimensional manifold $\hat{\Sigma}$ into the four-dimensional manifold $\mathcal{M}$. The embedding Φ maps $\hat{\Sigma}$ to its image Σ, a hypersurface in $\mathcal{M}$. Φ directly translates any curve C from $\hat{\Sigma}$ to Σ, thereby defining the push-forward of a tangent vector $\mathbf{V}$ on C to $\Phi_*\mathbf{V}$ being a tangent vector to $\Phi(C)$.

the hypersurfaces Σ_t as its level surfaces, the explicit coordinate form of γ is given by

$$\gamma_{ij} = g_{ij}\,. \tag{2.16}$$

Strictly speaking this *slicing* of $\mathcal{M}$ into different Σ_t is only possible for a continuous set of hypersurfaces $(\Sigma_t)_{t\in\mathbb{R}}$ that covers the whole manifold M. This implies that $(\mathcal{M}, g_{\mu\nu})$ has to be a globally hyperbolic spacetime (see for example Gourgoulhon, 2007). The metric dual to the gradient $\mathbf{d}t$ of the scalar field t is indicated by ∇t and is always normal to the hypersurfaces Σ_t. If Σ is not null, i.e. $\nabla t \neq 0$, the normalization of ∇t is defined as

$$\mathbf{n} := \frac{\nabla t}{\sqrt{\pm \nabla t \cdot \nabla t}} \tag{2.17}$$

Specifying to space-like hypersurfaces Σ_t, i.e. the three-metric has to be positive definite, we define the *lapse* function

$$\alpha := \frac{1}{\sqrt{-\nabla t \cdot \nabla t}}\,. \tag{2.18}$$

α is associated with the normal $\mathbf{n}$ by $\mathbf{n} := -\alpha \nabla t$. The product $\mathbf{m} := \alpha\mathbf{n}$ is called the normal evolution vector and provides a way to evolve the hypersurface Σ_t along its normal by a small displacement $\delta t\mathbf{m}$ to the hypersurface $\Sigma_{t+\delta t}$. See Figure 2.2 for an illustration, where we show the "3+1" split in an adapted coordinate system $x^\mu = (t, x^i)$. The spatial coordinates x^i are supposed to vary smoothly from one hypersurface to the next. The vector $\partial_t := \frac{\partial}{\partial t}$, associated to the coordinate t, is called *time vector*. In general

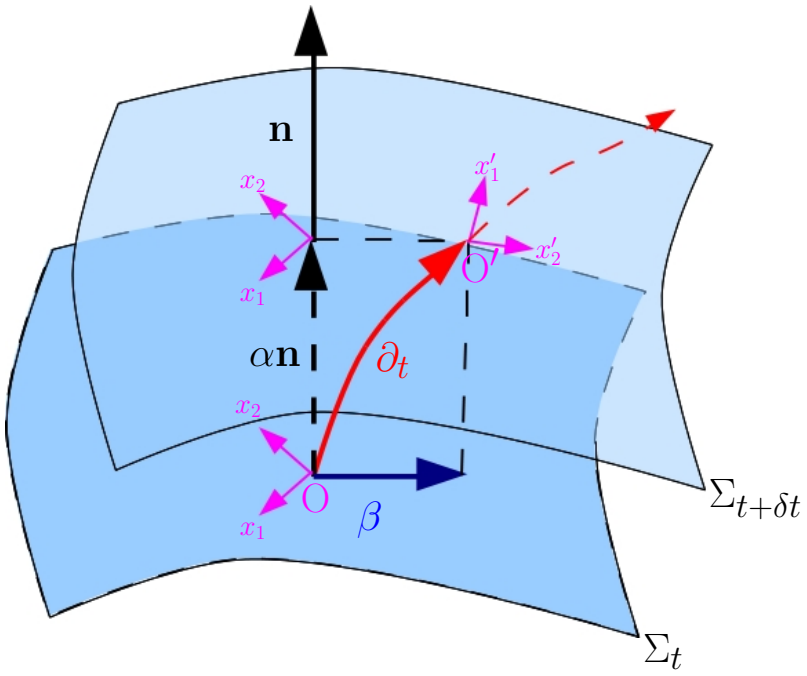

Figure 2.2: Illustration of the "3+1" split of General Relativity. The time vector $\partial_t = \alpha\mathbf{n} + \beta$ gives the change of coordinates from one hypersurface Σ_t to the next $\Sigma_{t+\delta T}$. $\mathbf{n}$ is the time-like surface normal, β is the shift vector and α the lapse.

∂_t is different from the normal evolution vector $\mathbf{m}$, because the coordinate system x^i on Σ_t may evolve from one hypersurface to the next (Figure 2.2). The coordinates change between the hypersurfaces by the *shift vector* β according to

$$\partial_t =: \mathbf{m} + \beta = \alpha \cdot \mathbf{n} + \beta \tag{2.19}$$

The metric $g_{\mu\nu}$ expressed in this coordinate system can be represented by the following line element:

$$g_{\mu\nu} dx^\mu dx^\nu = -\alpha^2 dt^2 + \gamma_{ij}(dx^i + \beta^i dt)(dx^j + \beta^j dt) \tag{2.20}$$

Above we have introduced the operations of pull-back and push-forward, which are maps from $\mathcal{T}_p^*(\mathcal{M}) \to \mathcal{T}_p(\Sigma)$ and $\mathcal{T}_p(\Sigma) \to \mathcal{T}_p(\mathcal{M})$, respectively. With the notion of the normal vector $\mathbf{n}$, we are able to provide the reverse mappings. We therefore define the orthogonal projector $\perp$ as a map from $\mathcal{T}_p(\mathcal{M}) \to \mathcal{T}_p(\Sigma)$ which can be expressed in the corresponding basis as

$$\perp^\alpha_\beta := \delta^\alpha_\beta + n^\alpha n_\beta \,. \tag{2.21}$$

$\perp_{\alpha\beta}$ acts in the same way as γ_{ij} on vectors $\mathbf{V}$ on Σ:

$$\perp_{\alpha\beta} V^\alpha V^\beta = g_{\alpha\beta} V^\alpha V^\beta + n_\alpha V^\alpha n_\beta V^\beta = g_{\alpha\beta} V^\alpha V^\beta = g_{ij} V^i V^j = \gamma_{ij} V^i V^j \,, \tag{2.22}$$

where the second equality comes from the orthogonality of $\mathbf{n}$ and any vector $\mathbf{V}$ on Σ, the third one from the definition of $\mathbf{V}$ in adapted coordinates $V^\alpha = (0, V^i)$, and the last one from Eq. (2.16). Therefore, $\perp$ can be regarded as the extended three-metric γ with the first index raised by the metric.

With the projections and maps between the four-dimensional manifold $\mathcal{M}$ and the three-dimensional submanifold Σ, we can express the Einstein equations (2.8) as a system of second-order, non-linear, partial differential equations. The unknown variables appearing in this formulation are (γ_{ij}, α, β^i, K_{ij}). Where K_{ij} is the extrinsic curvature and describes how the three-manifold Σ is "bend" by the embedding inside $\mathcal{M}$ (see Gourgoulhon, 2007).

The resulting set of equations splits into two classes: the evolution equations for the extrinsic curvature K_{ij} and the three-metric γ_{ij}, and the constraint equations. The latter can be obtained from the conservation conditions of the stress-energy tensor $\nabla_\nu T^{\mu\nu} = 0$ and its projections: the mass-energy density $E := T_{\alpha\beta} n^\alpha n^\beta$, and the momentum density $p_\alpha := -T_{\mu\nu} \perp^\nu_\alpha n^\mu$ (Gourgoulhon, 2007). These equations do not influence the evolution, but they have to be satisfied on each hypersurface at any time. In this formulation the Einstein equations are reduced to an initial value problem. Providing the three-metric and its time derivative at the initial slice Σ_0, γ can be evolved subject to the constraints. For further information about numerical relativity, we refer the reader to the review of York (1979), and the lecture notes of Gourgoulhon (2007).

To the end of this section we introduce two particular observers naturally arising in the geometry of the "3+1" split: the Eulerian and the Lagrangian observer. The first one is associated to the four-velocity $\mathbf{n}$. We can express its components as

$$n^\mu = \frac{1}{\alpha}(1, -\beta^1, -\beta^2, -\beta^3) \,, \tag{2.23}$$

$$n_\mu = (-\alpha, 0, 0, 0) \,. \tag{2.24}$$

The Lagrangian or co-moving observer can only be defined in spacetimes containing matter. It follows the path of fluid elements with the four-velocity $\mathbf{u}$. This velocity is related to the three-velocity of the fluid $\mathbf{v}$ as measured by the Eulerian observer

$$v^i := \frac{\perp^i_\mu u^\mu}{-n_\alpha u^\alpha} = \frac{u^i}{\alpha u^t} + \frac{\beta^i}{\alpha}, \tag{2.25}$$

where $-n_\alpha u^\alpha = W$ is the relative Lorentz factor between $\mathbf{u}$ and $\mathbf{n}$. The last equality can be easily verified when inserting the previous definitions of $\perp$ and $\mathbf{n}$.

2.2 General-relativistic magneto-hydrodynamics

2.2.1 Conservation equations

To describe magnetized fluids in the context of General Relativity it is necessary to provide the right-hand side of the Einstein equations (2.8), i.e. the stress-energy tensor $T_{\mu\nu}$. In this work we follow the Valencian formulation of general-relativistic magneto-hydrodynamics (GRMHD) mainly presented in Antón et al. (2006). A very comprehensive review on the topic of GRMHD containing references to different approaches is given by Font (2008). More information on the mathematical structure of the equations and some general applications of the formalism can be found in a textbook by Anile (1989).

For simplicity the matter is assumed to be in the state of a perfect fluid and perfect conductor. Thereby we neglect physical properties/effects like shear stresses, electric resistivity, viscosity, superfluidity, superconductivity, heat conduction, and radiation transfer for the moment. Later in Section 2.3 we treat the effect of shear stresses appearing in the solid crust. The other non-adiabatic processes mentioned here are assumed to have only a small influence on the dynamics of the neutron star interior under the conditions which we are studying. A perfect fluid is completely described by its rest frame mass density ρ and the isotropic pressure P. The corresponding stress-energy tensor is given by

$$T^{\mu\nu}_{\text{Fluid}} = \rho h u^\mu u^\nu + P g^{\mu\nu} \,, \tag{2.26}$$

where $h := 1 + \epsilon + P/\rho$ is the specific enthalpy and ϵ the specific internal energy.

The contribution of the electromagnetic field to the stress-energy tensor is given by (see Jackson, 1975, for details)

$$T^{\mu\nu}_{\text{EM}} = F^{\mu\lambda} F^{\ \nu}_{\lambda} - \frac{1}{4} g^{\mu\nu} F^{\lambda\delta} F_{\lambda\delta} \,. \tag{2.27}$$

Here we introduced the Faraday electromagnetic tensor $\mathbf{F}$. This tensor completely describes the electromagnetic field, and defines the electric field $\mathbf{E}$ and the magnetic field $\mathbf{B}$, as they are measured by an arbitrary observer with four-velocity $\tilde{\mathbf{U}}$. With $\mathbf{E}$, $\mathbf{B}$ and $\tilde{\mathbf{U}}$ we can express $\mathbf{F}$ as:

$$F^{\mu\nu} = \tilde{U}^\mu E^\nu - \tilde{U}^\nu E^\mu - \eta^{\mu\nu\lambda\delta} \tilde{U}_\lambda B_\delta \,. \tag{2.28}$$

Here $\eta^{\mu\nu\lambda\delta}$ is defined as

$$\eta^{\mu\nu\lambda\delta} = \frac{1}{\sqrt{-g}} \varepsilon^{\mu\nu\lambda\delta} \tag{2.29}$$

with $g = det(g_{\mu\nu})$ and $\varepsilon^{\mu\nu\lambda\delta}$ is the completely antisymmetric Levi-Civita symbol. Note that the electromagnetic stress-energy tensor in Eq. (2.27) is given in the Heaviside-

Lorentz system of electromagnetic units with $c = 1$ (Jackson, 1975).

For a co-moving observer with $\tilde{U}^\mu = u^\mu$, the electric field vanishes as a consequence of the ideal MHD condition. In this case $\mathbf{F}$ can be expressed in terms of the magnetic field b^μ alone: $F^{\mu\nu} = -\eta^{\mu\nu\lambda\delta} u_\lambda b_\delta$. The contribution of the magnetic field to the stress-energy tensor becomes:

$$T^{\mu\nu}_{\rm EM} = \left(u^\mu u^\nu + \frac{1}{2} g^{\mu\nu} \right) b^2 - b^\mu b^\nu \,, \tag{2.30}$$

where $b^2 = b^\mu b_\mu$. The complete stress-energy tensor of magneto-fluids is thus given by

$$T^{\mu\nu} = T^{\mu\nu}_{\rm Fluid} + T^{\mu\nu}_{\rm EM} = \rho h^* u^\mu u^\nu + P^* g^{\mu\nu} - b^\mu b^\nu \,, \tag{2.31}$$

where we introduced the generalized enthalpy h^* and pressure P^*, containing the magnetic pressure $P_{\rm magn} := \frac{1}{2} b^2$ and the specific magnetic energy $\varepsilon_{\rm magn} := \frac{1}{2\rho} b^2$:

$$h^* := h + \frac{b^2}{\rho} = 1 + \varepsilon^* + \frac{P^*}{\rho} \tag{2.32}$$

$$\varepsilon^* := \varepsilon + \varepsilon_{\rm magn} = \varepsilon + \frac{1}{2} \frac{b^2}{\rho} \tag{2.33}$$

$$P^* := P + P_{\rm magn} = P + \frac{1}{2} b^2 \tag{2.34}$$

Knowing the stress-energy tensor we are able to integrate the Einstein equations in order to obtain an evolution for the spacetime geometry. However, we have no information about the behavior of the matter variables ρ, P, v^i, ε, and b^μ. To evolve these unknowns we use the conservation of energy and momentum (Eq. (2.10))

$$\nabla_\nu T^{\mu\nu} = 0 \,, \tag{2.35}$$

and the baryon number conservation

$$\nabla_\nu J^\nu = 0 \,, \tag{2.36}$$

where $\mathbf{J}$ is the rest mass current $J^\nu = \rho u^\nu$. Following Antón et al. (2006) by writing these equations in terms of an Eulerian observer, Eqs. (2.35) and (2.36) can be expressed as a general-relativistic conservation law:

$$\frac{1}{\sqrt{-g}} \left(\frac{\partial \sqrt{\gamma} \mathbf{U}}{\partial t} + \frac{\partial \sqrt{-g} \mathbf{F}^i}{\partial x^i} \right) = \mathbf{S} \,. \tag{2.37}$$

The conserved variables $\mathbf{U}$, fluxes $\mathbf{F}^i$, and sources $\mathbf{S}$ are given by

$$\mathbf{U} = \begin{bmatrix} D \\ S_j \\ \tau \end{bmatrix} \,, \tag{2.38}$$

$$\mathbf{F}^i = \begin{bmatrix} D\hat{v}^i \\ S_j\hat{v}^i + \delta^i_j\left(P + \frac{1}{2}b^2\right) - \frac{b_j B^i}{W} \\ \tau\hat{v}^i + \hat{v}^i\left(P + \frac{1}{2}b^2\right) - \frac{\alpha b^0 B^i}{W} \end{bmatrix}, \tag{2.39}$$

$$\mathbf{S} = \begin{bmatrix} 0 \\ \frac{1}{2}T^{\mu\nu}\frac{\partial g_{\mu\nu}}{\partial x^j} \\ \alpha T^{\mu\nu}\left(\delta^0_\nu \frac{\partial ln\alpha}{\partial x^\mu} - \Gamma^0_{\nu\mu}\right) \end{bmatrix}, \tag{2.40}$$

where $\hat{v}^i := v^i - \beta^i/\alpha$, and we have introduced the following projections of the different tensors:

$$D := J_\nu n^\nu = \rho W\,, \tag{2.41}$$

$$S_j := -T^\mu_j n_\mu = \rho h^* W^2 v_i - \alpha b_i b^0\,, \tag{2.42}$$

$$\tau := T^{\mu\nu} n_\mu n_\nu = \rho h^* W^2 - P^* - \alpha^2 (b^0)^2 - D\,. \tag{2.43}$$

with D being the relativistic mass density, S_j the relativistic momentum density in the j-th direction, and τ the relativistic energy density.

Eqs. (2.38) and (2.39) contain the four-vector of the magnetic field in the co-moving frame b^μ and the three-vector measured by an Eulerian observer B^i. Both are related to each other by the following expressions

$$b^0 = \frac{W B^i v_i}{\alpha}\,, \tag{2.44}$$

$$b^i = \frac{B^i + \alpha b^0 u^i}{W}\,. \tag{2.45}$$

To close the system (2.38), (2.39), and (2.40) requires an equation of state (EoS) which relates the thermodynamical quantities pressure P, energy density ρ, internal energy ε, and temperature. The temperature of a cold, not extremely young neutron star of $T \approx 10^6$ K is much lower than the Fermi energy of the neutrons $T_F \gtrsim 10^{11}$ K. Therefore, we can safely neglect any dependence of the physical variables on the temperature. This simplifies the relations between the different thermodynamical quantities and a one parameter EoS is sufficient. Such a barotropic EoS can be expressed as follows:

$$P = P(\rho)\,, \tag{2.46a}$$

$$\varepsilon = \varepsilon(\rho)\,. \tag{2.46b}$$

This choice of an EoS simplifies the system of equations in the sense that the equation for the relativistic energy density is redundant.

2.2.2 Maxwell equations

The EoS (2.46) and the system of equations (2.37) with Eqs. (2.38), (2.39) and (2.40) provide evolution equations for the matter variables D and S_j. However, we also require

the information about how to propagate the magnetic field. For this purpose we use the relativistic Maxwell equations:

$$\nabla_\nu {}^*F^{\mu\nu} = 0\,, \tag{2.47a}$$
$$\nabla_\nu F^{\mu\nu} = 4\pi \mathcal{J}^\mu\,, \tag{2.47b}$$

where ${}^*F^{\mu\nu} = \frac{1}{2}\eta^{\mu\nu\lambda\delta}F_{\lambda\delta}$ is the dual of the Faraday electromagnetic tensor and $\mathcal{J}^\mu$ is the electric four-current. This four-current is related to the proper charge density ρ_q in the co-moving frame by Ohm's law

$$\mathcal{J}^\mu = \rho_q u^\mu + \sigma F^{\mu\nu}u_\nu\,. \tag{2.48}$$

Here σ is the electric conductivity. We model the fluid as perfect conductor and therefore assume the conductivity to be infinite. This condition implies that, in order to keep the current finite, the term $F^{\mu\nu}u_\nu$ has to vanish exactly. This signifies that the co-moving electric field is assumed to be zero $e^\mu = F^{\mu\nu}u_\nu = 0$. The electric field measured by an Eulerian observer $\mathbf{n}$ is thus determined by the magnetic field $\mathbf{B}$

$$E^\mu = \frac{1}{W}\eta^{\mu\nu\lambda\delta}u_\nu n_\lambda B_\delta\,, \tag{2.49}$$
$$E^0 = 0\,, \tag{2.50}$$
$$E^i = -\alpha\eta^{0ijk}v_j B_k\,. \tag{2.51}$$

With ${}^*F^{\mu\nu} = \left(u^\mu B^\nu - u^\nu B^\mu\right)/W$ the Maxwell equations (2.47) lead to

$$\frac{\partial\sqrt{\gamma}B^i}{\partial x^i} = 0\,, \tag{2.52}$$
$$\frac{1}{\sqrt{\gamma}}\frac{\partial\sqrt{\gamma}B^i}{\partial t} = \frac{1}{\sqrt{\gamma}}\frac{\partial}{\partial x^j}\left(\sqrt{\gamma}\left[(\alpha v^i - \beta^i)B^j - (\alpha v^j - \beta^j)B^i\right]\right)\,. \tag{2.53}$$

2.2.3 Eigenvalues of the equations

The wave structure of the system of equations is best analyzed in terms of the corresponding eigenvalues, which describe how different types of waves propagate according to the equations. The analysis of the GRMHD system in terms of the co-variant variables (u^μ, b^μ, P, s), s being the specific entropy, was done by Anile (1989). In the present description the eigenvalues along the coordinate directions are given by Antón et al. (2006)

$$\lambda_e = \alpha v^i - \beta^i\,, \tag{2.54}$$
$$\lambda_{a\pm} = \frac{b^i \pm \sqrt{\rho h + B^2}u^i}{b^0 \pm \sqrt{\rho h + B^2}u^0}\,, \tag{2.55}$$

where λ_e and $\lambda_{a\pm}$ are the eigenvalues for entropy, and Alfvén waves, respectively. The third class of eigenvalues for the magneto-sonic waves cannot be expressed explicitly. They are found by numerically solving a quartic equation (see Antón et al., 2006, for details).

2.3 Relativistic elasticity

In this section we follow the work of Karlovini and Samuelsson (2003) who developed a framework to describe elastic matter in General Relativity in a series of papers including Karlovini et al. (2004); Karlovini and Samuelsson (2004). In the last paper of this series, Karlovini and Samuelsson (2007) apply their framework to axial perturbations of the crust of neutrons stars for the first time in full General Relativity. The work of Karlovini and collaborators is based on the fundamental contribution to the field by Carter and Quintana (1972), who for the first time developed a consistent theory of *perfectly elastic* matter in a general relativistic framework. In Newtonian physics the term perfect or *hyper elasticity* is reserved for materials, whose shape under equal conditions is always the same, i.e. the deformation is independent of the history of the material. The latter always preserves its shape when the same strain is applied.[1] This implies that any deformation of the material is thermodynamically reversible, or in other words the entropy of the medium is conserved. Similar to the perfect fluid approximation this excludes viscous media. However, in General Relativity the condition of perfect elasticity has to be generalized to include the following requirements (Carter and Quintana, 1972): First, no energy of the material is allowed to be transported relative to the local rest frame of the medium, i.e. u^μ has to be an eigenvector of the stress-energy tensor $T^{\mu\nu}$. Second, external fields are not allowed to do work on the medium. In other words, the force density f^μ caused by external fields has to obey the energy momentum conservation $\nabla_\nu T^{\mu\nu} = f^\mu$, and simultaneously has to satisfy the orthogonality condition $f^\mu u_\mu = 0$. An example for an external field fulfilling these conditions is the electromagnetic field of an unpolarizable, perfect conductor given by the Faraday tensor $F^{\mu\nu}$ described in the previous section. This property is essential to combine the two physical effects of elasticity and magneto-hydrodynamics in order to study the magneto-elastic oscillations of neutron stars.

Recently, a number of existence and uniqueness theorems concerning local solutions to the equations of relativistic elasticity have been proved by Beig and Schmidt (2003).

Here we sketch the theory of previous work by Carter and Quintana (1972) and Karlovini and Samuelsson (2003). To start with we introduce a three-dimensional manifold $\mathcal{X}$, which is referred to as the *material space* (see Figure 2.3). The points in $\mathcal{X}$ can be thought of as being idealized particles of the medium. On this manifold $\mathcal{X}$ tensors

[1] For an introduction to the theory of elasticity in the Newtonian framework see Landau and Lifshitz (1986).

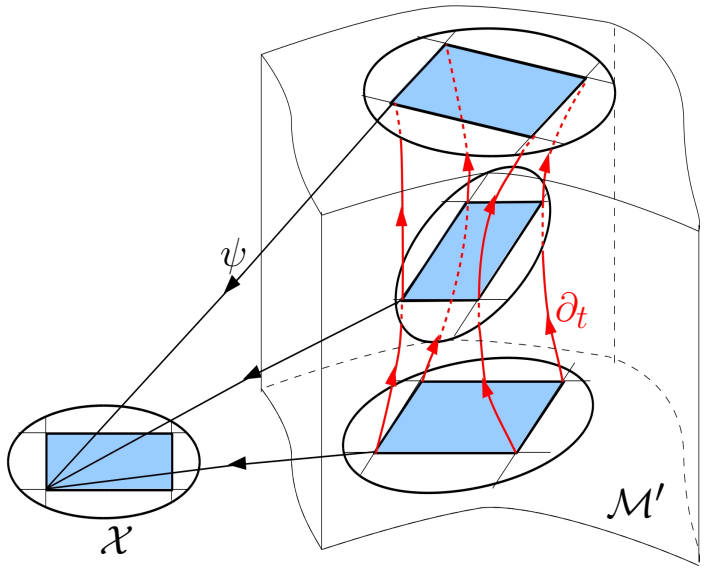

Figure 2.3: Illustration of the projection ψ from the material filled part of the four-dimensional spacetime manifold $\mathcal{M}' \subset \mathcal{M}$ onto the three-dimensional material space $\mathcal{X}$. Red lines indicate the world lines of virtual particles following the flow vector u^μ.

can be defined as usual. We further introduce a differentiable mapping ψ

$$\psi : \mathcal{M}' \to \mathcal{X} \,, \tag{2.56}$$

which relates $\mathcal{X}$ to a material-filled, open four-dimensional submanifold $\mathcal{M}' \subset \mathcal{M}$ of the full spacetime manifold $\mathcal{M}$. One may interpret $\mathcal{M}'$ as that part of the spacetime $\mathcal{M}$ through which the medium passes. The mapping ψ introduces the corresponding pull-back ψ^* and the push-forward ψ_* as defined in Section 2.1.2. Note that ψ in the current context maps points from $\mathcal{M}'$ to a lower-dimensional manifold $\mathcal{X}$. Contra-variant tensors t^λ from $\mathcal{M}'$, are pushed forward to $t^\Lambda = \psi_* t^\lambda$ on $\mathcal{X}$ and co-variant material space tensors t_Λ from $\mathcal{X}$ are pulled back to $\mathcal{M}'$ as $t_\lambda = \psi^* t_\Lambda$. Here we introduced the short-hand notation that upper case Greek indices $\{\Theta, \Gamma, \Lambda\}$ are used to refer to tensors on $\mathcal{X}$ and lower case Greek indices $\{\theta, \gamma, \lambda\}$ to tensors on $\mathcal{M}'$. The mapping ψ further gives the preimage of any point $p \in \mathcal{X} = \psi(\mathcal{M}')$, and $\psi^{-1}(p)$ is assumed to be a single time-like curve in $\mathcal{M}'$. Therefore, it can be interpreted as the flowline of an idealized particle represented by p (see the red lines in Figure 2.3).

The fundamental tensor of the theory of relativistic elasticity is the totally antisymmetric *particle density* $n_{\Gamma\Theta\Lambda} = n_{[\Gamma\Theta\Lambda]}$. Its integral over some volume in $\mathcal{X}$ is the particle number inside this volume. The pull back on $\mathcal{M}'$ $n_{\gamma\theta\lambda} = \psi^* n_{\Gamma\Theta\Lambda}$ defines the flowline tangential particle current

$$n^\alpha = \frac{1}{3!} \eta^{\alpha\beta\gamma\delta} n_{\beta\gamma\delta} \,, \tag{2.57}$$

which is conserved ($\nabla_\alpha n^\alpha = 0$), and we can set $n^\alpha = nu^\alpha$. This directly provides the continuity equation. Here n is the usual particle density fulfilling $n_{\alpha\beta\gamma} = n\eta_{\alpha\beta\gamma}$. Note that $\eta_{\alpha\beta\gamma} = \eta_{\alpha\beta\gamma\delta}u^\delta$ is the spatial volume form[2] of the material.

Our aim is to set up evolution equations for elastic solids. Therefore, the stress-energy tensor $T^{\mu\nu}$ has to be determined. The latter can be derived from an action principle (Karlovini and Samuelsson, 2003) and has the following general form

$$T_{\mu\nu} = -\rho' g_{\mu\nu} + 2\frac{\partial\rho'}{\partial g^{\mu\nu}} = \rho' u_\mu u_\nu + P_{\mu\nu}\,, \tag{2.58}$$

where $P_{\mu\nu} := 2\frac{\partial\rho'}{\partial g^{\mu\nu}} - \rho' h_{\mu\nu}$ is the pressure tensor, $\rho' := \rho(1+\varepsilon)$ is the total rest frame energy density, and $h_{\mu\nu} := u_\mu u_\nu + g_{\mu\nu}$ is the projection onto the co-moving material. We follow Karlovini and Samuelsson (2003) and search for an explicit expression of $T^{\mu\nu}$ in terms of scalars s_1, s_2, ... , which can be formed from pull backs of the material tensor fields $t_{\lambda\ldots}$ by contractions with $g^{\gamma\lambda}$. One already known example of such a scalar is the particle density n. To get $T^{\mu\nu} = T^{\mu\nu}(n, s_1, s_2, ...)$ one thus has to find an explicit expression for the total rest frame energy density ρ' in terms of this/these scalar/s. This relation is called an equation of state:

$$\rho' = \rho'(n, s_1, s_2, \dots)\,, \tag{2.59a}$$

$$P_{\mu\nu} = P_{\mu\nu}(n, s_1, s_2, \dots)\,. \tag{2.59b}$$

In what follows it is convenient to express ρ' in terms of n and the energy per particle ϵ: $\rho' = n\epsilon$. The kind of scalars required above can alternatively be obtained on the material space by using the pushed forward tensor $g^{\Gamma\Lambda}$ to contract with material tensors $t_{\Lambda\ldots}$. With this definition the total energy density is a function of $g^{\Gamma\Lambda}$. At a given particle density n we therefore can look for a minimum of ϵ under variations of $g^{\Gamma\Lambda}$. This $\check{\epsilon}$ describes the *unsheared* state of the material. If there exists an absolute minimum of ϵ, it can be called the completely relaxed state. However, under the extreme conditions in the crust of a neutron star whose crystal structure exists only due to the very strong pressure, the existence of such a completely relaxed state is not expected. The unsheared state will be used as a reference state, and we will denote the metric tensor at $\epsilon = \check{\epsilon}$ with the symbol $\check{g}_{\Gamma\Lambda}$ such that $g^{\Theta\Gamma}\check{g}_{\Gamma\Lambda} = \delta^\Theta_\Lambda$. To measure the strength of the strain causing a certain deformation on the material, one expands the deviation around a locally unsheared state. We therefore define the *constant volume shear tensor* $s_{\mu\nu}$

$$s_{\mu\nu} = \frac{1}{2}\left(h_{\mu\nu} - \check{g}_{\mu\nu}\right)\,. \tag{2.60}$$

Hereafter we call $s_{\mu\nu}$ in short the shear tensor. At this point we specify the equation of state. In addition to n only one further scalar of the shear tensor the shear scalar s^2 is considered. Furthermore we adopt the quasi-Hookean idealization and only

[2]The integral of the volume form in a given volume is the value of the volume itself $V = \int_{\text{vol}} \eta_{\alpha\beta\gamma} dx^\alpha dx^\beta dx^\gamma$

consider the lowest non-vanishing contributions to the equation of state. The prefix quasi in quasi-Hookean refers to an expansion around a unsheared state, instead of around a totally relaxed state. The definition of s^2 is not unique and different authors use different expressions. For perfect solids, i.e. for materials with isotropic symmetry in the elastic properties of the unsheared state, Carter and Quintana (1972) define $s^2 = \check{g}^{-1\mu\nu}\check{g}^{-1\lambda\delta}s_{\nu\lambda}s_{\delta\mu} - \frac{1}{3}\left(\check{g}^{\mu\nu}s_{\mu\nu}\right)^2$, while Karlovini and Samuelsson (2003) use the expression $s^2 = \frac{1}{36}\left[(\check{g}^{\mu}_{\mu})^3 - \check{g}^{\mu}_{\nu}\check{g}^{\nu}_{\lambda}\check{g}^{\lambda}_{\mu} - 24\right]$. In the following discussion the particular choice for s^2 is unimportant, and we do not specify it. In terms of n and s^2 an equation of state can be shown to have the following form (Carter and Quintana, 1972, see)

$$\rho' = \check{\rho}' + \mu_{\mathrm{S}} s^2 \,, \tag{2.61a}$$

$$P^{\mu\nu} = \left[\check{P} + \left(n\frac{\partial \mu_{\mathrm{S}}}{\partial n} + \frac{1}{3}\mu_{\mathrm{S}}\right)s^2\right]h^{\mu\nu} - 2\mu_{\mathrm{S}}\left[\check{g}^{\mu(\lambda}\check{g}^{\delta)\nu} - \frac{1}{3}\check{g}^{\mu\nu}\check{g}^{\lambda\delta}\right]s_{\lambda\delta} \,, \tag{2.61b}$$

where checked quantities refer to an unsheared state, and $\mu_{\mathrm{S}} = \mu_{\mathrm{S}}(n)$ is the shear modulus of the material. Eqs. (2.61) define the stress-energy tensor given in Eq. (2.58) and one could solve the corresponding system of equations in principle. The total stress-energy tensor of an elastic solid is:

$$\begin{aligned} T^{\mu\nu} =& T^{\mu\nu}_{\mathrm{Fluid}} + T^{\mu\nu}_{\mathrm{Elas}} \\ =& (\check{\rho}' + \check{P})u^{\mu}u^{\nu} + \check{P}g^{\mu\nu} + \\ & \mu_{\mathrm{S}}s^2u^{\mu}u^{\nu} + \left(n\frac{\partial \mu_{\mathrm{S}}}{\partial n} + \frac{1}{3}\mu_{\mathrm{S}}\right)s^2h^{\mu\nu} - 2\mu_{\mathrm{S}}\left[\check{g}^{\mu(\lambda}\check{g}^{\delta)\nu} - \frac{1}{3}\check{g}^{\mu\nu}\check{g}^{\lambda\delta}\right]s_{\lambda\delta} \end{aligned} \tag{2.62}$$

However, in Eq. (2.60) the shear tensor is defined in an abstract manner, but to solve the system of equations numerically we require to express $s_{\mu\nu}$ explicitly. Such a relation is obtained with the Lie derivative $\mathcal{L}$ of $s^{\mu\nu}$ along the four-velocity u^{μ}. $\mathcal{L}_u s^{\mu\nu}$ can be related to the rate of strain tensor $\sigma^{\mu\nu}$

$$\sigma^{\mu\nu} := \frac{1}{2}\left(u^{\mu}_{;\alpha}h^{\alpha\nu} + u^{\nu}_{;\alpha}h^{\alpha\mu}\right) + \frac{1}{3}h^{\mu\nu}u^{\alpha}_{;\alpha} \,, \tag{2.63}$$

by (Carter and Quintana, 1972; Schumaker and Thorne, 1983):

$$\sigma^{\mu\nu} = \mathcal{L}_u s^{\mu\nu} \,. \tag{2.64}$$

In Section 2.4.1 we show that if an appropriate coordinate system is selected, this equation gives rise to an expression for the strain tensor $s^{\mu\nu}$ in terms of the displacement ξ^i. The latter is related to the four-velocity of the fluid by $\xi^i_{,t} := \alpha v^i$

2.3.1 Eigenvalues of the equations

For simplicity we only give the eigenvalues obtained for the limit of vanishing shear. For the general expressions we refer to Karlovini and Samuelsson (2003). There the complete analysis for the Euler equations $\nabla_{\nu}T^{\mu\nu} = 0$ of elastic media in General Relativity is

presented, including also the non-zero shear case. The principal speeds of the evolution for longitudinal and for transverse propagation are

$$v_{\parallel}^2 = \frac{d\check{P}}{d\check{\rho}'} + \frac{4}{3}\frac{\mu_{\rm S}}{\check{\rho}' + \check{P}} \tag{2.65}$$

$$v_{\perp}^2 = \frac{\mu_{\rm S}}{\check{\rho}' + \check{P}}\,. \tag{2.66}$$

It is satisfactory that these correspond perfectly to their Newtonian counterparts, where we have to assume $\check{P} \to 0$, and in case of vanishing shear $\mu_{\rm S} = 0$ we recover purely sound waves with $v_{\parallel}^2 = \frac{d\check{P}}{d\check{\rho}'}$.

2.4 Elastic GRMHD equations for spherically symmetric background/ unsheared state

The combined stress-energy tensor of a perfectly conducting and perfectly elastic material with magnetic fields was presented in Carter and Samuelsson (2006a) and Carter and Samuelsson (2006b). In contrast to the previous section we omit the check on the unsheared variables ρ and P hereafter, because give all deviations from the unsheared state in terms of $s_{\lambda\sigma}$. The stress-energy tensor takes the form

$$\begin{aligned}
T^{\mu\nu} =& T^{\mu\nu}_{\rm Fluid} + T^{\mu\nu}_{\rm Elas} + T^{\mu\nu}_{\rm EM} \\
T^{\mu\nu} =& \left(\rho(1+\varepsilon) + P\right) u^\mu u^\nu + P g^{\mu\nu} + \\
& \mu_{\rm S} s^2 u^\mu u^\nu + \left(n\frac{\partial \mu_{\rm S}}{\partial n} + \frac{1}{3}\mu_{\rm S}\right) s^2 h^{\mu\nu} - 2\mu_{\rm S}\left[\check{g}^{\mu(\lambda}\check{g}^{\delta)\nu} + \frac{1}{3}\check{g}^{\mu\nu}\check{g}^{\lambda\delta}\right] s_{\lambda\delta} + \\
& \left(u^\mu u^\nu + \frac{1}{2} g^{\mu\nu}\right) b^2 - b^\mu b^\nu \\
=& \rho h^\sharp u^\mu u^\nu + P^\sharp g^{\mu\nu} - b^\mu b^\nu - 2\mu_{\rm S}\left[\check{g}^{\mu(\lambda}\check{g}^{\delta)\nu} - \frac{1}{3}\check{g}^{\mu\nu}\check{g}^{\lambda\delta}\right] s_{\lambda\delta}
\end{aligned} \tag{2.67}$$

Here we introduced the generalized enthalpy $h^\sharp$ and pressure $P^\sharp$, containing the magnetic pressure $P_{\rm EM} := \frac{1}{2}b^2$, the non-linear elastic pressure $P_{\rm elas} := \left(n\frac{\partial \mu_{\rm S}}{\partial n} + \frac{1}{3}\mu_{\rm S}\right) s^2$, the specific magnetic energy $\varepsilon_{\rm EM} := \frac{1}{2\rho}b^2$, and the specific elastic energy $\varepsilon_{\rm elas} := \mu_{\rm S} s^2/\rho$:

$$h^\sharp := h + \frac{b^2}{\rho} = 1 + \varepsilon^\sharp + \frac{P^\sharp}{\rho} \tag{2.68}$$

$$\varepsilon^\sharp := \varepsilon + \varepsilon_{\rm EM} + \varepsilon_{\rm elas} = \varepsilon + \frac{1}{2}\frac{b^2}{\rho} + \frac{\mu_{\rm S} s^2}{\rho} \tag{2.69}$$

$$P^\sharp := P + P_{\rm EM} + P_{\rm elas} = P + \frac{1}{2}b^2 + \left(n\frac{\partial \mu_{\rm S}}{\partial n} + \frac{1}{3}\mu_{\rm S}\right) s^2 \tag{2.70}$$

We are now able to write down the system of conservation equations describing magneto-elastic oscillations in neutron stars. This includes the conservation of energy and mo-

mentum $\nabla_\nu T^{\mu\nu}$, baryon number conservation $\nabla_\nu \rho u^\nu = 0$, and the Maxwell equations $\nabla_\nu F^{\mu\nu} = 4\pi \mathcal{J}^\mu$ for the magnetic field. The general metric is given by Eq. (2.20). In compact form the equations for the evolution of the matter variables and the magnetic field can be cast into a general-relativistic conservation law:

$$\frac{1}{\sqrt{-g}}\left(\frac{\partial\sqrt{\gamma}\mathbf{U}}{\partial t}+\frac{\partial\sqrt{-g}\mathbf{F}^i}{\partial x^i}\right)=\mathbf{S}\,. \tag{2.71}$$

The conserved variables $\mathbf{U}$, the fluxes $\mathbf{F}^i$, and the sources $\mathbf{S}$ are given by

$$\mathbf{U} = [D, S_j, \tau, B^k]\,, \tag{2.72}$$

$$\mathbf{F}^i = \begin{bmatrix} D\hat{v}^i \\ S_j\hat{v}^i + \delta^i_j P^\sharp - \frac{b_j B^i}{W} - 2\mu_{\rm S}\left[\check{g}^{i(\lambda}\check{g}^{\delta)}{}_j - \frac{1}{3}\check{g}^i{}_j\check{g}^{\lambda\delta}\right]s_{\lambda\delta} \\ \tau\hat{v}^i + \hat{v}^i P^\sharp - \frac{\alpha b^t B^i}{W} \\ \hat{v}^i B^k - \hat{v}^k B^i \end{bmatrix}, \tag{2.73}$$

$$\mathbf{S} = \left[0, \frac{1}{2}T^{\mu\nu}\frac{\partial g_{\mu\nu}}{\partial x^j}, \alpha T^{\mu\nu}\left(\delta^t_{\ \nu}\frac{\partial ln\alpha}{\partial x^\mu} - \Gamma^t_{\ \nu\mu}\right), 0, 0, 0\right], \tag{2.74}$$

where

$$D = \rho W\,, \tag{2.75}$$

$$S_i = \rho h^\sharp W^2 v_i - \alpha b_i b^t\,, \tag{2.76}$$

$$\tau = \rho h^\sharp W^2 - P^\sharp - \alpha^2 (b^t)^2 - D\,. \tag{2.77}$$

2.4.1 GRMHD equations for torsional oscillations of neutron stars

In this subsection we specify the rather general expressions of the previous section to the case of torsional oscillations of neutron stars by applying a number of simplifications.

- When neglecting the magnetic field, the background neutron star is assumed to be spherically symmetric. The natural choice of coordinates is thus the system of spherical coordinates $x^\mu = (t, r, \theta, \phi)$. The corresponding slices Σ_t can be trivially mapped with the three-dimensional spheres characterized by (r, θ, ϕ). Spherical symmetry excludes the effects of the deformation caused by the magnetic field. However, these deviations are supposed to be negligible for realistic magnetic field strength of $B \lesssim 5 \times 10^{15}\,\mathrm{G}$ (see Bocquet et al. (1995)).

- Additionally we neglect any effect due to rotation, i.e. $\beta^i = 0$ and consequently $\hat{v}^i = v^i$. This simplification applies, in particular, in the case of magnetars which have ultra-strong magnetic fields and very long, sub-Keplerian rotation periods. Taking these considerations into account, the four-metric(2.20) takes the form

$$ds^2 = -\alpha^2 dt^2 + \Phi^4\left(dr^2 + r^2 d\theta^2 + r^2\sin\theta^2 d\varphi^2\right)\,. \tag{2.78}$$

This is the metric in isotropic coordinates. It trivially prescribes a slicing into $\Sigma_t = (r, \theta, \phi)$, where all Σ are constant in time, i.e. $\Sigma_{t+\delta t} = \Sigma_t$.

- The adopted slicing of the equilibrium configuration also describes the unperturbed, and hence unsheared state of the neutron star. The mapping on the material space ψ (see the previous section (see Eq. (2.56)) can be expressed as $t^\Lambda = \psi_*(t^\lambda) = t^i$ such that the coordinates on $\mathcal{X}$ are (r, θ, φ) of the unperturbed metric in $\mathcal{M}$. $\breve{\mathbf{g}}$ is given by $\breve{g}_{\mu\nu} = g^{(0)}_{\mu\nu}$, where $g^{(0)}_{\mu\nu}$ is the unperturbed metric at $t = 0$ of the unsheared equilibrium model. $T^{\mu\nu}_{\text{Elas}}$ takes the following form

$$T^{\mu\nu}_{\text{Elas}} = \mu_{\text{S}} s^2 u^\mu u^\nu + \left(n \frac{\partial \mu_{\text{S}}}{\partial n} + \frac{1}{3}\mu_{\text{S}} \right) s^2 h^{\mu\nu} - 2\mu_{\text{S}} \left[s^{(\mu\nu)} - \frac{1}{3}\breve{g}^{\mu\nu} s^\lambda_\lambda \right] \tag{2.79}$$

  Because $s_{\mu\nu}$ is a symmetric and trace-free tensor the last term further simplifies to $2\mu_{\text{S}} \left[s^{(\mu\nu)} - \frac{1}{3}\breve{g}^{\mu\nu} s^\lambda_\lambda \right] = 2\mu_{\text{S}} s^{\mu\nu}$.

- For simplicity we consider first-order contributions from the elastic part of the stress-energy tensor only. This is justified in case of small oscillations. For larger perturbations assumptions like adiabaticity, required for the quasi-Hookean approximation of the elastic properties to be applicable, break down. From the physical point of view this could happen when the crust is close to breaking or melting. In this work we are not interested in these processes and our goal is to study magneto-elastic oscillations. Therefore, we assume the oscillations to have sufficiently small amplitudes in order to apply the approximation of perfect elasticity. After performing the computations, this assumption has to be tested for validity. Finally, the elastic contribution to the stress-energy tensor is given by

$$T^{\mu\nu}_{\text{Elas}} = -2\mu_{\text{S}} \left[s^{(\mu\nu)} - \frac{1}{3}\breve{g}^{\mu\nu} s^\lambda_\lambda \right] = -2\mu_{\text{S}} s^{\mu\nu} \,, \tag{2.80}$$

  where we have neglected terms of the order s^2 and the last equality holds for any symmetric and trace-less strain tensor $s^{\mu\nu}$.

- As was mentioned in Section 2.2 the temperature of typical neutron stars is well below the Fermi temperature of the neutrons. Therefore, we restrict the current study to barotropic EoS. The equation for the generalized total energy density τ is thus redundant and should be fulfilled automatically during the evolution at least at the linear level.

- In this work we consider only purely poloidal and axisymmetric background magnetic field configurations. For these magnetic fields and spherically symmetric matter backgrounds, torsional and spherical oscillations decouple at the linear level. Assuming small amplitude oscillations it is thus allowed to evolve the φ components of $\mathbf{B}$ and $\mathbf{S}$ separately from the r and θ components. In that case B^r, B^θ, S^r and S^θ are kept constant and the corresponding evolution equations need

not to be solved. Therefore, when providing initial data with vanishing amplitude in r and θ directions the corresponding perturbations of B^r, B^θ, v^r, and v^θ vanish by construction.

- The previous simplification directly implies that

$$\frac{\partial\sqrt{\gamma}D}{\partial t} + \frac{\partial D\hat{v}^\varphi}{\partial x^\varphi} = \frac{\partial\sqrt{\gamma}D}{\partial t} = 0\,, \tag{2.81}$$

  where the first equality is due to axisymmetry. Therefore, D is constant during the evolution and the continuity equation is not required to be solved explicitly. A consequence of this result is that the eigenvalues of the system do no longer depend on the speed of sound (see below in this section). Otherwise the time step would be strongly restricted because the sound speed is much larger than the Alfvén speed for reasonable magnetic field strength $< 10^{16}$ G. In more general models the problem of the time step size arises again. However, Bonazzola et al. (2007) suggested that the removal of the pressure dependencies from the fluxes F^i could solve this issue. This is known as the anelastic approximation and could be a promising approach when extending the current study to more realistic configurations, where density and pressure perturbations are allowed, and more complicated magnetic fields couple spherical and torsional oscillations.

- We are interested, in particular, in torsional oscillations of neutron stars. As these couple only very weakly to matter perturbations and the gravitational field, this allows us to neglect the evolution of the gravitational degrees of freedom. Hence, we keep the spacetime fixed, i.e. we set $\delta g_{\mu\nu} = 0$. This well known Cowling approximation is widely applied in the context of neutron star oscillations.

- In the Cowling approximation and for spherically symmetric stars the unperturbed metric is diagonal $g^{\mu\nu} = \mathrm{diag}(g^{\mu\mu})$. For the chosen slicing it is possible to derive the shear tensor $s^{\mu\nu}$ for linear dependence on the displacements explicitly from $\sigma^{\mu\nu} = \mathcal{L}_u s^{\mu\nu} = u^t s^{\mu\nu}_{\ ,t}$ (Eq. (2.64)):

$$s^{ij} = \frac{1}{2\alpha}\left[g^{ik}\left(\xi^j\alpha\right)_{,k} + g^{jk}\left(\xi^i\alpha\right)_{,k}\right] - \frac{g^{ij}}{3\alpha}\left(\xi^k\alpha\right)_{,k}\,. \tag{2.82}$$

  Here we have introduced the displacement ξ^j, which is related to the three-velocity of the fluid by

$$\xi^j_{\ ,t} := \alpha v^j = \frac{\delta u^j}{u^t}\,. \tag{2.83}$$

  The components $s^{t\mu}$ and $s^{\mu t}$ vanish. In the current context, for purely torsional

oscillations Eq. (2.82) specifies to

$$s^{ij} = \frac{1}{2} \begin{bmatrix} 0 & 0 & g^{rr}\xi^{\varphi}_{,r} \\ 0 & 0 & g^{\theta\theta}\xi^{\varphi}_{,\theta} \\ g^{rr}\xi^{\varphi}_{,r} & g^{\theta\theta}\xi^{\varphi}_{,\theta} & 0 \end{bmatrix} . \tag{2.84}$$

- The explicit appearance of the displacement ξ^{φ} and its derivatives in the shear tensor requires one to include an evolution equation for ξ^{φ}. One could evolve Eq. (2.83) directly, but in the course of the computations it turned out to be numerically advantageous to evolve $\xi^{\varphi}_{,r}$ and $\xi^{\varphi}_{,\theta}$ instead of ξ^{φ}. This has a number of reasons:

  (i) By using directly the derivatives $\xi^{\varphi}_{,r}$ and $\xi^{\varphi}_{,\theta}$, we avoid an explicit numerical evaluation of the spatial derivatives of ξ^{φ} in the fluxes F^i. This may lead to some numerical inaccuracy, in particular, in regions where the displacement changes strongly.

  (ii) A possibility to avoid this problem would be to move the terms including the derivatives of ξ^{φ} to the sources S, but then one would have to evaluate spatial derivatives of the shear modulus. The latter is provided in tabular form only, and thus the corresponding derivatives might produce spurious oscillations. Additionally, the introduction of sources would destroy the conservation form of the equations, and is thus numerically not desirable.

  (iii) The most important argument, however, appears during the set-up of the interface conditions at the crust-core interface. The conditions are given in terms of $\xi^{\varphi}_{,r}$ and $\xi^{\varphi}_{,\theta}$ (see below in Section 2.6.2). It turned out that it is essential to accurately describe the values of $\xi^{\varphi}_{,r}$ at the interface.

  The corresponding evolution equations for $\xi^{\varphi}_{,r}$ and $\xi^{\varphi}_{,\theta}$ are derived from the definition of $\xi^{\varphi}_{,t}$ (Eq. (2.83))

$$(\xi^{\varphi}_{,r})_{,t} - (v^{\varphi}\alpha)_{,r} = 0 , \tag{2.85a}$$
$$(\xi^{\varphi}_{,\theta})_{,t} - (v^{\varphi}\alpha)_{,\theta} = 0 . \tag{2.85b}$$

To summarize all aspects we will state the system of equations we integrate numerically in this work:

$$\frac{1}{\sqrt{-g}} \left(\frac{\partial \sqrt{\gamma} U}{\partial t} + \frac{\partial \sqrt{-g} F^k}{\partial x^k} \right) = 0 , \tag{2.86a}$$
$$(\xi^{\varphi}_{,k})_{,t} - (v^{\varphi}\alpha)_{,k} = 0 . \tag{2.86b}$$

Here $k = \{r, \theta\}$ and

$$U = [S_\varphi, B^\varphi]\,, \tag{2.87}$$

$$F^r = \left[-\frac{b_\varphi B^r}{W} - 2\mu_{\rm S} s^r{}_\varphi, -v^\varphi B^r\right]\,, \tag{2.88}$$

$$F^\theta = \left[-\frac{b_\varphi B^\theta}{W} - 2\mu_{\rm S} s^\theta{}_\varphi, -v^\varphi B^\theta\right]\,. \tag{2.89}$$

The corresponding eigenvalues are derived in Appendix A:

$$\lambda^k_{1/2} = \sqrt{\frac{(B^k)^2 + \mu_S/g_{kk}}{A}}\,, \tag{2.90}$$

where $A = \rho h W^4(1+v_\varphi v^\varphi) + B^r B_r + B^\theta B_\theta$. Without magnetic field we recover the shear speed $v_\perp$ of Eq. (2.65), because we are considering oscillations in φ-direction propagating in the $r-\theta$ plane. For zero shear the eigenvalue corresponds to the Alfvén velocity for transverse propagation.

2.5 Boundary conditions at the surface

The system of equations for magneto-elastic torsional oscillations contains two degrees of freedom related to the two non-vanishing eigenvalues (2.90). Therefore, we have to impose boundary conditions at the surface of the star that mimic the incoming waves from the magnetosphere, which are not included in our simulations. In the core, where $\mu_{\rm S} = 0$, there are still two degrees of freedom. Since we are simulating both regions (crust and core) having the same number of degrees of freedom there is no need for boundary conditions at the crust-core interface (although there is a need for a special treatment for numerical reasons, see Section 2.6.2).

We assume that there are no current sheets at the surface of the star, i.e. the tangential magnetic field components have to be continuous

$$b^\varphi_{\rm crust} = b^\varphi_{\rm atmosphere} \tag{2.91}$$

at the surface.

The conservation of momentum gives the continuity of the traction t^φ

$$t^\varphi = T(\tilde{\mathbf{n}}, \tilde{\varphi}) = T(\tilde{\mathbf{r}}, \tilde{\varphi}) = T^{r\varphi}\,, \tag{2.92}$$

i.e. the tangential stresses inside and outside the star have to balance each other. Here the tilde indicates normalized vectors, $\tilde{\mathbf{n}}$ is the normal to the surface of the star and thus $\tilde{\mathbf{n}} = \tilde{\mathbf{r}}$.

The continuous traction condition can be simplified in the case of continuous b^φ and

leads to a condition for $\xi^{\varphi}{}_{,r}$:

$$T^{r\varphi}_{\text{crust}} = T^{r\varphi}_{\text{atmosphere}} \tag{2.93}$$

$$b^r b^{\varphi}_{\text{crust}} + \frac{\mu_{\text{S}}}{\Phi^4}\xi^{\varphi}_{\text{crust},r} = b^r b^{\varphi}_{\text{atmosphere}} \tag{2.94}$$

$$\xi^{\varphi}_{\text{crust},r} = 0\,. \tag{2.95}$$

Trivially, the same condition applies for the time derivative of the displacement

$$\left(\xi^{\varphi}_{\text{crust},r}\right)_{,t} = \left(\xi^{\varphi}_{\text{crust},t}\right)_{,r} = 0\,. \tag{2.96}$$

Eqs. (2.91), (2.95) and its time derivative are the set of boundary conditions that we apply at the surface of the star. We need the additional condition (2.96), because we are evolving more variables than the system has the degrees of freedom. In fact, Eq. (2.95) is a direct consequence of Eq (2.91) and hence no separate condition. In principle we could set a condition for continuous $\xi^{\varphi}_{,\theta}$ at the surface, but this variable is not needed for the fluxes at radial cell interfaces.

The assumptions made here are motivated by the picture that the magnetospheric field close to the surface will move with its foot-points in the crust, i.e. the exterior solution relaxes to a force-free field on a much shorter time scale than the interior evolves. This implies that currents can be maintained in the magnetosphere, which is necessary to support more general equilibrium configurations than considered here and hence to create a twisted magnetospheric field. A more detailed discussion of the coupling to the magnetosphere is postponed to Chapter 4.

Our boundary conditions are similar to those used in previous work without the presence of a crust (Sotani et al., 2008b; Cerdá-Durán et al., 2009; Colaiuda et al., 2009) and in simulations with a crust (Gabler et al., 2011; Colaiuda and Kokkotas, 2011). However, our boundary conditions differ from those of Lander et al. (2010) and Lander and Jones (2011) who impose zero displacement and magnetic field perturbations at the surface. This requires the introduction of a current sheet at the surface, which increases the complexity of the problem. We see no physical reason to prescribe some ad hoc configuration of currents at the surface. Other approaches (Braithwaite and Nordlund, 2006; Lasky et al., 2011; Ciolfi et al., 2011) involve the evolution of some parts of the neutron star's atmosphere. For purely toroidal oscillations it is possible, however, to impose appropriate boundary conditions and to avoid that evolution.

2.6 Numerical implementation

The numerical code used to simulate the torsional oscillations of magnetars is an extension of the non-linear GRMHD code described in Cerdá-Durán et al. (2009). The code has been developed in order to investigate various astrophysical scenarios where both magnetic fields and strong gravitational fields play an important role in the evolution of the system. (Dimmelmeier et al., 2002a,b, 2005; Cerdá-Durán et al., 2008).

The code uses high-resolution shock-capturing schemes to solve the GRMHD equations for a dynamical spacetime, under the approximation of the conformally flat condition (CFC) for the Einstein's equations (Isenberg, 2008; Wilson et al., 1996). For a spherically symmetric spacetime the CFC metric is an exact solution of Einstein's equations, and reduces to the solution in isotropic coordinates. Therefore, this numerical code is well suited to describe the spacetime used in the simulations of the present work. The equations are cast in a first-order, flux-conservative hyperbolic form, supplemented by the flux constraint transport method to ensure the solenoidal condition of the magnetic field.

The basic version of the code including the solution of the ideal GRMHD equations was thoroughly tested in Cerdá-Durán et al. (2008), who demonstrate the robustness of the code for a number of stringent tests, such as relativistic shocks, highly magnetized fluids, equilibrium configurations of magnetized neutron stars, and the magneto-rotational core collapse of a realistic progenitor. One important feature is the ability of the code to handle different classes of EoS which range from simple analytical expressions to microphysically derived tables. We want to emphasize that although the current project is concerned with small-amplitude perturbations in order to apply simplifications appropriate to a linear regime, the code can in principle handle large amplitudes and in general is nonlinear.

In this section we describe the main features of the code, i.e. we discuss how to solve the magneto-hydrodynamical equations with appropriate high-resolution shock-capturing (HRSC) methods. The generalization to materials with elastic properties is shown and the numerical implementation of the additional evolution equations for the derivatives of the displacement (Eq. (2.85)) is given. When calculating models of neutron stars with solid crust numerically, the treatment of the crust-core interface is non-trivial and requires further considerations (see Section 2.6.2).

In all simulations we use a grid of spherical polar coordinates $\{r, \theta, \phi\}$ and assume axial symmetry with respect to the rotation axis. The azimuthal grid is equidistant, while the radial grid is equidistant only for simulations where the detailed structure of the crust plays a minor role for the overall dynamics. For the study of (the damping of) crustal modes, however, it is necessary to increase the resolution inside the crust. In this case we use a radial grid with a grid spacing Δr that decreases from the center towards the crust-core interface, and that is equidistant inside the crust. We ensure that the size of the grid zones in the core is comparable to that of simulations without crust (Cerdá-Durán et al., 2009).

2.6.1 Riemann solver methods

The GRMHD equations are a system of non-linear equations which may produce discontinuities like shocks from initially smooth data. In this case standard finite difference methods fail to reproduce the correct evolution. Fortunately, there exists a class of numerical schemes tailored to solve this kind of hyperbolic equations, i.e. HRSC methods. These methods are based on the finite volume approach where the variables given at

the cell center represent cell-averaged quantities. To obtain the evolution of the system, the numerical fluxes of the conservation law (2.37) are evaluated at the cell interfaces between adjacent cells. Therefore, one interpolates the cell-centered quantities to reconstruct the values at the cell interfaces. The two state vectors obtained in this way, one on each side, are in general different from each other and represent a discontinuity, i.e. they define a Riemann problem. At each time step the solution is propagated by solving the corresponding Riemann problems at the cell interfaces. There exist a number of different approaches of how to reconstruct the state vector and how to calculate the numerical fluxes. The functionality and application of HRSC methods have been described extensively in the literature. See Toro (1999) and Leveque (2002) for the general formulation and for applications.

The solution of the Riemann problem involves an inversion from the conserved variables (here $\mathbf{U} = \{D,\, S^i,\, \tau,\, B^j\}$) to the primitive variables ($\rho,\, v^i,\, \varepsilon,\, B^j$). This is trivial in a Newtonian framework where an explicit dependence is given, but becomes cumbersome in General Relativity, because the primitive variables cannot be obtained in closed form from the conserved ones. To recover the primitive variables from the conserved ones, we use an iterative Newton-Raphson method. For general application of HRSC schemes in special-relativistic hydrodynamics we refer to Martí and Müller (2003), and to Font (2008) for the GRMHD case.

The specific methods used in the simulations are the piecewise-hyperbolic method (PHM) reconstruction (Toro, 1999) and the flux approximation by Kurganov and Tadmor (2000). The Kurganov-Tadmor scheme is approximative in the sense that only the information of the fastest traveling waves is used to solve the Riemann problem. The required eigenvalues for the GRMHD case were obtained by Antón et al. (2006), and are given in Eq. (2.90) for the application to torsional magneto-elastic oscillations.

When evolving the conserved quantities according to the conservation law of GRMHD, the condition of $\nabla \cdot \mathbf{B} = 0$ will not be necessarily fulfilled numerically. This may produce non-physical data or in the worst case render the evolution unstable. Therefore, special care has to be taken when evolving the magnetic field. Numerically the problem can be avoided by using the constraint-transport (CT) scheme (Evans and Hawley, 1988). The latter conserves the magnetic flux by construction and after a reformulation gives an evolution scheme for the magnetic field, which fulfills the divergence constraint for $\mathbf{B}$.

The conserved variables are propagated in time using the method of lines combined with an explicit Runge-Kutta method of second-order accuracy in time.

As we included the elastic effects of the crust up to linear order in the displacements, the statements of this section are not affected, and we can use the same numerical methods as described above. However, one has to include additional terms in the equations (see Eqs. (2.88) and (2.89)). These terms involve the derivatives of the displacement $\xi^{\varphi}_{,r}$ and $\xi^{\varphi}_{,\theta}$ which are not present in the problem without crust. The evolution of these two quantities is performed by evaluating Eqs. (2.85a) and (2.85b) in the following way. We calculate the (non-relativistic) fluxes $-\alpha v^{\varphi}$ at cell interfaces with the corresponding approximate Riemann solver. The derivatives of the fluxes are approximated by divid-

ing the difference of the fluxes at the two opposite cell interfaces of a zone by the zone spacing. This method provides a second-order approximation and is applicable also in the presence of discontinuities. As for the conservation law (2.37) the time update is performed by the method of lines combined with a Runge-Kutta algorithm.

2.6.2 Treatment of the crust-core interface

In the core, where $\mu_{\rm S} = 0$, there are two degrees of freedom. Since we are simulating the crust and core, and both regions have the same number of degrees of freedom there is no need for boundary conditions at the crust-core interface. Knowing the variables at one instant of time on both sides of the crust-core interface one should be able to evolve the system. However, the stability of the employed scheme turned out to depend sensitively on the particular treatment of the reconstruction of the variables, which are allowed to be discontinuous or to have discontinuous spatial derivatives (see below).

In the case of ideal-MHD without charges, the electric field is continuous everywhere, and hence the velocity v^φ, too. This implies continuity of the displacement, ξ^φ, and of its time derivative, $\xi^\varphi_{,t}$. Consequently, in spherical symmetry the tangential derivative, $\xi^\varphi_{,\theta}$, is continuous at the surface of the star and at the core-crust interface, while no restrictions apply to the continuity of $\xi^\varphi_{,r}$.

Since the conservation of energy has to hold everywhere, the traction is continuous, in particular, at the crust-core interface

$$T^{r\varphi}_{\rm core} = T^{r\varphi}_{\rm crust}\,, \tag{2.97}$$

$$-b^r b^\varphi_{\rm core} = -b^r b^\varphi_{\rm crust} - \frac{\mu_{\rm S}}{\Phi^4}\xi^\varphi_{,r}\,. \tag{2.98}$$

This can be transformed by virtue of the linearized induction equation

$$b^\varphi = b^r \xi^\varphi_{,r} + b^\theta \xi^\varphi_{,\theta}\,, \tag{2.99}$$

the continuity of the displacement, and thus $\xi^\varphi_{{\rm core},\theta} = \xi^\varphi_{{\rm crust},\theta}$, into

$$b^r(b^r\xi^\varphi_{{\rm core},r} + b^\theta\xi^\varphi_{{\rm core},\theta}) = b^r(b^r\xi^\varphi_{{\rm crust},r} + b^\theta\xi^\varphi_{{\rm crust},\theta}) + \frac{\mu_{\rm S}}{\Phi^4}\xi^\varphi_{{\rm crust},r} \tag{2.100}$$

$$\xi^\varphi_{{\rm core},r} = \left(1 + \frac{\mu_{\rm S}}{\Phi^4 (b^r)^2}\right)\xi^\varphi_{{\rm crust},r}\,. \tag{2.101}$$

Obviously the discontinuous radial derivative allows b^φ to be discontinuous, too (see Eq. 2.99). Hence, in general, there are current sheets present at the crust-core interface, which are unavoidable, and a consequence of the coupled evolution and the assumption of ideal MHD.

We have shown that due to the discontinuity of the shear modulus $\mu_{\rm S}$ we do not expect all variables to be continuous at the crust-core interface. In principle, Riemann solvers are able to cope with discontinuities at cell interfaces. Therefore, we define the crust-core interface to be located at a cell interface. However, it turned out to be crucial to ensure

that the reconstruction procedure gives a value for $\xi^{\varphi}_{,r} \sim s^{r}{}_{\varphi}$ which is consistent with the continuous traction condition (Eq. 2.101). Any standard reconstruction method not taking this condition explicitly into account failed, and the simulations produced spikes in the radial profiles that spoilt the evolution, or in the worst case rendered the whole evolution unstable. The main cause for this behavior is the discontinuity of the shear modulus at the crust-core interface. For intermediate and weak magnetic fields, the very large shear modulus on one side and the vanishing shear modulus on the other cause the different terms in the momentum equation for the radial flux Eq. (2.88) to be much larger on the side of the crust than on the side of the core, i.e.,

$$\left|\frac{b_{\varphi}B^{r}}{W}\right|_{\text{crust}}, \left|\mu_{\text{S}}s^{r}{}_{\varphi}\right|_{\text{crust}} >> \left|\frac{b_{\varphi}B^{r}}{W}\right|_{\text{core}}. \tag{2.102}$$

The evaluation of the flux at the core-crust interface is numerically problematic due to non-cancellations of the two terms on the side of the crust. However, when taking the continuous traction condition appropriately into account, this problem does not arise and the flux at the core-crust interface is well behaved, allowing one to perform simulations also for intermediate and weak magnetic fields.

We are using the following numerical treatment based on the continuous traction condition $\xi^{\varphi}_{\text{core}}(r_{\text{cc}}) = \xi^{\varphi}_{\text{crust}}(r_{\text{cc}}) \equiv \xi^{\varphi}(r_{\text{cc}})$ and $\xi^{\varphi}_{\text{core},r}(r_{\text{cc}}) = \eta\xi^{\varphi}_{\text{crust},r}(r_{\text{cc}})$ with $\eta = 1 + \mu_{\text{S}}/\left(\Phi^4(b^r)^2\right)$. For an illustration see Figure 2.4. The derivatives at the crust-core interface can be approximated by

$$\xi^{\varphi}_{\text{core},r}(r_{\text{cc}}) = \frac{\xi^{\varphi}(r_{\text{cc}}) - \xi^{\varphi}_{\text{core}}(r_{\text{cc}} - 0.5\Delta r)}{0.5\Delta r}, \tag{2.103}$$

$$\xi^{\varphi}_{\text{crust},r}(r_{\text{cc}}) = \frac{\xi^{\varphi}_{\text{crust}}(r_{\text{cc}} + 0.5\Delta r) - \xi^{\varphi}(r_{\text{cc}})}{0.5\Delta r}, \tag{2.104}$$

where r_{cc} is the radius of the crust-core interface and Δr the grid spacing in radial direction. The combination of both equations leads to the following expression for ξ^{φ}:

$$\xi^{\varphi}(r_{\text{cc}}) = \frac{\xi^{\varphi}_{\text{core}}(r_{\text{cc}} - 0.5\Delta r) + \eta\xi^{\varphi}_{\text{crust}}(r_{\text{cc}} + 0.5\Delta r)}{1 + \eta}. \tag{2.105}$$

Knowing ξ^{φ} at the crust-core interface one can calculate the radial derivatives $\xi^{\varphi}_{\text{crust},r}$ and $\xi^{\varphi}_{\text{core},r}$, and finally the fluxes. Since relation (2.101) has to be fulfilled at all times, a corresponding relation has to hold for the time derivative $\xi^{\varphi}_{,t}$, too. This provides a reconstruction for the velocity field v^{φ}. For the calculations presented in this work we used a second-order approximation of the derivatives instead of Eqs. (2.103) and (2.104).

The accuracy of the reconstruction of the magnetic field can also be improved by using the traction condition Eq. (2.98). For simplicity, we introduce the following abbreviation

$$\Lambda := \frac{\mu_{\text{S}}}{\Phi^4 b^r}\xi^{\varphi}_{,r}, \tag{2.106}$$

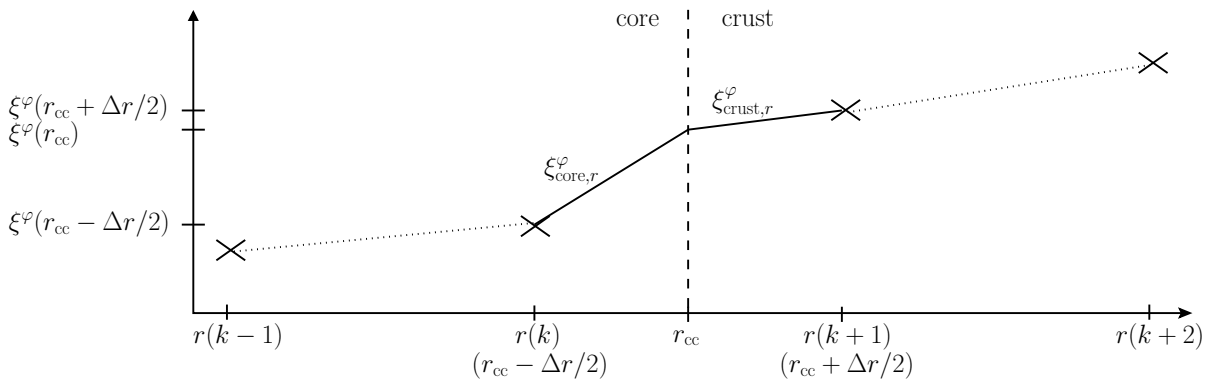

Figure 2.4: Illustration of the reconstruction of ξ^φ, and thus $\xi^\varphi_{,r}$. A very careful treatment of the interface is required in order to ensure the continuity of the traction across this interface.

such that Eq. (2.98) becomes

$$b^\varphi_{\rm core} = b^\varphi_{\rm crust} + \Lambda\,. \tag{2.107}$$

To reconstruct the magnetic field on each side of the crust-core interface we set up ghost cells, whose magnetic field is given by

$$b^\varphi_{\rm core}(k+2) = b^\varphi_{\rm crust}(k+2) + \Lambda(k+2)\,, \tag{2.108a}$$
$$b^\varphi_{\rm core}(k+1) = b^\varphi_{\rm crust}(k+1) + \Lambda(k+1)\,, \tag{2.108b}$$
$$b^\varphi_{\rm crust}(k) \quad = b^\varphi_{\rm core}(k) - \Lambda(k)\,, \tag{2.108c}$$
$$b^\varphi_{\rm crust}(k-1) = b^\varphi_{\rm core}(k-1) - \Lambda(k-1)\,. \tag{2.108d}$$

Here the crust-core interface is set between the k-th and $(k{+}1)$-th zone in radial direction, $b^\varphi_{\rm core}$ ($b^\varphi_{\rm crust}$) is defined on a grid of $i = \{0\ldots k\}$ ($i = \{k+1\ldots i_{\rm max}\}$), and has two ghost cells at $i = \{k{+}1, k{+}2\}$ ($i = \{k, k{-}1\}$). This is illustrated in Fig. 2.5. The reconstruction of b^φ on each side is performed with the corresponding ghost cells. This procedure gives a more accurate reconstruction taking the magnitude of the discontinuity of the magnetic field at the crust-core interface $\Lambda(r_{\rm cc}) = b^\varphi_{\rm core}(r_{\rm cc}) - b^\varphi_{\rm crust}(r_{\rm cc})$ into account.

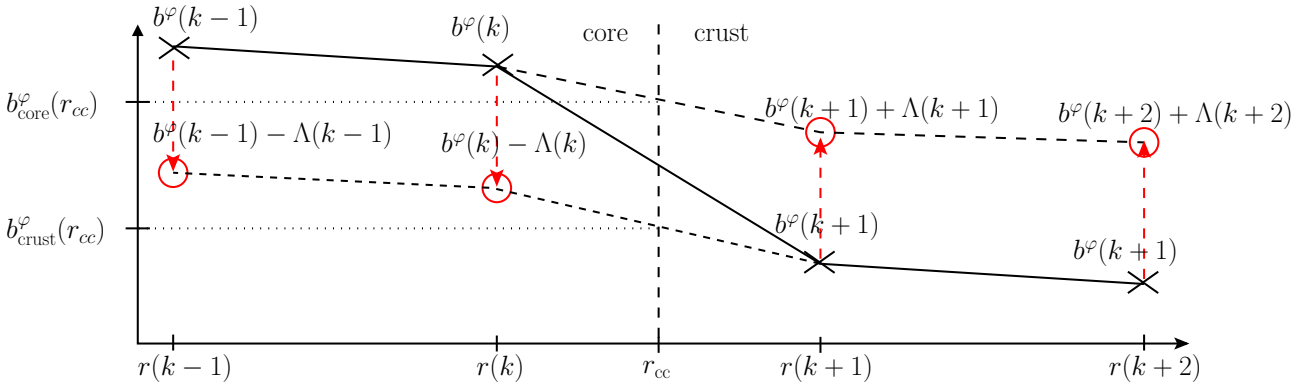

Figure 2.5: Illustration of the reconstruction of b^φ. $\Lambda(k)$ is a correction to the magnetic field used for the reconstruction, corresponding to $\Lambda(k) = \mu_{\rm S}(r_{cc})\xi^\varphi_{,r}(k)/\left(\Phi(k)^4 b^r(k)\right)$. Crosses indicate positions of the evolved values of the magnetic field b^φ, while circles are the values in ghost cells used for the reconstruction only.

3 Magneto-elastic oscillations of magnetars

In this chapter we present the results of our two-dimensional simulations of magnetized neutron stars with an extended, solid crust. We first state which equilibrium models are used in Section 3.1. This includes the choice of the EoS and the numerical tool to construct the initial data. Furthermore we describe how to calculate the shear modulus, which is an essential ingredient for the calculation of the shear oscillations. As a test case for our dynamical code we calculate the purely shear oscillations of the crust in Section 3.2. Additionally, the corresponding eigenvalue problem is computed in Appendix D. Section 3.3 is concerned with the basic properties of purely Alfvén oscillations of neutron stars. There, we extend the corresponding discussion of Cerdá-Durán et al. (2009) to tabulated EoS. In Section 3.4 the coupled magneto-elastic oscillations are studied. The discussion includes the absorption of crustal shear modes, the behavior of Alfvén QPOs which are confined to the core for magnetic field strengths $\lesssim 10^{15}\,\mathrm{G}$ and the magneto-elastic QPOs at even stronger fields. We further investigate at which magnetic field the QPOs begin to be have significant amplitudes in the crust, and search for crustal modes which might not be damped, because their frequencies do not match any frequency of the Alfvén continuum of the core. In the last section of this chapter we discuss a different magnetic field configuration, and its influence on the magneto-elastic oscillations.

3.1 Equilibrium models

The initial models are self-consistent general relativistic equilibrium models of magnetized non-rotating neutron stars with a purely poloidal magnetic field (Bocquet et al., 1995). We use the numerical code "magstar" of the LORENE library[1] to compute these models, which include the effects of the magnetic field on the matter and the spacetime. The magnetic field is generated by a current of the form $\mathcal{J}^{\varphi} = \rho h C$, where C is a constant which determines the strength of the magnetic field. Hereafter, we will label the different models by the surface value of their magnetic field strength at the pole.

As we assume a spherically symmetric spacetime and matter background in our simulations we angle-average the density of the background model to obtain a spherically symmetric model from the LORENE data. In the most extreme cases, i.e. for a very strong magnetic field this simplification changes the structure of the neutron star by at most about one per cent. For example the density at different angles but constant radius

[1] http://www.lorene.obspm.fr

varies within less than one per cent at $B = 5 \times 10^{15}$ G. Therefore, the influence on the oscillations is in general less than that of other approximations we are applying.

3.1.1 Equation of state and used models

For the EoS we can choose between different realistic barotropic models including the description of a crust. We use four combinations of two EoS in the core matched to two distinct EoS for the crust. For the core we chose the APR EoS (Akmal et al., 1998) and the stiffer EoS L (Pandharipande and Smith, 1975), while for the low density region of the crust we select EoS NV (Negele and Vautherin, 1973) and EoS DH (Douchin and Haensel, 2001). The recent discovery of a 2 $M_\odot$ neutron star by Demorest et al. (2010), excludes EoS which cannot reproduce such large masses. The properties of the equilibrium models used in this work are summarized in Table 3.1. These models are a subset of the models used in Sotani et al. (2007). We note that table 1 of Sotani et al. (2007) shows $\Delta r/r_{\rm cc}$, instead of $\Delta r/r_{\rm s}$ and thus the percentage for the relative size of the crust is different in their case. However we, checked that the value of Δr is the same in both cases. The frequency of the crustal modes with $n > 0$ depend sensitively on the size of the crust (Samuelsson and Andersson, 2007). Therefore, good accuracy in the determination of the size of the crust is important to properly determine the former.

If not state otherwise we select one particular model to discuss the main results in the remainder of this work. The model of reference uses the APR core EoS combined with the DH crustal EoS. For the mass we chose 1.4 M$\odot$.

3.1.2 Shear modulus

The shear oscillations of the crust are mainly determined by the shear modulus $\mu_{\rm S}$ which we obtain from the zero-temperature limit of Strohmayer et al. (1991) given by

$$\mu_{\rm S} = 0.1194 \frac{n_i (Ze)^2}{a}\,, \tag{3.1}$$

where n_i is the ion density, (Ze) the ion charge and $a = [3/(4\pi n_i)]^{1/3}$ the average ion spacing. This equation is derived for a perfect bcc lattice, and the shear modulus, which has different magnitude along different crystal axes is averaged in order to obtain an isotropic effective shear modulus $\mu_{\rm S}$ (see Strohmayer et al., 1991). For the NV EoS of the crust we use a simple fitting formula derived by Duncan (1998)

$$\mu_{\rm S} = 1.267 \times 10^{30} {\rm erg\,cm^{-3}} \rho_{14}^{4/5}\,, \tag{3.2}$$

where $\rho_{14} = \rho/(10^{14} {\rm g\,cm^{-3}})$.

To calculate the shear modulus for the DH EoS, one has to evaluate n_i in Eq. (3.1) in terms of the nucleon number A, the proton number Z, and the neutron fraction X_n (Piro, 2005): $n_i = \rho_i m_i$ and $A\rho_i \sim \rho(1 - X_n)$. The composition at a given density is

EoS	mass $[M_\odot]$	circumferential radius r_s[km]	inner radius of crust [km]	relative size of crust $\frac{\Delta r}{r_s}$ [%]
APR+DH	1.4	12.10	11.22	7.2
	1.6	12.07	11.38	5.7
	1.8	12.00	11.43	4.8
	2.0	11.90	11.44	3.9
	2.2	11.63	11.31	2.8
APR+NV	1.4	11.94	10.85	9.1
	1.6	11.93	11.07	7.2
	1.8	11.92	11.19	6.1
	2.0	11.81	11.23	4.9
	2.2	11.56	11.12	3.8
L+DH	1.4	14.74	13.33	9.6
	1.6	14.85	13.72	7.6
	1.8	14.93	13.94	6.6
	2.0	14.99	14.13	5.7
	2.2	14.94	14.22	4.8
L+NV	1.4	13.29	11.88	10.6
	1.6	13.58	12.35	9.1
	1.8	13.86	12.76	7.8
	2.0	14.02	13.08	6.7
	2.2	14.12	13.30	5.8

Table 3.1: EoS, masses, radii of the star, radii of the crust-core interface, and sizes of the crust of the models studied in this paper (without magnetic field).

given in Douchin and Haensel (2001). The shear modulus can be estimated to be

$$\begin{aligned}\mu_{\rm S} &= 1.2\times10^{30}{\rm erg\,cm^{-3}}\rho_{14}^{4/3}\left(\frac{Z}{38}\right)^2\left(\frac{302}{A}\right)\\ &\quad\times\left(\frac{1-X_n}{0.25}\right)^{4/3}.\end{aligned}\tag{3.3}$$

Sotani et al. (2007) introduced the following fit to this equation

$$\begin{aligned}\mu_{\rm S} &= 10^{30}{\rm erg\,cm^{-3}}(0.02123+0.37631\rho_{14}+3.13044\rho_{14}^2\\ &\quad-4.718141\rho_{14}^3+2.46792\rho_{14}^4)\,.\end{aligned}\tag{3.4}$$

This function provides a good approximation for densities larger than $\rho = 5\times10^{11}{\rm g\,cm^{-3}}$, but below we will rely on the more general expression in Eq. (3.3). The main motivation to use this fit is to allow for a direct comparison of the results obtained in this work to the results presented in Sotani et al. (2007) and Colaiuda and Kokkotas (2011).

The crust-core boundary for the NV and DH EoS is defined at $\rho_{\rm cc,NV} = 2.4\times10^{14}{\rm g\,cm^{-3}}$, and $\rho_{\rm cc,DH} = 1.28\times10^{14}{\rm g\,cm^{-3}}$, respectively.

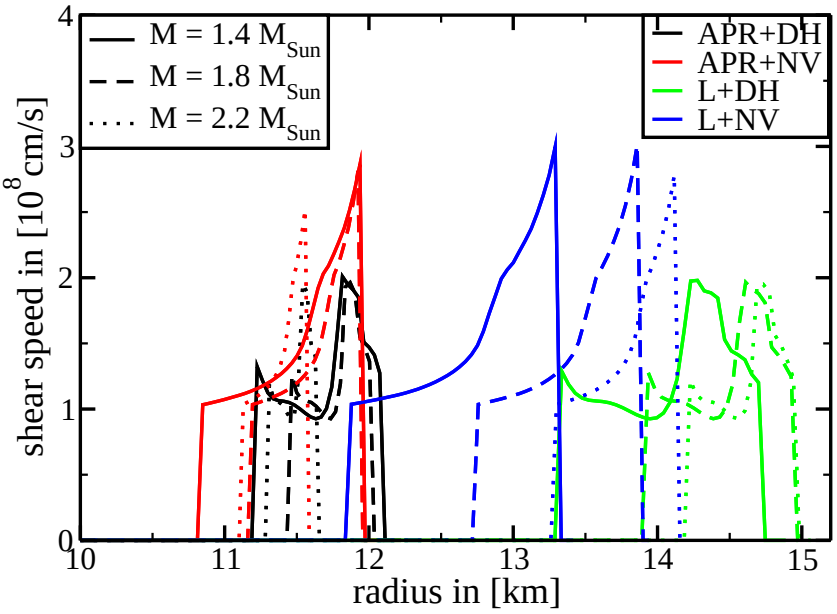

Figure 3.1: Shear speed of different stellar models. The color gives the EoS and the line style the mass of the model (solid - $1.4M_\odot$, dashed - $1.8M_\odot$, dotted - $2.2M_\odot$). The NV EoS gives thicker crusts and higher shear velocities compared to the DH EoS. The range of speeds is similar in all models.

Equipped with the shear modulus we can calculate the corresponding shear speeds in the crust with Eq. (2.90). In Fig. 3.1 we give the shear speed as a function of the radius r for the different equilibrium models introduced in the previous subsection.Comparing models obtained with the DH EoS for the crust with those of the NV EoS shows that the latter EoS not only leads to thicker crusts, but also to higher shear speeds. The shear speed for all models lies in the range between 0.3 to 1 % of the speed of light.

3.2 Crustal shear oscillations

The task of calculating the crustal shear oscillations can be cast into an eigenvalue problem (Appendix D). The solution of the latter consists of an infinite number of discrete eigenmodes which form a complete and orthogonal set. The different solutions can be labeled by the number of nodes in radial direction inside the crust ($n = 0, 1, 2, \dots$) and by the angular number l of the Legendre polynomials which are related to the solution in θ-direction. We test our numerical implementation including the shear terms against the expected results for the crustal shear modes by evolving neutron star models without a magnetic field.

The purely shear oscillations for various realistic EoS in general relativity have been calculated for the linearized problem by Messios et al. (2001) and Sotani et al. (2007). To recover their results, we performed a series of simulations for a selection of models with zero magnetic field strength. As initial velocity perturbation we use a simple radial

Model	n=0 mode frequency in Hz (±1Hz)				
	l = 2	l = 3	l = 4	l = 5	l = 6
APR+DH 1.4	25.4 (24.6) [25.1]	40.0 (38.9)	53.6 (52.2)	67.3 (65.1)	80.0 (77.8)
APR+DH 1.6	24.3 (23.4) [24.0]	38.5 (37.0)	51.2 (49.6)	64.3 (61.9)	76.5 (73.9)
APR+DH 2.0	21.9 (21.3) [21.7]	34.6 (33.6)	46.3 (45.1)	58.0 (56.3)	69.2 (67.3)
L+DH 1.6	21.0 (20.6) [20.9]	33.1 (32.5)	44.8 (43.7)	55.6 (54.5)	66.8 (65.1)
L+DH 2.0	19.5 (18.9) [19.2]	30.7 (29.9)	40.9 (40.2)	51.2 (50.1)	61.4 (59.9)
APR+NV 1.6	23.9 (23.8) [23.6]	37.5 (37.6)	50.7 (50.5)	62.9 (63.0)	75.5 (75.3)
APR+NV 2.0	21.5 (21.4) [21.2]	33.7 (33.9)	45.4 (45.5)	56.5 (56.7)	67.8 (67.8)
L+NV 1.6	22.0 (21.8) [21.8]	34.7 (34.5)	46.8 (46.3)	58.6 (57.7)	69.7 (69.0)
L+NV 2.0	19.5 (19.7) [19.6]	31.2 (31.1)	41.9 (41.7)	52.2 (52.1)	62.5 (62.2)

Model	mode frequency in Hz (±20Hz)	
	n = 1	n =2
APR+DH 1.4	741 (761) [734]	1190 (1270)
APR+DH 1.6	829 (860) [825]	1340 (1430)
APR+DH 2.0	1052 (1083) [1045]	1842 (1810)
L+DH 1.6	565 (586) [567]	917 (980)
L+DH 2.0	682 (713) [677]	1100 (1190)
APR+NV 1.6	692 (689) [684]	1230 (1220)
APR+NV 2.0	838 (858) [827]	1501 (1520)
L+NV 1.6	526 (525) [522]	936 (930)
L+NV 2.0	615 (615) [608]	1092 (1090)

Table 3.2: Frequencies of some torsional shear modes of the crust for different EoS. Numbers following the abbreviation of the EoS give the mass of the stellar model in solar mass units. The frequencies in round parenthesis are from Sotani et al. (2007), and the squared brackets give the result of the eigenmode analysis (see Appendix D). For the $n = 1$ and $n = 2$ modes we compare to the $l = 2$ case only. The frequencies of the eigenvalue calculation for $n = 0$ and $l > 2$ can be obtained by multiplying the corresponding frequencies for $l = 2$ with $\sqrt{(l-1)(l+2)}/2$. The error ranges shown in the table header have their origin in the Fourier transformation, which should dominate other numerical errors.

law in the form $v \approx \sin(\pi/2 * (r - r_{\rm cc})/(r_{\rm s} - r_{\rm cc}))$ multiplied by a sum of the first ten vector spherical harmonics for the angular dependence. With this kind of perturbation we ensure to excite single modes with different values for the radial and angular mode numbers n and l. We evolve the system for 1 s in the case of $n = 0$ modes and 50 ms for the modes with $n \geq 1$. The resolution of the simulations was $120(r) \times 60(\theta)$ points in the domain $[0, r_{\rm s}] \times [0, \pi/2]$, the grid is equidistant in both directions and we used equatorial symmetry. The chosen grid corresponds to about 20 radial zones inside the crust.

Table 3.2 gives the oscillation frequencies of our dynamical simulations extracted from the Fourier analysis at points inside the crust. The frequencies of the modes agree up to

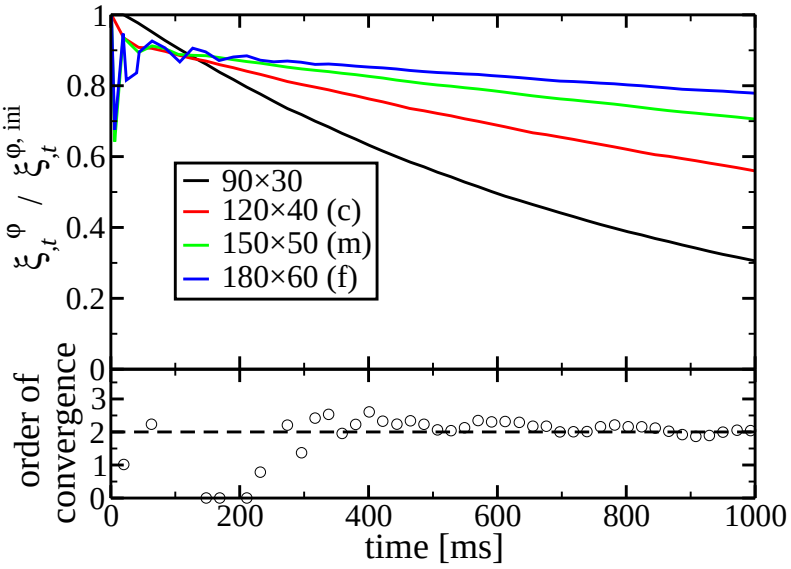

Figure 3.2: Numerical damping of crustal oscillations. The upper panel shows the evolution of the maximal amplitude of $\xi^{\varphi}_{,t}$ normalized to its initial value, at a point in the crust near the pole for different grid resolutions. The numerical damping decreases with increasing resolution. The lower panel shows the order of convergence (circles) computed using the three highest resolution simulations compared to the expected second order convergence (dashed line).

a few percent with those of the linear approximation (given in round parenthesis). For modes with $n \geq 1$, the frequency resolution of the Fourier transform does not allow us to resolve modes with the same n but different l, which are only separated from each other by a few Hz. Therefore, the measured frequency is a mixture of different l contributions, and its value is expected to be slightly larger than that of Sotani et al. (2007) for $l = 2$, which are reported in the Table 3.2 as well.

Additionally, we have computed the frequencies from the associated eigenvalue problem (Appendix D). For the computation of these frequencies we used a radial grid of about 80 zones in the crust. The results for the $n = 0$, $l = 2$ and $n = 1$ modes are given in squared brackets in Table 3.2. They agree up to a similar accuracy with those that have been obtained in the literature.

To investigate the convergence properties of our code when no magnetic field is present, we have calculated the evolution of the $n = 0$ and $l = 2$ mode of our reference neutron star model for different grid resolutions: 180×60, 150×50, 120×40, and 90×30. The angular grid is equidistant, while the radial grid is equidistant only in the crust, where 40 percent of the zones are located, and coarsens towards the center of the star. The finer mesh in the crust ensures higher accuracy without significant increase of the

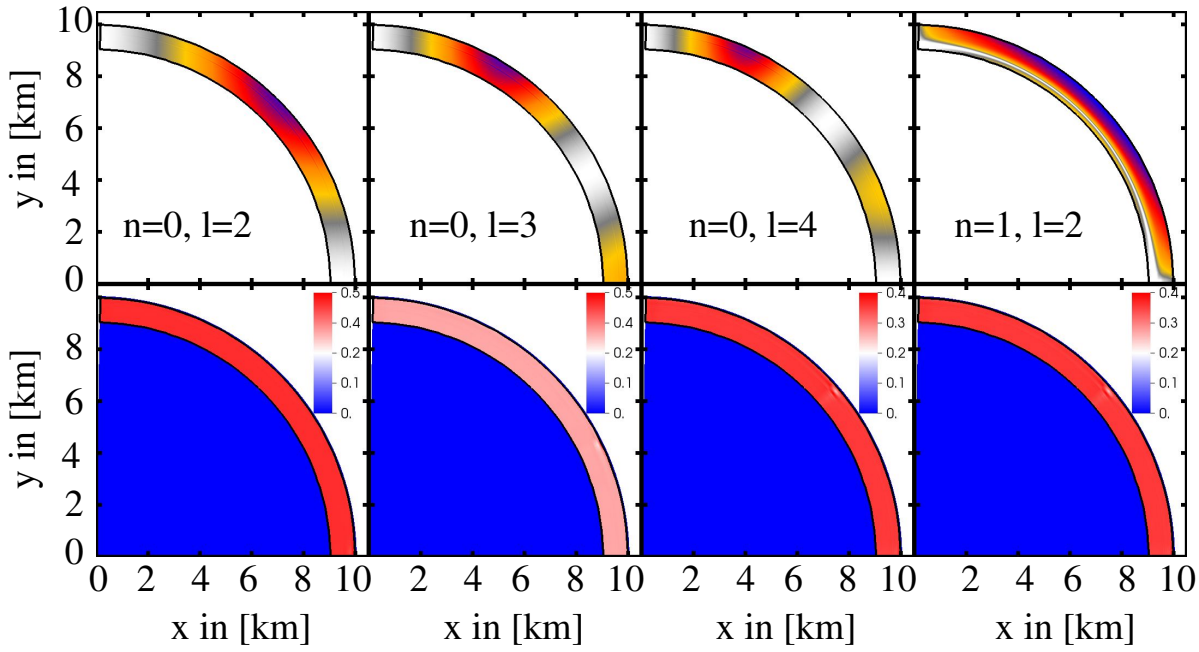

Figure 3.3: *Upper row of panels:* Fourier amplitude at the frequencies of some crustal modes with l and n given in the corresponding panel. We recover the expected behavior of the vector spherical harmonics. In the fourth panel the node in radial direction of the $n = 1$, $l = 2$ mode is visible. *Lower row of panels:* Phase corresponding to the modes in the upper row. For all modes the phase inside the crust can be considered to be constant.

computational costs. In order to save further computational power we assume equatorial symmetry. The mode frequencies extracted from the simulations at different resolutions agree within the frequency resolution of the Fourier transform. The upper panel of Fig. 3.2 shows the time evolution of the maximum amplitude of $\xi^{\varphi}_{,t}$ at the crust for different grid resolutions. One clearly sees that the numerical damping decreases with increasing resolution. For this simple test case it is possible to compute the order of convergence using the results for the three highest resolutions, when one assumes that the error in the interesting variable, f, scales as Δ^p, where Δ is the size of the numerical cell and p the order of convergence. To compute p one searches for roots of

$$\frac{f_{\text{coarse}} - f_{\text{medium}}}{f_{\text{medium}} - f_{\text{fine}}} = \frac{\Delta^p_{\text{coarse}} - \Delta^p_{\text{medium}}}{\Delta^p_{\text{medium}} - \Delta^p_{\text{fine}}}\,, \tag{3.5}$$

where the subscripts denote fine, medium or coarse grid resolution. The lower panel of Fig. 3.2 shows that after a short initial transient the order of convergence, p, rapidly converges to 2, which is the expected order of convergence of our numerical scheme.

In Fig. 3.3 we show exemplary the first three $n = 0$ and the $n = 1$, $l = 2$ crustal modes and their phases as obtained from the simulations. The plots are obtained from a Fourier analysis at the expected frequencies provided in Table 3.2. The dependence

on the angular number l of the vector spherical harmonics is recovered as expected. We also obtain the correct structure in r-direction including one node for the $n = 1$ mode (compare with Appendix D and Fig. D.1). The phase of all modes is constant as one would expect for a solution in terms of eigenfunctions (lower row of panels in Fig. 3.3).

3.3 Alfvén oscillations

Purely Alfvén oscillations of neutron stars with dipolar magnetic fields have been studied by Sotani et al. (2008b) and Cerdá-Durán et al. (2009). Colaiuda et al. (2009) investigated the effect of an additional toroidal background field. In this section we discuss the main features of these oscillations and extend the investigation of Cerdá-Durán et al. (2009) to tabulated EoS.

In the lower left panel Fig. 3.4 we show the frequency spectrum of the field lines as obtained with the semi-analytic model of Appendix B. The frequencies of the open field lines (black in the figure) form a continuum. This is in contrast with the crustal modes which have discrete frequencies. The continuum formed by the first overtones of all open field lines connects in frequency space to the continuum formed by oscillations occurring the closed field lines (red lines). From the analysis of toy models (Levin, 2006, 2007) one would expect to observe QPOs at turning points and edges of the different continua. The expected QPOs of the fundamental oscillations and the first overtone are marked in the left panel of Fig. 3.4. Following Cerdá-Durán et al. (2009) we label the QPOs related to the turning point in the spectrum of the overtones of the open field lines close to the pole *upper* QPOs $U_n^{(\pm)}$, the ones related to the overtones of the turning point of the closed field lines *lower* QPO $L_n^{(\pm)}$ and the ones related to spectrum of the last open field line and overtones *edge* QPOs $E_n^{(\pm)}$.

To understand why the QPOs appear at the edges or turning points of the continuum, we sketch the argumentation of Levin (2007). He considers a toy model which is based on a big pendulum (crust) coupled to many smaller pendula (magnetic strings of the core). Neighboring pendula have slightly different oscillation frequencies, and hence form a continuum of frequencies. The described frequency difference is the reason why different pendula get out of phase when excited coherently in the beginning. The phase difference between nearby oscillators may be so large, that they swing in opposite directions, and thus give opposite contribution to the overall oscillation of the big pendulum. This process is often called phase mixing. However, there exist regions like continuum edges where no neighboring pendula exist, which could annihilate the contribution of the pendula near the edge. Therefore, the net effect of the small pendula on the big one is reduced to the oscillations occurring near an edge. In other words, only the pendula near the edge pull coherently on the big pendulum. Similar arguments hold near a turning point of the continuum, where neighboring pendula contribute coherently. With time also the pendula near the edge/turning point get out of phase, and the corresponding QPOs are damped. In the case of pure Alfvén oscillations the crust is emulated by the boundary condition at the surface and neighboring magnetic strings are coupled numerically.

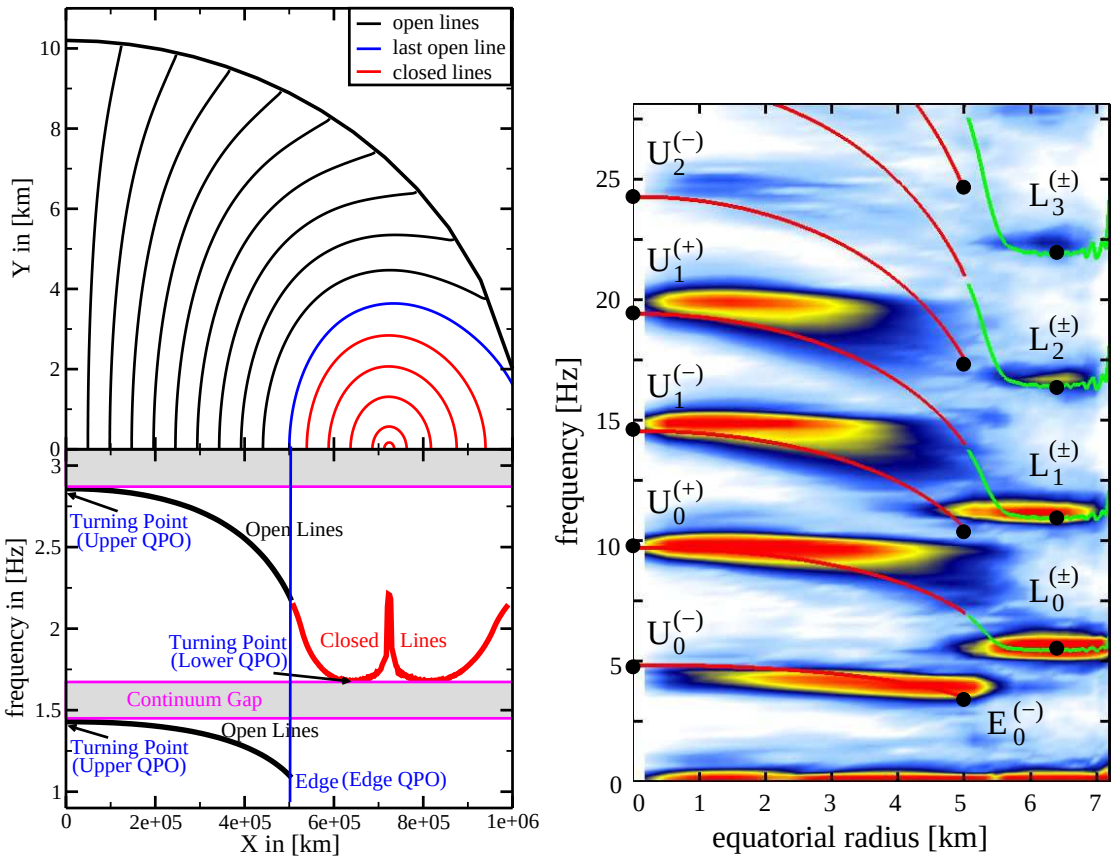

Figure 3.4: *Upper left panel:* Illustration of the dipolar magnetic field configuration including field lines which close inside the neutron star (red) and open lines which extend to the exterior (blue and black).
Lower left panel: Frequencies of the fundamental oscillation and its first overtone for the corresponding field lines. The ensemble of the frequencies of all field lines forms a continuum with edges and turning points as indicated with the arrows. We call the QPOs related to the turning point of the open field lines upper QPOs, the QPOs related to the turning point of the closed field lines lower QPOs, and the QPOs related to the edge of the continuum at the last open field line edge QPOs.
Right panel: Frequency continuum of the reference model APR+DH 1.4 at $B = 4 \times 10^{15}$ G. The colors show the Fourier amplitude averaged along individual field lines. The x-axis is the crossing radius of the field lines with the equatorial plane. Black dots highlight the location where QPOs are expected. The QPOs observed with significant Fourier amplitude are indicated by the corresponding name: upper $U_n^{(\pm)}$, lower $L_n^{(\pm)}$ or edge $E_n^{(-)}$ QPO. The color scale ranges from white-blue (minimum) to orange-red (maximum).

In the right panel of Fig. 3.4 we show a realistic spectrum obtained for the reference model APR+DH 1.4 at $B = 4 \times 10^{15}$ G and compare it with the magnitude of the Fourier amplitude of the corresponding simulation (grid resolution 100×80, evolution time 4.5 s).

Thereby, we average the Fourier amplitude along individual field lines and label each field line with its crossing point with the equatorial plane, which is given in the x-axis of the figure. As expected from toy models (Levin, 2006, 2007) we observe QPOs at the frequencies of the turning points of the spectrum near the pole and equator. However, the fundamental QPO $U_0^{(-)}$ has a very low amplitude, probably because the particular initial data used in this simulation did not excite this particular QPO significantly. The theory of the toy models also predicts QPOs at the edges of the continuum. We find only one edge QPOs with significant amplitude, namely $E_0^{(-)}$. For polytropic models no edge QPOs was observed. We interpret the absence of the major part of the edge QPOs to be caused by the steep gradients of the spectrum near the edge of the continuum which enhance the phase mixing (Levin, 2007; Cerdá-Durán et al., 2009). Furthermore, the numerical coupling of open field lines and closed ones introduces an additional channel which may cause phase mixing, i.e. the sharp edges of the continuum may be coupled to the continuum of the closed field lines. Consequently, one would expect a very rapid damping of the oscillations due to the phase mixing.

The spatial structure of the first nine QPOs with significant amplitudes is displayed in Fig. 3.5, and the corresponding frequencies are given in Table 3.3. As above we distinguish between upper QPOs near the pole (panels b, d, e, and h), lower QPOs near the equator (panels c, e, g, and i), and edge QPOs related to the last closed field line (panel a). The frequencies obtained in the simulations are in good agreement with the ones predicted by the semi-analytic model (see Table 3.3).

Upper QPOs can be divided into two families: one symmetric (+) and one antisymmetric (-) with respect to the equatorial plane. Edge QPOs exist only for the continua of the antisymmetric overtones. In Fig. 3.5 the geometrical interpretation of the index k in $U_k^{(\pm)}$ becomes clear. It describes the number of nodes along the field lines inside the star, i.e. there are $2k+1$ nodes for antisymmetric QPOs and $2(k+1)$ nodes for symmetric QPOs, respectively.

The relation of the frequencies of the different families of QPOs is

$$f\left(U_n^{(-)}\right) = (2n+1) f\left(U_0^{(-)}\right) \tag{3.6}$$

$$f\left(U_n^{(+)}\right) = (n+1) f\left(U_0^{(+)}\right) = 2(n+1) f\left(U_0^{(-)}\right) \tag{3.7}$$

$$f\left(E_n^{(-)}\right) = (2n+1) f\left(E_0^{(-)}\right) \tag{3.8}$$

$$f\left(L_n^{(\pm)}\right) = (n+1) f\left(L_0^{(\pm)}\right) \tag{3.9}$$

In Fig. 3.6 we display the phase of the Fourier transform shown in Fig. 3.5. In contrast to the eigenmodes in the crust (see lower row of panels in Fig. 3.3) the phase changes continuously in direction perpendicular to the field lines, which is best seen for the edge and upper QPOs (panels a, b, d, f, and h). The Fourier analysis gives phase values between $-\pi/2$ and $\pi/2$. By adding π each time when the phase jumps from $\pi/2$ to $-\pi/2$ in the computed values for the edge and upper QPO, we are able to follow the increase of the phase in direction perpendicular to the field lines over a larger range of

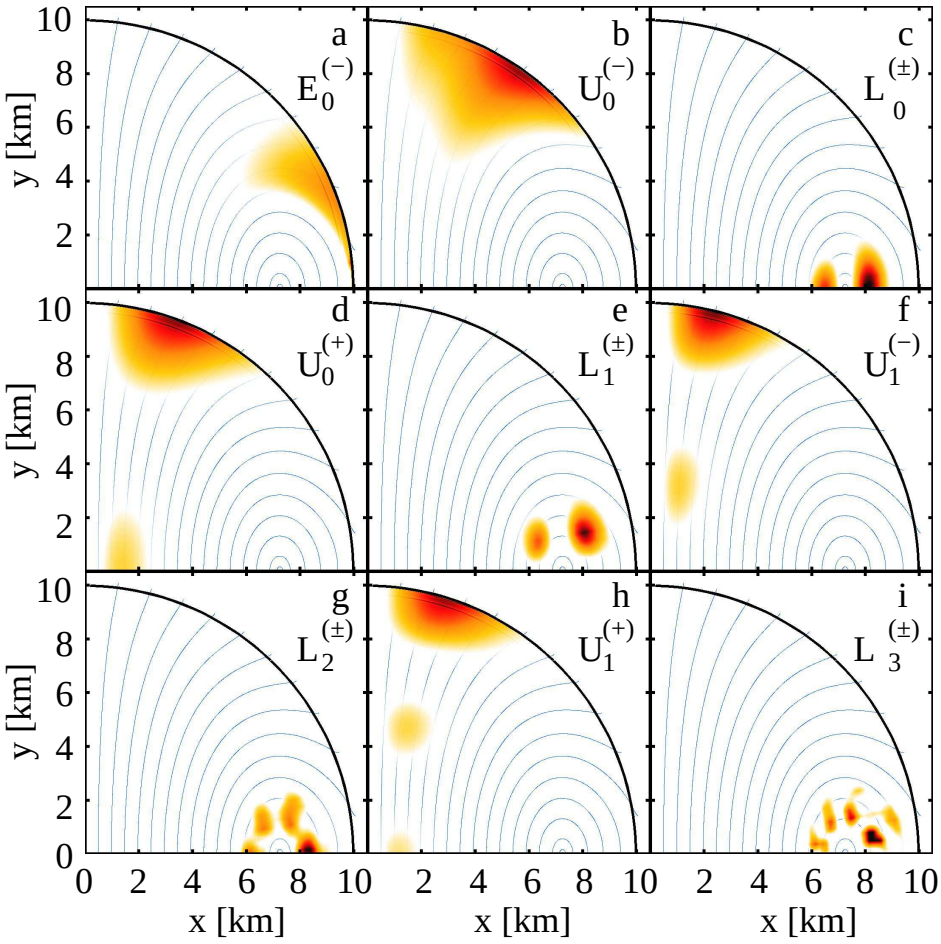

Figure 3.5: Fourier amplitude of the lowest frequency QPOs of model APR+DH 1.4. We discriminate upper QPOs (panels b,d,f, and h), lower QPOs (panels c, e, g, and i), and edge QPOs (panel a). The frequencies corresponding to each panel are given in Table 3.3. Blue lines indicate the magnetic field, and the color scale ranges from white (minimum) to red-black (maximum).

values (-5π to 8π). Therefore, the range of phases in different panels may be different. However, the important feature is the continuous change of the phase, which all graphs have in common. For the lower QPOs (panels c, e, g, and i) the procedure is not practicable, because there are more nodes on smaller spatial scales. Nevertheless one can clearly follow the phase change in direction perpendicular to the field lines in panels c and e. Note that some features appear because of the very low amplitude of the Fourier amplitude near the nodes of the QPOs, see e.g. the dark region for $r < 2\,\mathrm{km}$ in panel b, or the line in θ direction at about 5 km in panel d.

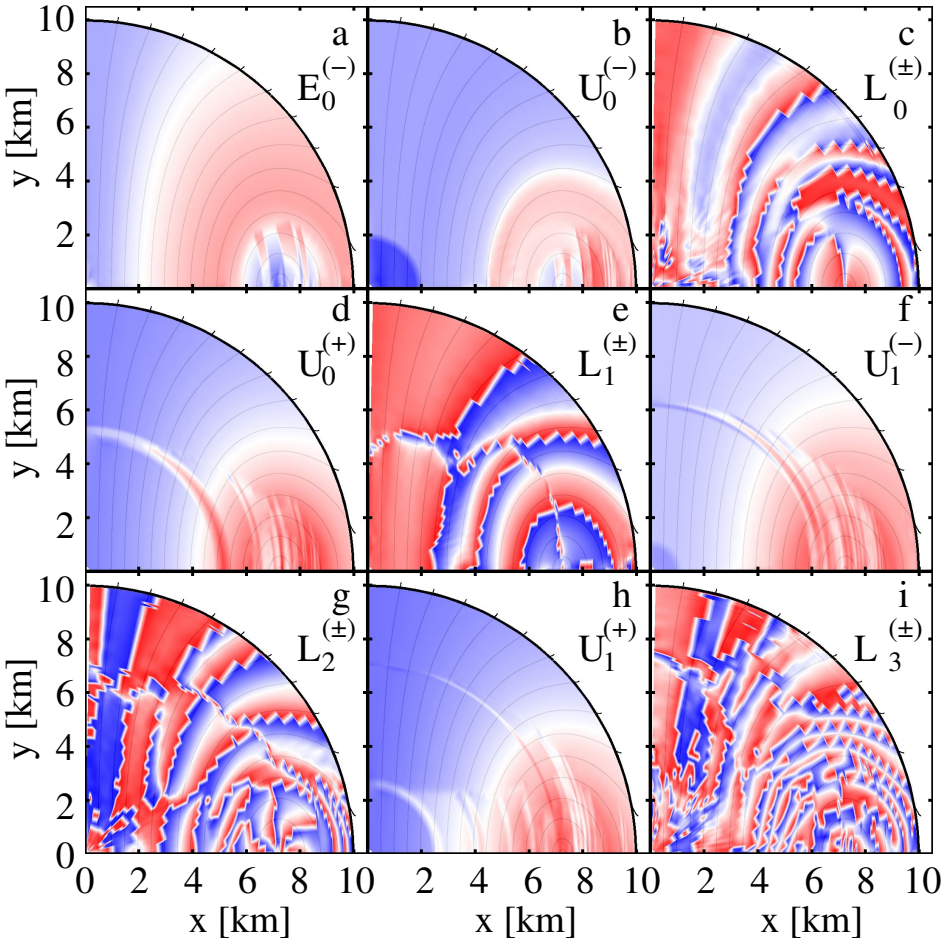

Figure 3.6: Phase of the Fourier transform of the first QPOs of model APR+DH 1.4. Solid lines indicate the magnetic field, and the color scale ranges from blue (minimum) to red (maximum). The minimum in the different panels varies between -5π and $-\pi$, and the maximum between 4π and 8π. For panels c, e, g, and i the minimum and maximum are $-\pi/2$ and $\pi/2$, respectively.

panel in Fig. 3.5	a	b	c	d	e	f	g	h	i
QPO name	$E_0^{(-)}$	$U_0^{(-)}$	$L_0^{(\pm)}$	$U_0^{(+)}$	$L_1^{(\pm)}$	$U_1^{(-)}$	$L_2^{(\pm)}$	$U_1^{(+)}$	$L_3^{(\pm)}$
frequency in Hz (± 0.2 Hz)	3.9	4.6	5.6	9.8	11.1	15.0	16.7	19.9	22.3
frequency expected from the semi-analytic model in Hz	3.6	4.85	5.5	9.7	11.0	14.6	16.5	19.4	22.0

Table 3.3: Frequencies of the QPOs displayed in Fig. 3.5 compared to the frequencies predicted by the semi-analytic model.

3.4 Magneto-elastic oscillations of a liquid core coupled to a solid crust

In the two preceding sections we have studied the two extreme cases of pure shear modes in the crust and pure Alfvén oscillations in the core. We have seen that they are of very distinct type. The crustal oscillations form a complete set of orthogonal eigenmodes, while the magnetic oscillations of the core are characterized by a frequency continuum, and quasi-periodic oscillations at the turning points and edges of the latter. It is very interesting to see how the system of coupled magneto-elastic oscillations behaves. For very weak magnetic fields $B < 5 \times 10^{13}\,\mathrm{G}$ the crust dominates the dynamics and we effectively recover the pure shear modes, which are practically unaffected by the presence of the magnetic field. In contrast the Alfvén oscillations are effected drastically and are confined to the core. However, they occur on much longer time scales than the crustal oscillations such that their effect on the crustal modes is negligible at that low magnetic field strength. In Section 3.4.2 we discuss the properties of these QPOs in detail. For very strong magnetic fields $B > 5 \times 10^{15}\,\mathrm{G}$ the crustal shear modes disappear completely and global, predominantly Alfvén oscillations dominate the evolution. The results at such strong magnetic fields are qualitatively the same as in Section 3.3. As in this preceding section we restrict ourselves here to dipolar magnetic field configurations.

3.4.1 Absorption of crustal shear modes by the Alfvén continuum

This subsection is concerned the absorption of purely shear $n = 0$ and $n > 0$ modes of the crust into the Alfvén continuum of the core. We will often refer to this process as the *damping* of crustal shear modes. This expression may mislead the reader to think of dissipation processes. However, damping in the current context refers to the transfer of energy from crustal modes into the continuum of the core, but not to dissipation of energy. Only when referring to numerical damping we mean the usual concept describing the loss of ordered kinetic energy by numerical dissipation.

$n = 0$ crustal shear modes

As we have shown in Gabler et al. (2011) purely shear oscillations are absorbed very efficiently by the Alfvén continuum of the core for magnetic field strengths $B \gtrsim 5 \times 10^{13}\,\mathrm{G}$. In this case the amplitude of the perturbations of the crust is damped by transferring their energy to the Alfvén continuum. To analyze how this damping scales with the magnetic field strength, we have performed a series of simulations for different crustal modes with $n = 0$, $l \geq 2$ for different magnetic fields (0, 10^{13},2×10^{13}, 5×10^{13}, 8×10^{13},10^{14} and $2 \times 10^{14}\,\mathrm{G}$). For these simulations we use a grid of 150×100 zones covering a domain $[0, r_\mathrm{s}] \times [0, \pi]$, which is equivalent to the medium grid of the previous section but not assuming equatorial symmetry. Here, we use the solution of the eigenvalue problem for the unmagnetized crust (see Appendix D) as initial

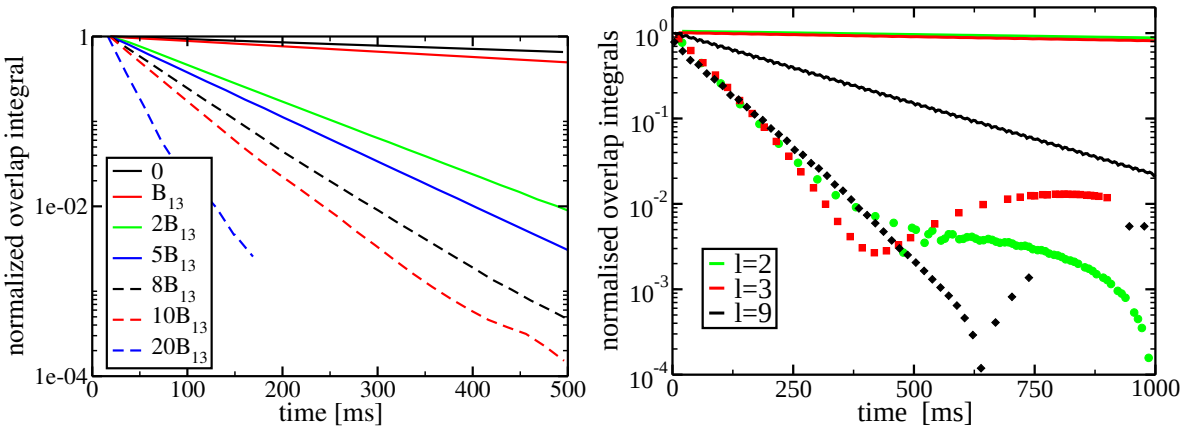

Figure 3.7: *Left panel:* The maximum of the normalized overlap integral for the $n = 0$, $l = 2$ eigenmode of the crust as a function of time. Stronger magnetic field results in faster damping of the initially excited crust mode. Orthogonality of different eigenmodes is fulfilled numerically up to about 10^{-5}. In the legend we introduced the abbreviation $B_{13} = 10^{13}$ G. *Right panel:* Damping of $l = 2, 3$, and 9 initial perturbations due to resonant absorption of the fundamental ($n = 0$) crustal shear modes for a magnetized model with 5×10^{13} G (dots). In the corresponding unmagnetized models (solid lines) only numerical damping occurs which increases with the angular order l of the mode.

perturbation for the velocity. Symmetries are exploited whenever a perturbation is purely symmetric or antisymmetric with respect to the equatorial plane.

In the following we will discuss our results by using so-called overlap integrals (derived in Appendix D). These overlap integrals are the expansion coefficients of an arbitrary spatial function in the basis of the crustal oscillation eigenmodes, i.e. they give a measure of how strong the different eigenmodes are excited (see Gabler et al., 2009, for an application to radial oscillations of neutron stars). In Fig. 3.7 we show the time dependence of the maxima of the overlap integrals defined in Eq. (D.11) corresponding to the $n = 0$, $l = 2$ crustal mode for different magnetic field strengths. The stronger the field is the faster the damping of the shear mode proceeds. For high field strength, $B > 2 \times 10^{14}$ G, it is not possible to obtain a characteristic damping time τ, because the time scale is shorter than one oscillation period. Therefore, the latter can be used as an upper bound for τ. For 2×10^{14} G we show the evolution of the overlap integral only up to the time when global magneto-elastic oscillations start to dominate and interfere with the purely shear modes of the crust.

In the right panel of Fig. 3.7 we show the maximum (absolute) amplitudes of the overlap integrals for different initial perturbations and for simulations both without magnetic field (solid lines) and with a polar magnetic field of 5×10^{13}G (dots) . In the field-free case the lines represent the numerical damping of crustal modes due to finite-differencing. When a magnetic field is present, the damping (now due to resonant

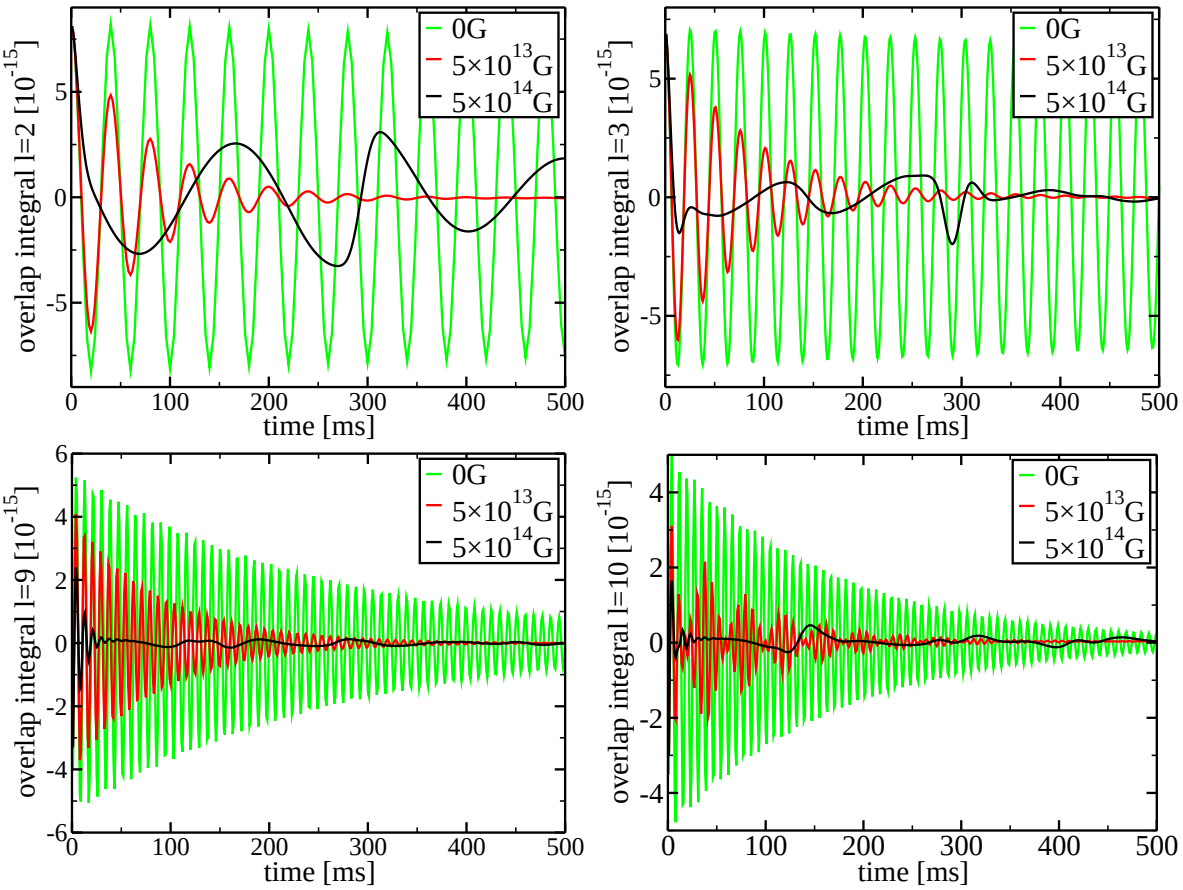

Figure 3.8: Overlap integrals for different $n = 0$ crustal modes at 0, 5×10^{13}, and 5×10^{14} G. Resonant absorption of the modes becomes stronger with increasing magnetic field strength. The displayed modes are $l = 2$ (upper left), $l = 3$ (upper right), $l = 9$ (lower left), and $l = 10$ (lower right).

absorption) increases with the magnetic field strength. For all modes, the timescale of resonant absorption is much shorter than that of numerical damping (see Table 3.4). After about 500 ms, the overlap integrals no longer sample the crust oscillations, but instead the magneto-elastic oscillations which then dominate the evolution (see below). We show the overlap integrals for different crustal modes ($l = \{2, 3, 9, 10\}$) as a function of time for different magnetic field strengths in Fig. 3.8. For all modes we find almost complete damping of the crustal mode after ~ 0.5 s at a magnetic field strength of 5×10^{13} G (red line in Fig. 3.8). For a stronger magnetic field ($B = 5 \times 10^{14}$ G, black line in the figure) the crustal modes become damped after a few msec, and only the dominant magneto-elastic oscillations remain. As observed before, the numerical damping of the unmagnetized models (green lines) increases with the mode number l.

Table 3.4 shows the damping timescales, obtained by analyzing the overlap integrals, for different $n = 0$, $l \geq 2$ modes and different magnetic field strengths. The values for zero magnetic field serve as a measure of the numerical damping of the code. As

magnetic field [G]	τ [ms] for mode $n=0$						
	$l=2$	$l=3$	$l=4$	$l=5$	$l=6$	$l=7$	$l=8$
0	1130	1110	1030	874	654	466	313
1×10^{13}	688	835	846	764	599	441	302
2×10^{13}	102	287	478	534	481	385	279
5×10^{13}	83	85	72	54	38	63	104
8×10^{13}	58	60	43	38	37	34	28
1×10^{14}	46	48	37	38	40	33	27
2×10^{14}	20	21	21	23	19	21	21

Table 3.4: Damping timescale τ in ms for different $n=0$, crustal shear modes for different magnetic field strengths.

expected for numerical dissipation processes, modes with higher l suffer stronger from numerical damping than lower l (see also Cerdá-Durán, 2010). For weak magnetic fields, e.g. 10^{13} G, the damping of high l modes is dominated by numerical dissipation, while for low l modes it is caused by the interaction with the Alfvén continuum of the core. For magnetic fields stronger than 5×10^{13} G, we are confident that the damping time of all studied modes is physical and not due to numerical dissipation. Above 2×10^{14} G the oscillations are damped on shorter time scales than the respective oscillation period, and hence it is impossible to obtain accurate damping times.

Figure 3.9 shows $\tau/t_{\rm A}$, where $t_{\rm A}$ is the Alfvén crossing time of the star at the pole. The damping time of crustal modes due to the absorption by the Alfvén continuum scales linearly with $t_{\rm A}$, i.e. τ decreases with increasing magnetic field. The mean damping time is about $0.04\,t_{\rm A}$. Deviations from this value (see Fig. 3.9) depend non-trivially on the magnetic field and the mode number l. The spread decreases with increasing magnetic field strength, being smallest for our $B=2\times10^{14}$ G simulation. Low l-modes (filled circles in Figure 3.9) show a smaller spread around the mean value than the higher l-modes (crosses in the same figure).

These deviations are expected, because the damping depends on a variety of parameters as for example the frequency of the crustal mode, the frequencies available in the Alfvén continuum of the core, and the spatial structure of the crustal modes. Numerical effects may also affect the damping times. These are: Firstly, the grid resolution necessary to obtain a comparable accuracy for different modes increases with increasing mode number l. Secondly, waves in the crust reaching the core-crust interface will propagate into the core as Alfvén waves. Due to the jump in the wave velocity at the interface, the wave number increases, i.e. the resolution requirements in the core are more restrictive. This holds, in particular, for weak magnetic fields, where the jump in the wave velocity is larger, and for large l modes with higher frequencies.

The damping time at a given magnetic field strength $B>10^{13}$ G varies only by at most a factor of two between different l, but may vary significantly with the magnetic field strength. This indicates that the damping is dominated by the magnetic field and

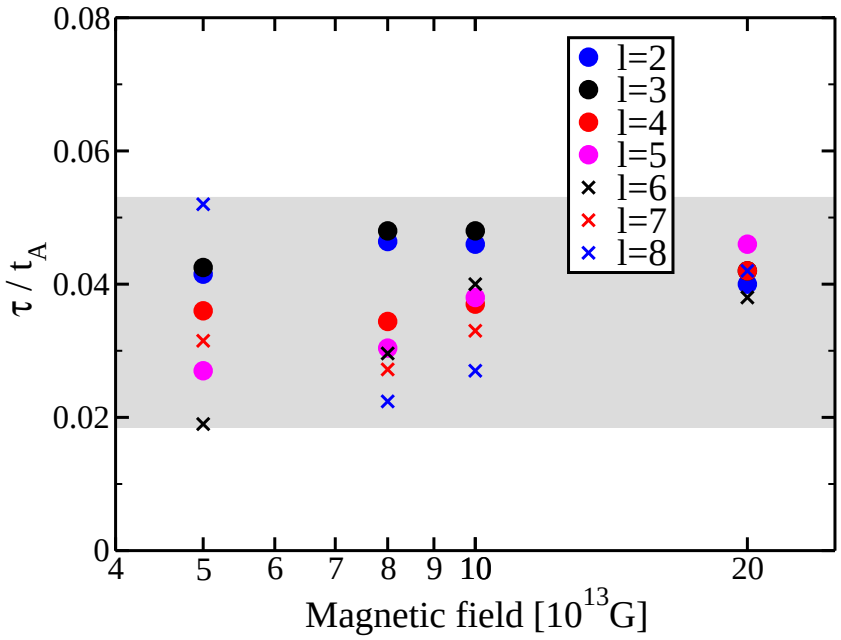

Figure 3.9: The dependence of $\tau/t_{\rm A}$ on the magnetic field. The stronger the magnetic field the less is the spread of the numerical values for different l around this value. The shaded area indicates the maximum range of variation of $\tau/t_{\rm A}$ around the mean value (~ 0.04).

does not depend sensitively on the mode structure itself, i.e. there will always be a part of the continuum that is able to drain the energy from the crustal oscillations.

A more detailed discussion of the damping of the different crustal modes is beyond the scope of this work. Our results do not favor a crustal-mode interpretation of the observed QPOs in SGRs, because any crustal shear mode is damped sufficiently fast for magnetic field strengths well below the typical magnetar field strengths $\sim 5 \times 10^{13}$ G. Although there might exist SGRs with weaker magnetic fields (Rea et al., 2010), QPOs have only been observed so far in magnetars with the strongest fields.

Different equilibrium models

All previous results were obtained for a model based on the APR+DH EoS and a mass of $1.4\,{\rm M}_\odot$. Simulations using other EoS or different masses for the equilibrium model yield qualitatively similar results.

In table 2 of Gabler et al. (2011) we showed that the damping of purely crustal shear modes occurs on the order of 100 ms or less for a variety of EoS and masses at a magnetic field strength of $B = 10^{14}$ G. The initial models that we used in those simulations employed a different prescription for the internal energy (ideal gas) than the values provided in the EoS tables. As these models were thus thermodynamically inconsistent, we have recomputed them with the appropriate internal energy values. The resulting damping times are at most 20% longer than the values reported in Gabler et al.

EoS	τ [ms] at $B = 10^{14}$ G		
	$n = 0$, $l = 2$	$n = 0$, $l = 3$	$n = 0$, $l = 9$
APR+DH 1.6	45	47	21
APR+DH 2.0	38	41	17
L+DH 1.6	57	61	27
L+DH 2.0	52	56	25

Table 3.5: Damping timescales τ due to resonant absorption of crustal shear modes by the Alfvén continuum for initial perturbation modes $l = 2$, $l = 3$, and $l = 9$ for different combinations of equations of state at $B = 10^{14}$ G. The number in the labeling of the EoS represents the mass of the neutron star model in $M_\odot$.

(2011). Some of the corrected damping times are shown in Table 3.5. The other EoS used to calculate the models in Gabler et al. (2011) cannot reproduce neutron stars with solar masses of about $2M_\odot$, and are thus no longer considered in the present work.

The variation of the damping times with the EoS at a given magnetic field is not surprising. The relative size of the crust of these models varies roughly by a factor of 3 (see Sotani et al., 2007), and the shear modulus of both crustal EoS is of comparable size. This explains the smallness of the observed variations in Gabler et al. (2011) which do not exceed a factor of 5. A significantly lower shear modulus, as proposed in Steiner and Watts (2009), would lead to even shorter damping times of the crustal shear modes.

The influence of the details of the EoS are not substantial because when trying to explain the frequencies of the QPOs observed in SGRs as shear oscillations, the shear modulus should lie in the range we use in this work. Otherwise it is already impossible to reproduce the correct range of frequencies within the crustal oscillation model. Changing the shear modulus somewhat would have only a modest effect on the damping times. However, even for a hypothetically exotic shear modulus, which could be one order of magnitude larger than the actual values we use, the crustal shear oscillations would be damped much too fast to explain long-lived QPOs. We therefore argue that we can safely exclude shear oscillations as a viable explanation of observed magnetar QPOs, for the magnetic field configurations studied here.

$n > 0$ crustal shear modes

The higher radial overtones ($n > 0$) of the shear modes have frequencies above 500 Hz (see Table 3.2) and are usually used to explain the QPOs of SGR 1806-20 with the highest frequencies of 625 and 1840 Hz. As these modes have at least one node inside the crust computing their evolution demands much higher spatial resolution than necessary for the $n = 0$ modes. Thus, it was practically impossible for us to follow their evolution over several Alfvén crossing times to the same accuracy as for the $n = 0$ modes. However this would have been necessary to draw more reliable conclusions about damping times or interaction of these modes with the Alfvén continuum in the core. Nevertheless, we can make some qualitative statements.

The time needed for a shear wave ($v_S \sim 1000\,\mathrm{km/s}$) to travel through the crust ($\Delta r_{\mathrm{crust}} \sim 1\,\mathrm{km}$) corresponds to the inverse of the frequency of the first overtone ($n = 1$), which is of the order of $f \sim 1\,\mathrm{kHz}$. Assuming that the wave travels inside the crust along the θ-direction (travel path $\Delta r \sim 10\pi\,\mathrm{km}$), a similar estimate results in frequencies $v_S/\Delta r \sim 30\,\mathrm{Hz}$ which is of the order of the frequency of the fundamental $n = 0$ oscillation. Therefore, we may conclude that the $n = 0$ modes represent waves that travel predominantly parallel to the crust-core interface, while the $n = 1$ modes correspond to waves that travel radially. This may explain the strong dependence of the $n = 0$ modes on the angular number l and the weak dependence of the $n = 1$ modes (see Table 3.2 with the corresponding discussion, and Sotani et al., 2007). Hence, we expect the $n = 0$ modes, derived with isotropic shear modulus, to be much more affected by the presence of an anisotropic magnetic field than the $n = 1$ modes. In particular, near the equator where the coupling between the crust and the core is weaker than close to the pole (see Eq. 2.101) the shear waves may travel back and forth in the crust without interacting strongly. Additionally, at the equator the magnetic field is almost parallel to the θ-direction, i.e. the direction of the Alfvén waves is perpendicular to the direction of the $n = 1$ shear waves. This suggests that the $n = 1$ shear waves are not influenced strongly by the presence of moderate magnetic fields ($\lesssim 10^{15}\,\mathrm{G}$). According to these theoretical considerations we expect the overtones of the shear modes to survive longer than the $n = 0$ modes.

To investigate this issue, we have performed two simulations with our reference model at magnetic field strengths of $2\times10^{14}\,\mathrm{G}$ and $5\times10^{14}\,\mathrm{G}$. The resolution for antisymmetric simulations ($l = \{2, 4, 6, ..\}$) was 150×50 zones. The initial perturbation consisted of the $n = 1$, $l = 2$ mode of the crust only. In Figure 3.10 we show the main contributions to the oscillations as obtained by Fourier analyzing the time evolution of the simulation with $5\times10^{14}\,\mathrm{G}$. The QPO patterns are compressed towards the equator and strongly distorted from the typical l-dependence of spherical harmonics of the purely shear eigenmodes of the crust (see Appendix D). To account for this difference we label these QPOs with l'. Naturally, the initial data of the undistorted l-mode excites many distorted l'-QPOs. As expected from the theoretical considerations above, the strongest amplitudes of the oscillations appear near the equator, where the coupling to the core is weakest (see Fig. 3.10). The magnetic field also increases the spacing between the frequencies of successive $n = 1$, l' modes from $\Delta f \approx 1\,\mathrm{Hz}$ without field to $\Delta f \approx 10\,\mathrm{Hz}$ (see Sotani et al., 2007, for a discussion of purely shear eigenmodes).

To study the behavior of the different QPOs, we calculate the corresponding overlap integrals (Eq. (D.11)) but taking the spatial structure obtained from the Fourier analysis (Fig. 3.10) as basis functions. The time evolution of the maxima of these overlap integrals for $l' = \{2, 4, 6, 8\}$ can be seen in the left panel of Figure 3.11. Indeed all of l'-QPOs are excited by the purely shear $n = 1$, $l = 2$ eigenmode perturbation. Since the frequencies of the different $n = 1$ modes are very similar, i.e. hard to disentangle in any analysis of the simulations, we average all $n = 1$ modes to estimate the total damping time of the $n = 1$ QPOs. To this end we calculate the overlap integral with the radial function

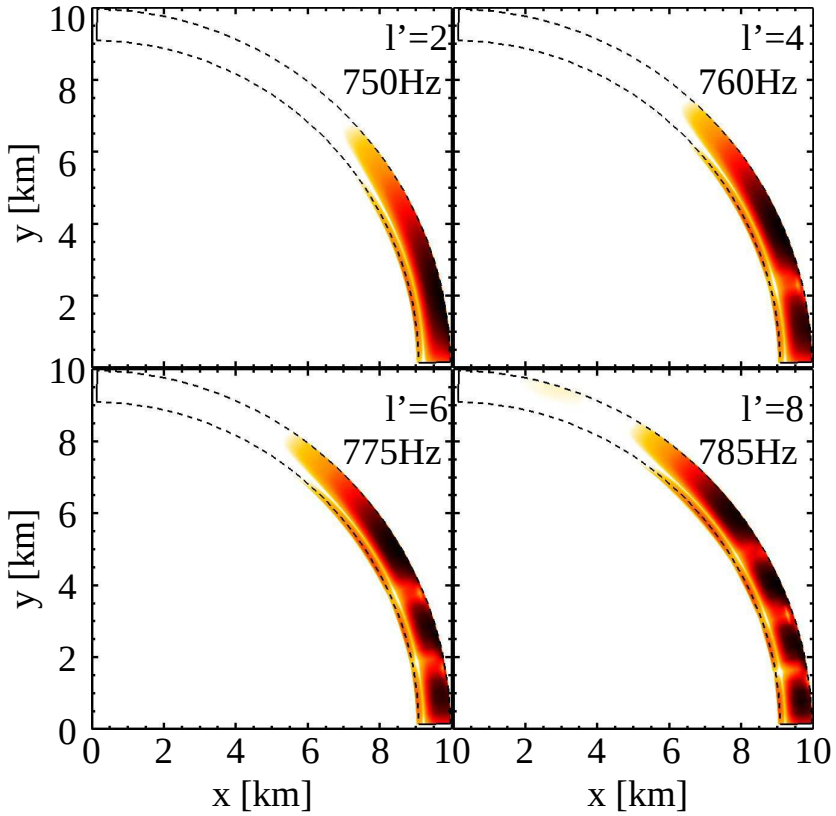

Figure 3.10: The spatial structure of the first $n = 1$, antisymmetric crustal shear modes in the presence of a moderate magnetic field of 5×10^{14} G. The oscillation patterns are strongly distorted from the typical l-dependence of the spherical harmonics and only exist in regions close to the equator, where the coupling between the core and the crust is weakest. We therefore label their angular dependence with l'. The dashed lines indicate the region of the crust and the color scale ranges from white (minimum) to red-black (maximum).

$\Xi_i(r, \theta) = R_{\lambda_r}$ corresponding to the pure shear eigenmodes obtained with Eq. (D.8). This effectively averages over the angular dependence, and provides a measure of how strong the ensemble of all l', $n = 1$ QPOs is excited. The corresponding plots for $B = 2 \times 10^{14}$ G and $B = 5 \times 10^{14}$ G are shown in the right panel of Fig. 3.11.

As indicated by the fitting functions with damping times of 150 and 230 ms, the damping timescale of the $n = 1$ QPOs is much longer than for the $n = 0$ modes at the given magnetic field strength of a few 10^{14} G.

However, one has to be very cautious at this point. With the resolution used here, we are not able to resolve the Alfvén oscillations inside the core of the neutron star which could damp the crustal shear oscillations resonantly. At 5×10^{14} G the fundamental Alfvén oscillation is about 2 Hz. To resolve the resonant coupling to the crustal $n = 1$ mode of roughly 500 Hz one would need the 250th overtone. Simulations with appro-

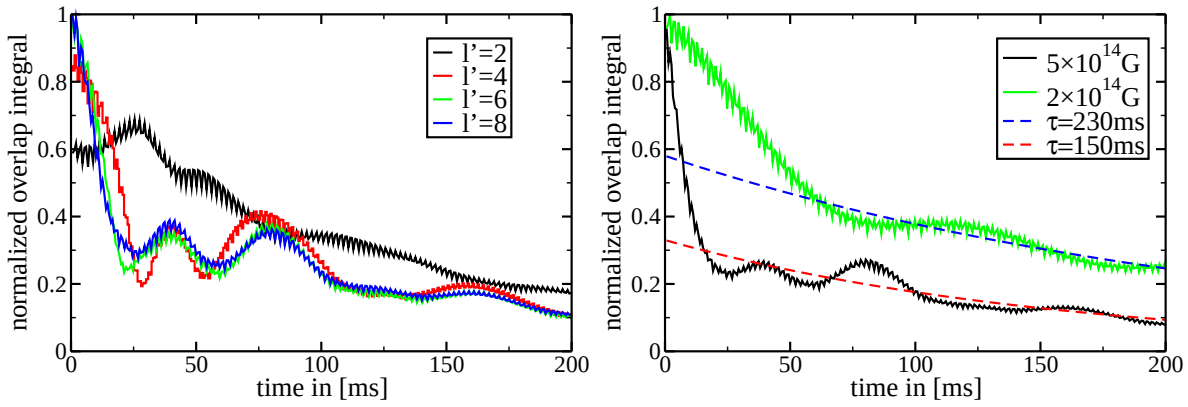

Figure 3.11: *Left panel*: The normalized overlap integrals of the evolution for the first few $n = 1$, antisymmetric magneto-elastic modes at $B = 5\times10^{14}$ G. The approximate mode structure is taken from the Fourier analysis (see Fig. 3.10). Strictly speaking there are no modes in terms of the result of the linear analysis, but the influence of the magnetic field is insufficient to destroy the coherent oscillations in all parts of the crust. The initial perturbation of the $n = 1$, $l = 2$ crustal mode excites a large number of the magneto-elastic modes which are all damped on a timescale of ~ 150 ms. *Right panel*: The overlap integral performed for a basis with purely radial dependence $\Xi_i(r, \theta) = R_{\lambda_r}$ (see Appendix D) of the $n = 1$ modes. These integrals are a measure of how strong the ensemble of all l', $n = 1$ modes is excited. The damping time, indicated by the fits to an exponential (dashed lines), for 2×10^{14} G (5×10^{14} G) of $\tau = 230$ ms (150 ms) is much longer than that of the $n = 0$ modes, which is of the order of several ms only.

priate grid resolution would take of the order of years. For the damping process itself this lack of resolution should not be a problem, because the numerical method employed should take all necessary information into account, i.e. the Riemann solver at the crust core interface considers all the local information of possible waves traveling into the core. The problem arises inside the core, where a low resolution leads to an averaging out of all fine-scale structure. Hence, the energy of the Alfvén overtones of the continuum is transformed to resolved low order oscillations, i.e. we cannot trust the oscillations inside the core. However, as long as the Alfvén oscillations do not reach the crust at the opposite side of the star at $t \approx t_A = 0.5/f_A = 1.2$ s (for $B = 5 \times 10^{14}$ G), a simulation of the crust region should give correct results. Therefore, the present estimate of the damping time of the $n = 1$ overtones should be considered as a lower limit, because the main effect we are missing is the excitation of crustal magneto-elastic QPOs by incoming Alfvén oscillations of the core.

3.4.2 Predominantly Alfvén QPOs in the core at intermediate magnetic fields $5 \times 10^{13} < B < 10^{15}$ G

In Gabler et al. (2010, 2011) we have shown that the crust significantly changes the structure of the QPOs for intermediate magnetic field strengths between $5 \times 10^{13} - 10^{15}$ G compared to models without crust. In this section we investigate the behavior of the Alfvén QPOs of the core in this regime further.

QPO structure at 4×10^{14} G

In this subsection we will analyze the results of two simulations with a resolution of 100×40 zones and computational domain $[0, r_s] \times [0, \pi/2]$. We perform one simulation with $l = 2$ initial data and antisymmetry with respect to the equatorial plane, and another symmetric one with $l = 3$ initial data. Both runs were evolved up to $t \approx 5$ s.

For the model APR+DH 1.4 with a magnetic field strength of $B = 4 \times 10^{14}$ G we find three different families of QPOs. Following Cerdá-Durán et al. (2009) we label the *lower* QPOs as $L_n^{(\pm)}$ and the *upper* QPOs as $U_n^{(\pm)}$. A new family of QPOs appears, which we call *edge* QPOs and label them as $E_n^{(\pm)}$. To avoid confusion with the previous work of Cerdá-Durán et al. (2009), and because the fundamental upper symmetric QPO has special properties as we will show below, it will be labeled as $U_*^{(+)}$ at low magnetic field strength. The plus and minus sign in the description of the QPOs indicate symmetry (+) or antisymmetry (-) of the QPO with respect to the equatorial plane.

In Fig. 3.12 we plot the local maxima of the Fourier amplitude inside the star. Similar to the case without crust lower QPOs (panels a and b) are attached to field lines which close inside the core, upper QPOs are located closer towards the magnetic poles at open field lines (panels c, d-f), and edge QPOs are connected to the open field line inside the core of the neutron star which just fails to close inside (panels g-i). The two QPOs $U_1^{(+)}$ and $E_4^{(+)}$ have very similar frequencies. Due to limited evolution time and hence limited resolution for the Fourier transform both QPOs contribute significantly to the Fourier signal as can be seen in panel i. Similarly the figure for $E_3^{(+)}$ contains some contribution of $U_0^{(+)}$ along the field lines crossing the equator between a radius of 1 and 4 km. In both panels the edge QPO is concentrated on the field lines around 5 km.

In Fig. 3.12 we plot the distribution of the Fourier amplitude inside the star. Lower QPOs, as shown in panels a and b, are attached to field lines which close inside the core. In contrast, upper QPOs are located closer towards the magnetic poles at open field lines (panels c, d-f). A third family, the edge QPOs, are connected to the open field line inside the core of the neutron star which just fails to close inside (last open field line). These QPOs can be seen in panels g-i of Fig. 3.12. The two QPOs $U_1^{(+)}$ and $E_4^{(+)}$ have very similar frequencies. Due to limited evolution time and hence limited resolution for the Fourier transform both QPOs contribute significantly to the Fourier signal at the corresponding frequency as can be seen in panel i. Similarly, the figure for $E_3^{(+)}$ contains some contribution of $U_0^{(+)}$ along the field lines crossing the equator between a radius of 1 and 4 km. In both panels the edge QPOs are concentrated on the field lines which cross

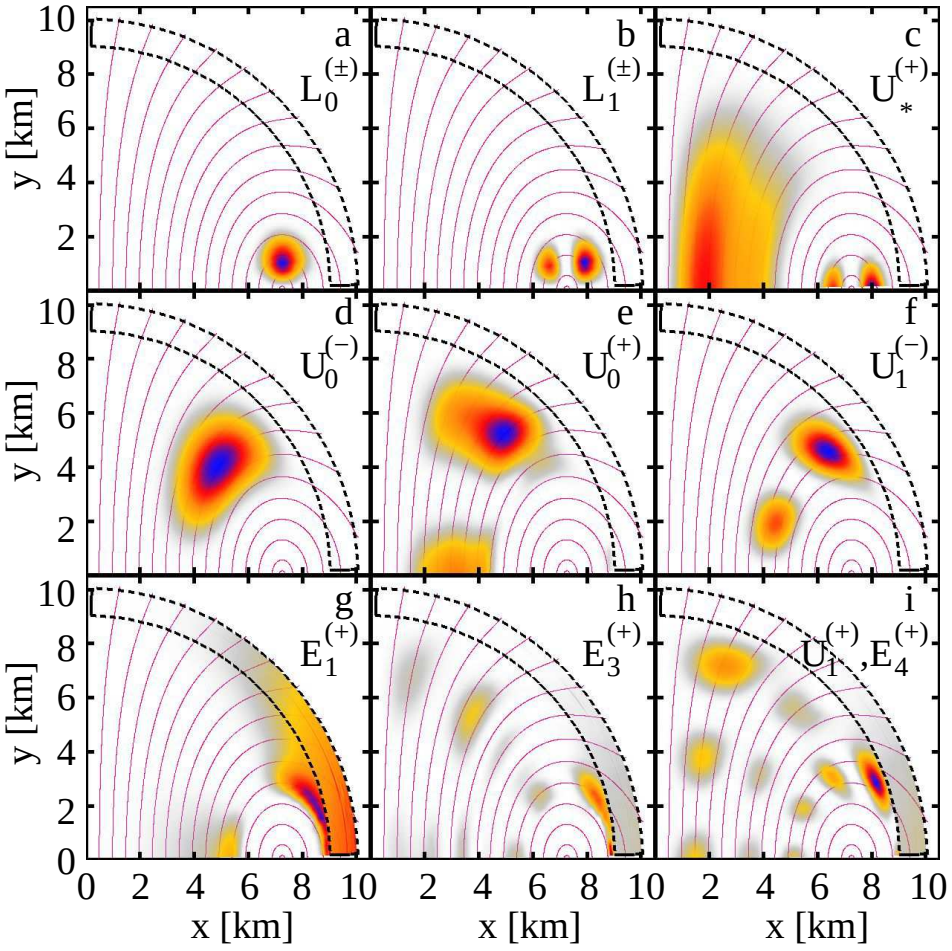

Figure 3.12: The Fourier amplitude inside the neutron star for the model APR+DH 1.4 at $B = 4 \times 10^{14}$ G. Shown are the first two lower QPOs $L_0^{(\pm)}$ and $L_1^{(\pm)}$, the first four upper QPOs $U_*^{(+)}$, $U_0^{(-)}$, $U_0^{(+)}$, and $U_1^{(-)}$ and some selected edge QPOs $E_1^{(+)}$, $E_3^{(+)}$, and $E_4^{(+)}$. (The figure for $E_2^{(+)}$ was not very clear due to contamination with other QPOs.) The plus and minus sign indicate symmetry (+) and antisymmetry (-) with respect to the equatorial plane. Magenta lines indicate magnetic field lines, and black, dashed lines the location of the crust. The color scale ranges from white-blue (minimum) to red-black (maximum).

the equatorial plane at around 5 km. The naming of the edge QPOs becomes clearer in Fig. 3.13, where we plot the Fourier amplitude of the velocity, averaged per field line in the frequency-radius plane. The maxima indicate the position of the QPOs. The red and green lines are the continuum of frequencies obtained with the semi-analytic model introduced in Cerdá-Durán et al. (2009) and adopted here to the problem in the presence of the crust.

The different families of QPOs mentioned above and shown in Fig. 3.12 can also be identified in Fig. 3.13. The lower QPOs are attached to the closed field lines which

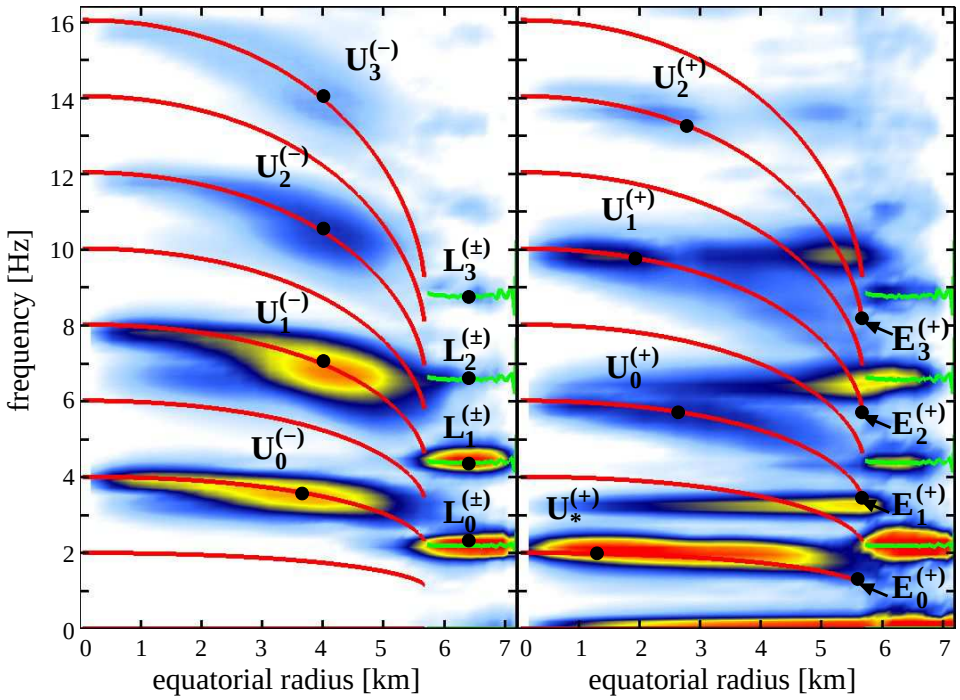

Figure 3.13: The averaged Fourier amplitude along different magnetic field lines labeled by the radius where they cross the equator for model APR+DH with $M = 1.4\,\mathrm{M}_\odot$ and $B = 4 \times 10^{14}$ G. Red and green lines give the Alfvén continuum obtained with the semi-analytic model. The locations of the QPOs are indicated by black dots. *Left panel*: antisymmetric simulation; *right panel*: symmetric simulation. The color scale ranges from white-blue (minimum) to orange-red (maximum).

cross the equatorial plane near 6.5 km. Since they are connected to the closed field lines these QPOs do not have a preferred symmetry, and hence are present in symmetric and antisymmetric simulations. The continuum of frequencies derived with the semi-analytic model (green lines in Fig. 3.13) has a minimum at the point where we find the lower QPOs. We thus interpret the $L_n^{(\pm)}$ as turning point QPOs (see Levin, 2007). With the exception of the fundamental $U_*^{(+)}$, which is located almost at the turning point of the semi-analytic model, the upper QPOs are localized in the continuum of the open field lines (red lines in Fig. 3.13) that cross the equatorial plane at $2 - 4$ km.

The members of the new family of QPOs, also obtained in Colaiuda et al. (2009), are called edge QPOs because of their position in Fig. 3.13. These QPOs are related to those parts of the continuum, obtained with the semi-analytic model (red lines), which do not connect to the continuum of the closed field lines (green lines) (see also the sketch in Fig. 3.4). For more details on the interpretation of the QPO structure without crust we refer to Cerdá-Durán et al. (2009) and with crust to Gabler et al. (2010).

Differences caused by the presence of the crust

The lower QPOs attached to the closed field lines are reproduced qualitatively similar as in the case without crust. The only difference is that they are limited to the field lines which close inside the core and do not extend into the crust.

However, the upper QPOs which are located near the pole in models without crust (Sotani et al., 2007; Cerdá-Durán et al., 2009; Colaiuda et al., 2009), can now be found at substantial distance from the poles, i.e. at lower latitudes (see also figure 4 in Gabler et al., 2011). In simulations without crust the oscillations were associated with the maximum at the turning point of the continuum at the pole, while if the crust is included, we obtain the maximal amplitudes away from the pole and inside the continuum predicted by the semi-analytic model in the absence of a crust. One possible interpretation of this new feature is that the shear modulus in the crust alters the propagation of magneto-elastic oscillations in the region near the pole in such a way that standing waves cannot form at all along individual field lines or, if they form, they go quickly out of phase with nearby field lines in this region.

At this point it is helpful to recall the problem of the reflection of plane-parallel waves, where the reflection coefficient depends on the jump in the propagation velocity or equivalently on the index of refraction. The stronger the jump in the index is, the larger is the fraction of the incident wave which becomes reflected. Using this analogy we would expect that the smaller the difference in propagation velocity at the crust-core interface is, the more refraction into the crust should occur and less reflection back into the core should be produced. If significant refraction into the crust occurs, no stable standing waves can be maintained during the evolution. When following the crust-core interface from the pole towards the equator the coupling between crust and core becomes weaker, see Eq. (2.101) where the θ dependence of the coupling factor is realized in b^r. The magnetic field in the radial direction, and hence the Alfvén velocity, decreases with increasing θ. Therefore, the jump in the propagation velocity increases, and thus the fraction of the wave which is reflected will also increase along this trajectory. For sufficiently low magnetic fields there should always be a region near the equator were almost perfect reflection occurs. However, when following the crust-core interface from the equator towards the pole, one will reach a characteristic magnetic field strength where insufficient reflection occurs to maintain stable standing waves along a certain field line. At this point we find the maximum amplitude of the QPO in the presence of a crust. We will investigate the reason for this behavior further in Sec. 3.4.2.

The new position of the maximum amplitude of the QPOs is thus determined by two effects. Near the pole the magnetic field lines get out of phase due to the interaction through the extended crust, because a significant fraction of the oscillation is refracted. The magnetic field lines can be seen like strings which are not attached to a rigid but rather "moving" boundary, i.e. the crust which responds to the oscillations. The resulting effect is a strong coupling of different magnetic field lines and, consequently, an energy transfer between the lines due to the scalar shear modulus. In this region and for magnetic field strengths studied here, each field line seems to act as a damped oscillator.

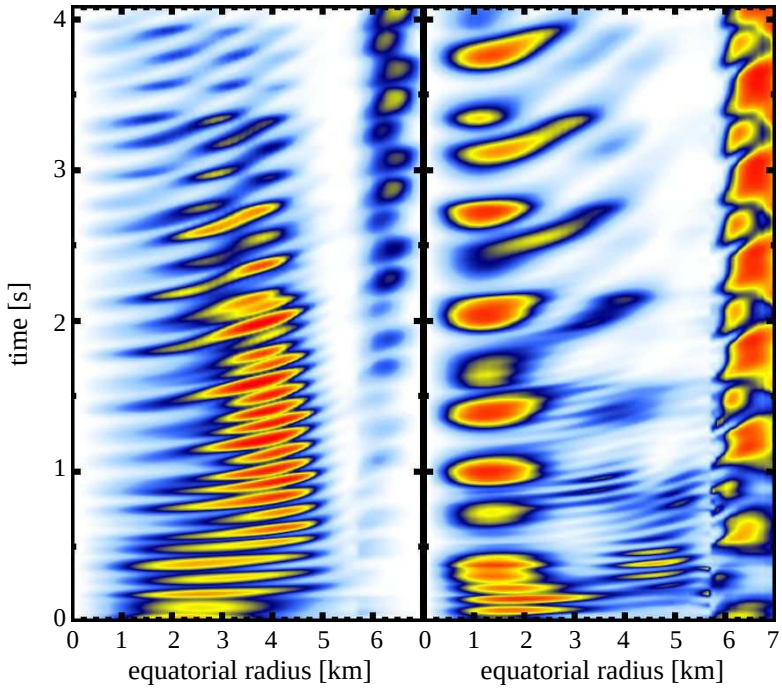

Figure 3.14: Evolution of the magnetic plus kinetic energy per field line divided by the sum of the energy over all field lines. The field lines are labeled by their crossing point with the equator. Note that as the total energy decreases with time the apparent increase of the energy of the lower QPOs is due to color rescaling at every time step. Their amplitude actually decreases, but more slowly than that of the upper QPOs. The *left panel* shows antisymmetric and the *right panel* symmetric simulations. The color scale ranges from white-blue (minimum) to orange-red (maximum).

Near the equator the magnetic field lines get out of phase due to phase mixing like in the case without extended crust. The additional damping close to the pole makes the corresponding upper QPOs to be shorter lived than in the case without crust. This effect can be observed in the right panel of Fig. 3.14, where we show the magnetic plus the kinetic energy per field line divided by the total magnetic plus kinetic energy at the given time as a function of time for different field lines. The initially excited QPOs attached to the field lines between 4.5 and 5 km disappear rapidly after about 0.5 s. In contrast, the lower QPOs and the fundamental symmetric QPO near the pole persist during the whole evolution. Fig. 3.14 may suggest that the lower QPO gain energy with time. However, this apparent energy increase is not a physical effect, because the total energy decreases with time due to numerical dissipation. Hence, the relative amplitudes of the energy of the lower QPOs increase, while their absolute amplitude decrease slightly because of numerical dissipation.

Compared to simulations without crust (Cerdá-Durán et al., 2009) we find a new fundamental upper QPO $U_*^{(+)}$. This QPO appears because the boundary condition at the crust-core interface causes a reflection which results in a node at this surface.

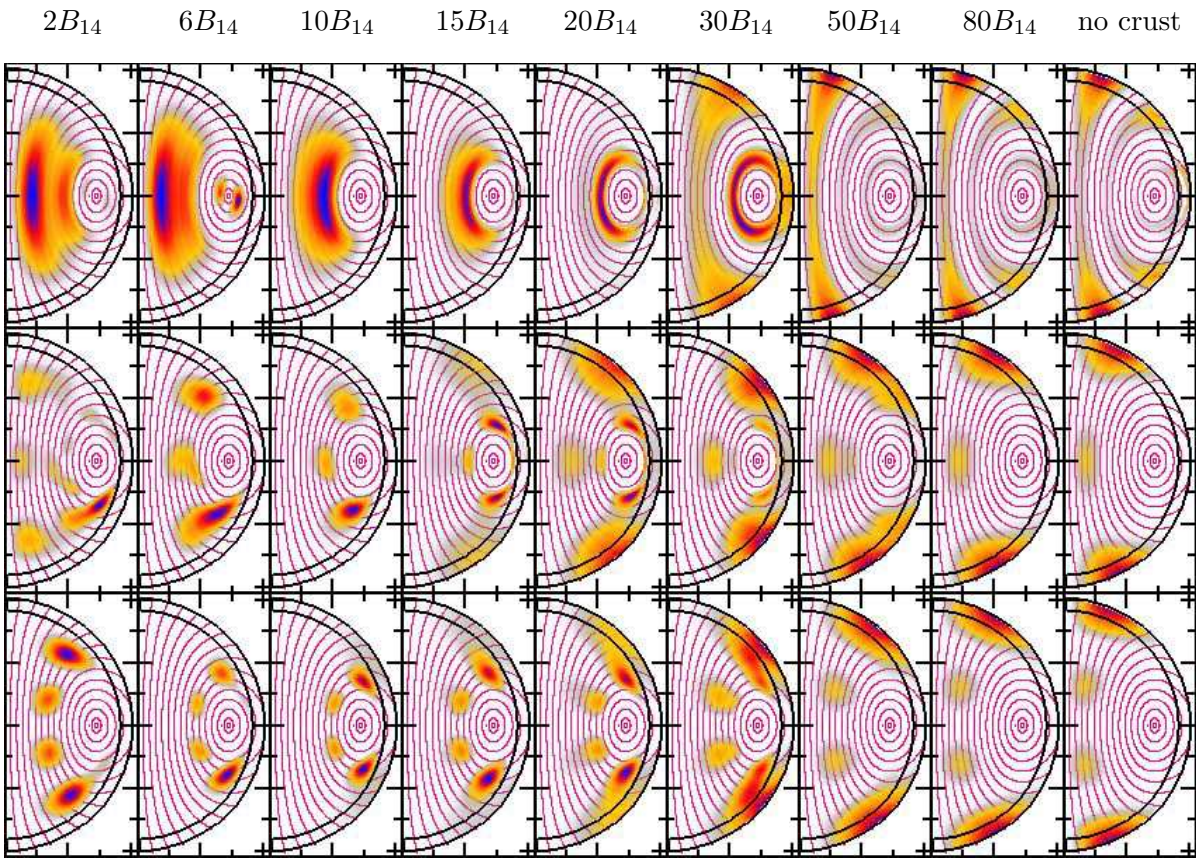

Figure 3.15: Structure of upper QPOs at different magnetic field strengths for the model APR+DH 1.4. The panels show the fundamental symmetric $U_*^{(+)}$ (upper panels), the symmetric $U_0^{(+)}$ (middle panels) and antisymmetric $U_1^{(-)}$ QPOs (lower panels). The frequencies of the QPOs shown here are given in Table 3.6. The color scale ranges from white-blue (minimum) to red-black (maximum).

Without crust the boundary condition at the surface of the star implies a maximum there and the fundamental oscillation has the node at the equator in this case. Therefore, the symmetric QPO $U_0^{(+)}$ must have an additional node inside the core (see panel e in Fig. 3.12 or the second row of Fig. 3.15). $U_*^{(+)}$ situated between 1 and 2 km (Fig. 3.14, the right panel) decays less rapid than the other upper QPOs, $U_0^{(-)}$, $U_{n\geq 0}^{(+)}$, and $U_{n>0}^{(-)}$. This may be related to the fact, that at $B = 4 \times 10^{15}$ G, $U_*^{(+)}$ is located close to the maximum of the continuum (see Fig. 3.13). There, the gradient of the continuum is less steep, and neighboring field lines get out of phase less rapidly. This behavior is similar to a turning point QPO, which persists for longer time than edge QPOs (Levin, 2007).

Changing QPO position with increasing magnetic field

For magnetic field strengths between 10^{14} and 10^{15} G the simulations reveal that the location of the upper QPO, $U_n^{(\pm)}$ changes within the neutron star. This was not observed

in the case of pure Alfvén oscillations in Cerdá-Durán et al. (2009) or Sotani et al. (2008b), where the upper QPOs were always observed close to the pole. Fig. 3.15 (first three columns) shows the new effect, where we plot the spatial structure of the Fourier amplitude of the QPOs. When increasing the magnetic field from 2×10^{14} to 10^{15} G the upper QPOs $U_n^{(\pm)}$ move from a location near the pole towards the equator. The change in position of the $U_n^{(\pm)}$ is shown in Fig. 3.15 only for $U_0^{(+)}$ and $U_1^{(-)}$, but holds for all higher overtones as well and does not depend on the symmetry. For the fundamental $U_*^{(+)}$ the dislocation is less (upper row in Fig. 3.15). One can understand this behavior at least partially with the help of the semi-analytic model. Fig. 3.13 shows that the frequencies and the symmetry of the QPOs are correctly predicted, if we assume that the Alfvén wave is reflected at the crust-core boundary. However, the semi-analytic model cannot explain where within the continuum the QPOs are situated.

Remembering the analogy with the reflection of plane-parallel waves in the preceding subsection and bearing in mind that with increasing magnetic field b^r the relative jump in the propagation velocity on both sides of the crust-core interface at a given position θ decreases, more parts of an incident wave get refracted into the crust. This means that the point where stable standing waves can be maintained should move towards the equator. This is exactly confirmed in Fig. 3.15, where for magnetic fields $\lesssim 10^{15}$ G the QPOs move from close to the pole towards the equator, as the magnetic field strength increases.

Reflection of pulses and spread in crust

In the absence of an elastic crust, Alfvén wave packets are supposed to travel approximately along magnetic field lines, as the characteristic direction of propagation of any magnetic perturbation coincides with the direction of the magnetic field. However, when a crust is added this picture changes. The direction of propagation of magneto-elastic waves no longer coincides with the magnetic field direction (compare the different eigenvalues in this case given in Eq. (2.90)). One would therefore expect a perturbation, traveling along magnetic field lines from the center of the star towards the surface to spread out past the crust-core interface. Such a spread is strong for low magnetic field strengths, when the isotropic shear modulus dominates in the crust region and weak for high magnetic field strengths, when the opposite is true. This behavior is shown in Fig. 3.16, where we display the renormalized sum of the kinetic and magnetic energy per field line for simulations at 5×10^{14} G. The initial perturbation is restricted to a limited region of the star about 4 km above the equator. The left panels show the expected behavior for a pulse which travels along a field line with no crust present. Two initial perturbations differing only by the location of the star get reflected at the surface and travel back towards the center. Any deviations from traveling perfectly along the initially excited field lines is caused by a numerical coupling of different field lines and the very weak coupling through the boundary condition at the surface of the star. Taking a crust into account but imposing the same initial perturbations the wave packets are spread whenever entering the crust, which happens at around 70 ms for the first

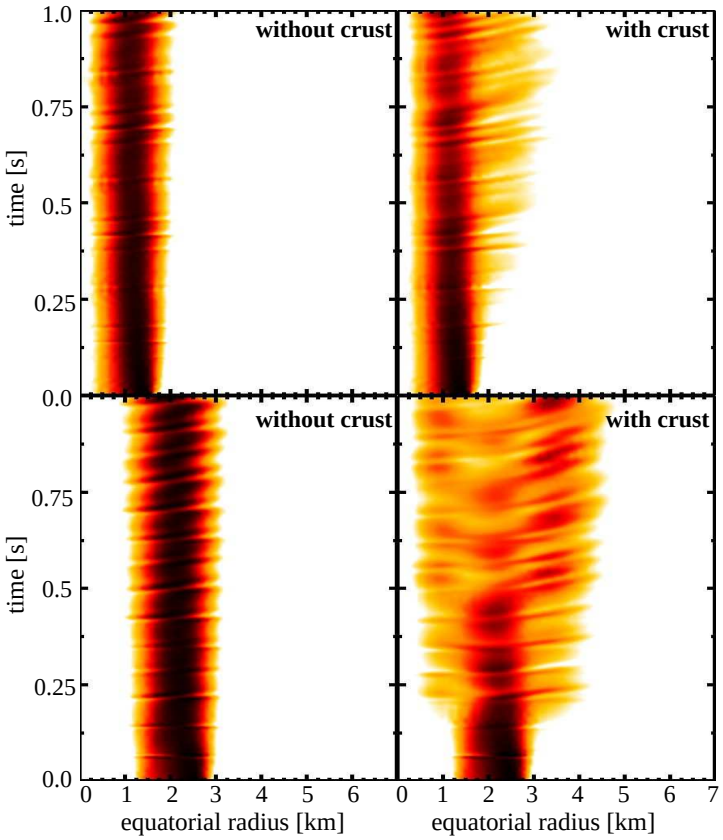

Figure 3.16: Evolution of the magnetic plus kinetic energy per field line divided by the sum of the energy of all field lines for the model APR+DH 1.4. The field lines are labeled by their crossing point with the equator. The pulse reaches the surface at around 70 ms for the first time and the crossing time is about 130 ms. *Left panels:* simulation without crust, *right panels:* simulation including crust. The upper and low panels differ by the location of the initial perturbation. Color scale ranges from white (minimum) to red-black (maximum).

time, and subsequently after about every 130 ms (right panels). For initial data located at field lines crossing the equator around 2 to 3 km (lower right panel), the spread is more drastic. After some reflections there are phases (around 700 and 850 ms), when no significant perturbation amplitudes can be found around the field lines which initially carried the perturbation.

However, the scenario of an initially localized wave packet considered here cannot rule out the existence of standing waves along individual field lines. Nevertheless, it suggests that additional effects may be introduced by the spreading of wave packets in the crust which probably change the Alfvén continuum of our semi-analytic model, where one assumes standing waves which get reflected at the crust-core interface (or at the surface for stronger magnetic fields).

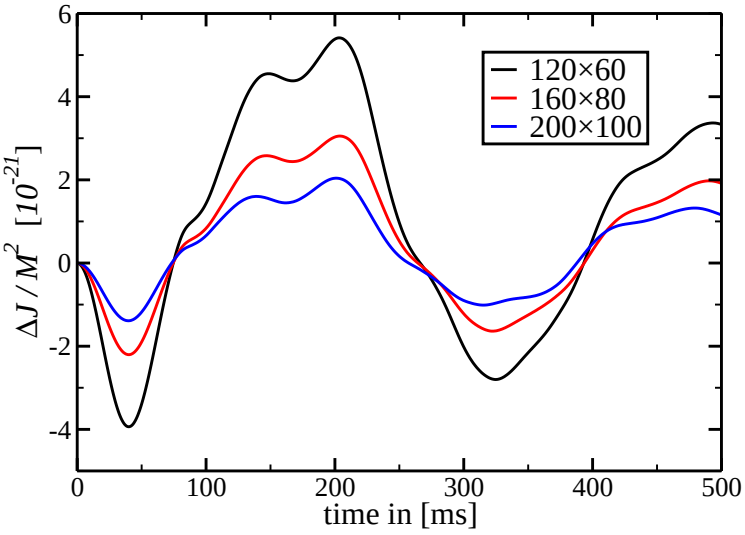

Figure 3.17: Variation of the total angular momentum of the star $J_{\rm tot}/M^2$ during the evolution for three different grid resolutions:120×60, 160×80 and 200×100 zones, respectively. The model used in the simulation is APR+DH 1.4.

Conservation of angular momentum

Analyzing the convergence properties of our numerical simulations in the intermediate magnetic field case is more complicated because the contributions to the stress-energy tensor from the magnetic field and the shear are of the same order of magnitude. The two extreme regimes have been tested above (purely shear oscillations) or in Cerdá-Durán et al. (2009) (purely Alfvén oscillations). In the present approach, the total angular momentum $J_{\rm tot} \equiv \int S_\varphi dV$ is the only globally conserved quantity, with $dV = \sqrt{\gamma} dr d\theta d\phi$. We do not expect conservation of the energy of the perturbation in our simulations, because neglecting the coupling to poloidal oscillations and assuming purely poloidal magnetic fields, renders the deviations of the total energy from the energy of the unperturbed background configuration to be of second order in the perturbations, while our approach is accurate to first order.

The total angular momentum $J_{\rm tot}$ should be conserved inside the computational volume, but the boundary condition we have chosen (see Sec. 2.5) allows for non-vanishing flux through the surface. As we chose initial perturbations with the angular dependence of the vector spherical harmonics the angular momenta in both hemispheres cancel by construction and the total angular momentum of the star is zero. For antisymmetric perturbations the losses/gains through the surface cancel respectively, while for symmetric perturbations there remains a non-zero contribution.

Fig. 3.17 shows the variation of the total angular momentum during the evolution for an symmetric simulation with $l = 3$ initial data at three different grid resolutions.

When analyzing the differences between the curves (see Section 3.2) we obtain the order of convergence of 1.95, which is near the expected second-order convergence. To estimate the absolute magnitude of the resulting angular momentum error we compare our perturbation to a rigidly rotating sphere with the same total angular momentum. Taking the typical total angular momentum during the simulation, and comparing it to that of a rigidly rotating sphere $J = 2/5MR^2\Omega = 2/5MRv_{\rm rot}$, where $\Omega = v_{\rm rot}/R$ is the rotation frequency, we obtain a maximal velocity which is only a fraction of the perturbation used in the simulations $v_{\rm rot}/v_{\rm pert} \sim 10^{-10}$. Thus, the total angular momentum introduced by our perturbation is very small. Moreover, the total angular momentum variations converge to zero, i.e. compared to the numerical errors the losses of angular momentum through the surface is a small effect not affecting our simulations.

3.4.3 Strong magnetic fields $B > 10^{15}$ G

For strong magnetic fields we are interested in the structure of magneto-elastic QPOs, but not in the damping of crustal modes, as the latter are damped already at much lower field strengths (see Sec. 3.4.1). Therefore, we can reduce the grid resolution, i.e. the computational costs. In the strong field case we thus use a uniform radial grid with 100 zones and an angular grid with 80 zones in the interval $[0, \pi]$.

For very strong magnetic fields, $B \gtrsim 5 \times 10^{15}$ G, the maxima of the Fourier transform align towards the polar axis. With increasing magnetic field the influence of the shear inside the crust becomes negligible, and the QPO pattern approaches that expected for the purely magnetic limit (see figure 3 in Cerdá-Durán et al., 2009), in agreement with the semi-analytic model. Another effect caused by the anisotropy of the shear modulus is a more wide-spread spatial structure of the QPOs compared to the case without crust. This can be inferred from the last two columns of Fig. 3.15, where QPOs are still quite extended inside the crust ($B = 8 \times 10^{15}$ G), and in the model without crust.

Between the two extremes, the QPOs are confined in the core ($B \lesssim 10^{15}$ G). For strong magnetic fields ($B \gtrsim 10^{15}$ G) there is a transition from the QPO structure observed in Section 3.4.2 to the purely magnetic case (see Fig. 3.15 from the 3 - 6 column). Between 10^{15} and 2×10^{15} G the QPOs begin to have significant amplitudes in large parts of the crust.

This transition becomes clearer in Fig. 3.18, where we plot the Fourier amplitude for individual field lines averaged over the length of the line and labeled by their crossing point with the equatorial plane. The solid lines represent the continuum as obtained by the semi-analytic model, where we assume reflection at the crust-core interface in the upper row and reflection at the surface of the star in the lower row. The obtained frequencies are very similar in both cases, because the travel time of the waves is dominated by the time spent in the core. We note a change of the structure of the QPOs with the different boundary conditions. We have already noted in Fig. 3.15 that in the case of weak magnetic fields the QPOs move from being near the pole towards the equator, for increasing magnetic field strength below 10^{15} G. The same can be observed in the first two panels of Fig. 3.18 for $U_0^{(-)}$, $U_1^{(-)}$, and $U_1^{(+)}$. Between 10^{15} and 2×10^{15} G a

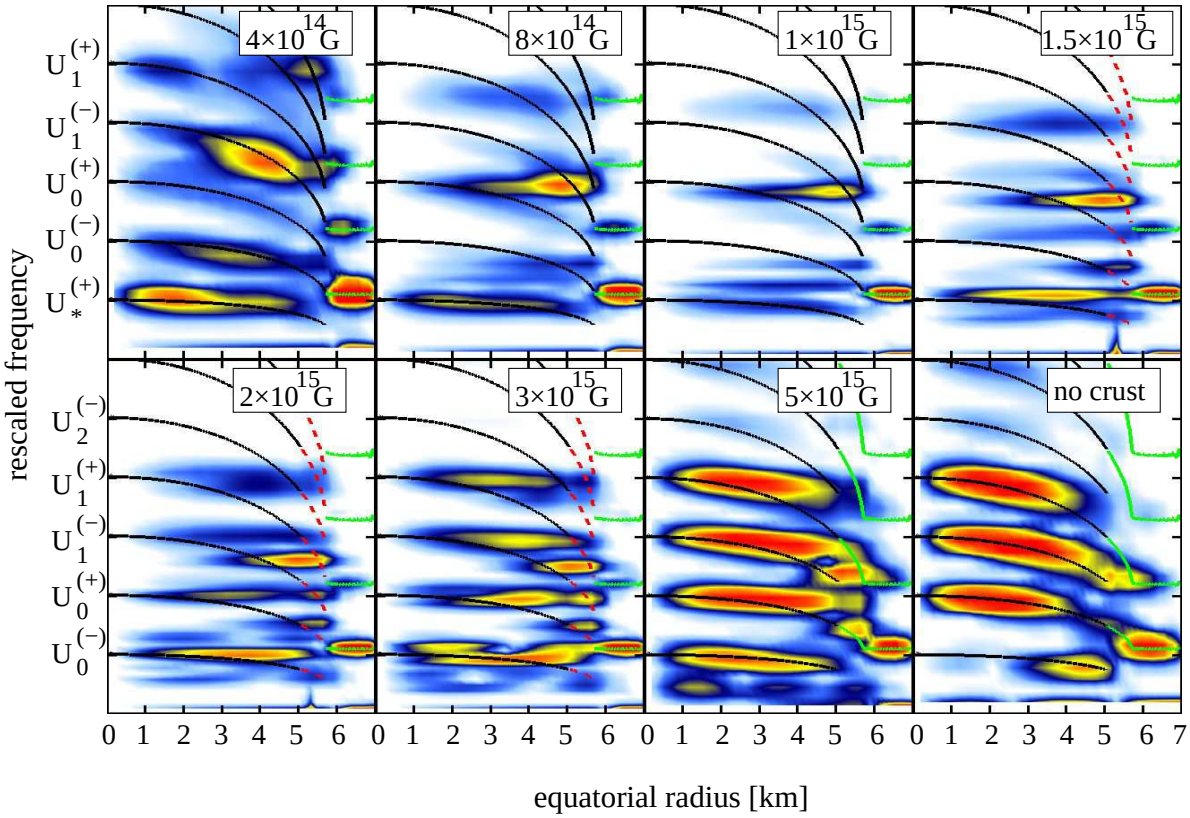

Figure 3.18: The averaged Fourier amplitude along different field lines labeled by the radius where they cross the equatorial plane for different magnetic field strengths. In the last panel we show the expected behavior for a model without crust. The y-axis represents the frequency rescaled to the fundamental QPO frequency predicted by the semi-analytical model (see Table 3.6). The color scale ranges from white-blue (minimum) to orange-red (maximum). Black and green lines represent the continuum when taking the crust into account. Dashed, red lines indicate regions where the semi-analytic model is not supposed to work. We do not know where the waves get reflected and thus cannot identify whether to consider the lines as open or closed.

transition occurs from reflection at the crust-core interface (for weaker magnetic fields) and reflection at the surface of the star (for stronger fields). Therefore, we do not expect any of the two approximations to agree with the semi-analytic model. Neither can we assume that the oscillations get reflected only at the crust-core boundary nor only at the stellar surface. When increasing the magnetic field beyond 2×10^{15} G the maximum amplitude of the QPO aligns again towards the polar axis, and the numerically obtained pattern approaches the expected structure, which is similar to the case without the crust. The main differences are the presence of the fundamental $U_*^{(+)}$ at finite frequency and a broader maximum because of the anisotropic shear contribution. The QPOs are moving from the pole towards the equator according to the frequency predicted by the semi-analytic model for reflection at the crust-core interface, but when the effects of the

$B_{\rm pole}$ [G]	f(U_0) [Hz]	$U_*^{(+)}/U_0$	$U_0^{(-)}/U_0$	$U_0^{(+)}/U_0$	$U_1^{(-)}/U_0$	$U_1^{(+)}/U_0$	$U_2^{(-)}/U_0$	$\delta U_n^{(\pm)}/U_0$
2×10^{14}	1.0	1.0	1.9	2.9	3.6	5.0	5.7	± 0.24
4×10^{14}	2.0	1.0	1.8	2.8	3.5	4.9	5.5	± 0.20
6×10^{14}	3.0	1.0	1.8	2.8	3.1	4.7	5.0	± 0.10
8×10^{14}	4.0	1.0	1.8	2.5	3.5	4.3	5.1	± 0.20
10^{15}	5.0	0.9	1.3	2.4	3.3	4.2	5.3	± 0.10
1.5×10^{15}	7.4	0.8	1.1	2.2	3.2	4.1	5.1	± 0.10
2×10^{15}	9.8	0.7	1.0	2.0	3.0	4.0	5.1	± 0.10
3×10^{15}	14.7	0.5	0.9	2.0	3.0	4.0	5.1	± 0.10
5×10^{15}	24.4	0.5	1.0	2.0	3.0	4.0	5.1	± 0.10
8×10^{15}	39.1	0.3	0.9	2.0	3.0	4.1	5.1	± 0.10

Table 3.6: The relation of the frequencies of the lowest QPOs for the model APR+DH 1.4, obtained by analyzing the local maxima of the Fourier amplitudes, to the fundamental frequency U_0, obtained by the semi-analytic method. Note that the fundamental of the semi-analytic model changes symmetry at a magnetic field of about 10^{15} G, such that $U_0 \simeq U_*^{(+)}$ for $B \leq 10^{15}$ G and $U_0 \simeq U_0^{(-)}$ for $B > 10^{15}$ G. The last column shows the uncertainty in the separation of two successive frequencies in the Fourier spectrum. It gives an estimate of the error caused by choosing the position of the local maxima, but it does not include other numerical errors.

magnetic field become comparable to those of the shear modulus in the crust, the QPOs reach the end of the continuum and *jump* from the symmetric (antisymmetric) branch to the antisymmetric (symmetric) branch of the next part of the continuum.

What happens to $U_*^{(+)}$, which has no possibility to jump to? For strong magnetic fields, $B \gtrsim 2 \times 10^{15}$ G $U_*^{(+)}$ has different features. First, there is no node along the field lines, due to the change of the boundary conditions, which require a maximum at the surface. Second, as can be seen in the last few columns of the upper row of Fig. 3.15, there are nodes perpendicular to the field lines at a given frequency, and we even find two different contributions to the $U_*^{(+)}$ at slightly different frequencies. Between 2×10^{15} G and 5×10^{15} G there is one node perpendicular to the field lines, while for $B \geq 6 \times 10^{15}$ G the QPO has predominantly two nodes in that direction. Note that both features are always present for $B \gtrsim 2 \times 10^{15}$ G. This splitting can also be seen in the leftmost three panels of the lower row in Fig. 3.18. The corresponding features are located at frequencies below the fundamental, $U_0^{(-)}$. The same panels also show, that with increasing magnetic field strength, the relative Fourier amplitudes and the frequencies of those features decrease with respect to the fundamental frequency.

The picture of the transition from one asymptotic behavior (reflection at the crust-core interface) to the other (reflection at the surface) gets supported by the frequencies obtained for the different QPOs shown in Table 3.6. There we compare the frequencies corresponding to the maxima of the Fourier amplitude with those of the fundamental

oscillation obtained with the semi-analytic model. Thus, we use the version with reflection at the crust-core interface up to 10^{15} G, while we set the boundary at the surface of the star for stronger fields. For magnetic fields up to $B \lesssim 8 \times 10^{14}$ G, $U_*^{(+)}$ has a similar frequency as the fundamental obtained with the semi-analytic model. The frequencies of the other QPOs approximately behave as $1\,(U_*^{(+)}) : 3\,(U_0^{(+)}) : 5\,(U_1^{(+)})$ and $2\,(U_0^{(-)}) : 4\,(U_1^{(-)}) : 6\,(U_2^{(-)})$. For stronger magnetic fields $B \gtrsim 3 \times 10^{15}$ G the frequencies ratios approach $1\,(U_0^{(-)}) : 3\,(U_1^{(-)}) : 5\,(U_2^{(-)})$ and $2\,(U_0^{(+)}) : 4\,(U_1^{(+)})$. The two asymptotic integer relations between successive overtones and their order is what is expected from the semi-analytic model in the two regimes. In the intermediate regime $8 \times 10^{14} \lesssim B \lesssim 3 \times 10^{15}$ G the frequencies change smoothly from one relation to the other.

Deviations from exact integer ratios may have different reasons. First, the time of numerical integration is limited. Therefore, the spectral resolution of the Fourier analysis is limited, too. Second, for the lowest magnetic field shown here, $B \approx 2 \times 10^{14}$ G, not all upper QPOs have reached their position near the polar axis, i.e. their frequencies still lie in the continuum, resulting in lower frequencies. Third, in particular in the transition regime it is sometimes difficult to identify where the maximum of a QPO is located. The interesting QPO may be excited only very weakly by our initial data, and/or some other QPO may be excited more strongly at a similar frequency. This occurs more frequently for higher overtones, because there the different continua overlap (see Fig. 3.13 or 3.18).

3.4.4 Crustal modes in the gaps of the Alfvén continuum?

van Hoven and Levin (2011) and Colaiuda and Kokkotas (2011) have pointed out the possibility of crustal modes, which may have frequencies outside of the continuum of the core. These modes would be only very weakly coupled to core oscillations, because no Alfvén wave of any field line could match the necessary frequency. In the models we have studied here, we find gaps in the continuum only between the lowest overtones of Alfvén oscillations (see Fig. 3.13), e.g. for model APR+DH 1.4 already the continua of $U_1^{(-)}$ and $U_1^{(+)}$ overlap and there are only gaps between $U_1^{(-)}$ and $U_0^{(+)}$, $U_0^{(+)}$ and $U_0^{(-)}$ and below $U_0^{(-)}$. For the other models shown in the Table 3.2 the number of gaps is limited to a maximum of about three for models with the crust EoS NV and to two for models with the DH EoS. Note that we only consider the continua of the open field lines indicated by the black lines in Fig. 3.13, because they are decoupled from the continua related to the closed field lines (green lines). To have the fundamental $n = 0$, $l = 2$ oscillation of the crust in one of the gaps, very strong magnetic fields $B > 10^{15}$ G are required

As an example we choose the EoS L+DH 1.4, because the corresponding model has broader gaps than the APR+DH EoS. Furthermore, models with lower mass have shorter Alfvén crossing times, and therefore weaker magnetic fields are necessary to have the shear mode in the gap between the lowest overtones of the continua (see Table 3.8). The spectral structure of this model is displayed in Fig. 3.19, where we show the edges of the continua of the open field lines as a function of the magnetic field strength. The

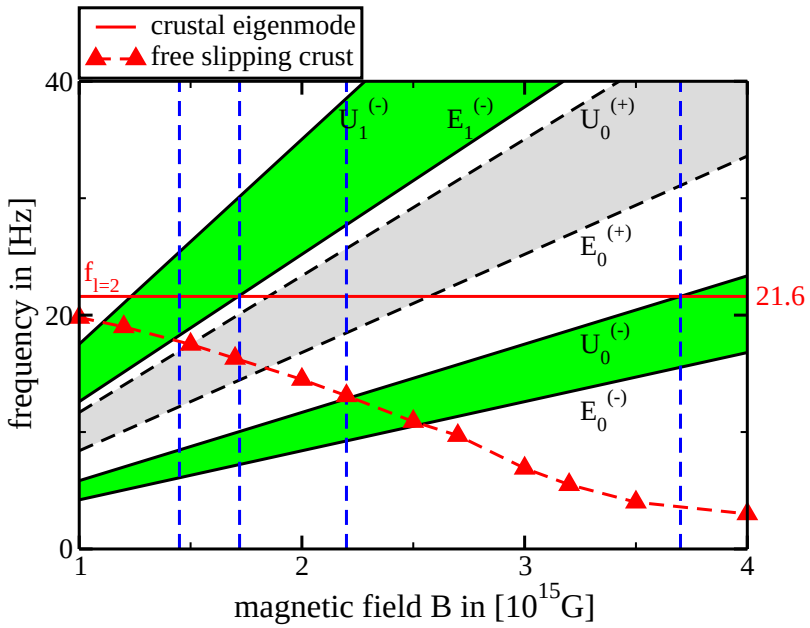

Figure 3.19: Frequency continua of model L+DH 1.4 at magnetic fields between $B = 10^{15}$ G and $B = 4 \times 10^{15}$ G. Black, solid lines indicate the edges of the continua of the open field lines as indicated by the names $E_n^{(\pm)}$ and $U_n^{(\pm)}$. The horizontal red line gives the frequency of the $l = 2$ crustal shear mode and the dashed red lines gives the frequency obtained by simulations with a free slipping crust (see text). The green shaded areas show continua having the same symmetry with respect to the equator as the $l = 2$ shear mode. The gray area shows the continuum with opposite symmetry. Blue dashed lines show the range of magnetic field strength where we the frequency of the $n = 0$, $l = 2$ crustal mode lies in the gap between allowed Alfvén continua.

shaded areas between two edges represent the corresponding continuum, where crustal modes can be absorbed resonantly. The red line indicates the frequency 21.6 Hz of the purely shear, $n = 0$, $l = 2$ mode of the crust. Using model L+DH 1.4, we performed simulations with initial data with the crustal $n = 0$, $l = 2$ mode, allowing only for antisymmetry with respect to the equatorial plane. The oscillations of the continuum associated with symmetric QPOs, as for example $U_0^{(+)}$, are thus not allowed and cannot be excited. These forbidden oscillations are indicated by the gray shaded region in Fig. 3.19. We also confirmed that without imposing equatorial symmetry only Alfvén QPOs having the same symmetry as the corresponding crustal mode can be excited with significant amplitude during the evolution. Therefore, the antisymmetric $n = 0$, $l = 2$ shear mode of the crust lies in the gap between $U_0^{(-)}$ and $E_1^{(-)}$ for magnetic fields between 1.74 and 3.7×10^{15} G (Fig. 3.19). Following previous works by van Hoven and Levin (2011) or Colaiuda and Kokkotas (2011) the crustal mode in the gap should not be damped significantly, because there is no oscillation at the resonant frequency available in the continuum.

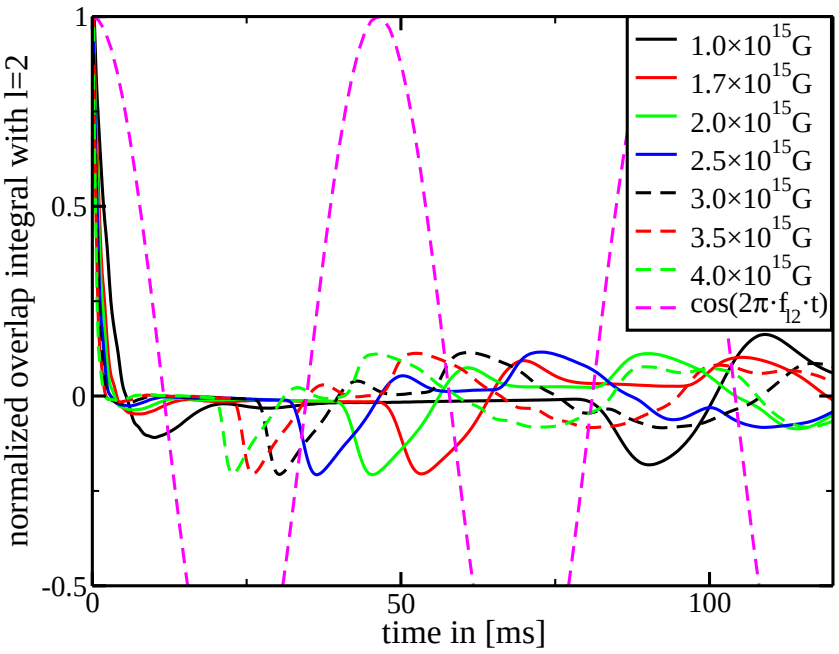

Figure 3.20: Evolution of the overlap integral of the $n = 0$, $l = 2$ mode of the crust at different magnetic field strengths: $B = \{1.0, 2.0, 2.5, 3.0, 3.5, 4.0\} \times 10^{15}$ G. The dashed magenta line shows the expected oscillation of the purely shear $l = 2$ mode of the crust. All other lines show strong damping of the excited $l = 2$ mode at early times ($t < 20$ ms). Contributions to the overlap integral at later times $t > 20$ ms originate from magneto-elastic oscillations.

However, we still find very strong damping of this crustal mode in our simulations, as indicated by the overlap integral of the $n = 0$, $l = 2$ shear mode in Fig. 3.20. Clearly the mode is damped after a few msec for all considered magnetic field strengths. Later contributions originate from coupled magneto-elastic pulses traveling through the whole star. Therefore, the time when they contribute to the overlap integrals depends inversely on the magnetic field strength, a behavior which is completely different from that of discrete oscillations for purely crustal shear modes. These observations indicate that we do not have a weakly coupled system of two sub-systems (the crust and the core) but we are dealing with coupled, global magneto-elastic oscillations. To compare with what one would expect for an undamped purely crustal mode, we plotted the magenta, dashed line in Fig. 3.20.

We checked the influence of the magnetic field on the frequency of the purely shear mode by performing a series of simulations, where we apply an artificial boundary condition at the crust-core interface, i.e. we use the same condition $\xi^{\varphi}_{,r} = 0$ that would apply in the absence of the magnetic field (see also Sotani et al., 2007). This allows the crust to slip freely on top of the core, and the oscillations inside the crust cannot be damped into the core. The frequency of the some $n = 0$ crustal modes are displayed in Fig. 3.21 (see also Fig. 3.20). This is expected, because global, poloidal magnetic fields of the order

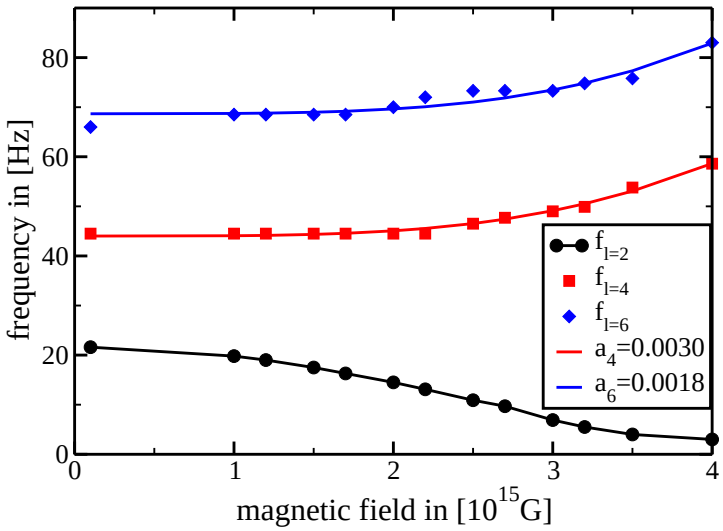

Figure 3.21: Frequencies of some $n = 0$ crustal modes as a function of magnetic field strength. In the simulations a free slipping crust is assumed. The frequency of the $l = 2$ mode decreases, while the frequencies of the overtones increase with the magnetic field strength. The fitting functions of $l = 4$ and $l = 6$ mode are given by $f_B/f_0 = \sqrt{1 + a_l B_{15}^4}$, where $B_{15} = B/10^{15}$ G.

of $B \sim 10^{15}$ G and stronger begin to have measurable effects (Duncan, 1998; Messios et al., 2001; Sotani et al., 2007, 2008a; Shaisultanov and Eichler, 2009). Intuitively, one would expect the shear mode frequencies to increase with the magnetic field strength, because the magnetic tension could be interpreted as effectively augmenting the shear modulus (Messios et al., 2001; Sotani et al., 2007). In contrast to Sotani et al. (2007) we find a decrease of the $l = 2$ mode frequency with increasing dipolar magnetic field strength (see Fig. 3.19). In their work Sotani et al. (2007) neglected couplings between l- and $l \pm 2$-modes due to the magnetic field, which led to discrete modes. However, by analyzing the evolution of the corresponding overlap integrals we observe strong excitation of the $l = 4$ mode by the $l = 2$ mode in our simulations. This strong coupling may explain the opposite change of frequency than expected from the study by Sotani et al. (2007). For a different magnetic field configuration also Messios et al. (2001) and Sotani et al. (2007) find that the frequency of the fundamental $l = 2$ crustal mode decreases with increasing magnetic field strength.

If the frequency of the $l = 2$ crustal mode changes according to our simulations with the free slipping crust, the magnetic field strengths for which the mode lies in the continuum gap is limited to 1.4×10^{15} to 2.2×10^{15} G. In this regime we have performed four simulations at 1.5×10^{15}, 1.7×10^{15}, 2.0×10^{15}, and 2.2×10^{15} G (triangles in Fig. 3.19). In all of them we find the strong damping of the crustal mode. We further note that we find a different scaling with the magnetic field strength of the frequencies of the other crustal modes. According to Sotani et al. (2007) they increase with B, but

the best fits for the $l = 4$ and $l = 6$ mode are given by

$$\frac{f(B_{15})}{f(B=0)} = \sqrt{1 + a_l B_{15}^4}\,, \tag{3.10}$$

where $B_{15} = B/10^{15}\,\mathrm{G}$. The fitted values for a_l are: $a_4 = 0.003$ and $a_6 = 0.0018$.

A second problem of matching of crustal frequencies into the gaps of the Alfvén continuum emerges at the field strengths ($\gtrsim 10^{15}\,\mathrm{G}$) at which we find the crustal frequencies in the continuum gaps, as there is no clear way of how to compute the Alfvén frequencies. In this transition regime, reflection neither occurs predominantly at the crust-core interface nor at the surface, therefore, we do not claim that the continuum shown in Fig. 3.19 is perfectly valid at all magnetic field strengths (compare the panels for $1.5 \times 10^{15}\,\mathrm{G}$ to those of $3 \times 10^{15}\,\mathrm{G}$ in Fig. 3.18). However, by performing simulations for 10 different magnetic field strengths between 10^{15} and $4 \times 10^{15}\,\mathrm{G}$ for the current model L+DH 1.4, we can ensure that the $l = 2$ crustal frequency lies in the gap between the Alfvén continua at least for one of the models. In none of the above simulations we find a different behavior than the one reported, i.e. we do not observe any of the crustal shear modes.

In the example shown above, we may have just missed to match the frequency of the crustal mode to a gap of the continuum, as the frequency may have been changed due to the presence of the strong magnetic field, and because the continuum is probably not reliably predicted by the semi-analytic model. To this end we performed a large number (> 50) of simulations at different magnetic field strengths $> 10^{15}\,\mathrm{G}$ and different equilibrium models but we never found any crustal shear mode at such strong magnetic fields.

Generalizing the dipolar magnetic field configuration, which is our main model simplification in the current context, would probably increase the complexity of the continuum, making it even harder to find gaps. However, there might arise new effects due to an entanglement of the magnetic field (see van Hoven and Levin, 2011). Crustal modes in the gaps of the Alfvén continua of the core have been reported by Colaiuda and Kokkotas (2011), but our results do not confirm their existence.

3.4.5 Threshold for the outbreak of the QPOs through the crust

In Section 3.4.3 we noticed that for weak magnetic fields, $B \lesssim 10^{15}\,\mathrm{G}$, the QPOs are largely confined to the fluid core, and that there exists a threshold magnetic field strength beyond which QPOs can be observed with significant amplitudes at the surface of the star. To quantify when magneto-elastic QPOs have a significant amplitude in the crust of the neutron star, we studied their maximum amplitude at the surface.

In Fig. 3.22 we plot the amplitude of the Fourier transform at the surface for different magnetic field strengths as a function of the polar angle θ and the frequency. The color scaling is rescaled in each panel to enhance the main contributions at each magnetic field strength. We consider APR+DH 1.4 as our reference model. First we note, that for very strong fields ($> 5 \times 10^{15}\,\mathrm{G}$), the frequencies approach those predicted by the

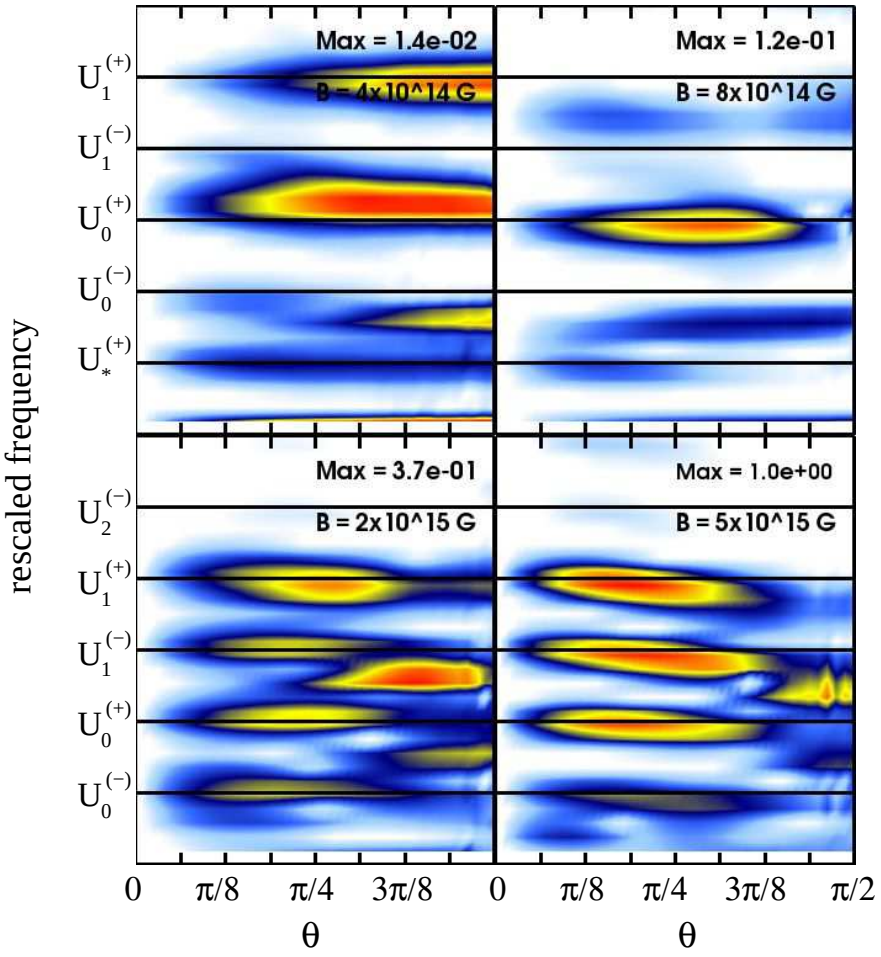

Figure 3.22: Normalized amplitude of the Fourier transform at the surface of the star (between pole and equator) as a function of the frequency for the stellar model APR+DH with 1.4 solar masses. The horizontal lines indicate the frequency for the upper QPOs predicted by the semi-analytic model. The color scale ranges from white-blue (minimum) to orange-red (maximum).

semi-analytic model, because the influence of the crust should decrease for increasing magnetic field strength. There is some low frequency oscillation which corresponds to $U_*^{(+)}$ (compare with Fig. 3.18), and there are some additional, strong Fourier modes near to $\pi/2$ resulting from the edge modes, which are stronger than in the case without crust.

However, when decreasing the strength of the magnetic field from 5×10^{15} G to 2×10^{15} G, the Fourier amplitude of the QPOs at the surface decreases, e.g. the maximum decreases from 1.0 to 0.37 in units normalized to the maximum amplitude at $B = 5 \times 10^{15}$ G. As we have already seen in Fig. 3.15, this is expected, because for decreasing field strength the crust will shield the QPOs. We further see that the additional structure in the Fourier amplitude at about the fundamental frequency of $U_0^{(-)}$ and the strong feature just below the frequency of $U_1^{(-)}$ close to the equator are increasing in amplitude relative to the upper QPOs. We note here that in the transition region of magnetic field

Model	$\frac{\mathrm{FFT}(10^{15}\,\mathrm{G})}{\mathrm{FFT\,(no\,crust)}}$	Model	$\frac{\mathrm{FFT}\,(10^{15}\,\mathrm{G})}{\mathrm{FFT\,(no\,crust)}}$
APR+DH 1.4	0.07	APR+NV 1.4	0.06
APR+DH 1.8	0.11	APR+NV 1.8	0.005
APR+DH 2.2	0.33	APR+NV 2.2	0.04
L+DH 1.4	0.16	L+NV 1.4	0.016
L+DH 1.8	0.36	L+NV 1.8	0.03
L+DH 2.2	0.15	L+NV 2.2	0.009

Table 3.7: The maximal magnitude of the Fourier transform at the surface of the star for a dipole magnetic field strength of $10^{15}\,\mathrm{G}$. Simulations for different EoS, and with and without crust are considered and compared.

strengths the correspondence between the frequencies of the semi-analytic model and the simulated QPOs should be taken with caution and we do not expect a simple QPO structure as in the two limiting cases.

When decreasing the magnetic field strength towards $8 \times 10^{14}\,\mathrm{G}$ a dominant feature originates from $U_0^{(+)}$. In a sequence of similar plots for different magnetic fields not shown here, one can follow the slight change in frequency until reaching approximately the value predicted by the semi-analytic model for reflection at the crust-core interface. Comparing with Fig. 3.15 the corresponding spatial structure of the mode has still some amplitude inside the crust, i.e. our interpretation in terms of the $U_0^{(+)}$ QPO makes sense. The general trend is that the magneto-elastic upper QPOs exhibit a decreasing amplitude near the surface for decreasing magnetic field strength.

For the weakest magnetic field ($4 \times 10^{14}\,\mathrm{G}$), the upper QPOs have no strong amplitudes, because they are confined to the fluid core. The dominant contribution at the surface results from the edge modes in this case (see Fig. 3.12). The QPO with the largest amplitude inside the crust is the edge QPO $E_2^{(+)}$ (see Fig. 3.22) with a frequency slightly above $U_0^{(+)}$ (see also the right panel of Fig. 3.13). Other contributions to the Fourier signal at the surface stem from the two edge QPOs $E_1^{(+)}$ and $E_3^{(+)}$ at frequencies just below $U_0^{(-)}$ and close to $U_1^{(+)}$, respectively. However, the edge QPOs are damped much faster than turning-point QPOs, and the amplitude in the Fourier analysis for the same initial data is about two orders of magnitude smaller than for a reference model without crust. Therefore we doubt that edge QPOs are the explanation for the observed frequencies in SGR for magnetic fields $B \lesssim 5 \times 10^{14}\,\mathrm{G}$.

In Table 3.7 we give the maximum of the Fourier amplitude at the surface for a simulation with crust at $10^{15}\,\mathrm{G}$ with respect to the corresponding simulation without crust. The closer this value is to 1.0 the stronger is the amplitude of the QPO at the surface. For very low values the crust shields the QPOs efficiently, i.e. they are confined to the core of the neutron star. For the DH crustal EoS there is already a considerable amount of oscillations penetrating the crust and reaching the surface. We therefore argue that magneto-elastic oscillations break through the crust around $10^{15}\,\mathrm{G}$. However, for the NV EoS the amplitudes for models with crust never reach 10% of the values for

Model	$B_{30\mathrm{Hz}}[10^{15}\,\mathrm{G}]$	$B_{28\mathrm{Hz}}[10^{15}\,\mathrm{G}]$
APR+DH 1.4	6.2	5.8
APR+DH 1.8	8.9	8.3
APR+DH 2.2	13.8	12.9
L+DH 1.4	5.1	4.8
L+DH 1.8	6.9	6.4
L+DH 2.2	9.0	8.4
APR+NV 1.4	6.4	6.0
APR+NV 1.8	9.2	8.6
APR+NV 2.2	14.2	13.2
L+NV 1.4	5.8	5.5
L+NV 1.8	7.7	7.2
L+NV 2.2	10.1	9.5

Table 3.8: Magnetic field strength required to match the frequency of the fundamental Alfvén QPO to 30 Hz observed in SGR 1806-20 and 28 Hz of SGR 1900+14.

models without crust, as the crust is more extended in this case, and QPOs can break through the crust only for even stronger magnetic fields. Nevertheless, the threshold of $B \sim 10^{15}\,\mathrm{G}$ should be a good approximation for all models. Interestingly, this result is comparable with estimates of the magnetic field strengths for SGRs showing giant flares.

3.5 Magnetic fields confined to the crust

In the preceding sections we focused on dipolar magnetic fields which penetrate the whole neutron star. However, it is not guaranteed that such configurations exist in nature. In this section we study magnetic fields which are still purely poloidal, but which are confined to the region of the crust. This scenario may be realized when the protons in the core of the neutron star form a type-I superconductor, and hence expel the magnetic field from the core due to the Meissner-Ochsenfeld effect. As in the preceding sections the model of reference is calculated with the APR + DH EoS and has a mass of 1.4 solar masses.

3.5.1 Magnetic field configuration

The details of how to construct the magnetic fields confined to the crust are given in Appendix E. We study different configurations which are, in particular, magnetic fields matched to an exterior dipole, quadrupole, or octupole field. The amplitudes of the magnetic field at the surface of the such configurations have different angular dependence. Therefore, to compare the results, we label the different configurations with their averaged magnetic field strength at the surface of the star and use this value as reference magnetic field strength.

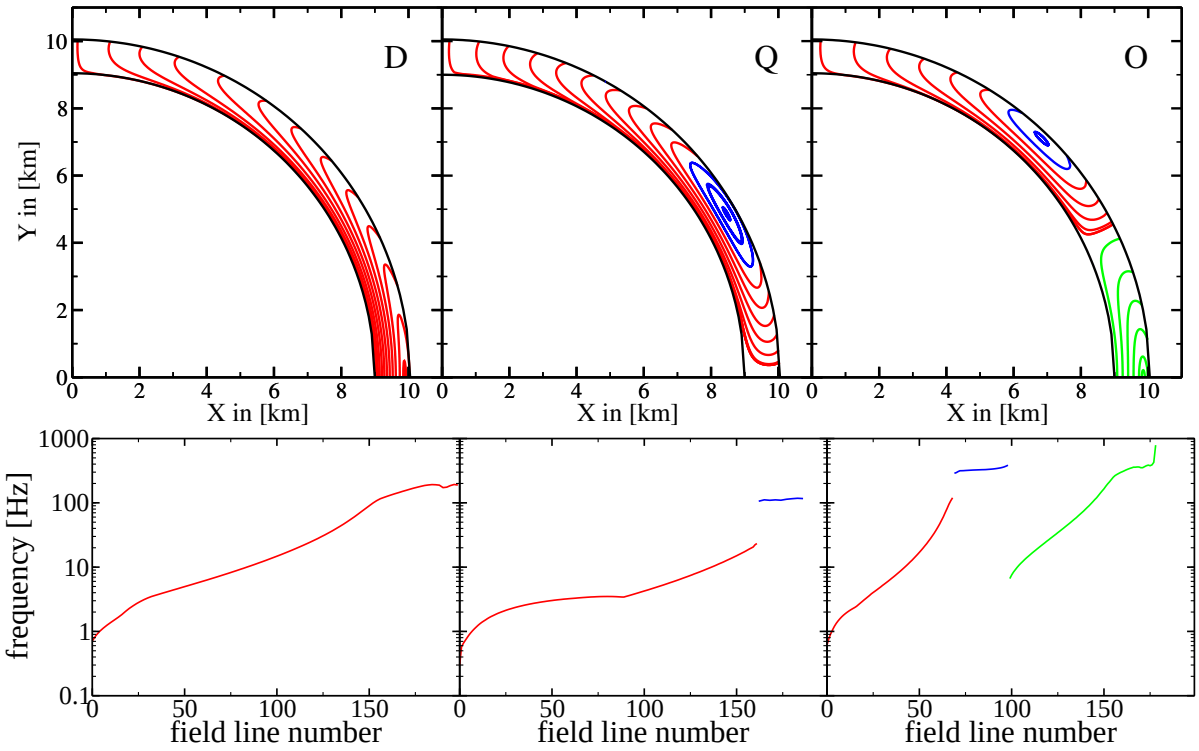

Figure 3.23: *Upper panels*: Magnetic field configurations for models matched to an exterior dipole (left panel), quadrupole (middle panel), and octupole (right panel), respectively. *Lower panels*: Alfvén spectra of the magnetic field configurations given in the corresponding upper panel obtained with the semi-analytic model for an averaged surface magnetic field of $B = 10^{14}$ G. The field lines are labeled by integer numbers increasing with angle θ. The θ range for the labeling of the red lines in the middle (right) panel is $[0°, 50°]$ ($[0°, 40°]$), and for the blue lines $[50°, 60°]$ ($[40°, 45°]$). The labels for the green lines in the right panel start at $\theta = 65°$. The color denotes the field lines which define the corresponding spectrum.

The field topology of the configurations and the corresponding spectra of the purely Alfvén oscillations at $B = 10^{14}$ G are given in Fig. 3.23. The parts of the Alfvén spectrum associated with a particular family of field lines are indicated by using the same color in the graphs showing the spectrum and the magnetic field configuration. If the magnetic field is confined to the crust the maximum field strength is found at the crust-core interface. The maximum strength for the dipolar (quadrupolar, octupolar) configuration is about 5 (12, 5.3) times the average value at the surface. This is a factor of a few stronger than the central value of the interior field of configurations penetrating the core. Consequently, the structure of the magnetic field varies on smaller scales. There are field lines which close inside the crust, e.g. near the equator for the dipole (red lines in Fig. 3.23) and octupole (green lines) configurations, or at $\theta \sim 60°$ for quadrupole and octupole configurations (see blue lines in Fig. 3.23). Because of stronger magnetic fields on smaller spatial scales, we require higher numerical grid resolution and expect higher

frequencies of the Alfvén oscillations.

Let us discuss the spectra obtained with the semi-analytic model of Appendix B as given in the lower panels of Fig. 3.23. First, we note that for configurations matched to an exterior dipole and octupole, there are no turning points present. Therefore, one would expect QPOs only at the edges of the different branches of the continua. Second, the frequencies of the fundamental oscillation of the short closed field lines are higher than the frequencies we observe in the case of magnetic fields penetrating the core (a few Hz at 10^{14} G). The same holds for the frequencies of the field lines located around the closed lines (corresponding to the upper end of the red colored part of the spectrum) and the short lines near the equator for the octupole configuration. The frequencies of the field lines near the pole for the current magnetic field configurations are similar to the ones of the magnetic field configuration penetrating the core. Third, in the spectrum for the configuration matched to an exterior quadrupole we find two turning points at the field lines between 80 and 100. However, the frequencies of the neighboring field lines increase (for higher field line number) or decrease (for decreasing field line number). We thus expect that there is a significant phase mixing due to numerical coupling, because near to the crust-core interface the field lines are packed very densely. In the following we will refer to magnetic field configurations matched to an exterior dipole as configuration D, to an exterior quadrupole as Q, and to an octupole as O.

3.5.2 Alfvén oscillations

The spectra of magnetic fields confined to the crust are very steep near the edges compared to the spectra of magnetic fields penetrating the core (see Section 3.3) and we only find turning points in configuration Q. Moreover, the field lines near this turning points are packed very densely and thus couple numerically to each other leading to enhanced phase mixing. Therefore, we expect more difficulties to observe QPOs with significant amplitudes in the simulations. Additionally, the requirements on the grid resolution are more stringent than before, because of the finer spatial structure of the magnetic field. We performed simulations of three different magnetic field configurations at $B = 10^{14}$ G. The grid resolution was 30×80 ($r \times \theta$) for $[r_{\rm cc}, r_{\rm s}] \times [0, \pi]$, and the models were evolved up to 5 s.

The Fourier analysis shows less significant amplitudes of the QPOs than in the case of global magnetic field configurations. This does not come as a surprise, because of the steep gradients in the spectra which are expected to cause faster phase mixing. However, we were able to identify some QPOs as local maxima of the Fourier amplitude (see Fig. 3.24).

The QPOs for the dipole configuration (upper left panel) have their maximum amplitudes near the pole. This is expected, because the edge of the continuum is located there. With the numerical resolution used we were not able to see the other edge of the continuum at much higher frequencies, because the associated field lines near the equator have a very small spatial extension.

The quadrupole magnetic field has closed field lines near $\theta \sim 60^\circ$ (see Fig. 3.23).

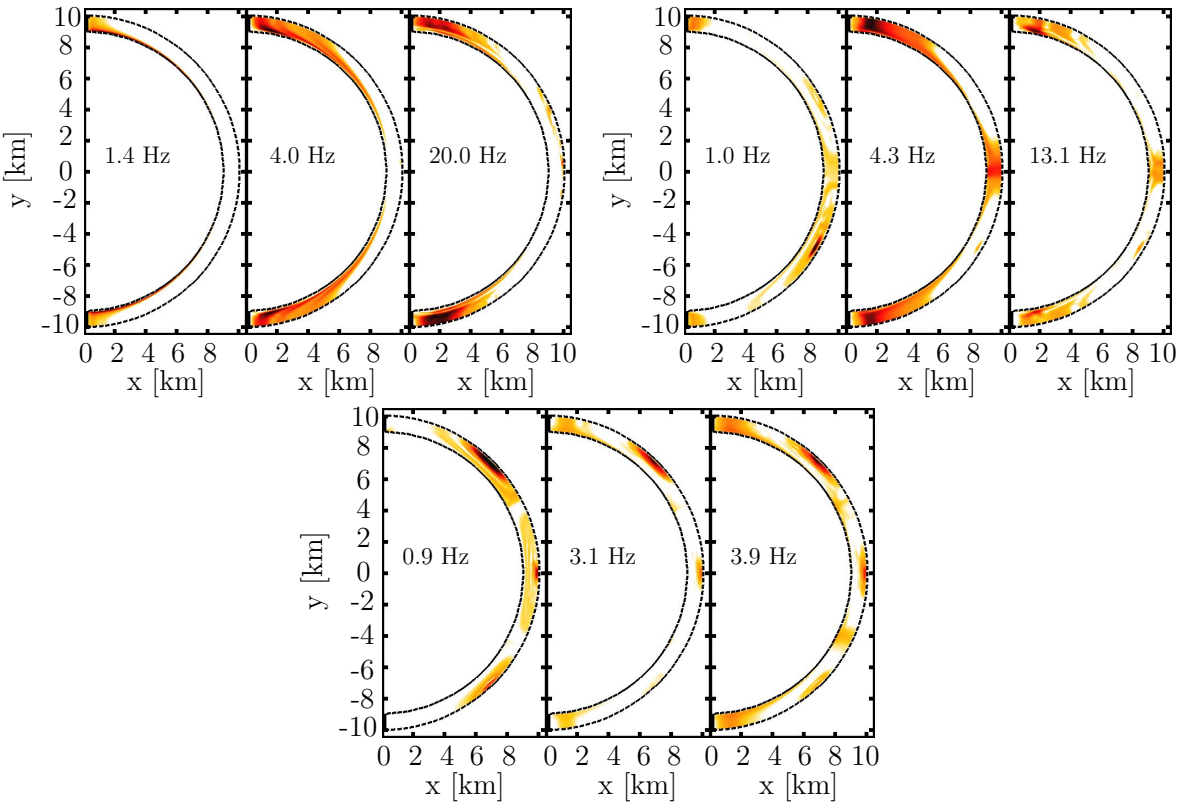

Figure 3.24: Spatial structure of the low-frequency QPOs obtained by a Fourier analysis for different magnetic field configurations. *Upper left panel*: configuration D; *Upper right panel:* configuration Q: *Lower panel:* configuration O. The corresponding frequencies are given, too. The color scale ranges from white (minimum) to red-black (maximum).

The corresponding frequencies of the continuum are $\sim 100\,\mathrm{Hz}$. Unfortunately, the grid resolution was too low to analyze potential QPOs for these field lines, i.e. we find QPOs only for the continuum of the open field lines. These are best seen in the plot for 4.3 Hz in the upper right panel of Fig. 3.24. Only open field lines oscillate at the given frequency and have large Fourier amplitudes near the pole and equator. Closed field lines do not participate in the oscillations, as is clearly visible in Fig. 3.24

When the magnetic field is matched to an exterior octupole, we find oscillations of the open field lines (best visible for $f = 3.9\,\mathrm{Hz}$ in the lower panel of Fig. 3.24). The red colored field lines in the right panel of Fig. 3.23 do not extend until the equator and the corresponding QPO has a large amplitude around $\theta \gtrsim 60°$. At 0.9 Hz we find oscillations with significant amplitudes also for the field lines near the equator. At almost all frequencies there is a non-vanishing Fourier amplitude at the closed field lines around $\theta \sim 50°$, which is probably caused by the too low grid resolution.

In none of the cases it is possible to clearly associate the observed QPOs with parts of the spectrum. The most reliable interpretation is that some QPOs associated with the open field lines near the pole have frequencies comparable to those the corresponding

to edges of the continuum. The closed field lines are expected to oscillate at frequencies above 100 Hz which we cannot confirm because of lack of spatial resolution. Furthermore, we are mainly interested in the frequency range below 100 Hz and models where the elastic properties of the crust are included (see Section 3.5.3). Additionally, as a consequence of the finer spatial structure of the magnetic field confined to the crust, there is a much stronger numerical coupling of different field lines, which leads to an enhanced phase mixing, and hence weaker QPOs. We expect this defect to be less important in the coupled scenario, because for sufficiently low magnetic fields, the oscillations will be dominated by the shear in the crust. The corresponding modes are sufficiently resolved with the numerical resolution applied here.

3.5.3 Coupled magneto-elastic oscillations

We investigate the behavior of coupled magneto-elastic oscillations of the crust for the magnetic field configurations introduced in Section 3.5.1. Therefore, a number of simulations are performed with initial data consisting of a general perturbation with an angular dependence $l = 2$ and $l = 3$ at different magnetic field strengths. The grid resolution is the same as in the preceding section, namely 30×80 $(r \times \theta)$ for $[r_{\rm cc}, r_{\rm s}] \times [0, \pi]$, and the integration time is $t \sim 2\,{\rm s}$ at $B = 10^{14}\,{\rm G}$. For stronger fields, the integration time scales inversely with the magnetic field strength.

The results of the Fourier analysis of these simulations are given in Figs. 3.25 and 3.26, where the Fourier amplitude of the first four crustal shear modes, and their magneto-elastic generalization are shown for different magnetic field strengths and different field configurations (dipolar, quadrupolar, and octupolar). The averaged surface magnetic field strengths are

$$B_{\rm dip} = 3.75 \times 10^{14}\,{\rm G}\,, \tag{3.11}$$

$$B_{\rm quad} = 2.35 \times 10^{14}\,{\rm G}\,, \tag{3.12}$$

$$B_{\rm octu} = 2.23 \times 10^{14}\,{\rm G}\,. \tag{3.13}$$

When making general statements holding for all three magnetic field configurations we use the label $B_{\rm x}$.

At $B = B_{\rm x}$ the structure of the magneto-elastic QPOs is very similar to that of the purely crustal shear modes (see Section 3.2) for all three field configurations, and for all shear modes. The corresponding plots in Figs. 3.25 and 3.26 show how the unchanged purely crustal shear modes approximately look like.

The assumed magnetic field configuration changes the structure of the former shear modes in a different way. For example, the $l = 2$ QPO gets compressed towards field lines entering the star near the pole in the presence of a dipolar surface field. The stronger the field is, the closer to the pole the maximum can be found. This resembles the behavior of the QPOs of purely Alfvén oscillations for this configuration (see Fig. 3.24). The QPO structure of quadrupolar surface fields behaves completely opposite, i.e. the maximum amplitude gets shifted towards the equator with increasing magnetic field strength. For

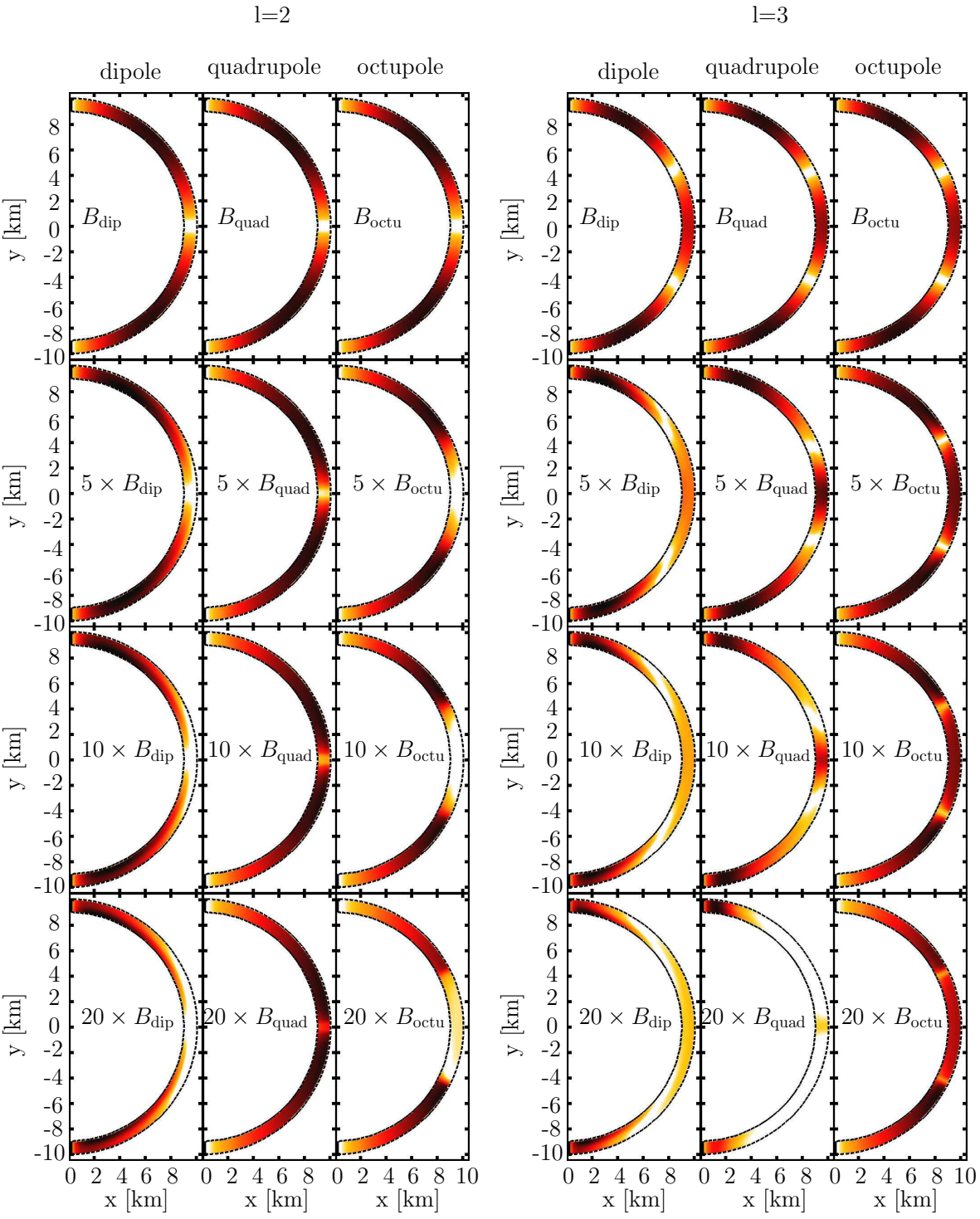

Figure 3.25: Fourier amplitude of $l = 2$ and $l = 3$ crustal shear modes and their magneto-elastic generalization for different magnetic field configurations and different field strengths. The color scale ranges from white (minimum) to red-black (maximum).

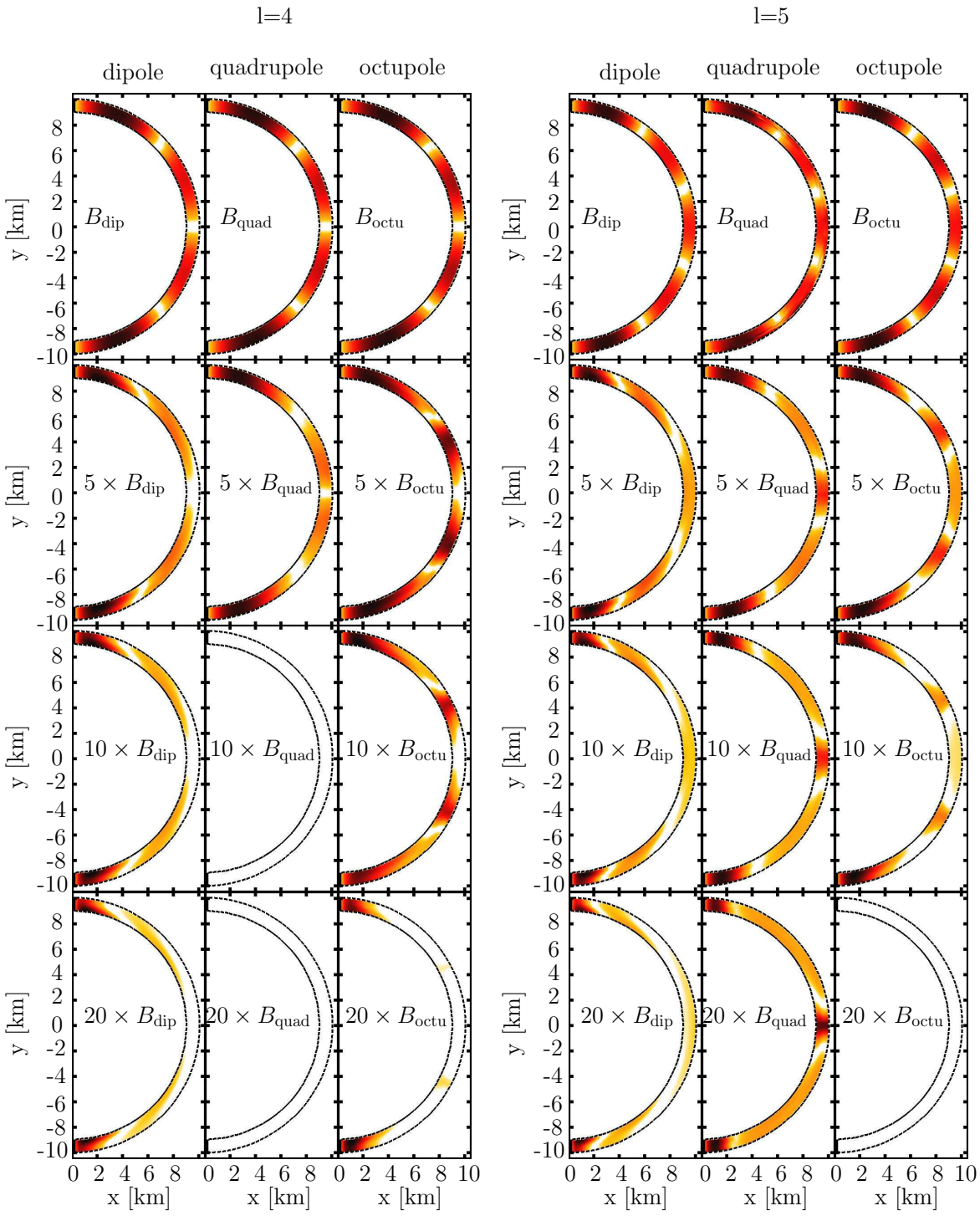

Figure 3.26: Fourier amplitude of $l = 4$ and $l = 5$ crustal shear modes and their magneto-elastic generalization for different magnetic field configurations and different field strengths. The color scale ranges from white (minimum) to red-black (maximum). A completely white panel indicates that no QPOs were observed in the respective simulations.

an octupole configuration the maximum remains at approximately its original position, but it becomes narrower with increasing magnetic field strength.

For the change of the former $l > 2$ crustal shear modes we observe a similar behavior depending on the particular field configuration. Additionally, there appear some peculiarities. For the configuration matched to an exterior dipole, the observed structures of the QPO align with the magnetic field lines. For low magnetic field strength the structure is oriented parallel to the crust-core interface, but with increasing magnetic field strength it becomes clearly distorted and begins to look similar to that of purely Alfvén QPOs. The amplitude of the maxima near the pole is always strongest. For symmetric QPOs the node at the equator becomes more spatially extended compared to the case of lower magnetic field strengths. This may be explained by the presence of closed field lines, which decouple from their neighboring open field lines, and thus do not oscillate in phase with them. For configuration Q, which has closed field lines at $\theta \sim 60°$, we see that the maxima near these lines have lower amplitudes compared to the maxima at the pole or the equator (best visible in the right panel of Fig. 3.26). This structure agrees with the one of the field lines. The open field lines surround the closed ones and reach the surface near the pole and the equator. The behavior of the QPOs of configuration O can be explained similarly. Here, we see an extended node at the equator for symmetric QPOs as we found for configuration D. In the left panel of Fig. 3.26, configuration O and $B = 10 \times B_{\rm octu}$, one can even guess the extension of the region of closed field lines near the equator by looking at the structure of the QPOs. Similarly, the closed field lines around $\theta \lesssim 45°$ are reflected in the structure of the $l = 5$ QPO at $B = 10 \times B_{\rm octu}$ (see right panel of Fig. 3.26).

A common feature of all configurations is that with increasing magnetic field strength the identification of QPOs gets harder, because their amplitudes decrease. That is why some QPOs are not present at all field strengths. We have not succeeded in identifying the following QPOs: $l = 4$ at $B = 10 \times B_{\rm quad}$ and $B = 20 \times B_{\rm quad}$, and $l = 5$ at $B = 20 \times B_{\rm octu}$. For even stronger magnetic fields $B = 50 \times B_{\mathbf{x}}$ it is almost impossible to identify the magneto-elastic generalizations of the crustal shear modes, as the evolution is completely dominated by the magnetic field.

How do the frequencies of the former purely shear modes change in the presence of the magnetic field? To answer this question we display the frequencies of the QPOs shown in Figs. 3.25 and 3.26 as a function of the averaged surface magnetic field strength in the left panel of Fig. 3.27. Different colors indicate different QPOs associated to the zero magnetic field shear modes (black: $l = 2$; red: $l = 3$; magenta: $l = 4$; blue: $l = 5$) and the line style indicates the magnetic field configuration (solid: dipole; dashed: quadrupole; dotted: octupole). At a surface magnetic field strength of about a few$\times 10^{14}$ G the frequencies of the QPOs begin to deviate significantly from those of purely shear crustal modes, which are labeled along the y-axis. For the $l = \{2, 3, 4, 5\}$ modes the zero magnetic field frequencies are 24.6, 38.9, 52.2, and 65.1 Hz, respectively.

Sotani et al. (2008a) studied similar magnetic field configurations and found an increase of the frequency of the QPOs with increasing magnetic field. Sotani et al. (2007)

mode l	field	$B_{\rm crit}$ $[10^{14}\,{\rm G}]$	b_l	mode l	field	$B_{\rm crit}$ $[10^{14}\,{\rm G}]$	b_l
2	dipole	4.8	1.656	4	dipole	6.6	1.503
	quadrupole	11.1	1.072		quadrupole	8.3	1.604
	octupole	9.0	0.999		octupole	6.6	1.493
3	dipole	6.0	1.569	5	dipole	6.0	1.359
	quadrupole	6.8	1.706		quadrupole	10.6	1.794
	octupole	13.9	1.202		octupole	9.2	1.767

Table 3.9: Parameters $B_{\rm crit}$ and b_l of Eq. (3.15) for different magnetic field configurations and strengths, respectively.

give an approximate formula of the dependence of the frequency on the magnetic field

$$\frac{f_l(B)}{f_l^0} = \sqrt{1 + a_l \left(\frac{B}{B_\mu}\right)^2}\,, \tag{3.14}$$

where f_l^0 is the frequency of the purely shear eigenmode, and $B_\mu = 4 \times 10^{15}\,{\rm G}$. We tried to match the frequencies obtained in our simulations with this formula, but it turned out that this approximation is not very accurate. Therefore, we generalized Eq. (3.14) to

$$\frac{f_l(B)}{f_l^0} = \sqrt{1 + \left(\frac{B}{B_{\rm crit}}\right)^{b_l}}\,, \tag{3.15}$$

where $B_{\rm crit}$, is the magnetic field at which the influence of magnetic field becomes important. The parameters $B_{\rm crit}$ and b_l are given in Table 3.9, and the corresponding fits are displayed in the left panel of Fig. 3.27. The observed exponents deviate significantly from $b_l = 2$, the majority being close to $b_l \sim 5/3$. For very strong magnetic fields one would expect a transition to Alfvén oscillations, where the frequency depends linearly on B, i.e. $b_l \to 2$. However, in the presence of such strong fields, shear oscillations no longer exist. In the regime studied here we expect a significant influence of the shear modulus such that the asymptotic regime of $b_l = 2$ is not reached yet, which may explain the deviation from $b_l = 2$.

There are three cases where the exponent b_l is significantly lower than 5/3, namely for $l = 2$ with configuration Q and O, and for $l = 3$ with configuration O. We assume that this deviation is caused by the smaller spatial scales of the respective magnetic field configuration compared to the scale of the shear modes. The proper oscillations of a small-scale magnetic field predominantly couple to shear oscillations of the same spatial size. If large parts of the crust oscillate without having strong spatial gradients like in the case of low l modes, small scale magnetic field lines may not be excited, and thus do not have a large influence on the oscillation.

We are able to extrapolate our results given by Eq. (3.15) to different values of the

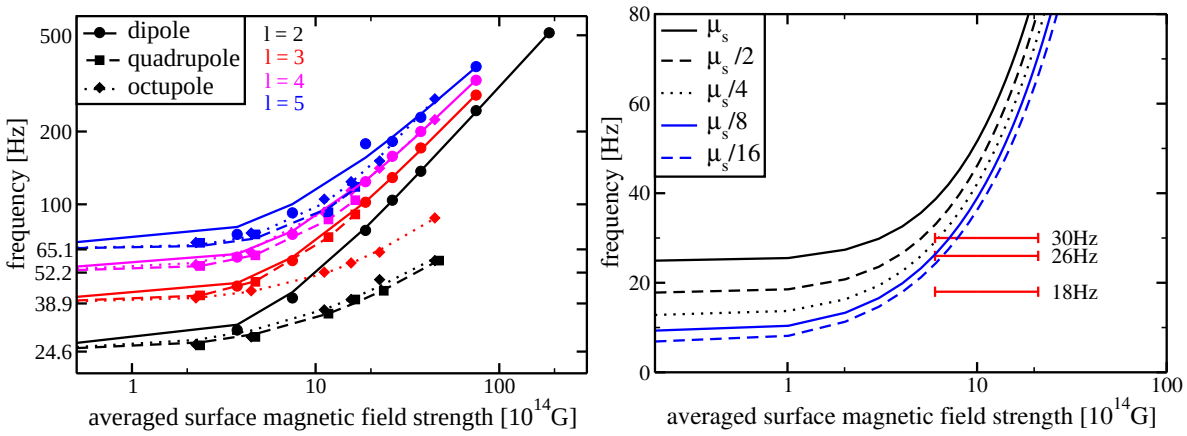

Figure 3.27: *Left panel*: Dependence of the frequencies of the $n = 0$, $l = \{2,\ 3,\ 4,\ 5\}$ QPOs on the magnetic field strength for different magnetic field configurations which are confined to the crust. The purely crustal shear mode frequencies are given in the axis label as 24.6, 38.9, 52.2, and 65.1 Hz. The lines correspond to the fits according to Eq. (3.15) and the parameters are given in Table 3.9. *Right panel*: Extrapolation of the QPO frequencies for different values of the shear modulus $\mu_{\rm s}$ in the presence of a dipolar magnetic field for the QPO with $l = 2$. The red lines indicate the lowest observed frequencies of the QPOs for the range of magnetic field strengths estimated for the three magnetars showing giant flares ($B = 6 \ldots 21 \times 10^{14}$ G).

shear modulus, i.e. we can test if a different magnitude of the shear modulus can explain the lowest observed frequencies of 18, 26, and 30 Hz (Steiner and Watts, 2009). If the shear modulus $\mu_{\rm s}$ in Eq. (2.86) is divided by any factor F, the equation conserves its form if we rescale the background magnetic field B^k by the square root of this factor and simultaneously multiply the time with $\sqrt{F}$:

$$\frac{\partial\sqrt{\gamma}S_\varphi}{\partial\tilde{t}} = \frac{\partial\sqrt{-g}(b_\varphi\tilde{B}^k + 2\tilde{\mu}_{\rm s}\tilde{s}^k{}_\varphi)}{\partial x^k}\,, \tag{3.16}$$

$$\frac{\partial\sqrt{\gamma}B^\varphi}{\partial\tilde{t}} = \frac{\partial\sqrt{-g}v^\varphi\tilde{B}^k}{\partial x^k}\,, \tag{3.17}$$

$$2g_{kk}g^{\varphi\varphi}\frac{\partial\tilde{s}^k{}_\varphi}{\partial\tilde{t}} = \frac{\partial\tilde{\xi}^\varphi_{,k}}{\partial\tilde{t}} = \frac{\partial v^\varphi\alpha}{\partial x^k}\,, \tag{3.18}$$

where

$$\tilde{t} = t\sqrt{F}\,, \qquad \tilde{s}^k{}_\varphi = s^k{}_\varphi\sqrt{F}\,, \qquad \tilde{B}^k = \frac{B^k}{\sqrt{F}}\,, \qquad \tilde{\mu}_{\rm s} = \frac{\mu_{\rm s}}{F}\,. \tag{3.19}$$

This rescaling of the time leads to a inverse rescaling of the frequency and we obtain the expected result that in the absence of a magnetic field, a decrease of the shear

modulus of a factor F leads to a corresponding decrease of the QPO frequency by $\sqrt{F}$. Consequently, the critical magnetic field for an equilibrium model with a rescaled shear modulus (divided by F) has to be divided by $\sqrt{F}$. Knowing $B_{\rm crit}$ and b_l for an equilibrium model we can compute the frequency of the QPOs for different shear moduli by

$$f_l(B) = \frac{f_l^0}{\sqrt{F}}\sqrt{1+\left(\frac{B}{B_{\rm crit}/\sqrt{F}}\right)^{b_l}}\,. \tag{3.20}$$

The corresponding curves for the dipolar background configuration, the lowest QPO with $l = 2$, and $F = \{2, 4, 8, 16\}$ are given in the right panel of Fig. 3.27. Clearly, the decrease of the shear modulus leads to a decrease of $B_{\rm crit}$, i.e. the magnetic field begins to be dynamically dominating at lower magnetic field strength than for large $\mu_{\rm s}$. With the dipolar configuration we are not able to get oscillations at frequencies of 18 Hz at any value of the shear modulus up to 1/16 of its tabulated value. To match the frequencies of the QPOs at 26 or 30 Hz we need to rescale the shear modulus by a factor $F \sim 8$ and are only able to reach the frequencies in the lower end of the magnetic field estimates for the magnetars showing giant flares $B \sim 6 \times 10^{14}$ G.

To summarize the findings of this section, we see a significant increase in the frequency of the magneto-elastic generalization of the crustal shear modes with increasing magnetic field strength. The details of this increase, like the dependence on the magnetic field strength or the spatial structure of the resulting QPOs, depend on the particular magnetic field configuration. At realistic magnetar field strengths at the surface of $B \sim 10^{15}$ G the frequencies of the former crustal shear modes are shifted to such high values that it is hard to explain the lowest frequencies of the QPOs observed in SGRs.

4 Force-free magnetic field configurations of the magnetosphere

In the preceding chapter we have discussed a model of magneto-elastic QPOs created in the interior of a neutron star. To complete this model developed for an understanding of the QPOs observed in giant flares of SGRs, we require a connection between the oscillations inside the neutron star, and the emission from the latter. In our model this is provided by the coupling through the magnetic field. In this chapter we thus investigate how the interior oscillations may change the magnetic field in the magnetosphere of a neutron star. A discussion of how the corresponding evolution of the magnetic field may change the emission is given in Chapter 5.

We first introduce the force-free approximation in the Newtonian framework and discuss its validity for neutron star magnetospheres. A further simplification in form of allowing only for self-similar solutions, leads to analytic expressions for the structure of the magnetic field. The application of these self-similar solutions is very limited (see Section 4.1.1), i.e. we have to apply more advanced techniques to construct magnetic fields which can be matched to the fields obtained by our simulations of the neutron star interior. For this purpose we present the magneto-frictional method in Section 4.1.3, which we adopt to the Schwarzschild spacetime. For simplicity and to speed up the calculation of the magnetospheric fields, we linearize the problem in the magnetic field perturbations. Consequently, the magnetic field configuration can be obtained analytically. We show that for certain configurations the magnetic field in the whole magnetosphere can be derived explicitly, which allows for a test of our methods. Finally, we present the computed magnetic field configurations in the magnetosphere, where the magnetic field obtained from the interior simulations serves as a boundary condition.

4.1 Theoretical methods and numerical tools

The Alfvén crossing time for a typical neutron star model with $B \sim 10^{15}\,\mathrm{G}$ is of the order of $\sim 0.1\,\mathrm{s}$ (see Table 3.8), and most of the observed QPOs have frequencies around 50 Hz (see Table 1.3). In the magnetosphere the Alfvén speed is almost equal to the speed of light. The dynamical time scale of the near magnetosphere $r \lesssim 1000\,\mathrm{km}$ is therefore $r/c \lesssim 1/300\,\mathrm{s}$, which is one order of magnitude less than the time scale on which the oscillations occur. We expect the important activities in the magnetosphere to happen at radii smaller than 500 km (see Chapter 5). Therefore, we can assume that any reconfiguration of the magnetosphere happens much faster than the interior

evolution, i.e. the magnetosphere reaches almost instantaneously an equilibrium state corresponding to the boundary conditions in terms of the magnetic field evolution of the interior. Consequently, we are interested in static equilibrium configurations of the magnetosphere.

In Newtonian physics we have the momentum equation of magneto-hydrodynamics

$$\rho\frac{\partial \mathbf{v}}{\partial t} + \rho\mathbf{v}\nabla\mathbf{v} = \mathbf{J}\times\mathbf{B} - \nabla p + \rho\mathbf{g}\,, \tag{4.1}$$

where $\mathbf{g}$ is the gravitational acceleration. We neglected rotation which has a minor influence in the case of magnetars. In magneto-statics Eq. (4.1) reduces to

$$0 = \mathbf{J}\times\mathbf{B} - \nabla p + \rho\mathbf{g}\,. \tag{4.2}$$

In the force-free approximation we further neglect all inertia and pressure contributions from charge carriers ($\{\rho, p\} << B^2$), but allow the current to change the magnetic field structure. Therefore, the momentum equation reduces to

$$\mathbf{J}\times\mathbf{B} = 0\,. \tag{4.3}$$

We will refer to this equation as the force-free condition. It states that the currents flow along magnetic field lines, and consequently there is no Lorentz force acting on the charge carriers.

Such a configuration can be maintained only under the assumption of ideal MHD, in particular, this means that there have to be sufficient charge carriers to make the medium perfectly conducting. The charge carriers, in the quiescent state of SGRs are provided by the strong and twisted magnetic field, whose B_φ component creates a large electric potential difference between the foot-points of the field lines anchored in the crust. This potential is sufficiently strong to accelerate electrons and light ions from the atmosphere of the neutron star, which is formed by thermally excited particles, along the magnetic field lines (Thompson et al., 2000). The number of these charge carriers is by far not sufficient to create the required currents. However, any particle which gets accelerated along the magnetic field lines creates e^+-e^- pairs when reaching the energetic threshold for this process, which is easily fulfilled in the case of magnetars. The pairs in turn get accelerated in direction of opposite potential and can create further pairs when having acquired sufficient kinetic energy. Finally, these pair avalanches fill the magnetosphere with sufficient plasma to conduct the current (Beloborodov and Thompson, 2007). How this scenario is changed in the case of a giant flare is not clear and needs further investigation.

Any static twist of the magnetic field will dissipate on the time-scale of years (Beloborodov and Thompson, 2007; Beloborodov, 2009). This is orders of magnitudes longer than the time scale of interest for giant flares ($\sim 400\,\mathrm{s}$) and their QPOs ($\sim 1\,\mathrm{min}$), i.e. we can safely neglect any dissipation in the magnetosphere, and the assumption of ideal MHD holds.

4.1.1 Self-similar solution

To fulfill Eq. (4.3) it suffices to impose that the induced current $\mathbf{J}$ is flowing along magnetic field lines

$$\mathbf{J} = \nabla \times \mathbf{B} = \mathcal{P}(\Gamma)\mathbf{B}\,. \tag{4.4}$$

Here $\mathcal{P}$ is a proportionality factor, and we introduced a flux parameter Γ which is constant along magnetic field lines $\mathbf{B}_{\rm poloidal}\cdot\nabla\Gamma = 0$. Γ can be related to the φ-component of the magnetic vector potential $\mathbf{A}$:

$$\Gamma(r,\theta) = r\sin\theta A_\varphi(r,\theta)\,. \tag{4.5}$$

It thus defines the poloidal magnetic field $\mathbf{B}_{\rm poloidal}$ according to

$$\mathbf{B}_{\rm poloidal} = \frac{\nabla\Gamma\times\hat{\varphi}}{r\sin\theta}\,, \tag{4.6}$$

where $\hat{\varphi}$ is the unit vector in the φ-direction.

In the self-similar model (Wolfson, 1995; Thompson et al., 2002) a particular ansatz is chosen for Γ

$$\Gamma = \Gamma_0\left(\frac{r}{r_{\rm S}}\right)^{-p} F(\cos\theta)\,, \tag{4.7}$$

where $\Gamma_0 = 1/2B_{\rm pole}r_{\rm S}^2$. From Eq. (4.4) one may then deduce the following dependence of $\mathcal{P}$ on Γ

$$\mathcal{P} = \frac{C^{1/2}}{r_{\rm S}}\left(\frac{p+1}{p}\right)^{1/2}\left(\frac{|\Gamma|}{\Gamma_0}\right)^{1/p}\,. \tag{4.8}$$

The parameter C is related to the strength of the current which creates the toroidal magnetic field. With the poloidal magnetic field given by Eq. (4.6), the r- and θ-components of Eq. (4.4) give each independently

$$B_\varphi = \frac{p}{p+1}\frac{\Gamma\mathcal{P}(\Gamma)}{r\sin\theta}\,. \tag{4.9}$$

Plugging this in the φ-component of Eq. (4.4) results in the following equation

$$(1-x^2)F''(x) + p(p+1)F(x) = -CF(x)|F(x)|^{2/p}\,. \tag{4.10}$$

Here $x = \cos\theta$ and a prime denotes the derivative with respect to x. Eq. (4.10) is the self-similar form of the Grad-Schlüter-Shafranov equation. This equation states an eigenvalue problem for the eigenvalue p. With C given, there exists an infinite number of eigenvalues p each characterizing a different family of multipoles (see Pavan et al., 2009). For $C = 0$ the solutions of Eq. (4.10) give the usual multipolar expansion of the

poloidal components of $\mathbf{B}$ in vector spherical harmonics.

Eq. (4.10) has to be solved numerically for p. The required boundary conditions are $F(1) = F(-1) = 0$ (only radial field at the axis), $F'(0) = 0$ (no B_r at equator) and $F'(1) = -2$ (normalization). The components of the magnetic field can be expressed explicitly in terms of the function $F(x)$

$$B_r = -\frac{B_{\rm pole}}{2}\left(\frac{r_{\rm s}}{r}\right)^{p+2}\frac{\partial}{\partial x}F(x) \tag{4.11}$$

$$B_\theta = \frac{B_{\rm pole}}{2}\left(\frac{r_{\rm s}}{r}\right)^{p+2}\frac{pF(x)}{\sin\theta} \tag{4.12}$$

$$B_\varphi = \sqrt{\frac{Cp}{p+1}}\frac{B_{\rm pole}}{2}\left(\frac{r_{\rm s}}{r}\right)^{p+2}\frac{F(x)|F(x)|^{1/p}}{\sin\theta} \tag{4.13}$$

Instead of C we can also characterize the self-similar magnetic fields by the angle $\Delta\Phi$, which measures the twist between the foot-points of a field line which is anchored at polar angle θ:

$$\Delta\Phi = 2\int_\theta^{\pi/2}\frac{B_\varphi(\theta)}{B_\theta(\theta)}\frac{d\theta}{\sin\theta}\,. \tag{4.14}$$

The corresponding parameter labeling the different configurations is the net twist of field lines anchored close to the magnetic pole $\Delta\Phi_{N-S} := \Delta\Phi(\theta \to 0)$.

In the self-similar model the choice of the form of Γ and the parameter $\Delta\Phi_{N-S}$ (or C) completely define the current distribution. However, only global twists can be prescribed, and the magnetic field at the surface of the neutron star has to have a particular form to provide the correct twist. Therefore, it is not possible to construct the self-similar magnetospheric field from its values at the surface given by the evolution of the interior of the neutron star. Nevertheless these configurations can serve as viable test cases for more general approaches as will be discussed below.

4.1.2 Force-free magnetic fields in the Schwarzschild spacetime

Near to the neutron star surface, its mass causes a significant curvature of the spacetime, and hence also effects the structure of the magnetic field of up to the level of several percent. To describe the field consistently, we thus consider a non-Euclidean metric. In the exterior we can assume the metric of a spherically symmetric body, i.e. the Schwarzschild metric

$$ds^2 = -\alpha^2 dt^2 + \alpha^{-2}dr^2 + r^2\left(d\theta^2 + \sin^2\theta d\varphi^2\right)\,, \tag{4.15}$$

with α being the lapse $\alpha := (1 - 2M/r)^{1/2}$.

We follow Uzdensky (2004) and use an orthonormal basis $\tilde{\mathbf{e}}_k = g_{kk}^{-1/2}\partial_k = \gamma_{kk}^{-1/2}\partial_k$, with $k = \{r, \theta, \varphi\}$ and γ being the 3-metric. The corresponding expression for the 3-dimensional vector operators gradient $\tilde{\nabla} f$, divergence $\tilde{\nabla}\cdot\mathbf{B}$, and curl $\tilde{\nabla}\times\mathbf{B}$ are given

in Appendix F. We use the tilde to indicate vector operations and vector components which are given in the orthonormal basis, where the components of co- and contravariant vectors are equal $\gamma_{kk}^{-1/2} V_k = V^{\tilde{k}} = V_{\tilde{k}} = \gamma_{kk}^{1/2} V^k$. In the following we will use the representation with lower indices exclusively.

In this chapter we consider only the spatial components of the vectors. The relevant Maxwell equations take the following form in the 3+1 split of the Schwarzschild geometry (MacDonald and Thorne, 1982; Uzdensky, 2004)

$$\tilde{\nabla} \cdot \mathbf{B} = 0 \tag{4.16}$$

$$\tilde{\nabla} \times (\alpha \mathbf{B}) = \alpha \mathbf{J} \,. \tag{4.17}$$

4.1.3 Magneto-frictional Method

A numerical method to construct force-free equilibrium magnetic field configurations is the magneto-frictional method (Roumeliotis et al., 1994; Yang et al., 1986). The starting point of this method is an initial guess for the configuration which does not fulfill the force-free condition (4.3). The corresponding Lorentz force is balanced by a fictitious friction term

$$\mathbf{J} \times \mathbf{B} - \mu \mathbf{v}_{\mathrm{frict}} = 0 \,. \tag{4.18}$$

This defines a fictitious velocity

$$\mathbf{v}_{\mathrm{frict}} = \frac{\mathbf{J} \times \mathbf{B}}{\mu} \,, \tag{4.19}$$

where μ is the proportionality factor. In the original version Roumeliotis et al. (1994) use a decomposition of the magnetic field into Clebsch variables $\hat{\alpha}$ and $\hat{\beta}$

$$\mathbf{B} = \tilde{\nabla}\hat{\alpha} \times \tilde{\nabla}\hat{\beta} \,. \tag{4.20}$$

This ansatz automatically ensures the solenoidal condition $\tilde{\nabla} \cdot \mathbf{B} = 0$ and gives

$$\mathbf{B} \cdot \tilde{\nabla}\hat{\alpha} = 0 \,; \qquad \mathbf{B} \cdot \tilde{\nabla}\hat{\beta} = 0 \,, \tag{4.21}$$

i.e. $\hat{\alpha}$ and $\hat{\beta}$ are constant along field lines. The induction equation (Eq. (2.53))

$$\frac{\partial \mathbf{B}}{\partial t} = \tilde{\nabla} \times (\mathbf{v}_{\mathrm{frict}} \times \mathbf{B}) \tag{4.22}$$

provides two equations for the evolution of the Clebsch variables,

$$\frac{\partial \hat{\alpha}}{\partial t} + \mathbf{v}_{\mathrm{frict}} \cdot \tilde{\nabla}\hat{\alpha} = 0 \,, \tag{4.23}$$

$$\frac{\partial \hat{\beta}}{\partial t} + \mathbf{v}_{\mathrm{frict}} \cdot \tilde{\nabla}\hat{\beta} = 0 \,. \tag{4.24}$$

With the velocity defined in Eq. (4.19) these equations take the following form

$$\frac{\partial \hat{\alpha}}{\partial t} = -\frac{\mathbf{J}\times\mathbf{B}}{\mu}\tilde{\nabla}\hat{\alpha}\,, \tag{4.25}$$

$$\frac{\partial \hat{\beta}}{\partial t} = -\frac{\mathbf{J}\times\mathbf{B}}{\mu}\tilde{\nabla}\hat{\beta}\,. \tag{4.26}$$

If the Clebsch variables $\hat{\alpha}$ and $\hat{\beta}$ are provided at the boundaries of the numerical integration domain, it is straightforward to solve these equations with a method of lines combined with a Runge-Kutta explicit time-stepping. We have implemented a corresponding scheme and recovered the configurations of Roumeliotis et al. (1994). However, the magneto-frictional method in the way presented here has some serious drawbacks. First, it is quite slow for strong twists $\Delta\Phi_{N-S} \gtrsim 0.5\pi$. Second, we are not able to achieve stable evolutions if we provide the boundary condition at the neutron star surface in terms of the magnetic field, as the numerical inversion of Eq. (4.20) at the neutron star surface leads to unstable evolutions.

Therefore, we (and Viganò et al., 2011) are using a more direct way of evolving the magnetic field to a force-free equilibrium configuration by integrating Eq. (4.22) (see also Valori et al., 2005). Using the induction equation (2.53) and the condition of perfect conductivity $\mathbf{E} = -\mathbf{v}_{\rm frict}\times\mathbf{B}$ we get

$$\begin{aligned}
\frac{\partial \mathbf{B}}{\partial t} &= \tilde{\nabla}\times(\mathbf{v}_{\rm frict}\times\mathbf{B}) \\
&= \tilde{\nabla}\times\left(\frac{(\mathbf{J}\times\mathbf{B})}{\mu}\times\mathbf{B}\right) \\
&= \frac{1}{\nu}\tilde{\nabla}\times\left(\frac{\mathbf{J}\times\mathbf{B}}{B^2}\times\mathbf{B}\right) \\
&= \frac{1}{\nu}\tilde{\nabla}\times\left(\frac{\alpha^{-1}[\tilde{\nabla}\times(\alpha\mathbf{B})]\times\mathbf{B}}{B^2}\times\mathbf{B}\right)\,,
\end{aligned} \tag{4.27}$$

where we have introduced $\nu = \mu/B^2$ in order to accelerate the relaxation towards an equilibrium in regions of weak magnetic field. This choice also makes the dimension of ν independent of the magnetic field $[\nu] = [\Delta t]/[(\Delta x)]^2$. As before we evolve this equation by a method of lines combined with a Runge-Kutta method for the time advance algorithm.

In this approach we need to provide boundary conditions for the computations at the outer boundary of the numerical domain in radial direction. Here we match the configuration to purely potential fields. However, the particular choice may have a non-negligible influence on the results and/or on the accuracy of the numerical solution near the outer boundary.

4.1.4 Linear approximation of the magneto-frictional method

Let us recall that our final aim is to find a mechanism which modulates the X-ray emission of a giant flare. In our model the origin of these modulations are the oscillations of the neutron star interior. If we find that this mechanism only works for very large amplitudes of the perturbations, the proposed model does not work. Large amplitudes would be inconsistent with our numerical approach for the stellar interior, which is based on the assumption of linear perturbations. Moreover, large amplitude oscillations would break the crust repeatedly causing further reorganizations of the magnetic field. In this case long time ($\gtrsim$ minutes) coherent oscillations seem not to be a realistic scenario. It is thus reasonable to expect that when matching the interior magnetic field to the exterior one that the perturbations stay in the linear regime in the magnetosphere, too.

We assume a dominant dipole field $\mathbf{B}_0 = B_{\tilde{r}}\tilde{\mathbf{e}}_r + B_{\tilde{\theta}}\tilde{\mathbf{e}}_\theta$ plus a perturbation of the toroidal field according to $\mathbf{B} = \mathbf{B}_0 + \delta B\tilde{\mathbf{e}}_\varphi$. The background field $\mathbf{B}_0$ is assumed to be a potential field, and can be determined by the potential A_φ. The latter is related to the Faraday tensor through

$$F_{\mu\nu} = A_{\mu,\nu} - A_{\nu,\mu}\,. \tag{4.28}$$

The poloidal magnetic field is given in orthonormal coordinates by the Faraday tensor

$$B^{\tilde{\theta}} = B_{\tilde{\theta}} = -F_{\tilde{\varphi}\tilde{r}} = -\frac{\alpha F_{\varphi r}}{r\sin\theta}\,, \tag{4.29}$$

$$B^{\tilde{r}} = B_{\tilde{r}} = F_{\tilde{\varphi}\tilde{\theta}} = \frac{F_{\varphi\theta}}{r^2\sin\theta}\,. \tag{4.30}$$

The currents induced by $\mathbf{B}$ can be calculated with Eq. (4.17). In axisymmetry all derivatives with respect to φ vanish such that we get

$$J_{\tilde{r}} = \frac{1}{r\sin\theta}\left(\sin\theta\delta B\right)_{,\theta}\,, \tag{4.31a}$$

$$J_{\tilde{\theta}} = -\frac{1}{r}\left(r\alpha\delta B\right)_{,r}\,, \tag{4.31b}$$

$$J_{\tilde{\varphi}} = \frac{1}{r}\left[\alpha\left(rB_{\tilde{\theta}}\right)_{,r} - B_{\tilde{r},\theta}\right] = 0\,, \tag{4.31c}$$

where the last equality applies if the poloidal magnetic field is a potential field. Then the cross product $\mathbf{J}\times\mathbf{B}$ reads

$$\mathbf{J}\times\mathbf{B} = \begin{pmatrix} J_{\tilde{\theta}}\delta B \\ -J_{\tilde{r}}\delta B \\ (\mathbf{J}\times\mathbf{B})_{\tilde{\varphi}} \end{pmatrix} = \begin{pmatrix} \mathcal{O}\left((\delta B)^2\right) \\ \mathcal{O}\left((\delta B)^2\right) \\ (\mathbf{J}\times\mathbf{B})_{\tilde{\varphi}} \end{pmatrix} = 0\,, \tag{4.32}$$

such that the only non-trivial equation which has to hold up to linear order in δB is the condition for the $\tilde{\varphi}$-component. Plugging $\mathbf{J}\times\mathbf{B}$ into Eq. (4.27) shows that the $\tilde{r}$- and $\tilde{\theta}$-components of the magnetic field are constant up to linear order. The final equation

for the evolution of δB is

$$\begin{aligned}\frac{\partial \delta B}{\partial t} =& A_1 \delta B + A_2 (\delta B)_{,\theta} + A_3 (\delta B)_{,r} + \frac{B_{\tilde{\theta}}^2}{r^2} (\delta B)_{,\theta,\theta} + \alpha^2 B_{\tilde{r}}^2 (\delta B)_{,r,r} \\ &+ 2\frac{B_{\tilde{\theta}} B_{\tilde{r}} \alpha}{r} (\delta B)_{,r,\theta} \,, \end{aligned} \tag{4.33}$$

with

$$\begin{aligned} A_1 =& -\frac{B_{\tilde{\theta}}^2}{r^2} + \frac{B_{\tilde{\theta}} B_{\tilde{\theta},\theta} \tan\theta}{r^2} - 2\frac{B_{\tilde{\theta}}^2 \tan^2\theta}{r^2} + \frac{\alpha^2 B_{\tilde{r}}}{r} \left(B_{\tilde{r},r} - 2\frac{B_{\tilde{r}}}{r} \right) + \alpha B_{\tilde{r}} (B_{\tilde{r}} \alpha_{,r})_{,r} \\ &+ \frac{\alpha B_{\tilde{\theta}} B_{\tilde{r},\theta}}{r^2} + \frac{\alpha B_{\tilde{r}} \tan\theta}{r} \left(B_{\tilde{\theta},r} - 3\frac{B_{\tilde{\theta}}}{r} \right) + \frac{B_{\tilde{\theta}} B_{\tilde{r},\theta} \alpha_{,r}}{r} - \frac{B_{\tilde{\theta}} \tan\theta B_{\tilde{r}} \alpha_{,r}}{r} \,, \end{aligned} \tag{4.34}$$

$$A_2 = \frac{B_{\tilde{\theta}} B_{\tilde{\theta},\theta}}{r^2} - \frac{\alpha B_{\tilde{r}} B_{\tilde{\theta}}}{r^2} + \frac{\alpha B_{\tilde{r}} B_{\tilde{\theta},r}}{r} + \frac{B_{\tilde{\theta}} B_{\tilde{r}} \alpha_{,r}}{r} \,, \tag{4.35}$$

$$A_3 = 2\alpha B_{\tilde{r}}^2 \alpha_{,r} + \frac{\alpha B_{\tilde{\theta}} B_{\tilde{r},\theta}}{r} + \alpha^2 B_{\tilde{r}} B_{\tilde{r},r} \,. \tag{4.36}$$

Eq. (4.33) can be evolved numerically like in the fully non-linear method using a method of lines combined with an explicit Runge-Kutta time integration.

This method converges much faster to a force-free equilibrium than the non-linear one. For axisymmetric fields it also automatically fulfills the divergence condition $\nabla \mathbf{B} = 0$. Moreover, the accuracy of the calculation of the $\tilde{\varphi}$-component of the magnetic field is much higher, because for the computation of the full 3-dimensional magnetic field vector one has to evaluate derivatives of the poloidal field numerically, which cancel each other analytically for potential fields. The numerical errors related to these computations become important in regions where the poloidal field is much stronger than the toroidal one. Therefore, the linear ansatz presented in this section is not only faster, but also more accurate than the full method presented in the preceding section. However, its main drawback is the limitation to small up to moderate twists which do not change the poloidal field structure significantly. When referring to the current method in subsequent sections we will call it the *magneto-frictional* method or short MF method.

4.1.5 Linear reconstruction of δB as a flux function

In the linear case we have an alternative possibility to obtain the toroidal magnetic field. Let us have a look at the $\tilde{\varphi}$-component of the force-free condition (4.3).

$$\begin{aligned} 0 &= (\mathbf{J} \times \mathbf{B})_{\tilde{\varphi}} \\ &= \frac{1}{r} \left[\frac{B_{\tilde{\theta}}}{\sin\theta} (\sin\theta \delta B)_{,\theta} + B_{\tilde{r}} (r\alpha \delta B)_{,r} \right] \\ &= \frac{1}{\alpha r \sin\theta} \left(\mathbf{B}_0 \cdot \tilde{\nabla} \right) (\alpha r \sin\theta \delta B) \,, \end{aligned} \tag{4.37}$$

where we have used the explicit expression of the gradient in Eq. (F.4). Eq. (4.37) states that $\alpha r \sin\theta \delta B$ does not change in the direction of the background field, i.e. it is a flux function which is constant along field lines. Moreover, the field lines coincide with the equipotential lines of $g_{\varphi\varphi}^{1/2} A_{\tilde{\varphi}} = r \sin\theta A_{\tilde{\varphi}} = A_\varphi$, i.e. A_φ itself is also a flux function[1]. We can use A_φ to map δB from the surface into the exterior, i.e. we have to get the value of the potential A_φ at a given point $\mathbf{r}_x$ and then check what is the corresponding magnetic field δB at the surface at the same potential. Thus δB has the same value at the location $\mathbf{r}_x$ in the magnetosphere.

The approach based on the linear reconstruction is very fast, because it provides directly an explicit expression of the $\tilde{\varphi}$-component of the magnetic field in the magnetosphere if the poloidal field $\mathbf{B}_0$ or its potential $A_{\tilde{\varphi}}$ is given. For the magnetic field configurations we study $\delta B / B_0 \lesssim 0.05$, the linear approximation should be valid and we do not expect large corrections of the poloidal magnetic field by the induced twist. Moreover, there are two major advantages. The first is that we can construct the magnetospheric field from the magnetic field at the boundary, which was not possible in the original approach of the magneto-frictional method which uses Clebsch variables. The second advantage is that we do not need to specify any boundary conditions in the outer part of the magnetosphere as in any version of the magneto-frictional method.

The poloidal component of the magnetic field is given by the output of the "magstar" routine of the LORENE library in our simulations. We use the latter to construct equilibrium models of the neutron star interior. "magstar" provides the potential A_φ (or $A_{\tilde{\varphi}}$) corresponding to the magnetic field in the exterior, and the boundary value of δB at the stellar surface is determined during the evolution of the interior. At the surface we thus have an explicit relation between δB and the potential $\delta B = \delta B\left(A_{\tilde{\varphi}}\right)$. To obtain the value of δB at any point in the magnetosphere, we take the potential $A_{\tilde{\varphi}}$ at the corresponding coordinates and locate the position at the surface with the same potential. Then δB is interpolated from its neighboring grid points by a four-point Lagrange polynomial. When referring to this method in subsequent sections we will call it the *flux-function reconstruction* or short FFR.

Analytical solution

In a Newtonian framework the poloidal currents are given by $J_r = \left(\sin\theta \delta B\right)_{,\theta} / (r \sin\theta)$ and $J_\theta = -\left(r \delta B_{,r}\right) / r$, respectively. Assuming a dipolar poloidal field $B_r = 2 m_B \cos\theta / r^3$ and $B_\theta = m_B \sin\theta / r^3$, where m_B is the measure of the magnitude of the magnetic field, Eq. (4.37) leads to the following expression

$$\begin{aligned} 0 &= \frac{1}{r^3}\left[2 m_B \cos\theta \left(r\delta B\right)_{,r} + \frac{m_B}{r}\left(r \sin\theta \delta B\right)_{,\theta}\right] \\ &= 2\cos\theta \left(r\delta B\right)_{,r} + \left(\sin\theta \delta B\right)_{,\theta} . \end{aligned} \tag{4.38}$$

[1]The $\tilde{\varphi}$-component of $0 = \tilde{\mathbf{B}} \times \tilde{\mathbf{B}}$ together with the definition of $\tilde{\mathbf{B}}$ in Eq. (4.29) gives $\tilde{\mathbf{B}} \cdot \tilde{\nabla} A_\varphi = 0$, i.e. the gradient of A_φ is perpendicular to the magnetic field direction, and hence A_φ is constant in direction of $\tilde{\mathbf{B}}$

Separating the variables $\delta B = f(\theta)g(r)$ gives

$$2\frac{[rg(r)]_{,r}}{g(r)} = -\frac{[\sin\theta f(\theta)]_{,\sin\theta}}{f(\theta)}\,. \tag{4.39}$$

With the ansatz $g(r) = r^{\lambda_r}$ and $f(\theta) = \sin^{\lambda_\theta}\theta$ we obtain the relation

$$\begin{aligned} 2(\lambda_r + 1) &= -(\lambda_\theta + 1) \\ \lambda_r &= -\frac{\lambda_\theta + 3}{2}\,. \end{aligned} \tag{4.40}$$

With $\lambda = \lambda_\theta$ we get

$$\delta B = r^{-\frac{\lambda+3}{2}}\sin^{\lambda}\theta \tag{4.41}$$

This result shows that the self-similar ansatz, i.e. all magnetic field components have to have the same fall-off behavior with the radius r, is only valid for a particular class of surface magnetic fields. In the present example of a dipolar background field the poloidal magnetic field components behave like $\mathbf{B_0} \sim r^{-3}$, such that the only allowed self-similar solution would be $\lambda = 3$.

The results of this short section can be used to test the methods presented earlier in this chapter. These can be simplified to the Newtonian framework by setting $\alpha = 1$.

4.2 Force-free configurations of neutron star magnetospheres

Before calculating the configurations of the magnetic field in the magnetosphere of neutron stars according to the evolution of the stellar interior, we perform two tests of the applicability of the methods we have given in the preceding section. Therefore, we check whether we can recover the analytical solution given in Eq. (4.41) and compare our results with the self-similar solutions of Section 4.1.1. During the latter step we also estimate up to which toroidal magnetic field strength our methods give sufficiently accurate results.

4.2.1 Comparison with analytical solution

In Section 4.1.5 we derived an analytical solution in a Newtonian background Eq. (4.41). We compare this solution with the results of the two different methods presented in Sections 4.1.4 (MF) and 4.1.5 (FFR), respectively. For this purpose we plot the ratio of the numerically obtained δB and the analytic solution (Fig. 4.1). The numerical grid is the same in both cases, and contains 100×80 cells for the domain $[r_\mathrm{s}, 500\,\mathrm{km}] \times [0, \pi]$. The radial grid is logarithmic, and the angular one equidistant.

For both methods we recover the analytical solutions inside major parts of the domain.

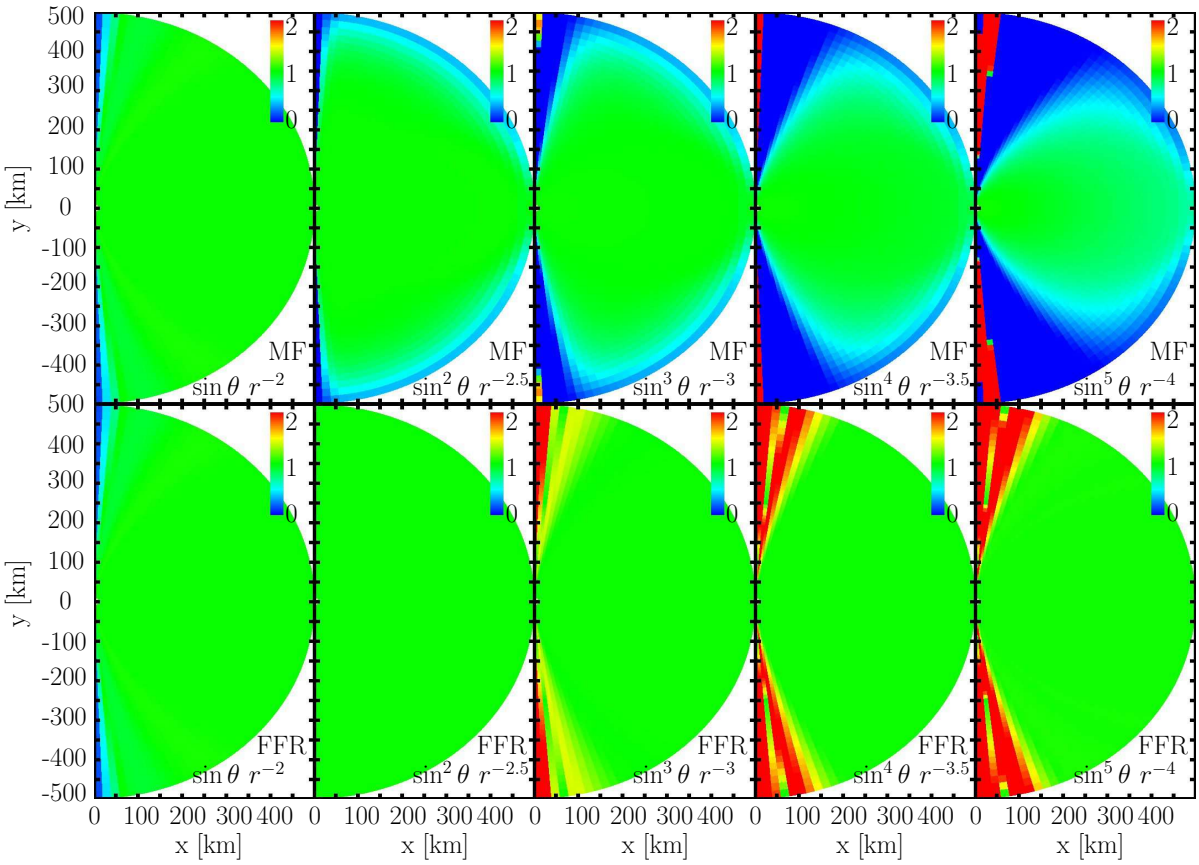

Figure 4.1: Ratio of the numerically obtained configuration and of the analytical solution of Section 4.1.5. The five different configurations shown are characterized by the functional behavior given in each panel. The *upper panels* show the results with the magneto-frictional method (MF) and the *lower* ones those of the flux-function reconstruction (FFR). Larger deviations found with the MF method near the outer boundary are due to the imposed boundary condition of zero δB. Near the polar axis the relative numerical error is mainly caused by the small absolute value of the magnetic field, where $\delta B \sim \sin^\lambda \theta$.

The most prominent deviations are found near the polar axis. This is natural, because there the absolute value of δB approaches zero. Consequently, the relative deviation from the analytical solution which is shown in the figure increases. Moreover, the decline of the surface field as $\sim \sin^\lambda \theta$ near the pole gives rise to numerical problems when computing the derivatives required in the MF method. The higher λ is, the larger is the θ-derivative, and hence the numerical error of the derivative. Similar arguments hold in the reconstruction of the magnetic field with the FFR method. Because of the strong gradient and small magnitudes of δB near the axis, the relative accuracy in the interpolation drops in this region.

The additional deviations found with the MF method near the outer boundary are caused by the boundary conditions chosen there. In the current example, the δB component of the magnetic field is set to zero, because we do not expect currents to extend

up to infinite spatial distance. This causes the magnetic field obtained with the MF method to be different from the analytic solution near the outer boundary. This difference also propagates inward through the evaluation of derivatives during the numerical procedure. However, it is clear from Fig. 4.1 that the field near to the neutron star is almost unaffected.

4.2.2 Comparison with self-similar models

The non-linear solution of the self-similar configuration serves as a further test of our implementation. Moreover, we can estimate up to which toroidal magnetic field strength our method reproduces the self-similar solutions with sufficient accuracy. In this section we study the results obtained with the FFR method. The MF method gives very similar configurations of the magnetic field, but is computationally much slower than the FFR method and produces less accurate results. For example, see Fig. 4.1, where the numerical result is influenced by the outer boundary condition.

In Fig. 4.2 we show the ratio of the toroidal and poloidal magnetic field strength of different self-similar solutions with increasing total twist angle $\Delta\Phi_{N-S} = \{0.1, \ldots, 1.0\}$. From here on we omit the subscript $N - S$ and refer to the total twist angle simply as $\Delta\Phi$. The solid lines in the figure are equipotential lines of the poloidal current caused by the toroidal magnetic field component, whereas dashed lines indicate equipotential surfaces of the current for a configuration obtained with the FFR method. Same colors represent same current magnitudes.

In the first panel of Fig. 4.2 ($\Delta\Phi = 0.1$) the solid (self-similar) and dashed (FFR method) lines are almost indistinguishable, i.e. the linear approximation and the FFR method give approximately the same currents as the full self-similar model. The stronger the twist gets the more the linear results differ from the self-similar ones. In the last panel ($\Delta\Phi = 1.0$) there are significant differences in the exact location of the equipotential surfaces of the poloidal current. For example, the solid blue line crosses the equator at around 400 km, while the corresponding dashed line crosses it at ~ 330 km. However, the general shape of the surfaces is still very similar in both the linear approximation and the full solution. We note that in the linear approach the current is underestimated. This is caused by two main effects. First, we neglect the toroidal current which in general has to be considered for non-linear configurations. Second, the poloidal magnetic field lines get inflated (Roumeliotis et al., 1994; Viganò et al., 2011). Consequently, the currents extend to larger radii as can be seen in Fig. 4.2.

We consider the configuration with $\Delta\Phi = 0.5$ as the limiting case up to which the linear FFR methods produces reliable results, because for stronger twists the deviations from the non-linear, self-similar model start to become significant. The ratio of the toroidal and poloidal magnetic field strength does not exceed 25% in this model. We thus take a more conservative estimate of the maximum acceptable toroidal magnetic field $\delta B/B_{\text{poloidal}} \leq 0.1$, which should give at most a couple of percent deviation of the magnetic field configuration.

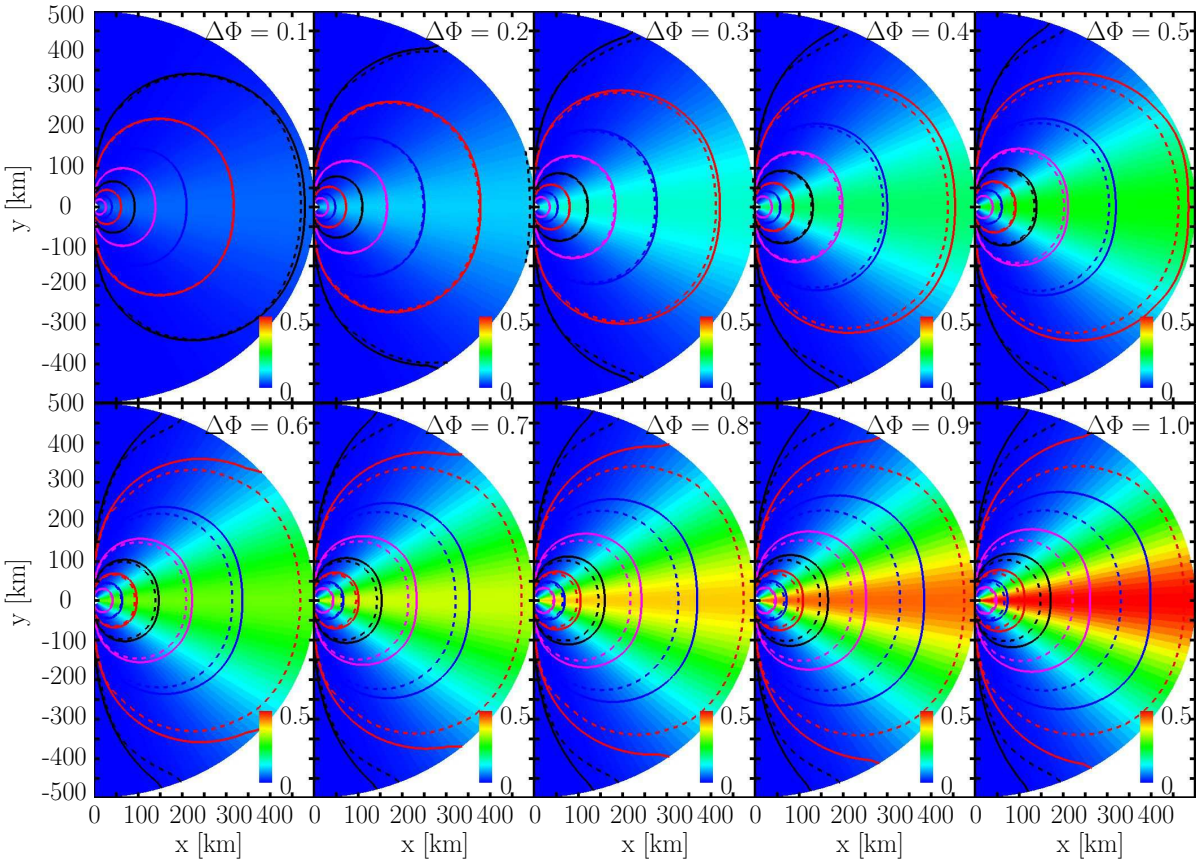

Figure 4.2: Amplitude of $\delta B/B_0$ in the magnetosphere around a neutron star for self-similar magnetic field configurations (color coded). *Solid lines*: Equipotential surfaces of the current of a self-similar solution. *Dashed lines*: Equipotential surfaces of the current of a numerical solution obtained with the FFR method. The boundary magnetic field at the surface of the neutron star agrees with that of the self-similar solution. The constant $\Delta\Phi$ given in the different panels is the total twist, and hence a measure of the toroidal magnetic field strength (see Eq. (4.14)).

4.2.3 Exclusion of antisymmetric configurations

In Section 4.1.5 we derived the equation for the FFR method (Eq. (4.37)). We found that the magnetic field has to be constant along magnetic field lines. In particular, this signifies that the magnetic field at the foot-points of the field lines has to be equal on both hemispheres. Therefore, magnetic field configurations which do not have this property are forbidden in the sense, that these configurations do not lead to force-free magnetic fields. Fig. 4.3 demonstrates what happens in the MF method when we give antisymmetric boundary conditions with respect to the equatorial plane.

As expected by the employed method the current starts to align with the magnetic field in order to reduce the Lorentz force $\mathbf{J} \times \mathbf{B}$. This is indicated by the displayed field lines in Fig. 4.3. Near the pole the alignment occurs quite fast, while near the

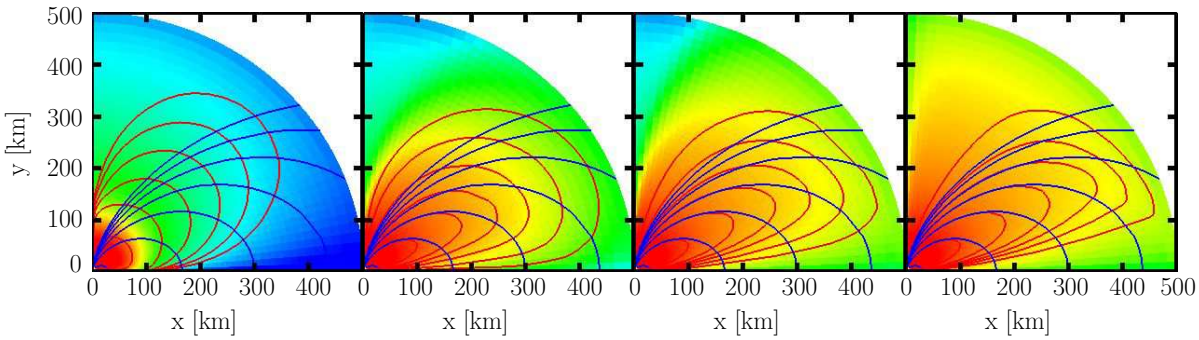

Figure 4.3: Integration steps of the MF method when imposing antisymmetric boundary conditions for the surface magnetic field. (Time increases from left to the right.) The background gives the toroidal magnetic field strength δB, and the corresponding color scale ranges from blue (10^4 G) to orange-red (5×10^9 G). The field lines of the current (red lines) align close to the pole with the field lines of the poloidal magnetic field (blue lines). Near the equator the alignment proceeds much slower, and a current sheet is produced.

equator it takes very long computational time, because to fulfill the given antisymmetric boundary condition on the magnetic field, strong currents have to be created at the equator. Therefore, the final configuration will have a current sheet there. However, this current violates the force-free condition, because it is orthogonal to the poloidal magnetic field lines.

One possible solution to this problematic behavior is that the corresponding currents do not enter into the magnetosphere, i.e. a current sheet is created at the surface of the neutron star. These currents have to be such that the magnetic field at the surface is only allowed to be symmetric with respect to the equator, i.e. the formation of an antisymmetric magnetic field at the surface is prohibited by these currents. The details of how this might happen quantitatively is beyond the scope of the current work.

Since we did not know about the constraint on the symmetry of the surface magnetic field when computing the interior solutions, the resulting configurations do not posses any preferred symmetry in general. In order to apply our MF and FFR methods derived in the preceding sections, we thus symmetrize the surface magnetic field and use only the symmetric contribution to construct the exterior magnetic field.

4.2.4 Configurations matched to interior solutions

Finally we present the magnetic field configurations of the magnetosphere which are determined by results of the simulations of the interior of the neutron star (see Chapter 3). We take the numerically obtained surface magnetic field, symmetrize it, and create the magnetospheric field with the FFR method.

In Fig. 4.4 we give snapshots of the corresponding evolution of δB in the magnetosphere. We display the absolute value of δB in order to apply a logarithmic scale. This

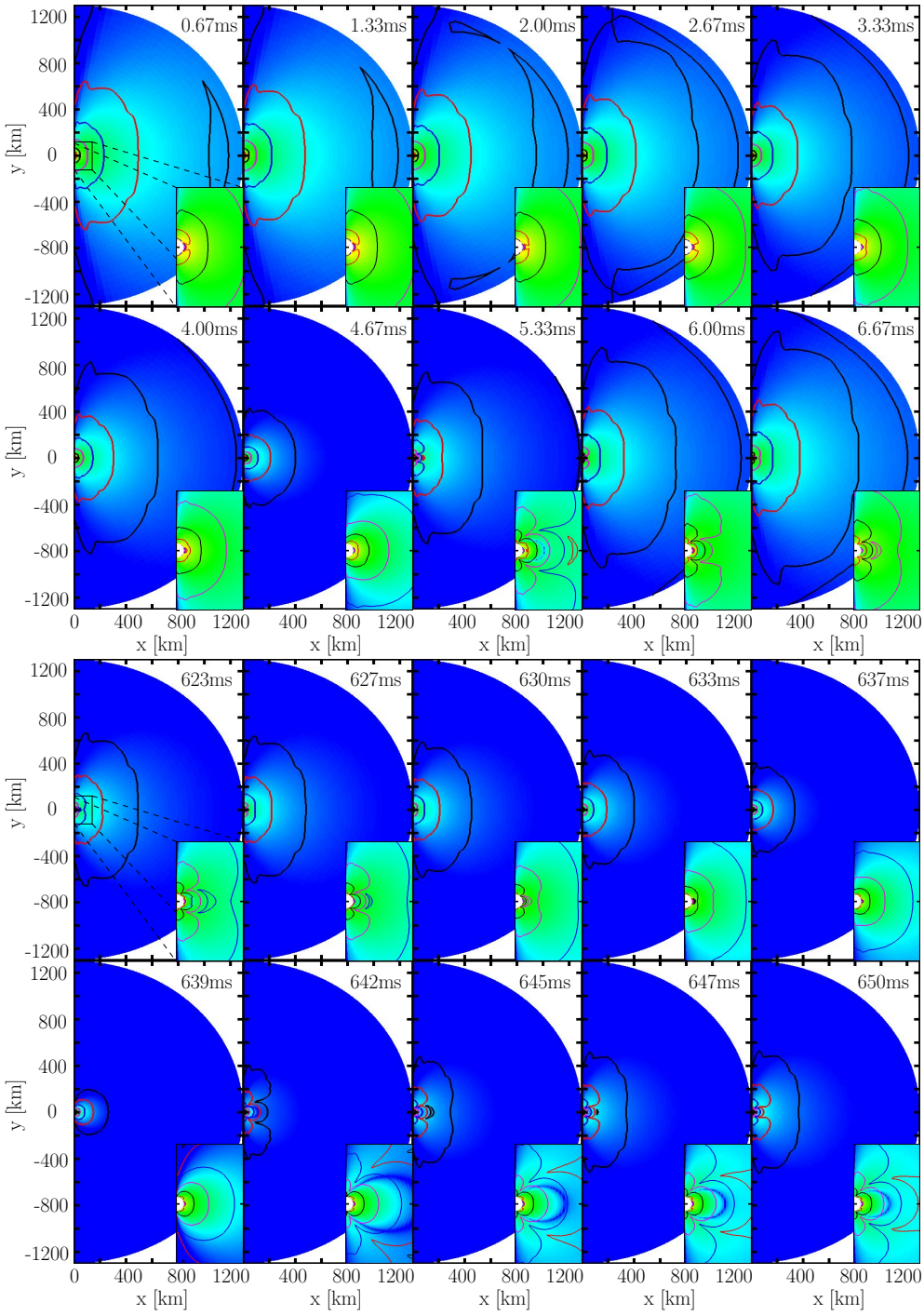

Figure 4.4: Snapshots of the evolution of the magnetic field in the exterior of a neutron star matched to an interior evolution. The model is APR+DH 1.4 with $B = 3 \times 10^{15}\,\mathrm{G}$, and the toroidal magnetic field strength is $\sim 10^{14}\,\mathrm{G}$ (color coded). Solid lines give equipotential surfaces of poloidal current magnitudes. The inserts display a magnification of the region close to the stellar surface as indicated in the first panel. *Upper 10 panels*: Beginning of the evolution. *Lower 10 panels*: End of the evolution. The color scale ranges from blue ($10^8\,\mathrm{G}$) to orange-red ($10^{14}\,\mathrm{G}$).

is necessary to visualize the change of the magnetic field over several orders of magnitude. The solid lines indicate the equipotential surfaces of the poloidal current caused by the toroidal magnetic field. The inserts display a magnification of the region of the magnetic field near to the stellar surface. The numerical grid in the magnetosphere of 100×80 ($r \times \theta$) zones covers the range $[r_\mathrm{s}, 1200\,\mathrm{km}] \times [0, \pi]$. The radial grid is increasing logarithmically, and the angular one is equidistant.

At large distances the magnetic field and the currents decrease very smoothly, and the currents look qualitatively similar to those of the self-similar solutions given in Fig. 4.2. Features of the current, like the closed equipotential lines near the outer boundary of the computational zone, are caused exclusively by the boundary condition $\delta B = 0$. However, near the surface of the star the magnetic field can be very different from that of the self-similar solutions (see inserts in Fig. 4.4). The magnetic field may change its sign with increasing radius or with increasing polar angle, i.e. it may have a very different angular dependence than the simple self-similar models which have no nodes in θ-direction.

For a better understanding we plot the magnetic field at the surface at different times in the left panel of Fig. 4.5. Additionally, we give an example of a self-similar field (black dashed line). The magnetic field changes its structure completely having two nodes (without a node at the pole) at $t = 623\,\mathrm{ms}$, no nodes at $t = 637\,\mathrm{ms}$, and again two nodes at $t = 647\,\mathrm{ms}$. Self-similar configurations do not have nodes besides the one at the pole, and the amplitude is always maximum at the equator. The amplitude of the numerically obtained fields changes during the evolution (see Fig. 4.4). Note that there is always a maximum of δB at $\theta = \pi/2$, which may be explained with the linearized induction equation (2.99): $\delta B = (\delta B)_\varphi = B_r \xi_{\varphi,r} + B_\theta \xi_{\varphi,\theta}$. As a consequence of the symmetry constraint (see Section 4.2.3) only antisymmetric velocity and displacement ξ_φ perturbations are allowed. Therefore, the θ-derivative of the displacement is expected to be very large near to the equator, where ξ_φ has a node. Moreover, at this location the θ-component of the dipolar magnetic field has a maximum, i.e. we expect a very strong δB near to the equator.

The latter feature influences the magnetic field only very close to the star, because the strong $(\delta B)_\varphi$ component is localized at the equator, and the magnetic field lines of the poloidal background configuration (or equipotential surfaces of the magnetic potential) originating from this region extend only to about $\sim 1\,\mathrm{km}$ above the surface.

In the right panel of Fig. 4.5 we show the decrease of $|\delta B|$ as a function of radius near the equator at different times. As in the left panel the dashed line gives an exemplary self-similar solution which decreases as $\sim r^{-3}$. All δB with the exception of the one at 637 ms decrease initially much faster than $\sim r^{-3}$, and for $r \gtrsim 200\,\mathrm{km}$ the magnetic field strength of all our configurations decrease much slower than the self-similar solution. The corresponding exponents of the radial dependence are given in the legend of the right panel of Fig. 4.5, and all differ significantly from -3.

We associate the strong initial decrease of the magnetic field with increasing r to the strong decrease of the surface magnetic field with decreasing θ. The magnetic field δB along θ-direction at the surface can be mapped by the poloidal magnetic field lines along

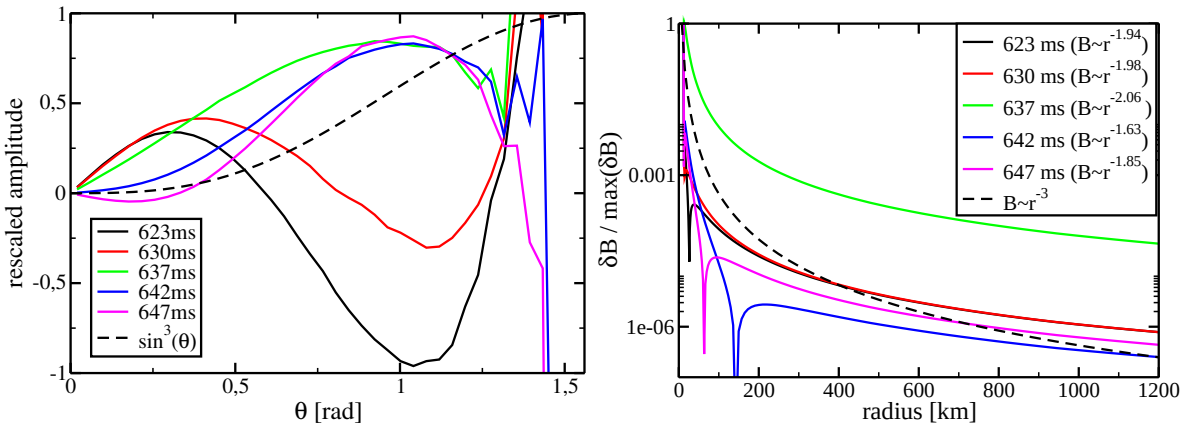

Figure 4.5: *Left panel*: Snapshots of the magnetic field at the surface of the neutron star. The black dashed line corresponds to a self-similar solution with angular dependence $\sim \sin^3\theta$. *Right panel*: Decrease of $(\delta B)_\varphi$ near the equator as a function of radius r for different snapshots of the evolution. The dashed line corresponds to a self-similar solution with $B \sim r^{-3}$ for all components of the magnetic field. The dependencies of B on r in the legend are the asymptotic rates of the decrease for large r.

r-direction at the equator. After the strong decrease all, but the field at 637 ms (green line), show a node at about $\theta \gtrsim 1.3$ (see left panel of Fig. 4.5). The corresponding node in r-direction occurs only few km away from the surface, and hence can not be recognized in the right panel. However, the next zero at $\theta < 0.8$ for the different configurations in the left panel is clearly visible as node in the right panel. First, the configuration at $t = 630$ ms (red line) crosses zero ($\theta \sim 0.8$, $r \sim 15$ km), then the configuration at $t = 623$ ms (black line, $\theta \sim 0.6$, $r \sim 25$ km), the one at $t = 647$ ms (magenta line, $\theta \sim 0.35$, $r \sim 65$ km), and finally the blue line for δB at 642 ms ($\theta \lesssim 0.05$, $r \sim 150$ km). The decrease of δB at larger radii is thus determined by its fall-off behavior very close to the pole. The steeper the latter decrease is (steep for $t = 637$, 623, and 630 ms, less steep for $t = 647$ and 642 ms), the steeper is the decrease at large r (compare the exponent of the fitting functions in the legend of the right panel in Fig. 4.5).

Our examples show that the self-similar approximation of the magnetosphere is not sufficiently accurate to describe the magnetosphere of oscillating magnetars.

5 Modulation of the X-ray emission by magneto-elastic oscillations of the magnetar

As a first step to explain the QPOs observed in giant flares of SGRs we computed the magneto-elastic oscillations of the magnetar which in our model produce the observed frequencies. In the preceding chapter we constructed the magnetic field in the magnetosphere corresponding to these oscillations of the stellar interior. The missing link to the observations is provided in this chapter, where we discuss the modulation of the X-ray signal by resonant cyclotron scattering (RCS). This process occurs when the radiation interacts with the charge carriers of the currents caused by the twisted magnetosphere.

The possibility of significant RCS in the magnetosphere of magnetars has been discussed in Thompson et al. (2002). They showed in a simplified self-similar magnetic field configuration with reasonable twists $\Delta\Phi \lesssim 1.0$ that the charge carriers of the currents are sufficiently numerous to provide significant optical depth for RCS of the emitted X-ray photons. The first quantitative analysis of RCS in magnetar magnetospheres was performed in a 1-dimensional semi-analytic model by Lyutikov and Gavriil (2006). They found that photons traversing a resonant surface[1] of RCS are on average up-scattered in frequency by a factor $\sim 1 + 2\beta_{\mathbf{T}}$, with $\beta_{\mathbf{T}}$ being the thermal velocity of the scattering particles. In this thesis we calculate the photon propagation numerically using methods following Fernández and Thompson (2007), and Nobili et al. (2008a). Both groups independently developed 3-dimensional Monte-Carlo radiation transport codes able to compute photon propagation in a twisted magnetosphere.

The chapter is organized as follows: first, we discuss the physics of RCS in general, and then specify to the conditions in neutron star magnetospheres. Second, we present a numerical tool to solve the corresponding radiation transport with a Monte-Carlo method, and test our implementation against simple self-similar configurations given in the literature. Finally, we discuss the results of the application of our method to the coupled core-crust-magnetosphere oscillations of magnetars.

[1] A region around a neutron star at which the resonance condition for RCS is fulfilled (see Eq. (5.1)).

5.1 Resonant cyclotron scattering in neutron star magnetospheres

The motion of charged particles in a magnetic field is characterized by Landau quantization, i.e. the components of the momentum of the particles orthogonal to the magnetic field direction are allowed to have discrete values only (see Landau and Lifshitz, 1981). The energy difference between two successive *Landau Levels* is

$$\Delta E = \hbar\omega_{\rm c} := \hbar\frac{|Z|eB}{mc}\,, \tag{5.1}$$

where $\omega_{\rm c}$ is the cyclotron frequency, and Ze and m are the particle charge and mass, respectively. Consequently, only photons with the corresponding energies $n\Delta E = E_\omega = \hbar\omega$ can be absorbed by the particles (at rest). When restricting to the simplest case $n = 1$, we thus have the resonance condition

$$\omega = \omega_{\rm c} = \frac{|Z|eB}{mc}\,. \tag{5.2}$$

The resonant magnetic field strength $B_{\rm res}$ can be expressed as

$$B_{\rm res} = 0.088 E_\omega[{\rm keV}]\left(\frac{m}{m_e}\right)\times 10^{12}{\rm G}\,. \tag{5.3}$$

As long as the photon energy is less than a few keV, the resonant magnetic field is much weaker than the critical QED field ($B_{\rm res} << B_{\rm QED} = 4.4\times 10^{13}\,{\rm G}$). Knowing the resonant magnetic field we can find the radius at which resonant absorption by particles at rest occurs for a dipolar magnetic field configuration:

$$r_{\rm res}(\theta) := r_{\rm s}\left(\frac{B_{\rm pole}}{B_{\rm res}}\right)^{1/3}\left(1-\frac{3}{4}\sin^2\theta\right)^{1/6}\,. \tag{5.4}$$

This angle-dependent radius determines the resonant surface at which photons with the corresponding energy scatter resonantly.

After the excitation of a particle into a higher Landau Level it releases the gained energy almost immediately due to synchrotron radiation. This occurs on time scales $t_{\rm syn}\sim 1/\Gamma_{\rm L}$, where $\Gamma_{\rm L} = 4e^2\omega_c^2/3mc^3$ is the natural width of the first cyclotron line (Ventura, 1979). From $t_{\rm syn} << r_{\rm res}/c$ we get the following constraint on the minimal photon energy at which we can neglect the time delay between emission and absorption

$$E_\omega = \hbar\omega_c >> \hbar\sqrt{\frac{3c^2}{4r_{\rm res}r_0}} \sim 0.01\,{\rm eV}\sqrt{\frac{100\,{\rm km}}{r_{\rm res}}}\left(\frac{m}{m_e}\right)^{1/2}\,, \tag{5.5}$$

where $r_0 = e^2/mc^2$, in the case of electrons, is the classical electron radius $r_0 = 2.817940\times 10^{-13}\,{\rm cm}$. For photon energies above that of infrared radiation we thus can safely approximate the cyclotron absorption and synchrotron emission as a single

scattering process.

A characteristic quantity of any scattering process in a plasma is the optical depth τ of a photon which travels a distance l. It is defined by $I/I_0 = e^{-\tau}$, where I (I_0) is the intensity of the unscattered photons after a path with length l (at $l = 0$), and hence the negative logarithm of τ describes the fraction of unscattered photons. τ can be related to the cross section σ and the number density of the scattering targets n_Z of the medium the radiation passes through as follows

$$d\tau = \sigma n_Z dl\,. \tag{5.6}$$

From here on we constrain the discussion to RCS, which near the resonance provides much larger optical depths than the Thompson cross section (elastic scattering of electromagnetic radiation off electrons). The non-resonant contributions are negligible because of the tiny line width Γ_L, and the corresponding narrow and high resonance peak. The differential optical depth $d\tau(\omega, \hat{\mathbf{k}}, \mathbf{r})$ of a photon between $\mathbf{r}$ and $\mathbf{r} + dl\hat{\mathbf{k}}$ for RCS is (Nobili et al., 2008a)

$$d\tau(\omega, \hat{\mathbf{k}}, \mathbf{r}) = dl \int \sigma_{\mathbf{res}}(\omega, \hat{\mathbf{k}}, \mathbf{r}) dn_\mathrm{Z} = dl \int_{-1}^{1} \frac{dn_\mathrm{Z}}{d\beta} \sigma_{\mathbf{res}}(\omega, \hat{\mathbf{k}}, \mathbf{r}) d\beta\,, \tag{5.7}$$

where $\hat{\mathbf{k}}$ is the propagation direction, σ_res the resonant cross section, and $\beta\hat{\mathbf{B}}$ is the velocity of the charge carriers along the magnetic field $\mathbf{B} = B\hat{\mathbf{B}}$. The momentum distribution of the charge carriers $f_Z(W\beta, \mathbf{r})$ has the general form

$$f_Z(W\beta, \mathbf{r}) = \frac{1}{W^3 n_Z} \frac{dn_Z}{d\beta}\,, \tag{5.8}$$

where $W = (1 - \beta^2)^{-1/2}$ is the Lorentz factor and f_Z is normalized to

$$\int_0^\infty f_Z(W\beta, \mathbf{r}) d(W\beta) = 1\,. \tag{5.9}$$

The main ingredient in Eq. (5.7) is the resonant cross section σ_res. General expressions for σ_res have been presented in Canuto et al. (1971) and Herold (1979) (see also Daugherty and Ventura, 1978; Ventura, 1979). For particles at rest and in the non-relativistic limit the differential cross sections are given by Nobili et al. (2008a):

$$\left.\frac{d\sigma}{d\Omega'}\right|_{1-j} = \frac{3\pi r_0 c}{8} \delta(\omega - \omega_c) \cos^2\Theta \left(\cos^2\Theta' \delta_1^j + \delta_2^j\right) \tag{5.10a}$$

$$\left.\frac{d\sigma}{d\Omega'}\right|_{2-j} = \frac{3\pi r_0 c}{8} \delta(\omega - \omega_c) \left(\cos^2\Theta' \delta_1^j + \delta_2^j\right)\,, \tag{5.10b}$$

where Θ is the impact angle of the photon with the scattering target before the scattering, and the prime denotes quantities after scattering. The subscripts 1 (2) indicate the initial polarization, and the index $j = \{1, 2\}$ represents the polarization after scattering. Under

the conditions encountered in the magnetosphere of magnetars vacuum polarization dominates over plasma effects (Fernández and Thompson, 2007; Nobili et al., 2008a). Hence, the two normal modes of electromagnetic radiation are linearly polarized. The index 1 (2) represents the ordinary or O (extraordinary or E) mode whose direction is $\hat{\mathbf{e}}_1 = (\hat{\mathbf{B}} \times \hat{\mathbf{k}}) \times \hat{\mathbf{B}}$ ($\hat{\mathbf{e}}_2 = \hat{\mathbf{B}} \times \hat{\mathbf{k}}$). The total cross sections are obtained by integrating over all possible outgoing photon angles:

$$\sigma_{i-j} = \int_0^{2\pi} \int_0^{\pi} \left.\frac{d\sigma}{d\Omega'}\right|_{i-j} d\Omega' \,. \tag{5.11}$$

Inserting the different polarizations we obtain

$$\sigma_{1-2} = 3\sigma_{1-1} = \frac{3\pi^2 r_0 c}{2} \delta(\omega - \omega_c) \cos^2\Theta \tag{5.12a}$$

$$\sigma_{2-2} = 3\sigma_{2-1} = \frac{3\pi^2 r_0 c}{2} \delta(\omega - \omega_c) \tag{5.12b}$$

The total cross section of a photon with a given polarization is thus

$$\sigma_1 = \sigma_{1-1} + \sigma_{1-2} \tag{5.13a}$$

$$\sigma_2 = \sigma_{2-1} + \sigma_{2-2} \,. \tag{5.13b}$$

In the numerical implementation of the Monte-Carlo method (Section 5.2.1) we require the following integrals in order to determine the photon direction after the scattering. These integrals give the probability for scattering into an azimuthal angle smaller than ϕ'

$$\frac{1}{\sigma_{i-j}} \int_0^{\phi'} \int_0^{\pi} \left.\frac{d\sigma}{d\Omega'}\right|_{i-j} d\Omega' = \frac{1}{2\pi}\phi' \,, \tag{5.14a}$$

and into an polar angle smaller than Θ'

$$\frac{1}{\sigma_{1-1}} \int_0^{2\pi} \int_0^{\Theta'} \left.\frac{d\sigma}{d\Omega'}\right|_{1-1} d\Omega' = \frac{1}{\sigma_{2-1}} \int_0^{2\pi} \int_0^{\Theta'} \left.\frac{d\sigma}{d\Omega'}\right|_{2-1} d\Omega' = \frac{1}{2}(1 - \cos^3\Theta') \,, \tag{5.15a}$$

$$\frac{1}{\sigma_{1-2}} \int_0^{2\pi} \int_0^{\Theta'} \left.\frac{d\sigma}{d\Omega'}\right|_{1-2} d\Omega' = \frac{1}{\sigma_{2-2}} \int_0^{2\pi} \int_0^{\Theta'} \left.\frac{d\sigma}{d\Omega'}\right|_{2-2} d\Omega' = \frac{1}{2}(1 - \cos\Theta') \,. \tag{5.15b}$$

The previous cross sections are given in the particle rest frame. However, the charge carriers are required to move in order to allow for the presence of the currents. This motion changes the resonance condition because of the Doppler shift. One has to exchange ω_c in Eqs. (5.12) by

$$\omega_D = \frac{\omega_c}{W(1 - \beta\mu_{\rm SF})} \,. \tag{5.16}$$

Here, $\mu_{\rm SF} := \cos\Theta_{\rm SF}$ is the directional cosine of the photon with respect to the magnetic

field. We use the subscript SF to indicate quantities in the stellar frame and PRF when referring to the particle rest frame. The relation between the angles in the SF and the PRF is

$$\mu_{\rm PRF} = \frac{\mu_{\rm SF} - \beta}{1 - \beta\mu_{\rm SF}} \,. \tag{5.17}$$

Plugging this into Eq. (5.12) we arrive at the resonant cross section in the stellar frame:

$$\sigma_{1-2} = 3\sigma_{1-1} = \frac{3\pi^2 r_0 c}{2}\delta(\omega - \omega_D)\left(\frac{\mu_{\rm SF} - \beta}{1 - \beta\mu_{\rm SF}}\right) , \tag{5.18a}$$

$$\sigma_{2-2} = 3\sigma_{2-1} = \frac{3\pi^2 r_0 c}{2}\delta(\omega - \omega_D) \,. \tag{5.18b}$$

To solve the integral over β in Eq. (5.7), Fernández and Thompson (2007) have shown that it is possible to re-express the δ-function in $\sigma_{\rm res} = \sum \sigma_{ij}$ in terms of β. The transformation is based on

$$\delta(\omega - \omega_D) = \sum_k \frac{\delta(\beta - \beta_k)}{|\partial\omega_D/\partial\beta|_{\beta_k}} \,, \tag{5.19}$$

where β_k are the two solutions $k = \{1, 2\}$ which satisfy $\omega = \omega_D$

$$\beta_{1,2}(\mathbf{r}, \hat{\mathbf{k}}, \omega) = \frac{1}{(\omega_c/\omega)^2 + \mu_{\rm SF}}\left(\mu_{\rm SF} \pm \frac{\omega_c}{\omega}\sqrt{\left(\frac{\omega_c}{\omega}\right)^2 + \mu_{\rm SF} - 1}\right) . \tag{5.20}$$

The partial derivative of ω_D with respect to β can be obtained from the definition of ω_D (5.16). Substituting the δ-function, the integral is easily solved and the resulting optical depth is given by

$$d\tau_1 = d\tau_{1-1} + d\tau_{1-2} = dl \times 2\pi^2 r_0 c n_Z \frac{1}{\omega_c}\sum_{k=1,2} W^2(1 - \beta_k\mu_{\rm SF})|\mu_{\rm SF} - \beta_k| f_Z(\beta_k, \mathbf{r}) \,, \tag{5.21a}$$

$$d\tau_2 = d\tau_{2-1} + d\tau_{2-2} = dl \times 2\pi^2 r_0 c n_Z \frac{1}{\omega_c}\sum_{k=1,2} W^2 \frac{(1 - \beta_k\mu_{\rm SF})^3}{|\mu_{\rm SF} - \beta_k|} f_Z(\beta_k, \mathbf{r}) \,. \tag{5.21b}$$

Note that if $\omega_B^2/\omega^2 + \mu_{\rm SF} - 1 < 0$, there is no solution for β_k in Eq. (5.20). In this case scattering is not allowed, and the photon can propagate until leaving the magnetosphere or entering the region of allowed scattering again. Fernández and Thompson (2007) showed that the photon escapes if the tangent of the photon path in the $(\omega_B/\omega, \mu_{\rm SF})$-plane at $\omega_B^2/\omega^2 = 1 - \mu_{\rm SF}^2$ lies not between $(\mu_{\rm SF} + 1)/(\omega_B/\omega)$ and $(\mu_{\rm SF} - 1)/(\omega_B/\omega)$.

The treatment presented above makes use of some approximations which require further discussion. First, the photons are assumed to be linearly polarized. This is justified, because under the conditions in major parts of the magnetosphere vacuum polarization

effects dominate over plasma effects (see Fernández and Thompson, 2007).

The second and more limiting assumption is the use of non-relativistic cross sections in the Thompson limit. Nobili et al. (2008a) discuss this issue and argue that for photons with energies of $\sim 1\,\mathrm{keV}$ the resonant magnetic field B_{res} is far below the critical field of QED ($B_{\mathrm{QED}} = 4.4 \times 10^{13}\,\mathrm{G}$). Therefore, in the regime $E_\omega \lesssim 50\,\mathrm{keV}$ the recoil of particles is not important during the absorption if the particles are mildly relativistic, i.e. the Lorentz factor is $W \lesssim 10$. The recoil starts to be dynamically important if the photon energy becomes comparable to the energy of the scattering particle at about $E_\omega \gtrsim 50\,\mathrm{keV} \sim mc^2/W$. We are aware that this is a major limitation of the project in its current stage, and the next step planned is to follow Nobili et al. (2008b) to include a more appropriate description of the cross sections. In particular, for the giant flare whose spectrum peaks at about 10 keV these corrections are important for a quantitative analysis.

5.2 Monte-Carlo radiation transport

For simulating the propagation of photons through an interacting, but not opaque medium Monte-Carlo (MC) techniques are highly appropriate. The process of a single scattering event is probabilistic in the following sense. First, the exact location of the scattering of a single photon can not be obtained deterministically. It is only possible to calculate a probability for the scattering up to a certain point along the photon path. Second, depending on the process the direction of the photon after scattering follows a probability distribution.

To obtain significant statistics of the photons, a large number of photons propagating through the medium of interest has to be simulated. Therefore, in particular in optically thick media, where a large number of scattering events per photon may occur, MC methods can be computationally expensive. Under these conditions algorithms based on the diffusion approximation are usually preferred (Mihalas, 1978). Since we do not expect an optically thick atmosphere for our RCS problem[2], we can make use of MC methods and their advantages: the physics of the desired scattering process is simulated directly, it is possible to keep track of interesting physical quantities, and in principle MC algorithms are easy to implement and easy to be extended by the inclusion of additional scattering processes.

The MC method used to calculate the RCS of photons in magnetar magnetospheres is illustrated in the flowchart of Fig. 5.1. At the beginning of the loop, one specifies the properties of the photon, i.e. the location where the photon is emitted and the direction of propagation of the photon. Additionally, the polarization and energy (or frequency) of the photon are set. The next task is to calculate the differential optical depth Eq. (5.21) at the given location with a chosen travel distance dl. The optical depth is assumed to be

[2]The major part of the scattering is supposed to occur away from the neutron star or the fireball which are optically thick, and photons hitting the stellar surface or the fireball are assumed to be absorbed.

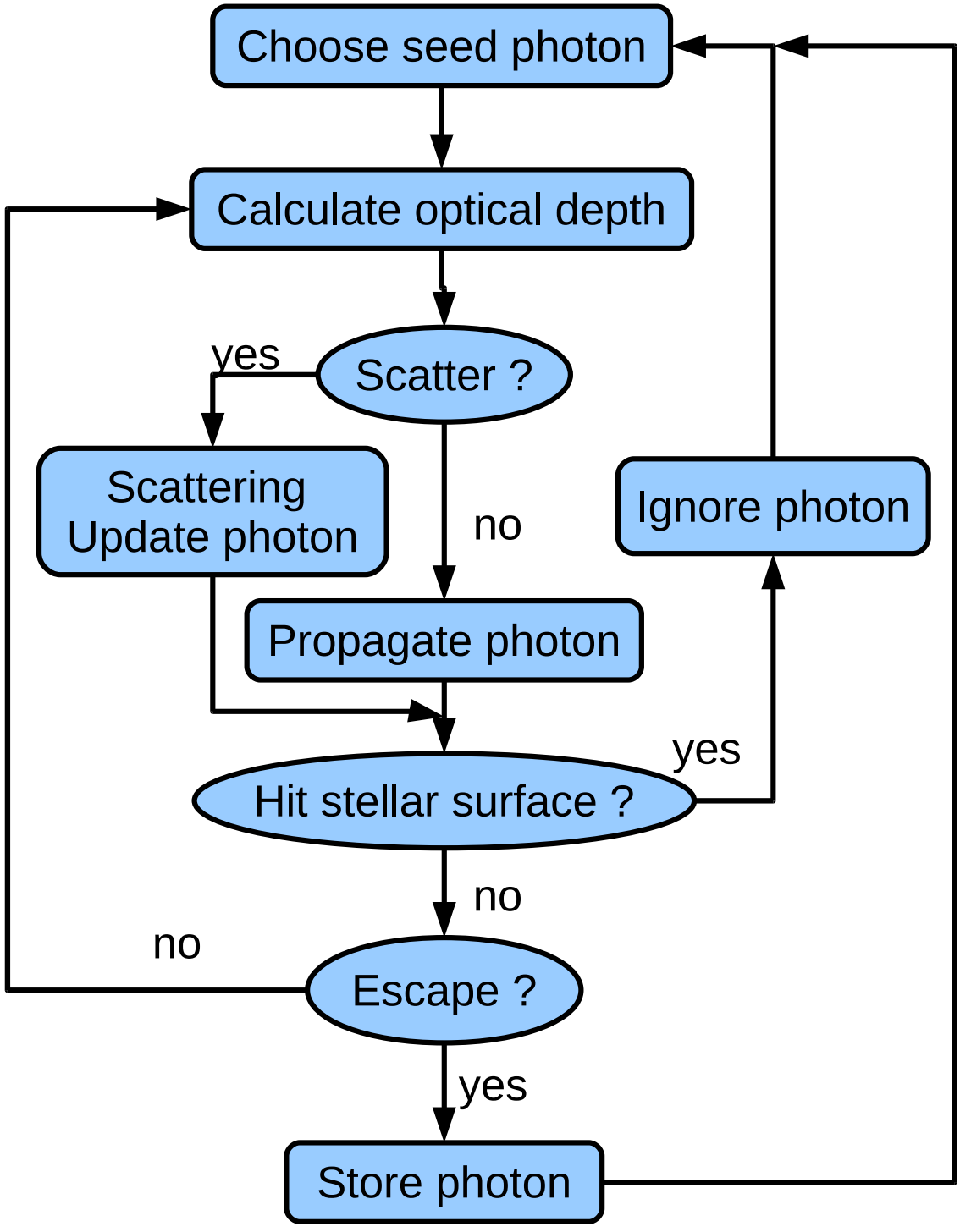

Figure 5.1: Schematic illustration of the implementation of the Monte-Carlo method of RCS in neutron star magnetospheres. Rounded rectangles are operating structures and ellipses represent decision points.

constant along $dl\hat{\mathbf{k}}$, so that dl has to be sufficiently small for an accurate approximation. If the accumulated optical depth along the photon trajectory (see below Eq. 5.22 for details) reaches a given value, determined as a random number at the beginning of the simulated propagation, the photon scatters and the state of the photon is updated. If the photon does not reach the given optical depth, it is propagated forward without scattering. After the photon has been propagated or scattered we check whether it hits the stellar surface or whether it leaves the computational domain. In the former case we ignore the photon, while in the latter case we store the photon and restart the MC scheme with a new one. If none of the two applies, we redo the loop starting with the calculation of the optical depth.

5.2.1 Numerical implementation

For the implementation we closely follow Nobili et al. (2008a) and Fernández and Thompson (2007) with slight deviations. The MC code is based on a spherical coordinate system with logarithmic spacing in radial direction and equidistant grids in θ and φ direction. It is written in the C programming language and OpenMP parallelized. The details of the different steps of the implementation (see previous section) are given in the following.

Properties of seed photons: The properties of the seed photons depend on the particular problem we consider. Therefore, the code is constructed such that we can specify the location, polarization, and the propagation direction of the seed photon arbitrarily. We are also free to specify the particular energy distribution of the seed photons, from which we get the photon frequency by drawing a random number.

Calculation of the differential optical depth: The optical depth is calculated according to Eq. (5.21). The required input here is the number density n_Z of scatterer. This is defined by the currents, and hence the magnetic field configuration. If the obtained optical depth is larger than 10^{-4}, we reduce the spatial distance dl to obtain more accurate results, in particular, near the resonances.

Scattering event: If the accumulated optical depth reaches a previously drawn random number

$$\tau_l = \int_0^l d\tau = -\ln U \,, \tag{5.22}$$

where U is an uniform deviate, the photon is scattered. To solve the integral numerically, we follow Nobili et al. (2008a) and propagate the photon in small steps with length dl (details see below). The accumulated optical depth is simply the sum of the differential optical depths of the different steps $\tau_i = \sum_i d\tau_i$. If we reach $\tau_i \geq \tau_l$ we linearly interpolate between the last two steps.

Specifying a scattering process requires several pieces of information. We have to decide whether the scattering particle has the velocity β_1 or β_2, whether the photon changes polarization, and we have to find the scattering angles after re-emission. The polarization can be randomly chosen by comparing the corresponding fractions of the cross sections and drawing a unit deviate U_1. We switch polarization if $U_1 > \sigma_{1-1}/(\sigma_{1-1}+$

$\sigma_{1-2} = 0.25$ [$U_2 > \sigma_{2-2}/(\sigma_{2-1} + \sigma_{2-2}) = 0.75$] for the mode 1 [2]. The decision in favor of β_1 or β_2 depends on another random number U_2. If $U_2 < d\tau(\beta_1)/[d\tau(\beta_1) + d\tau(\beta_2)]$ the velocity of the scattering particle is β_1, otherwise β_2.

The new propagation direction of the photon with respect to the magnetic field after the scattering is defined by the two angles Θ' and ϕ'. For linearly polarized light ϕ' is arbitrary in the sense that the corresponding distribution is isotropic. Therefore, we chose $\phi' = 2\pi U_3$. In Eqs. (5.15), we have given the angular distribution of the scattering cross section. We thus can chose Θ' for the final polarization state 1 (2) according to $\cos\Theta' = 2U_4 - 1$ ($\cos^3\Theta' = 2U_4 - 1$). Finally, ϕ' and Θ' have to be transformed to the stellar frame.

Due to the Doppler shifts caused by different incident and emergent angles, the frequency of the photon changes according to

$$\omega' = W^2\omega(1 - \beta_k\mu_{\rm SF}^{\rm incident})(1 + \beta_k\mu_{\rm SF}^{\rm emergent}) \tag{5.23}$$

Propagation of photons: We have implemented two different methods for the numerical integration of the photon paths between successive scatterings. The first is for a purely Newtonian background. The photon is propagated by transforming locally to Cartesian coordinates, integrating the three equations $x^i_{\rm new} = x^i_{\rm old} + dl\ \hat{k}^i$ with $i = \{1, 2, 3\}$, and transforming back to spherical coordinates. The second method takes into account the curvature of the spacetime caused by the neutron star. In this case we follow the photons along geodesic trajectories in the Schwarzschild spacetime. The corresponding equations describing the change of position $\mathbf{r}$, frequency ω, and direction $\hat{\mathbf{k}}$, which have to be integrated numerically, are given in Appendix G.

The propagation is stopped when the photon has either reached the defined outer boundary of the numerical domain, or if it enters the region in the $(\omega_B/\omega, \mu_{\rm SF})$-plane where scattering is forbidden and does not re-enter in regions where scattering is allowed again.

Storage of escaped photons: The photons are stored in a 3D array containing information about the two directional angles θ and φ (in the stellar frame) and the photon frequency. If not stated otherwise we chose the number of patches in the $(\theta - \varphi)$-grid to be 10×10 for the output of non-axisymmetric configurations. This means that the patches reach from $\theta = i\,\pi/10$ to $\theta = (i+1)\,\pi/10$ [$\varphi = j\,\pi/5$ to $\varphi = (j+1)\,\pi/5$] with $\{i, j\} = \{0, \ldots, 9\}$, and are labeled by the corresponding center values in degree $\theta = \{9\,^\circ, 27\,^\circ, \ldots, 171\,^\circ\}$ [$\varphi = \{18\,^\circ, 54\,^\circ, \ldots, 342\,^\circ\}$].

5.2.2 Specifying the physical ingredients

In the preceding section we described the numerical implementation of a MC method to simulate the RCS. Intentionally, we did not specify all physical ingredients at this point to have a numerical tool as general as possible. Additionally, several conditions and physical assumptions play a major role for the calculation of RCS spectra. They strongly depend on the model which is used and require further discussion.

Seed photons: The properties of the seed photons depend on the problem to be investigated. For the quiescent emission from the magnetar, the photons originate from any point at the surface. Therefore, we set the initial point by drawing two random numbers $\theta_0 = \pi U_1$ and $\varphi_0 = 2\pi U_2$. For axisymmetric problems we can chose $\varphi = 0$ everywhere. For simplicity we assume radially streaming photons $\hat{\mathbf{k}} = \{\hat{k}^r, \hat{k}^\theta, \hat{k}^\varphi\} = \{1, 0, 0\}$, which can easily be generalized. The spectral distribution is assumed to be black body with a temperature of about $\sim 0.5\,\mathrm{keV}$. It is no problem to change this set up to include hot spots at the surface with different temperatures. These anisotropic heat sources may arise due to particle bombardment at the surface as a consequence of magnetospheric currents or as a consequence of the anisotropic cooling of the neutron star caused by the magnetic field.

In the case of a giant flare, the photons originate from a fireball outside of the star. In the simplest model we pick one point ($r_0 = 20\,\mathrm{km}$, $\theta_0 = \pi/2$, $\varphi_0 = 0$) and let the photons start from there isotropically ($\{\hat{k}^r, \hat{k}^\theta, \hat{k}^\varphi\} = \{U_1, U_2, U_3\}/\sqrt{U_1^2 + U_2^2 + U_3^2}$). As before we assume a black body spectrum, but here with a temperature of about 10 keV. The fireball is not expected to be a point source, but rather it could be like an extended cloud oriented along the magnetic field lines. Our 3-dimensional MC code can handle any geometry. Unfortunately, there is no reliable prediction of the realistic structure of the fireball. However, the effects we intend to investigate, i.e. the modulation of the X-ray signal, should not depend sensitively on the particular shape of the fireball. The scattering is expected to occur outside of the source, such that the details of the magnetospheric currents and hence the magnetic field are much more important than the shape of the fireball.

We do not prescribe any particular form of the polarization. By performing two simulations each with the seed photons in one of the two polarization states, we can generate the results corresponding to any seed polarization by superposition.

Scattering targets: The spatial distribution of the plasma in the magnetosphere is given by the currents caused by the twisted magnetic field. In the simplest case the minimal charge number density required by the magnetospheric currents is given by

$$n_Z = \frac{J}{Zec}\,, \tag{5.24}$$

This minimal charge density is what we assume during this work as a lower estimate for n_Z. Moreover, we neglect the contributions from the ions to the plasma in the magnetosphere and consider only electrons and positrons. We thus have $Z = \pm 1$ and $m = m_e$ in all equations of the current chapter. The neglect of the ion contribution is reasonable, because the magnetic field at resonance is proportional to the mass (see Eq. (5.1)), i.e. at the given photon energies much stronger fields are necessary to scatter resonantly off the ions. Moreover, the cross section is indirectly proportional to the mass (see Eq. (5.18), i.e. it is reduced by three orders of magnitude for ions compared to electrons.

Momentum distribution of charge carriers: Another physical quantity related to the

model	$kT_{\rm bb}$	T_e	$\beta_{\rm bulk}$	B	$\Delta\Phi$
$\mathrm{SS}_{1.0}$	0.5 keV	30 keV	0.3	10^{14} G	1.0
SS_{x}	0.5 keV	30 keV	0.3	10^{14} G	x

Table 5.1: Specifications of the models for radiative transfer in the magnetosphere. $T_{\rm bb}$ is the black body temperature of the emerging radiation from the stellar surface, T_e is the thermal temperature of the electrons of the current, and $\beta_{\rm bulk}$ is their bulk velocity.

charge carriers is their momentum distribution. Up to date there has been no self-consistent calculation of the currents in a twisted magnetosphere. Beloborodov (2009) started work in this direction, but the results are not yet applicable. Therefore, a follow-up project of the current work will be concerned with the question of how these currents can be calculated more realistically. For the time being we consider electrons as the only charge carriers, and we use an ad-hoc momentum distribution which is an one-dimensional relativistic Maxwellian distribution superimposed to a bulk motion, as given by Nobili et al. (2008a):

$$f_e(\beta, \mathrm{r}) = \frac{\exp(-WW_{\rm bulk}(1-\beta\beta_{\rm bulk})/\Theta_e}{2K_1(1/\Theta_e)}\,. \tag{5.25}$$

Here $W_{\rm bulk}$ and $\beta_{\rm bulk}$ are the Lorentz factor and the velocity of the bulk motion, respectively. $\Theta_e := kT_e/m_ec^2$, and K_1 is the modified Bessel function of second kind of order 1. This model distribution has two free parameters: the velocity of the bulk motion $\beta_{\rm bulk}$, and the thermal temperature T_e of the electrons.

5.3 Monte-Carlo radiation transport for self-similar magnetic field configurations

We test our implementation of the RCS Monte Carlo algorithm by reproducing some results published by Nobili et al. (2008a). Therefore, we use the self-similar configuration given in the preceding chapter with a total twist angle of $\Delta\Phi = 1.0$. The parameters of the model are given in Table 5.1. The photons are assumed to stream radially away from the surface of the neutron star, and they are unpolarized, i.e. the polarization of each photon is determined by a random number in the beginning. The photons are emitted at an arbitrary location at the surface, and for storing the photon data we use 200 logarithmic spaced energy bins between 10 eV and 1 MeV. If not stated otherwise, we use an ensemble of $N = 10^7$ photons, a small fraction of which is always absorbed at the stellar surface. The number of numerical grid zones is 100×80 $(r \times \theta)$ in the range $[r_{\rm s}, 500\,\mathrm{km}] \times [0, \pi]$. Because of axisymmetry we are able to follow the photons on their trajectories in φ-direction by evaluating the required quantities at $\varphi = 0$

To get an estimate of the scattering probability we first integrate along a number of

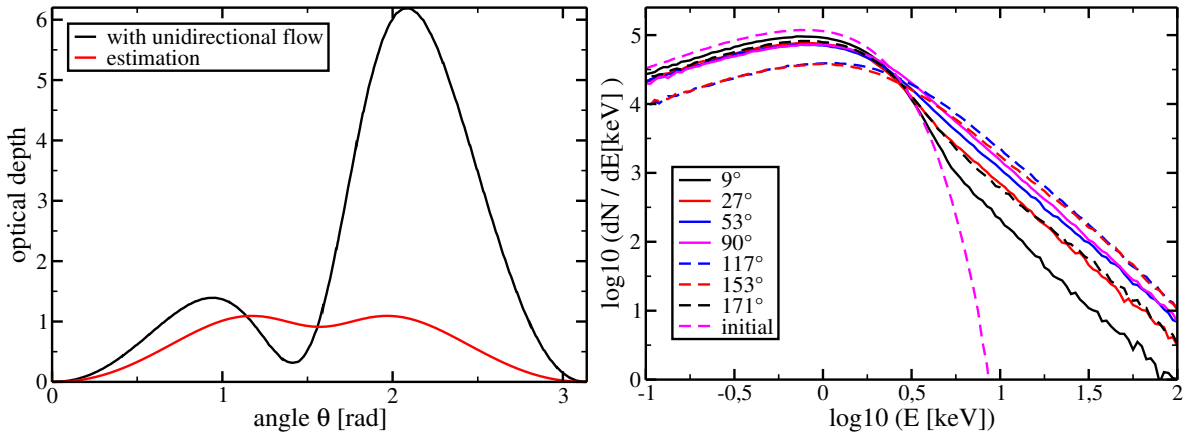

Figure 5.2: *Left panel*: Integrated optical depth for model $SS_{1.0}$. There is a clear asymmetry between the two hemispheres due to the unidirectional momentum distribution assumed for the current. The optical depth is of order unity or larger, such that one expects a large fraction of the photons to be scattered at least once. The black line is given by the integration of the differential optical depth corresponding to Eq. (5.21), and the red line represents the estimate of Eq. (5.26). *Right panel*: Spectrum of model $SS_{1.0}$ for different viewing angles with respect to the magnetic axis. The dashed magenta line represents the unscattered spectrum.

sample photon paths until reaching the outer grid boundary. In the left panel of Fig. 5.2 we give the integrated optical depth of model $SS_{1.0}$ as the black line. There is a clear asymmetry between the two hemispheres which is caused by the particular choice of the momentum distribution Eq. (5.25). For only one type of charge carriers (electrons), the direction of the current is outgoing on one side and incoming on the other. Because of the Doppler shift appearing in the resonance condition (5.16) and the particular form of the momentum distribution, there are more scatter targets with the required velocity β_k available in the case of incoming current. Consequently, we expect this north-south asymmetry to manifest itself also in the spectra calculated below. For the self-similar configuration the optical depth can be estimated if the resonant surface is close to the surface of the neutron star (see Viganò et al., 2011):

$$\tau(\theta) = \pi^2 \frac{J}{c} \left(1 + \frac{B_r^2}{B^2}\right) \left|\frac{dB}{dr}\right|^{-1} . \tag{5.26}$$

This estimate is represented by the red line in Fig. 5.2. It is of the same order of magnitude as our result obtained by integrating the differential optical depth. However, the estimate is too low, in particular, for the hemisphere where the current is directed towards the neutron star. Generally we can say that the optical depths reached in the model are of the order of unity or larger. Thus, we expect a large fraction of the photons emitted at the stellar surface to get scattered at least once.

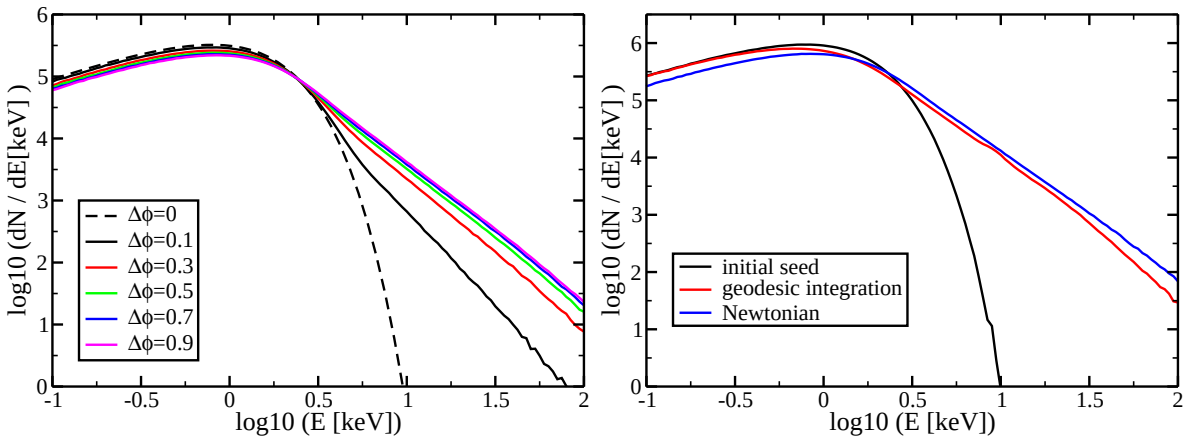

Figure 5.3: *Left panel*: Spectra of models SS_x with the total twist angles $\Delta\Phi$ given in the legend. The spectra are averaged over all directions. The dashed line gives the unscattered spectrum of the seed photons in form of a Planck law with temperature $kT_{\mathrm{bb}} = 0.5\,\mathrm{keV}$. *Right panel*: Comparison of the spectra obtained in the Newtonian framework and by integrating the photon paths along geodesics in the Schwarzschild spacetime of model $\mathrm{SS}_{1.0}$ with the same seed photon distribution. The inclusion of the gravitational redshift of the photons makes the spectrum peak at lower photon energy. Furthermore, the slope at higher photon energies is slightly steeper when integrating the photon paths along geodesics.

The right panel of Fig. 5.2 displays the spectrum obtained with our code for model $\mathrm{SS}_{1.0}$ for different viewing angles with respect to the magnetic axis. The simulation used a total of 10^7 photons. The φ-dependence is averaged out due to axisymmetry of the problem. The asymmetry between the two hemispheres shows up in the results as expected, i.e. the spectra at larger viewing angles have a stronger up-scattered contribution than those for smaller angles (compare the spectra for 9° and 171°).

The influence of the twist angle, and hence of the plasma density which is related to the magnitude of the current, on the spectrum is shown in the left panel of Fig. 5.3. As above we use 10^7 photons and average over all angles φ, but additionally we also average over all angles θ to obtain better statistics. The dashed line represents the unscattered spectrum of a black body with a temperature $kT_{\mathrm{bb}} = 0.5\,\mathrm{keV}$. The up-scattered part of the spectrum increases with increasing twist angle $\Delta\Phi$ almost linearly. This is expected, because for small twists the current density and hence the number of the scattering targets increases linearly with the twist angle. For a more thorough discussion of these examples, including the (small) influence of polarization effects, we refer to Nobili et al. (2008a). Our code is able to reproduce their results qualitatively, as shown above for selected examples. The only significant point at which our results differ from those in Nobili et al. (2008a) is that they find a much weaker scattered contribution to the spectrum for $\Delta\Phi = 0.3$. The almost linear dependence we observe in Fig. 5.3 encourages us to assume that our results are correct and, because the other

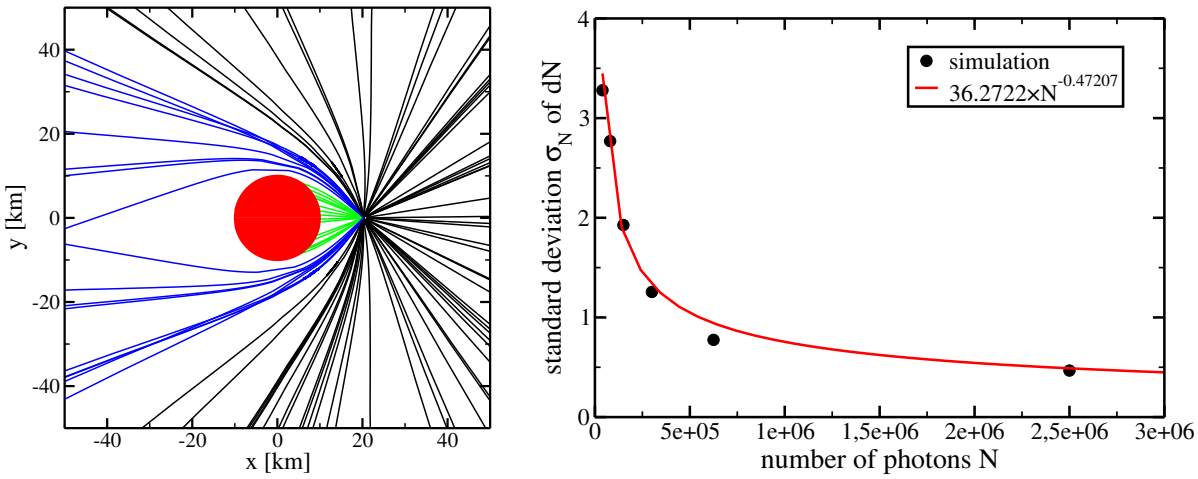

Figure 5.4: *Left panel*: Photon trajectories in the Schwarzschild spacetime originating at $r = 20\,\mathrm{km}$ and $\theta = \pi/2$. Green lines hit the stellar surface, blue lines deviate significantly from straight lines due to gravitational light bending caused by the neutron star, and black lines are less affected. The red disc indicates the neutron star. *Right panel*: The dependence of the standard deviation σ_N defined in Eq. (5.27) on the number of photons N for model $\mathrm{SS}_{1.0}$. The black dots are the results of numerical simulations, and the red line is a fit as given in the legend.

results agree qualitatively, we assume that there is a simple error in the labels of Nobili et al. (2008a).

Up to now we have presented the results of the RCS in a purely Newtonian framework. However, the gravity near the neutron star may have an influence of the order of 20% on various quantities. The most relevant effect here is the gravitational redshift of the frequency of the photons according to Eq. (G.11) when they leave the gravitational potential of the neutron star. Additionally, the photon trajectories in general are no straight lines but geodesics, as can be seen in the left panel of Fig. 5.4. The difference vanishes for radially streaming photons. However, for scattered photons or photons emitted by a fireball outside the neutron star towards the surface, the geodesics can differ significantly from straight lines (see, in particular, the blue lines in the left panel of Fig. 5.4). This may change the spectrum, in particular, on the side of the neutron star opposite to the fireball, where in the Newtonian framework only scattered photons would appear.

The difference in the spectrum between purely Newtonian photon paths and curved paths along geodesics can be seen in the right panel of Fig. 5.3. There we give the spectra of 10^7 photons obtained with both methods for the same model $\mathrm{SS}_{1.0}$. The main effect is the redshift of the maximum of the photon distribution of the GR calculation (red line) compared to the Newtonian one (blue line). Additionally, the slope at high photon energies is slightly steeper in the GR version.

The integration along geodesics is very time consuming. The main effect, i.e. redshift-

ing of the photon frequencies, could be included into a Newtonian treatment to speed up the computations. This should be sufficiently accurate for the quiescent emission, where one can assume radially streaming seed photons. However, it is not sure at this point how large the influence of the light bending on the spectra may be for the problem of a giant flare. Therefore, we keep the full geodesic integration as our standard method.

Convergence

For the analysis of the convergence properties of the code we take the self-similar model with $B = 10^{14}\,\mathrm{G}$ and $\Delta\Phi = 1.0$. We perform a series of simulations with different numbers of photons: $N = \{4\times10^4, 8\times10^4, 1.5\times10^5, 3\times10^5, 6.25\times10^5, 2.5\times10^6, 10^7\}$. The result for the simulation with $N = N_{\mathrm{ref}} := 10^7$ is used as reference solution.

For the analysis we use the standard deviation of the spectrum $u(\omega)$, which we define as

$$\sigma_N = \sqrt{\frac{1}{200}\sum_{i=\{1..200\}}\left(\frac{u_N^i}{N} - \frac{u_{\mathrm{ref}}^i}{N_{\mathrm{ref}}}\right)^2}\,, \tag{5.27}$$

where the factor 200 arises from the 200 energy bins in the energy range $E = 10\ldots10^6\,\mathrm{eV}$, u_N^i is the number of photons in the energy bin number i for the run with N photons, and u_{ref}^i is the corresponding number for the reference solution with $N_{\mathrm{ref}} = 10^7$. We have to renormalize these u_N^i and u_{ref}^i to the total number of photons of the corresponding simulation to get comparable numbers for the different runs. With the results for different N we are able to obtain a relation between σ_N and N as given in the right panel of Fig. 5.4. The fitted red line gives a proportionality $\sigma_N = \sigma_N(N) \sim N^{-0.47}$ and thus agrees well with the expected behavior of the convergence of the Monte Carlo method of $\sigma_N \sim N^{-1/2}$.

5.4 Modulated X-ray emission from magnetars

In this section we apply our MC code to the conditions of the quiescent state of a SGR whose exterior magnetic field is modulated by the magneto-elastic oscillations of the star. Therefore, we take an evolution of a particular model described in Chapter 3, construct the quasi-statically evolution of the magnetic field in the magnetosphere according to Chapter 4, and finally, calculate the corresponding spectrum which is changed by RCS as given in the preceding subsections of this chapter.

For the results presented here we select the model APR+DH 1.4 with a magnetic field strength $B = 3\times10^{15}\,\mathrm{G}$. This choice is motivated by the fact that the magneto-elastic QPOs of the stellar interior reach the surface with significant amplitudes at this magnetic field strength, and the QPOs at the surface can be clearly identified (see Fig. 3.18). Moreover, a magnetic field strength of $B = 3\times10^{15}\,\mathrm{G}$ is only slightly stronger than current estimates of the magnetar field strengths which give $B \lesssim 2\times10^{15}\,\mathrm{G}$. The

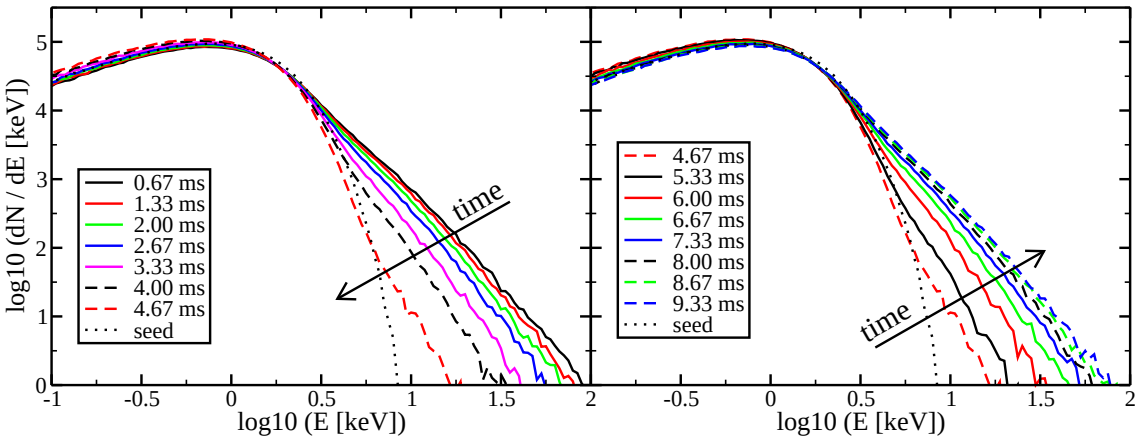

Figure 5.5: Spectra at selected times during the early evolution corresponding to the magnetic field configurations in Fig. 4.4. The fraction of the up-scattered photons decreases with decreasing toroidal magnetic field during the first 4.67 ms (*left panel*). At later times the toroidal field increases and leads to an enhanced scattering (*right panel*). The dashed line gives the unscattered spectrum of the seed photons emitted by the stellar surface. The spectra are angle averaged over θ and φ.

frequencies of the corresponding magneto-elastic QPOs reaching the surface are 13.5, 17.5, 29.4, 44.1, 58.8, and 75.0 Hz (see Table 3.6 and Fig. 3.18). However, we do not expect to see the oscillations occurring at 29.4 and 58.8 Hz, because these oscillations have antisymmetric magnetic field structure, and thus are excluded in our model.

Our simulations of the interior have been performed in the linear approximation for the perturbations. Keeping all quantities linear, we are allowed to rescale our data to any desired amplitude without changing the qualitative results. To obtain significant twists in the magnetosphere, we rescale the toroidal magnetic field at the surface to $B \sim 10^{13}$ G, which is one hundredth of the poloidal surface magnetic field strength. This toroidal magnetic field corresponds to a maximum amplitude of the displacement at the surface of ~ 100 m. The simulation covered about 0.67 s, and the total number of photons used in the MC calculation was 10^6.

In Fig. 5.5 we show the spectra obtained during the first 10 ms corresponding to the magnetic field configurations in Fig. 4.4. The spectrum is angle averaged over θ and φ to improve the statistics. The angular dependence of the X-ray signal is discussed below. We can follow the oscillation of the neutron star which shows up as a change of amplitude of the up-scattered part of the spectrum at high photon energies $E \gtrsim 10$ keV. The chosen perturbation causes strong scattering at $t = 0.67$ ms, which then decreases gradually due to the decreasing magnetic field strength (compare with Fig. 4.4). The minimum scattering occurs at $t = 4.67$ ms, and directly afterward the scattering increases again (right panel of Fig. 5.5). This modulation of the X-ray signal continues as long as the oscillations of the magnetic field last.

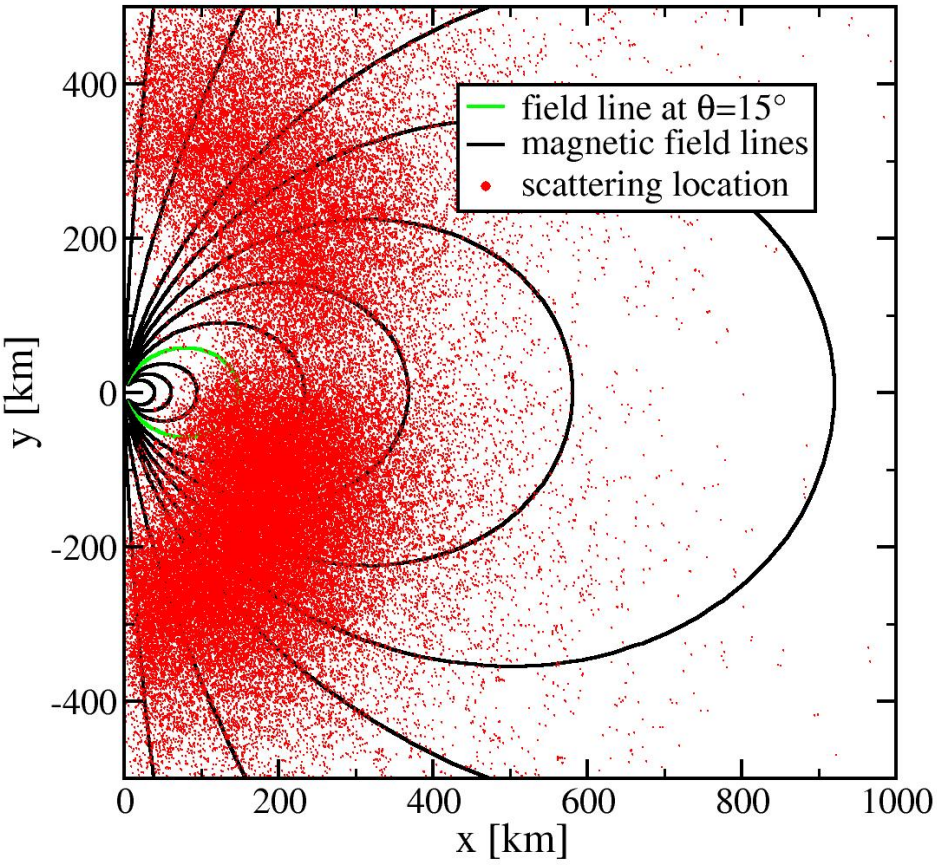

Figure 5.6: Locations of the scatterings at $t = 0.67\,\mathrm{ms}$ for model APR+DH 1.4 with $B = 3 \times 10^{15}\,\mathrm{G}$. Black lines indicate magnetic field lines, the green line gives the field line entering the star at $\theta \sim 15°$, and the red dots indicate the scattering locations.

In order to check our assumption that the scattering occurs at $r \leq 1000\,\mathrm{km}$ we plot exemplary the locations of about 10^5 scattering events in Fig. 5.6 at $t = 0.67\,\mathrm{ms}$. The majority of the scattering occurs at radii $< 500\,\mathrm{km}$, i.e. our assumption is valid, and this part of the magnetosphere can be evolved quasi-statically[3]. In the case of a giant flare the scattering is expected to occur at even smaller radii (see Eq. (5.4) for particles at rest), i.e. our model should work properly for this scenario, too.

The distribution of the scattering events in Fig. 5.6 concentrates around the magnetic field lines outside the green line which enters the neutron star at $\theta \sim 15°$. Therefore, the properties of the scattering are mainly determined by the currents, and hence by the polar toroidal surface magnetic field ($0° \leq \theta \leq 15°$). In the current example we have assumed a current regarding only electrons having the momentum distribution given in Eq. (5.25). We can see the effect of the asymmetric current, which leads to an enhanced scattering in the southern hemisphere. In a more realistic scenario we expect electron-

[3]Remember that the dynamical time scale for this region of the magnetosphere is much smaller than the time scale of the QPOs: $t_{\mathrm{magnetosphere}} \sim 500\,\mathrm{km}/c \sim 1\,\mathrm{ms} << 50\,\mathrm{ms} = 1/f_{\mathrm{QPO}} = t_{\mathrm{QPO}}$

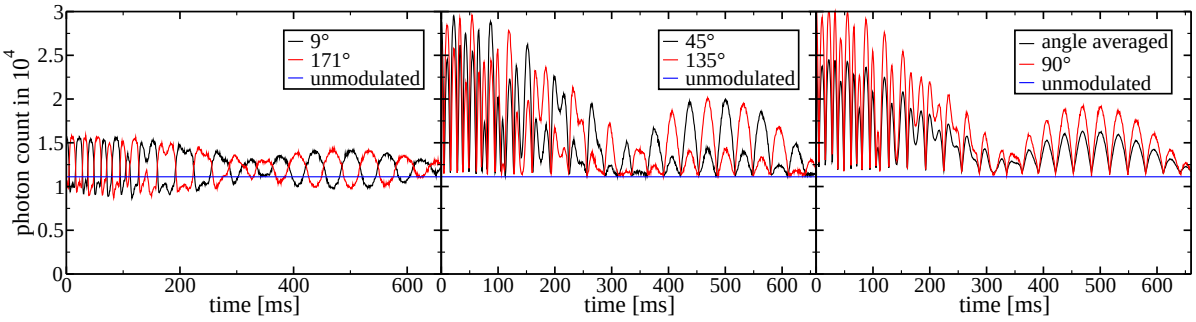

Figure 5.7: Light curves for model APR+DH 1.4 at $B = 3 \times 10^{15}$ G with a toroidal component $B_\varphi \sim 10^{13}$ G for different viewing angles θ in the energy band E= $2 \ldots 80$ keV. The different panels show the light curves for different viewing angles: left panel ($\theta = 9°$ and $\theta = 171°$), middle panel ($\theta = 45°$ and $\theta = 135°$), and right panel ($\theta = 90°$). The right panel further contains the photon counts angle averaged over θ (black line). The blue line gives the amplitude of the unmodulated radiation.

positron pairs to be created (Thompson et al., 2002; Beloborodov and Thompson, 2007) such that the current will be formed by e^+ and e^- streaming in opposite directions.

To produce a synthetic light curve of a SGR in a given energy band, we calculate the spectra (10^6 photons) at intervals of 0.67 ms during the evolution and integrate the photon number in the energy band $2\,\text{keV} \leq E \leq 80\,\text{keV}$, because the QPOs in giant flares are observed in this band (Israel et al., 2005) or a neighboring one with $E = 4 \ldots 90$ keV (Strohmayer and Watts, 2006). We are aware that this approach does not take into account the response function of the measuring instrument and that the results cannot directly be compared with actual observations. However, at this stage of the project other uncertainties in the model, like the momentum distribution of the currents, outweigh the inaccuracies introduced by not considering a realistic instrument response for the incoming signal. Additionally, our main interest is to explain an absolute change in the amplitude of the signal in a given energy band, but not in a single energy bin. Therefore, we believe that the modulation of the integrated signal can be calculated even without knowing the detailed properties of the measuring instrument.

The light curves of our reference model for different viewing angles θ are given in Fig. 5.7. We can identify the oscillation pattern of the stellar interior at all angles. The weakest contribution of the modulation to the X-ray signal in the given energy band occurs at angles close to the poles. This can be explained with the decreasing toroidal magnetic field in this region. The weak magnetic field is able to maintain only weak currents, and hence provides only few scattering targets. In the left and middle panel the asymmetry between the northern and the southern hemisphere leads to alternating minima and maxima for 9° and 171° (left panel), and alternating strong maxima and weak maxima for 45° and 135°. At 90° and for the angle-averaged signal we do not see any asymmetry.

The left panel shows that even a partial down-scattering of the photons can happen, if the impact angle before scattering between the current and the photon is in the following configuration. Near the poles the impact angle Θ is close to 0 or π, respectively, i.e the current flows approximately parallel to the photons. If Θ is on average very small, and thus $\mu_{\rm SF}^{\rm incident}$ is large and positive, the third factor in Eq. (5.23) is small. If additionally $\mu_{\rm SF}^{\rm emergent}$ is not preferably large and positive too, the third factor in Eq. (5.23) is much smaller than the fourth one. Consequently, the photon frequency is smaller than the initial one after scattering, i.e. the photon is down-scattered in energy.

To see whether we can recover the frequencies of the magneto-elastic oscillations in a light curve, we Fourier analyze the signal. The Fourier amplitudes for $\theta = \{9°, 45°, 90°\}$, and for the angle-averaged spectrum are given in the left panel of Fig. 5.8. The corresponding curves for $\theta = 171°$ and $\theta = 135°$ are qualitatively similar to the ones for $\theta = 9°$ and $\theta = 45°$, respectively. A Fourier analysis of the evolution of the surface magnetic field confirms the presence of the symmetric oscillations at 13.5, 17.5, 44.1, and 75.0 Hz, which correspond to the two features at frequencies slightly above and below $U_0^{(-)}$, and the two QPOs $U_1^{(-)}$ and $U_2^{(-)}$, respectively (see the second panel in the bottom row of Fig. 3.18 and Table 3.6)[4]. At similar frequencies we find significant Fourier amplitudes at $\theta = 9°$ (red line in the left panel of Fig.5.8), and $\theta = 45°$ (green line). However, at $\theta = 90°$ and in the Fourier amplitude of the angle-averaged spectrum we cannot find these frequencies. The Fourier analysis of the corresponding light curves gives oscillation frequencies at about 26, 35, 60, and 90 Hz, which are also present in the Fourier amplitude of $\theta = 45°$. These frequencies are artefacts of the Fourier transform, and are not related to the antisymmetric QPOs with very similar frequencies, because we have excluded them by their symmetry.

To explain this effect, we Fourier analyze the following periodic functions

$$f_1(x) = \sin x\,, \tag{5.28}$$

$$f_2(x) = |\sin x|\,, \tag{5.29}$$

$$f_3(x) = 1 + \sin x\,. \tag{5.30}$$

The Fourier amplitude of f_1 (right panel of Fig. 5.8) gives the expected single frequency $1/2\pi\,\text{Hz} \sim 0.16\,\text{Hz}$. f_2 has half the period of f_1, i.e. one would expect a doubling of the frequency to 0.32 Hz, which is indeed observed. However, we also find overtones at 0.64 Hz, 0.96 Hz, etc. , too. Evidently, the trigonometric functions are not an appropriate basis to analyze this kind of signal, i.e. functions with a discontinuous first derivative at the nodes. The function f_2 can only be approximated by an infinite sum over all overtones of the fundamental, and all the corresponding frequencies show up in the Fourier amplitude. When analyzing a function which is always positive and has continuous first derivative by construction, e.g. function f_3, the Fourier transform works without any problem and gives the single frequency 0.16 Hz.

[4]Note that a symmetric magnetic field implies antisymmetric velocity, which is analyzed in Chapter 3 and used to determine the symmetry of the modes

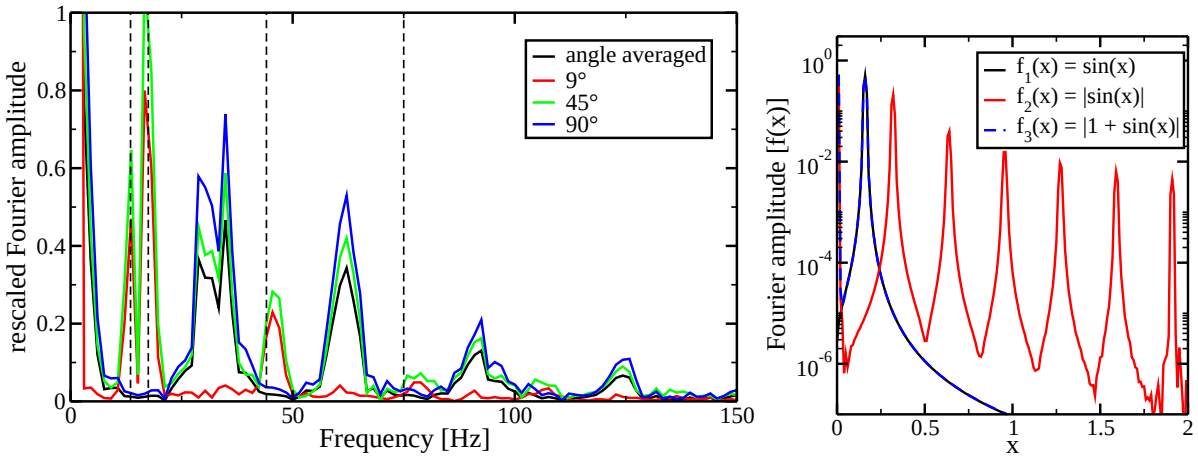

Figure 5.8: *Left panel*: Fourier amplitude of light curves obtained at different viewing angles θ, and for the spectrum averaged over angle θ. Black dashed lines indicate the frequencies of antisymmetric oscillations at the neutron star surface at 13.5, 17.5, 44.1, and 75.0 Hz, respectively (see second panel in bottom row of Fig. 3.18, and Table 3.6). *Right panel*: Fourier transform of the functions $f(x)$ indicated in the inset. The black and the blue line lie on top of each other.

The connection between the absolute value of the sine in f_2 and our simulations of the scattering becomes apparent when studying the angle-averaged spectrum, where no asymmetries are present. The stronger the absolute value of the toroidal field is in the magnetosphere, the stronger are the currents, and hence the more photons get scattered: $N_{\text{scattering events}} \sim |I| \sim |B_\varphi|$. For the angle-averaged spectrum it does not matter if the current flows from the northern hemisphere to the southern one, or in the contrary direction. In analogy to the behavior of function f_2, the periodicity of the absolute value of the current is half the period of the surface QPOs. Therefore, we see the maxima in the Fourier amplitude at twice the frequency of the expected QPOs at 26 and 35 Hz. The same is observed for a viewing angle $\theta = 90°$, where the photons travel in the direction orthogonal to the current, and hence their scattering angle does not depend on the direction of the latter, i.e. $\Theta = 90°$. Like in the case of the angle-averaged spectrum, only the absolute value of the current matters for the scattering.

The spectra computed at different angles show different features. For $\theta \neq 90°$ the two phases of the oscillation lead to different currents, because the momentum distribution is assumed to be unidirectional (see Eq. (5.25)). First, the electrons move in one direction and then in the second phase they move in the opposite direction. Therefore, the scattering angle between photons emitted at the stellar surface and the electrons changes, depending on the direction of the current. These different angles lead to different scattering properties, and hence effect the light curves at viewing angles $\theta \neq 90°$ (Fig. 5.7). Near the pole the change in angle is largest. In one phase the photons propagate almost parallel to the current $\Theta \sim 0°$, in the other phase anti parallel $\Theta \sim 180°$.

At viewing angles $\theta = 45°$ and $\theta = 135°$ the angles between photons and electrons are not so large, and hence the difference between the two phases of the current is smaller. However, neighboring maxima in the light curves still have significantly different amplitudes, i.e. a strong maximum alternates with a weak maximum (see, in particular, at late times $t > 300$ the middle panel of Fig. 5.7). The modulation is always positive in the sense that the amplitude of the light curve is always larger than the unmodulated background amplitude. At the equator and for the angle-averaged spectrum the neighboring maxima have comparable amplitudes. The asymmetry in the amplitude of successive maxima allows for the detection of the underlying frequencies at 13.5 and 17.5 Hz at $\theta = 45°$ and $\theta = 135°$. However, the time derivative of the light curve is discontinuous when reaching the unmodulated level of photon counts (blue line in Fig. 5.7). Therefore, the artefacts at 26 and 35 Hz, and the corresponding overtones appear in the Fourier analysis, too. Very close to the pole at $\theta \sim 9°$, these artificial features in the Fourier amplitude disappear completely (red line in the left panel of Fig. 5.8).

The appearance of the frequencies of the overtones would cause a problem for the interpretation of the observed frequencies of the QPOs. The latter are found by Fourier analyzing an observed light curve and thus, if the signal is modulated in the same way as we have described above, the same features should appear. However, there are only weak observational indications for a frequency relation $1 : 2 : 3 : 4 : \ldots$ (Hambaryan et al., 2011). Statistically it is unlikely, but not impossible that the viewing angles for both SGR 1806-20 and SGR 1900+14 are in a narrow range around $\theta \sim 0°$ or $\theta \sim 180°$, where the frequencies of the overtones do not appear. However, we expect e^+-e^- pairs to dominate the current. This current leads to a symmetric pattern of the scattering with respect to the two phases of the oscillation, because the electrons and positrons are flowing in opposite directions, but have the same scattering properties.

There is another possible solution to this problem. Let us consider once again the Fourier amplitudes of the functions f_1 and f_2, but now in addition also that of $f_3 = 1 + \sin\theta$. For the latter function the Fourier amplitude is almost identical to the one for f_1 (right panels of Fig. 5.8). None of the frequencies of the overtones appears, because f_3 is strictly positive and has no discontinuities in its derivatives.

To get a similar effect in our problem of the currents in the magnetosphere, we can add a static twisted magnetic field to the one induced by the magneto-elastic oscillations. Such a twisted field is expected and serves as a common model to explain the observational properties of SGRs after giant flares (Thompson et al., 2002). As the actual form of this static, twisted magnetic field is unknown, we assume a self-similar model with

$$B_\varphi^{\rm surface} = B_\varphi^{\rm QPO} + A_0 \times \sin^3\theta\,, \tag{5.31}$$

where A_0 is the maximum amplitude of the toroidal magnetic field determining the static twist. We performed simulations with different amplitudes A_0 of this static twist. The corresponding amplitudes and angle-averaged light curves are given in the left panel of Fig. 5.9, and the corresponding Fourier amplitudes in the right panel of the same figure. The light curve with the weakest twisted field $A_0 = 10^{13}$ G (black line) is qualitatively

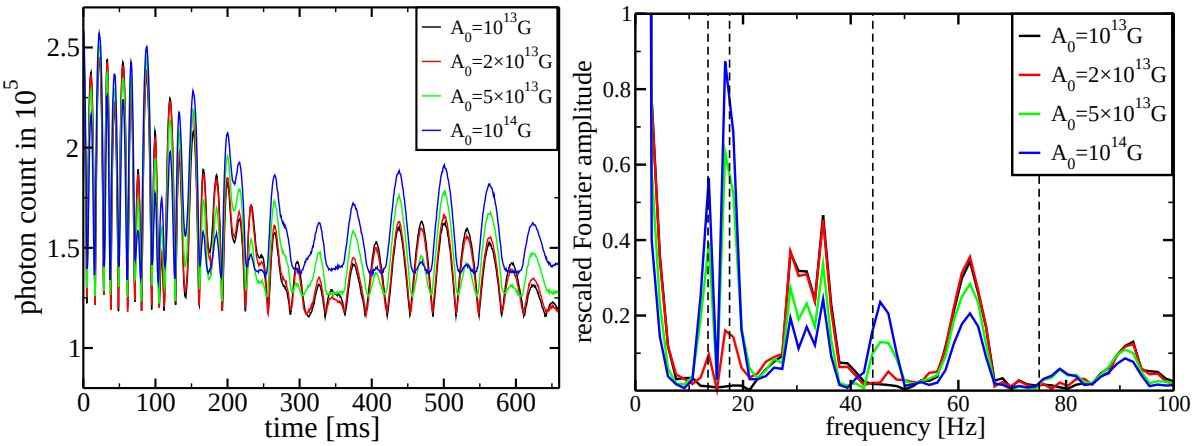

Figure 5.9: *Left panel*: Light curves for different static twists superimposed on the magnetic field caused by the magneto-elastic oscillations of the stellar interior averaged over all angles. *Right panel*: Fourier amplitude of the light curves given in the left panel. Black dashed lines indicate the frequencies of the antisymmetric oscillations at the stellar surface at 13.5, 17.5, 44.1, and 75.0 Hz.

similar to the case without static twist (right panel of Fig. 5.7). In the corresponding Fourier analysis we detect only frequencies at 26, 35, 60, and 90 Hz. When increasing the amplitude of the static twist to $A_0 = 2 \times 10^{13}$ G (red line) we see a significant Fourier amplitude also at 13.5 and 17.5 Hz. At stronger static twisted fields ($A_0 = 5 \times 10^{13}$ G, green line) the amplitudes at both frequencies increase, while those at the other frequencies (26, 35, 60, and 90 Hz) decrease. Additionally, we observe an oscillation at ~ 44.1 Hz. For the strongest twist studied here, $A_0 = 10^{14}$ G, the amplitudes at 13.5, 17.5, and 44.1 Hz increase further, those at 26, 35, 60 and 90 Hz decrease, and we observe an additional oscillation at ~ 80 Hz which may be related to the 75 Hz magneto-elastic QPO.

The inclusion of the static twist improves the significance of the expected signals at 13.5, 17.5, and 44.1 Hz, but very strong twists are necessary. Different functional forms of the static twist may lead to an even better result, but there is no clear physical reason to prefer one configuration over another. Thompson et al. (2002) expect toroidal magnetic field strengths of the order of the poloidal field, i.e. in this case the artefacts of the Fourier analysis probably disappear. Unfortunately, we cannot explore this regime with our methods, which are limited to linear twists.

The light curve in Fig. 5.9 further shows that even for a toroidal magnetic field induced by the magneto-elastic oscillations of the order of 10^{13} G we get a strong modulation of the X-ray signal reaching easily 30% of the total signal strength at $A_0 = 10^{14}$ G[5]. This finding is related to the behavior of the surface magnetic field near the pole. In Fig. 5.6 and in the corresponding discussion we have shown that the most important contribution

[5]This is slightly larger than the variation observed in the giant flare QPOs as given by Strohmayer and Watts (2006), and Watts and Strohmayer (2006)

to the scattering originates from the interaction with the currents leaving the star at polar angles $\theta \lesssim 15°$. Therefore, the toroidal magnetic field in this region is more important for the scattering process than the field closer to the equator. Near the pole the toroidal magnetic field strength of the self-similar model decreases much more rapid than that corresponding to our magneto-elastic oscillations (Fig. 4.5). A different static and twisted magnetic field may have larger amplitudes near to the pole than the self-similar configuration, but with much smaller global maximum amplitude at the surface. Such fields could lead to significant changes in the scattered spectrum as reported by Fernández and Thompson (2007) and Nobili et al. (2008a). Beloborodov (2009) showed that the twist of a model having initially a self-similar configuration for the magnetic field rapidly concentrates in the polar region due to dissipation in the magnetosphere. This is a different process than the one we study in this thesis, but indicates that the region close to the poles is probably more important for the magnetospheric field than the region near the equator.

If the current in the magnetosphere is conducted by electrons and positrons, we cannot solve the problem of observing many overtones in the Fourier analysis by restricting the viewing angle under which we see the radiation emitted by the SGR to values near the poles. When the current changes direction, both e^- and e^+ change their propagation direction, too, and the scattering only depends on the absolute value of the current. However, the explanation of the absence of the frequencies of the overtones in the observations with the presence of the strong, static, and twisted magnetic field is valid in the case of a e^--e^+ pair dominated current, too.

6 Conclusions

This thesis is concerned with the investigation of the origin of quasi-periodic oscillations (QPOs) observed during giant flares of soft gamma-ray repeaters (SGRs). In our model the frequencies are produced by torsional, magneto-elastic oscillations of a highly magnetized neutron star. The QPOs couple to the exterior through the magnetic field and create an additional toroidal component (a twist) of the magnetic field in the magnetosphere. The twisted magnetosphere is penetrated by large scale currents, which provide scattering particles (electrons and positrons) for resonant cyclotron scattering (RCS). The evolution of the interior changes continuously the configuration of the toroidal magnetic field, the corresponding currents, and hence the effectiveness of the scattering. The X-ray radiation emitted from the neutron star is, therefore, modulated by the frequencies of the stellar oscillations.

6.1 Magneto-elastic QPOs

We have presented results obtained from 2-dimensional, general-relativistic, magneto-hydrodynamical simulations of neutron stars with an extended solid crust, in continuation of our initial results communicated as a letter (Gabler et al., 2011). Performing a comprehensive set of simulations for several neutron star models and equation of state (EoS), we have been able to confirm our previous findings regarding the QPO structure for three different regimes of the magnetic field strength. Our main results can be summarized as follows:

For weak magnetic fields, $B \lesssim 5 \times 10^{13}\,\mathrm{G}$, purely shear oscillations of the crust dominate the evolution in the latter. For intermediate magnetic field strengths, $5 \times 10^{13} \lesssim B \lesssim 10^{15}\,\mathrm{G}$, the $n = 0$ crustal modes are damped very efficiently into the core of the neutron star on timescales of a fraction (~ 0.04) of the Alfvén crossing time of the star. For example, a model with $B = 10^{14}\,\mathrm{G}$ has a damping timescale of $\tau < 100\,\mathrm{ms}$. This effectively rules out purely shear oscillations of the crust as a possible explanation for the observed QPOs in SGRs for the poloidal magnetic field configurations studied here, since the observed QPOs survive for tens of seconds at estimated magnetic field strengths $B \gtrsim 6 \times 10^{14}\,\mathrm{G}$. The damping timescale depends on the magnetic field as $\sim B^{-1}$, dominated by the ability of the Alfvén continuum to absorb the energy of crustal modes.

In comparison to the $n = 0$ modes, the $n > 0$ modes of the crust damping have timescales of the order of hundreds of milliseconds at $5 \times 10^{14}\,\mathrm{G}$. The spatial structure of the $n > 1$ modes becomes significantly distorted in the presence of such a strong magnetic

field. Predictions for even stronger magnetic fields, $B > 5 \times 10^{14}\,\mathrm{G}$, are currently not possible, because the grid resolution needed to couple the $n > 0$ shear modes to Alfvén oscillations in the core is too high to perform such simulations in a reasonable time. We thus cannot safely exclude the $n > 0$ crustal shear modes as a possible explanation for the high frequency QPOs observed in SGR 1806-20 at 625 Hz and 1840 Hz, if the magnetic field is a purely dipolar one.

For magnetic fields, $B \gtrsim 5 \times 10^{14}\,\mathrm{G}$, we no discrete crustal shear modes. This is in contrast to the results of van Hoven and Levin (2011), who proposed that weakly damped crustal modes may survive if they lie in-between adjacent continua. In the most promising of our models we find gaps between the first four continua. Even when choosing the equilibrium model such that its fundamental crustal mode frequency falls in one of the existing gaps, the mode was damped very efficiently by the coupling to the Alfvén continuum in the core. Furthermore, we expect that the magnetic field begins to have significant influence on the shear oscillations of the crust at dipolar magnetic field strengths $B \gtrsim 10^{15}\,\mathrm{G}$, necessary to get the frequencies of crustal shear modes into a gap (Messios et al., 2001; Sotani et al., 2008a; Shaisultanov and Eichler, 2009). Our findings strongly support the interpretation that at high magnetic field strengths magnetar oscillations represent a strongly-coupled magneto-elastic system, where a division into purely crustal modes and Alfvén oscillations is no longer valid.

In the intermediate magnetic field regime ($5 \times 10^{13}\,\mathrm{G} \lesssim B \lesssim 10^{15}\,\mathrm{G}$) the QPOs are largely confined to the core of the neutron star. We find three families of QPOs: upper, edge and lower QPOs. Their spatial structure coincides very well with the expectations of our semi-analytic model, if we assume that the oscillations are reflected at the crust-core boundary. Together with the strong damping of the crustal shear modes, the reflection of Alfvén QPOs at the crust-core interface leads to very small oscillation amplitudes in the crust. Moreover, when changing the magnetic field strength, the position of the maximum of the corresponding upper QPO changes significantly within the star due to the interaction with the crust.

We have also determined the dipolar magnetic field strength at which the magneto-elastic QPOs break through the crust and reach the surface with significant amplitudes. This happens around $B \sim 10^{15}\,\mathrm{G}$ for the DH crust EoS (Douchin and Haensel, 2001) and at slightly stronger magnetic fields for the NV crust EoS (Negele and Vautherin, 1973). This difference can be understood, because the NV EoS leads to thicker crusts compared to equilibrium models obtained with the stiffer DH EoS. Additionally, the former EoS has larger shear moduli, in particular, near the crust-core interface.

Between $10^{15}\,\mathrm{G} \lesssim B \lesssim 5 \times 10^{15}\,\mathrm{G}$ the QPOs change from being confined to the core to being able to reach the surface. Their spatial structure is different from that at much lower or much higher magnetic field strengths. Colaiuda and Kokkotas (2011) report global, discrete Alfvén modes in gaps between continua, at magnetic fields around $4 \times 10^{15}\,\mathrm{G}$. In our model, the reported oscillations are not discrete Alfvén modes, but rather an effect of the transition between the two limiting regimes discussed above.

For dipolar magnetic field strengths $B \gtrsim 5 \times 10^{15}\,\mathrm{G}$ the magneto-elastic oscillations

have an almost Alfvén-like character in the whole star. The role of the shear modulus in the crust is diminished, in accordance with the results of Sotani et al. (2008b) and Cerdá-Durán et al. (2009).

We have further investigated the effects of different magnetic field configurations, which are confined to the crust, on the crustal shear modes. This scenario may be realized in the case of type I superconducting protons in the core of the neutron star. For magnetic fields confined to the region of the crust, crustal oscillations cannot be damped into the core. However, the properties of the former purely shear modes of the crust change significantly in the presence of sufficiently strong magnetic fields ($B > 10^{14}\,\mathrm{G}$). In agreement with Sotani et al. (2008a), we find a significant increase of the QPO frequencies for magnetic fields $B \gtrsim 5 \times 10^{14}\,\mathrm{G}$. In addition, the spatial structure of the QPOs is changed by the magnetic field. For very strong fields $B > 10^{15}\,\mathrm{G}$, it is possible to identify features of the magnetic field structure in the spatial distribution of the former shear modes. The structure of the QPOs and the rate of increase of the frequencies with the magnetic field strength depend on the considered magnetic field configuration. This change of frequency of the former crustal shear modes in the presence of a magnetic field confined to the crust makes it very difficult to accommodate the sequence of observed frequencies of the QPOs in SGRs. For the dipolar background configuration it is also very difficult to get the frequencies of the first few QPOs at 18, 26, and 30 Hz, because the frequencies of the former shear modes increase with increasing magnetic field. Moreover, the amplitudes of the Alfvén QPOs are less significant than in the case of magnetic fields penetrating the core. They are thus unlikely to serve as an alternative explanation for the observations. Therefore, magnetic field configurations confined to the crust are less likely to explain the observed QPOs. This result does not depend sensitively on the particular form of the magnetic field in the crust. Our results suggest that magnetic field configurations confined to the crust are unlikely to be realized in magnetars. This might indicate that the protons in the core are either superconducting at most in parts of the core such that the other parts can be penetrated by the magnetic field, or they form a superconductor of type II[1] which allows for the presence of flux tubes.

The model we have presented allows for a tentative interpretation of the observed QPOs in terms of predominantly Alfvén QPOs which reach the surface for magnetic field configurations penetrating the whole star. For dipolar magnetic fields the family of QPOs expected to play an important role in the explanation of the observed QPOs are the upper (turning-point) QPOs. As first pointed out by Sotani et al. (2007), the interpretation of the frequencies 30, 92 and 150 Hz in SGR 1806-20 in terms of the $U_0^{(-)}$, $U_1^{(-)}$ and $U_2^{(-)}$ QPOs is very tempting. Here we note that the 18 Hz oscillation may be interpreted as the first edge QPO $E_0^{(-)}$, which has a frequency of about $0.57 \times f_{U_0^{(-)}} \approx 17\,\mathrm{Hz}$ for the model APR+DH (this could also correspond to the frequency at 16.9 Hz found by Hambaryan et al., 2011). Similarly, the 36.4 Hz oscillation could be interpreted as the $E_1^{(-)}$ QPO. However, one should be cautious with these latter identifications, since edge QPOs are less long-lived than turning-point QPOs.

[1] A superconductor of type II is also theoretically favored (Baym et al., 1969)

If we require that the fundamental upper QPO matches the observed 30 Hz QPO in SGR 1806-20 or the 28 Hz QPO in SGR 1900+14, we obtain dipolar magnetic field strengths of $4.8\times10^{15}\,\mathrm{G}\lesssim B\lesssim 1.4\times10^{16}\,\mathrm{G}$ (for the particular choices of EoS and masses) as reported in Table 3.8. This is a rather narrow range, and it requires only somewhat larger magnetic field strengths than derived from simple estimates for magnetic fields in known magnetars.

We conclude by highlighting that our model provides two constraints on the magnetic field strength. According to the first constraint the dipolar magnetic field strength has to be larger than $B\sim10^{15}\,\mathrm{G}$ for QPOs to break out of the crust, which is a lower limit on the magnetic field. This constraint is independent of a particular identification of observed QPOs and only depends on the assumed purely dipolar magnetic field structure. The second constraint comes from matching the lowest-frequency observed QPO that appears at near-integer multiples with the fundamental $U_0^{(-)}$ QPO. It constrains the dipolar magnetic field strength to be in the range of $4.8\times10^{15}\,\mathrm{G}\lesssim B\lesssim 1.4\times10^{16}\,\mathrm{G}$ for the set of EoSs, and masses that we assumed here.

6.2 Magnetic field configurations in the magnetosphere

To construct the magnetic field in the magnetosphere matched to the results of our simulations of the neutron star interior, we restrict the model to linear perturbations in the toroidal magnetic field. We can chose between two methods: magneto-frictional method (MF) and flux-function reconstruction method (FFR) which both give similar results. Both approaches are compared with analytic solutions in the linear regime and self-similar configurations which can be non-linear in δB_φ. Our results agree well with those models, if the toroidal component of the magnetic field strength does not exceed 10% of the poloidal magnetic field strength. Above this level we underestimate the currents required to maintain the respective magnetic field, because we neglect the inflation of the poloidal field lines due to the strong toroidal field component, i.e. the poloidal field lines, and hence the current flowing along these field lines are expected to extend to larger radii than the ones we consider. Moreover, changing the poloidal field requires toroidal currents which we neglect, too.

When constructing the magnetic field configuration matched to our interior simulations we find complicated structures varying on the time scale of the magneto-elastic oscillations. Depending on the particular form of the surface magnetic field, we find configurations where the toroidal magnetic field changes sign causing currents flowing in opposite directions, and where there are nodes of the magnetic field in angular direction (close to the star). It is not possible to approximate these configurations with a self-similar model.

A very interesting result of this part of the thesis is that force-free magnetic field configurations are only possible in the magnetosphere for dipolar field if the toroidal magnetic field (the displacement) is symmetric (antisymmetric) with respect to the equatorial plane. The antisymmetric configuration would lead to currents in the equatorial plane

which violate the force-free condition. This result supports independently our interpretation of the observed frequencies in the giant flare QPOs in terms of symmetric magneto-elastic QPOs $U_n^{(-)}$, and possibly $E_n^{(-)}$. Note in this respect that we termed the QPOs according to the symmetry of the displacement, which is opposite to the symmetry of the magnetic field.

6.3 Modulation of the X-ray light curve

We showed in Chapter 5 that the resonant cyclotron scattering (RCS) provides an effective source of modulating the X-ray signal of a quiescent SGR. For toroidal fields $\delta B_\varphi = 10^{13}\,\mathrm{G}$ we obtain modulations of the signal at the 30% level. This amplitude is more than sufficient to explain the observed QPOs in SGRs (Israel et al., 2005; Strohmayer and Watts, 2006; Watts and Strohmayer, 2006).

Moreover, we found indications that a large static twist is created at the beginning of a giant flare. We need such a static twist in our model to avoid additional features in the spectrum, which may arise as a consequence of the fact that the photons on average up-scatter in energy independent of the sign of the current. In particular, for e^--e^+ pair dominated currents this causes the frequencies of the magneto-elastic oscillations to appear at twice their value in the Fourier analysis. Additionally, all overtones of these frequencies would appear in the spectrum, a behavior not confirmed by observations. It can be avoided by considering a static twist in addition to the toroidal magnetic field induced by the magneto-elastic oscillations of the star.

To obtain significant scattering in the self-similar models of the magnetic field, large amplitudes of the toroidal magnetic field component are required, i.e. the twist has to be of the order $\Delta\Phi \sim 1.0$ (Fernández and Thompson, 2007; Nobili et al., 2008a), because the toroidal magnetic field strongly decreases with polar angle ($\delta B \sim \sin^3\theta$) for these configurations, and because of the strong dependence of the scattering properties on the toroidal magnetic field near the pole. Configurations with a stronger toroidal magnetic field close to the pole lead to significant scattering even with much smaller global maximum of the magnetic field strength. As there is no physical reason to prefer the self-similar models to other configurations, the required twist, i.e. the amplitude of the twisted magnetic field at the stellar surface, is probably overestimated in these models.

The results presented here are valid for the quiescent state of the SGRs. For the giant flare scenario it is necessary to perform additional simulations with a much larger photon number (in the Monte-Carlo method), because if the photon source is not spherically symmetric, like the neutron star surface, the spectrum not only depends on the viewing angle θ, but also on φ. Furthermore, additional physics has to be included to describe the scattering of high energy photons appropriately, which is very important in the case of the giant flare. In this scenario a fireball is produced with a black body temperature of $T_{\mathrm{bb}} \sim 10\,\mathrm{keV}$.

Nevertheless, we have shown that RCS is a possible mechanism to explain the modulation of a X-ray signal for realistic, i.e. linear, amplitudes of the perturbation at the

surface for the quiescent emission of SGRs. Thus, RCS is also a very promising mechanism to modulate the emission occurring during a giant flare, which however requires further investigations.

6.4 Outlook

The constraints we found as a consequence of interpreting observed QPO as magneto-elastic QPO of magnetars, favor somewhat stronger magnetic fields than estimated for known magnetars. This could be a hint that the actual magnetic field structure of SGRs deviates from a global dipole, which would not be too surprising, as it is known that a purely dipolar or purely toroidal field is not a stable magnetic field configuration in compact stars (see Braithwaite and Nordlund, 2006; Lasky et al., 2011; Ciolfi et al., 2011; Kiuchi et al., 2011, and references therein). We may thus have an observational indication that the structure of the magnetic field in magnetars is in fact more complicated than a pure dipole. Alternatively, other physical effects like superfluidity of the neutrons and superconductivity of the protons in the core could also change the properties of the Alfvén oscillations in the core leading to lower estimates for the magnetic field strength required to match the magneto-elastic QPOs to the range of observed frequencies. These two physical effects are expected to influence the Alfvén speeds and the overall dynamics (Passamonti and Andersson, 2011).

We are planning to investigate the effects of different magnetic field configurations, and those caused by superfluidity and superconductivity of the neutrons and protons in the core. For the former, we need to investigate mixed poloidal-toroidal configurations, relax the assumption of axisymmetry and include the coupling to polar oscillations. For a description of the effects of superfluidity and superconductivity, we need to change our code to include the interaction between the different fluids (superfluid neutrons and superconducting protons). However, first estimates of the influence of the superconductivity can be obtained by assuming a single superconducting fluid, i.e. by neglecting the different properties of superconducting protons and superfluid neutrons, and by neglecting the decoupling of the neutrons from the protons due to their superfluidity.

Concerning the calculation of RCS in the magnetosphere the next step would be to replace the non-relativistic cross sections in the Thompson limit by the expressions given in Nobili et al. (2008b). When these more general cross sections are included, the scattering in the magnetosphere can be described consistently if the current distribution is provided. Moreover, we plan to refine our model by including a self-consistent micro-physical calculation of the currents flowing in the magnetosphere. This is necessary, in particular, in the case of the giant flares, where there may be feedback of the intense X-ray radiation on the currents. To cope with the very large number of photons necessary for fully three-dimensional simulations of the giant flare scenario, we plan to use the power of graphics processing units (GPUs) and to rewrite the Monte-Carlo code in CUDA (Compute Unified Device Architecture) language.

A Eigenvalues of the elastic GRMHD equations for torsional oscillations

The system of equations (2.86) can be expressed as a complete conservation law corresponding to Eq. (2.37). In this case the definitions of the conserved variables, fluxes, and sources take the following form

$$U = \begin{bmatrix} S_\varphi \\ B^\varphi \\ \alpha\xi_{,r} \\ \alpha\xi_{,\theta} \end{bmatrix} = \begin{bmatrix} (\rho h + b^2)W^2 v_\varphi - \alpha b_\varphi b^0 \\ B^\varphi \\ \alpha\xi_{,r} \\ \alpha\xi_{,\theta} \end{bmatrix} = \begin{bmatrix} (\rho h W^2 + B^r B_r + B^\theta B_\theta) v_\varphi \\ B^\varphi \\ \alpha\xi_{,r} \\ \alpha\xi_{,\theta} \end{bmatrix}, \tag{A.1}$$

$$F^k = \begin{bmatrix} -\frac{b_\varphi B^k}{W} - 2\mu_S s_\varphi{}^k \\ v^i B^k - v^k B^k \\ -v^\varphi \alpha \delta^k{}_r \\ -v^\varphi \alpha\ \delta^k{}_\theta \end{bmatrix}, \tag{A.2}$$

$$S = \begin{bmatrix} 0 \\ 0 \\ v^\varphi \alpha \delta^i_r \frac{1}{\sqrt{-g}} \frac{\partial g_{\mu\nu}}{\partial x^i} \\ v^\varphi \alpha \delta^i_\theta \frac{1}{\sqrt{-g}} \frac{\partial g_{\mu\nu}}{\partial x^i} \end{bmatrix}. \tag{A.3}$$

Here we have applied some simplifications to the general variables introduced in Chapter 2:

$$b^0 = \frac{W}{\alpha} B^\varphi v_\varphi \tag{A.4}$$

$$b^\varphi = \frac{B^\varphi}{W} + B^\varphi v_\varphi v^\varphi W \tag{A.5}$$

$$b^2 = \frac{B^r B_r + B^\theta B_\theta}{W^2} + B^\varphi B_\varphi \tag{A.6}$$

$$\alpha b_\varphi b^0 = g_{\varphi\varphi} W^2 B^\varphi B^\varphi v_\varphi \tag{A.7}$$

These expressions are a consequence of considering exclusively torsional oscillations.

By analyzing the matrices $\partial F^k / \partial U$, $k = \{r, \theta\}$, we can find the eigenvalues in the corresponding direction k by setting the determinants of the following matrices to zero:

$$\left(\frac{\partial F^r}{\partial U} - \lambda I\right) = \begin{bmatrix} -\lambda & -B^r g_{\varphi\varphi} & -\frac{\mu_S}{\alpha}\frac{g_{\varphi\varphi}}{g_{rr}} & 0 \\ -\frac{\partial v^\varphi}{\partial S_\varphi} B^r & -\lambda - \frac{\partial v^\varphi}{\partial B^\varphi} B^r & 0 & 0 \\ -\frac{\partial v^\varphi}{\partial S_\varphi}\alpha & -\frac{\partial v^\varphi}{\partial B^\varphi}\alpha & -\lambda & 0 \\ 0 & 0 & 0 & -\lambda \end{bmatrix}, \tag{A.8a}$$

$$\left(\frac{\partial F^\theta}{\partial U} - \lambda I\right) = \begin{bmatrix} -\lambda & -B^\theta g_{\varphi\varphi} & 0 & -\frac{\mu_S}{\alpha}\frac{g_{\varphi\varphi}}{g_{\theta\theta}} \\ -\frac{\partial v^\varphi}{\partial S_\varphi} B^\theta & -\lambda - \frac{\partial v^\varphi}{\partial B^\varphi} B^\theta & 0 & 0 \\ 0 & 0 & -\lambda & 0 \\ -\frac{\partial v^\varphi}{\partial S_\varphi}\alpha & -\frac{\partial v^\varphi}{\partial B^\varphi}\alpha & 0 & -\lambda \end{bmatrix}. \tag{A.8b}$$

To evaluate the determinants we require explicit expressions for $\frac{\partial v^\varphi}{\partial S_\varphi}$ and $\frac{\partial v^\varphi}{\partial B^\varphi}$. To obtain these, we write down the variable transformation from $U_1 = \{v_\varphi, B^\varphi\}$ to $U_2 = \{S_\varphi, B^\varphi\}$

$$\frac{\partial U_2}{\partial U_1} = \begin{bmatrix} \frac{\partial S_\varphi}{\partial v_\varphi} & \frac{\partial S_\varphi}{\partial B^\varphi} \\ 0 & 1 \end{bmatrix} = \begin{bmatrix} A & 0 \\ 0 & 1 \end{bmatrix}, \tag{A.9}$$

where $A := \rho h W^4(1+v_\varphi v^\varphi) + B^r B_r + B^\theta B_\theta$. The inverse of this matrix gives the required derivatives for the calculation of the eigenvalues of Eqs. (A.8):

$$\frac{\partial U_1}{\partial U_2} = \left(\frac{\partial U_2}{\partial U_1}\right)^{-1} = \begin{bmatrix} \frac{1}{A} & 0 \\ 0 & 1 \end{bmatrix} \tag{A.10}$$

$$\tag{A.11}$$

The explicit relations are thus $\frac{\partial v^\varphi}{\partial S_\varphi} = \frac{1}{g_{\varphi\varphi} A}$ and $\frac{\partial v^\varphi}{\partial B^\varphi} = 0$. The eigenvalues in r- and θ-direction are calculated by setting the determinants of the two matrices in Eqs. (A.8) to zero

$$det\left|\frac{\partial F^k}{\partial U} - \lambda I\right| = 0\,. \tag{A.12}$$

Finally, we get the eigenvalues:

$$\lambda^k_{1/2} = \sqrt{\frac{(B^k)^2 + \mu_S / g_{kk}}{A}} \tag{A.13}$$

B Semi-analytic model for the calculation of the Alfvén continuum

The two-dimensional simulations of the Alfvén oscillations are very time consuming. It is therefore very useful to use a method presented by Cerdá-Durán et al. (2009) which enables us obtain the frequencies of purely magnetic oscillations much more efficiently. In the linear regime and in the limit of short wavelengths it is possible to calculate the Alfvén continuum with a semi-analytic model. Here, we only sketch the method, and for more information we refer to Cerdá-Durán et al. (2009). In the aforementioned limit an Alfvén wave travels along magnetic field lines corresponding to

$$\frac{d\mathbf{x}}{dt} = \mathbf{v}_a(\mathbf{x})\,, \tag{B.1}$$

where $\mathbf{v}_a$ is the Alfvén velocity. Any displacement Y traveling along the magnetic field lines can be expressed as a function of *magnetic-field-line-adapted* coordinates (χ, ζ) and time, where χ labels the magnetic field line by the radius at which it crosses the equatorial plane, and $\zeta = t(r, \theta; \chi)/t_{\rm tot}(\chi) - 1/2$ is a dimensionless parameter along each field line. Here $t_{\rm tot}(\chi)$ is twice the total travel time of an Alfvén wave traveling along a magnetic field line starting from the equatorial plane and ending at the surface or at another point in the equatorial plane. Note that ζ used in this work corresponds to ξ in Cerdá-Durán et al. (2009), because here ξ denotes the displacement related to the 4-velocity of the fluid. For a traveling wave Y satisfies trivially the wave equation

$$\frac{\partial^2 Y(\chi,\zeta,t)}{\partial t^2} = \frac{1}{t_{\rm tot}(\chi)^2}\frac{\partial^2 Y(\chi,\zeta,t)}{\partial \zeta^2}\,. \tag{B.2}$$

Next we assume standing waves of the form

$$Y(\chi,\zeta,t) = a(\chi)\sin(\kappa\zeta + \phi_\zeta)\cos(2\pi f t + \phi_t)\,, \tag{B.3}$$

where κ is the wave number, $a(\chi)$ the amplitude, ϕ_t the temporal phase, ϕ_ζ a spatial phase, and f is the oscillation frequency. The dispersion relation then is simply given by

$$f = \frac{\kappa}{2\pi t_{\rm tot}}\,. \tag{B.4}$$

At this point the frequencies of the oscillations are completely determined by the magnetic field topology and the boundary conditions.

Cerdá-Durán et al. (2009) did not consider an extended crust, and hence the boundary condition was set at the surface and corresponded to the continuous traction condition. This resulted in a vanishing radial derivative of the displacement and a maximum amplitude of the perturbation at the surface. However, when an extended crust is present there exist two different regimes. For low magnetic field strengths ($B \lesssim 10^{15}\,\mathrm{G}$) the standing waves show a node at the crust-core interface (Gabler et al., 2011), which may be interpreted as a reflection of the standing wave at the crust-core interface. As we show below, this change of the boundary condition for the semi-analytic model is necessary to calculate the correct frequencies and to find the symmetry of the numerically obtained QPOs.

For stronger magnetic fields ($B > 10^{15}\,\mathrm{G}$), the oscillations reach the surface, and we can apply the boundary condition of Cerdá-Durán et al. (2009). In order to take the crust into account the velocity of the perturbation can be approximated by the eigenvalues (2.90), assuming that the perturbation Y is still traveling along the magnetic field lines. In an intermediate regime at around $10^{15}\,\mathrm{G}$ we do not expect the semi-analytic model to be valid, because in this case the shear and magnetic contributions to the evolution in the crust are of similar order.

C Linearized wave equation in the crust

In this appendix we derive a wave equation to describe the coupled crust-core oscillations of magnetars. To this end we expand all dynamical variables $f(\mathbf{r},t)$ into a static unperturbed part $\hat{f}(\mathbf{r})$, denoted by a caret, and a time-dependent perturbation $\delta f(\mathbf{r},t)$:

$$f(\mathbf{r},t) = \hat{f}(\mathbf{r}) + \delta f(\mathbf{r},t)\,. \tag{C.1}$$

For clarity we will omit the arguments $\mathbf{r}$ and t from now on.

In the subsequent subsections we derive the equation for the displacement, describe the numerical implementation and compare the performance of this alternative method with the standard approach using Riemann solvers on both sides of the crust-core interface.

In this appendix we generally use the notation of semi-colon to denote the co-variant derivative: $t^{\alpha}_{;\mu} := \nabla_\mu t^\alpha$

C.1 Linear wave equation

To derive the linearized wave equation governing the evolution of the displacement in the crust of a magnetized neutron star, we project the conservation equation of energy-momentum

$$h^{\mu}_{\beta} T^{\beta\nu}_{\ \ ;\nu} = 0 \tag{C.2}$$

$$(\rho h + b^2) u^{\mu}_{;\nu} u^\nu = -h^{\mu\nu}\left(P + \frac{1}{2}b^2\right)_{;\nu} + h^{\mu}_{\beta}(b^\beta b^\nu - 2\mu_{\rm S} s^{\beta\nu})_{;\nu}\,, \tag{C.3}$$

with $h^{\mu\nu} = g^{\mu\nu} + u^\mu u^\nu$ and apply the following simplifications: (i) we linearize in the perturbations δf and (ii) neglect all metric perturbations (Cowling approximation, $\delta g = 0$). Then Eq. (C.2) reads

$$\begin{aligned}(\hat{\rho}\hat{h} + \hat{b}^2)\delta u^{\mu}_{;\nu}\hat{u}^\nu = &-\left(\delta\rho\hat{h} + \hat{\rho}\delta h + 2\hat{b}_\beta \delta b^\beta\right)\hat{u}^{\mu}_{;\nu}\hat{u}^\nu - (\hat{\rho}\hat{h} + \hat{b}^2)\hat{u}^{\mu}_{;\nu}\delta u^\nu \\ &+ (\hat{u}^\mu \delta u_\beta + \delta u^\mu \hat{u}_\beta)\left[\hat{b}^\beta\hat{b}^\nu - \hat{g}^{\beta\nu}\left(\hat{P} + \frac{1}{2}\hat{b}^2\right)\right]_{;\nu} \\ &+ \hat{h}^{\mu}_{\beta}\left[\hat{b}^\beta \delta b^\nu + \delta b^\beta \hat{b}^\nu - \hat{g}^{\beta\nu}(\delta P + \hat{b}_\beta \delta b^\beta)\right]_{;\nu} \\ &- 2\hat{h}^{\mu}_{\beta}\left[\delta\mu_{\rm S}\hat{s}^{\beta\nu} + \hat{\mu}_{\rm S}\delta s^{\beta\nu}\right]_{;\nu}\,.\end{aligned} \tag{C.4}$$

Next we restrict ourselves to (iii) axisymmetry ($f_{,\varphi}=0$), and (iv) axial perturbations ($\delta u^t=\delta u^r=\delta u^\theta=0$, $\delta b^r=\delta b^\theta=0$, and $\delta\mu_{\rm S}=\delta h=\delta\rho=\delta P=0$). Furthermore, we consider (v) the spherical symmetric, non-rotating background described by the line element $ds^2=-\hat{\alpha}^2dt+\hat{\Phi}^4(dr^2+r^2d\theta^2+r^2\sin(\theta)^2d\varphi^2)$, and (vi) purely poloidal background fields ($\hat{b}^\varphi=0$). Applying all these simplifications one arrives at the following equation for δu^φ:

$$\begin{aligned}(\hat{\rho}\hat{h}+\hat{b}^2)\hat{u}^t\delta u^\varphi_{,t}=&\hat{b}^r\delta b^\varphi_{,r}+\hat{b}^\theta\delta b^\varphi_{,\theta}-2\hat{\mu}_{\rm S}\delta s^{\varphi\nu(s)}_{\ \ ;\nu}\\&+\delta b^\varphi\left[\left(\frac{2\hat{\Phi}_{,r}}{\hat{\Phi}}+\frac{2}{r}+\frac{\hat{\alpha}_{,r}}{\hat{\alpha}}\right)\hat{b}^r+2\cot(\theta)\hat{b}^\theta\right].\end{aligned}\tag{C.5}$$

Because of the dependence of $\Sigma^{\mu\nu}$ on the displacement ξ^φ, we express all other quantities in terms of the latter. Recalling the definition of the corresponding velocity $\xi^\varphi_{,t}=\delta u^\varphi/\hat{u}^t$, see Eq. (2.83), the perturbed magnetic field δb^φ remains the only missing ingredient.

To find an expression relating δb^φ to ξ^φ, we contract the Faraday equation

$$(u^\mu b^\nu-u^\nu b^\mu)_{;\mu}=0\tag{C.6}$$

with u_ν and obtain

$$u_\nu b^\nu_{\ ;\mu}u^\mu=u^\nu_{\ ;\mu}u_\nu b^\mu-b^\mu_{\ ;\mu}\,,\tag{C.7}$$

where we have used $u_\nu u^\nu=-1$ and $u_\nu b^\nu=0$. From $u_\nu b^\nu_{\ ;\mu}u^\mu=0$ (see Papadopoulos and Esposito, 1982) it follows that

$$b^\mu_{\ ;\mu}=u^\nu_{\ ;\mu}u_\nu b^\mu\,.\tag{C.8}$$

When linearizing Eq. (C.6) and using (C.8) Faraday's equation becomes:

$$\begin{aligned}\hat{u}^\mu\delta b^\nu_{\ ;\mu}=&-\hat{b}^\nu_{\ ;\mu}\delta u^\nu+\hat{h}^{\nu\beta}(\delta u_{\beta;\lambda}\hat{b}^\lambda+\hat{u}_{\beta;\lambda}\delta b^\lambda)+\hat{u}^\nu\delta u^\beta\hat{b}^\lambda\hat{u}_{\beta;\lambda}-\delta u^\mu_{\ ;\mu}\hat{b}^\nu-\hat{u}^\mu_{\ ;\mu}\delta b^\nu\\&+\hat{u}^\nu\hat{b}^\beta(\delta u_{\beta;\lambda}\hat{u}^\lambda+\hat{u}_{\beta;\lambda}\delta u^\lambda)+\hat{u}_{\beta;\lambda}\hat{u}^\lambda(\hat{b}^\beta\delta u^\nu+\delta b^\beta\hat{u}^\nu)\,.\end{aligned}\tag{C.9}$$

Taking the φ-component of this equation, we arrive at a relation between δb^φ and the spatial derivatives of the displacement ξ^φ which reads

$$\begin{aligned}\hat{u}^t\delta b^\varphi_{,t}=&\frac{\hat{\alpha}_{,r}}{\hat{\alpha}}\hat{b}^r\delta u^\varphi+\hat{b}^r\delta u^\varphi_{,r}+\hat{b}^\theta\delta u^\varphi_{,\theta}\\=&\hat{b}^r\hat{u}^t\left(\frac{\hat{\alpha}_{,r}}{\hat{\alpha}}\xi^\varphi_{,t}+\xi^\varphi_{,t,r}\right)+\hat{b}^\theta\hat{u}^t\xi^\varphi_{,t,\theta}+\hat{b}^r\hat{u}^t_{\ ,r}\xi^\varphi_{,t}\,,\end{aligned}\tag{C.10}$$

or

$$\delta b^\varphi_{,t}=\left(\hat{b}^r\xi^\varphi_{,r}+\hat{b}^\theta\xi^\varphi_{,\theta}\right)_{,t}\,,\tag{C.11}$$

where we have used that $\hat{u}^t = \hat{\alpha}^{-1}$. Plugging this relation into Eq. (C.5) we obtain

$$\hat{A}_0 \xi^{\varphi}_{,tt} = \hat{A}_1 \xi^{\varphi}_{,r} + \hat{A}_2 \xi^{\varphi}_{,\theta} + \left(\hat{b}^\theta \hat{b}^\theta + \frac{\hat{\mu}_\mathrm{S}}{r^2 \hat{\Phi}^4} \right) \xi^{\varphi}_{,\theta\theta} + \left(2 \hat{b}^r \hat{b}^\theta \right) \xi^{\varphi}_{,\theta r} + \left(\hat{b}^r \hat{b}^r + \frac{\hat{\mu}_\mathrm{S}}{\hat{\Phi}^4} \right) \xi^{\varphi}_{,rr} \quad \text{(C.12)}$$

with

$$\hat{A}_0 = \left(\hat{\rho} \hat{h} + \hat{b}^2 \right) \hat{\alpha}^{-2} , \quad \text{(C.13)}$$

$$\hat{A}_1 = \hat{A}_3 \hat{b}^r + \hat{b}^r \hat{b}^r_{,r} + \hat{b}^\theta \hat{b}^r_{,\theta} + \left(\frac{\hat{\mu}_\mathrm{S}}{\hat{\Phi}^4} \right)_{,r} + \left(\frac{\hat{\alpha}_{,r}}{\hat{\alpha}} + 10 \frac{\hat{\Phi}_{,r}}{\hat{\Phi}} + \frac{4}{r} \right) \frac{\hat{\mu}_\mathrm{S}}{\hat{\Phi}^4} , \quad \text{(C.14)}$$

$$\hat{A}_2 = \hat{A}_3 \hat{b}^\theta + \hat{b}^r \hat{b}^\theta_{,r} + \hat{b}^\theta \hat{b}^\theta_{,\theta} + \left(\frac{\hat{\mu}_\mathrm{S}}{r^2 \hat{\Phi}^4} \right)_{,\theta} + 3 \cot(\theta) \frac{\hat{\mu}_\mathrm{S}}{r^2 \hat{\Phi}^4} , \quad \text{(C.15)}$$

and

$$\hat{A}_3 = \left(4 \frac{\hat{\Phi}_{,r}}{\hat{\Phi}} + \frac{2}{r} + \frac{\hat{\alpha}_{,r}}{\hat{\alpha}} \right) \hat{b}^r + 2 \cot(\theta) \hat{b}^\theta . \quad \text{(C.16)}$$

Eigenvalues

The solution of the coefficient determinant of the second-order derivatives of Eq. (C.12)

$$0 = a_{ij} |x^i| |x^j| \frac{\partial^2 \xi}{\partial x^i \partial x^j} = c_{ij} \frac{\partial^2 \xi}{\partial x^i \partial x^j} \quad \text{(C.17)}$$

$$c_{ij} = \begin{pmatrix} \hat{\alpha}^2 \hat{A}^0 & 0 & 0 \\ 0 & \hat{\Phi}^4 \hat{b}^r \hat{b}^r + \frac{\hat{\mu}_\mathrm{S}}{r^2} & \hat{\Phi}^4 r \hat{b}^r \hat{b}^\theta \\ 0 & \hat{\Phi}^4 r \hat{b}^\theta \hat{b}^r & \hat{\Phi}^4 r^2 \hat{b}^\theta \hat{b}^\theta + \mu_\mathrm{S} \end{pmatrix} \quad \text{(C.18)}$$

leads to the following eigenvalues:

$$\lambda_1 = 1 , \quad \text{(C.19)}$$

$$\lambda_2 = \frac{\hat{\mu}_\mathrm{S} + \hat{b}^2}{\hat{\alpha}^2 \hat{A}_0} , \quad \text{(C.20)}$$

$$\lambda_3 = \frac{\hat{\mu}_\mathrm{S}}{\hat{\alpha}^2 \hat{A}_0} , \quad \text{(C.21)}$$

where the eigenvector corresponding to λ_2 (λ_3) is oriented along (orthogonal to) the magnetic field lines, i.e. they correspond to the linearized version of Eq. (2.90). All eigenvalues are real and distinct. Hence, Eq. (C.12) is hyperbolic.

C.2 Numerical implementation of the linearized wave equation in the crust

Compared to the case when using Riemann solvers on both sides of the crust-core interface, the equations and the numerical scheme in the fluid core of the neutron star remain unmodified. In order to evolve Eq. (C.12) numerically in the crust we split it into two equations for ξ^φ and $Y := \xi^\varphi_{,t}$

$$\xi^\varphi_{,t} = Y \tag{C.22}$$

$$\hat{A}_0 Y_{,t} = \hat{A}_1 \xi^\varphi_{,r} + \hat{A}_2 \xi^\varphi_{,\theta} + \left(\hat{b}^\theta \hat{b}^\theta + \frac{\hat{\mu}_\mathrm{S}}{r^2 \hat{\Phi}^4}\right) \xi^\varphi_{,\theta\theta} + \left(2\hat{b}^r \hat{b}^\theta\right) \xi^\varphi_{,\theta r} + \left(\hat{b}^r \hat{b}^r + \frac{\hat{\mu}_\mathrm{S}}{\hat{\Phi}^4}\right) \xi^\varphi_{,rr} \,. \tag{C.23}$$

These equations are integrated with an explicit Runge-Kutta method. Since we are now evolving two systems with different variables in the core and in the crust, we have to impose interface conditions. The reconstruction of the variables for the Riemann solver in the core works analog to the standard method of Section 2.6.2. For the corresponding procedure we require the magnetic field δb^φ and the velocity v^φ in the crust. We construct δb^φ from the linearized induction equation (C.11), and v^φ is related to Y by $Y = \xi^\varphi_{,t} = \delta u^\varphi / u^t = v^\varphi / u^t$. To set the boundary conditions for the variables in the crust, there is no need to provide a condition for the magnetic field, because the dynamical variables are Y and ξ^φ in the crust, which are reconstructed at the crust-core interface as in Section 2.6.2. With these cell-interface values one can approximate the derivatives at the cell centers near the crust-core interface in form of one-sided radial derivatives .

At the surface the same conditions as in Section 2.5 apply. Translated to the variables used in the linear approach these read

$$\xi^\varphi_{,r} = 0 \,, \tag{C.24}$$

$$Y_{,r} = 0 \,. \tag{C.25}$$

The evolutions computed with this method rapidly become unstable when increasing the magnetic field strength. It was therefore necessary to add some artificial dissipation. We used a fourth-order Kreiss-Oliger term $\epsilon_D \mathcal{D}_4 f$, where $\mathcal{D}_4 f$ is the fourth-order numerical derivative of any function f. The minimal coefficient found to give stable evolutions is $\epsilon_D = 10^{-2}$. We checked the code to ensure that this additional term does not influence the results of the simulations significantly.

C.3 Comparison of the two methods

To compare the results of the crustal mode damping (see Section 3.4.1) obtained with the two numerical methods presented in Section 2.4, 2.6 and in Appendix C we plot the evolution of the velocity at some point in the crust near the pole (Fig. C.1). Without

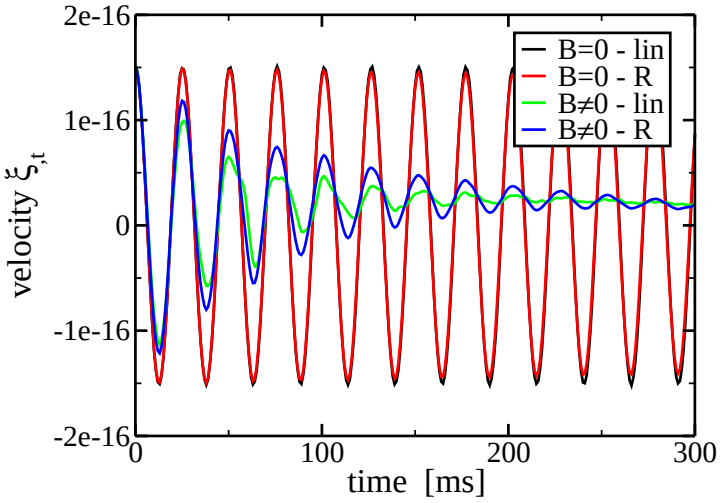

Figure C.1: Evolution of the velocity $\xi_{,t}$ at some point in the crust near the pole for $B = 5 \times 10^{13}$ G and without a magnetic field. The two different numerical methods are denoted by *lin* for the linear method and *R* for the Riemann solver approach. The linear method is less dissipative for zero magnetic field, while the opposite holds when the magnetic field is turned on.

magnetic field, the linear method is less dissipative, which is probably related to the set-up of the interface conditions at the crust-core interface in this particular case. While we use the general conditions described in Section 2.6 for the Riemann solver approach, it is possible to use a simplified expression for the linear method. Because there is no magnetic field the expression of continuous traction at the crust-core interface leads to $\xi^{\varphi}_{,r} = 0$ as at the surface. This provides a source of dissipation for the Riemann solver method, but none for the linear approach. In the presence of magnetic fields the picture changes, and the evolution computed with the Riemann solver has less dissipation of crustal modes than the linear method (see Fig. C.1). When using different coefficients in the Kreiss-Oliger term, the curves for the linear method are indistinguishable. We can therefore rule out that the artificial dissipation dominates the numerical damping observed for the linear approach.

Because of its superior behavior in the more generic case we generally used the Riemann solver method to obtain the numerical results. We checked that the linear approach agrees on the extracted frequencies with the Riemann solver for all regimes of the magnetic field strength considered by us.

D Calculations of crustal shear modes as eigenvalue problem

Without magnetic field Eq. (C.12) simplifies to

$$\begin{aligned}\hat{A}_0\xi^{\varphi}_{,tt} &= \hat{A}_1\xi^{\varphi}_{,r} + \hat{A}_2\xi^{\varphi}_{,\theta} + \frac{\hat{\mu}_{\rm S}}{r^2\hat{\Phi}^4}\xi^{\varphi}_{,\theta\theta} + \frac{\hat{\mu}_{\rm S}}{\hat{\Phi}^4}\xi^{\varphi}_{,rr} \\ &= \nabla_\nu\left(\mu_{\rm S} g^{\nu\nu}\xi^{\varphi}_{,\nu}\right)\,, \end{aligned} \tag{D.1}$$

with

$$\hat{A}_0 = \hat{\rho}\hat{h}\hat{\alpha}^{-2}\,, \tag{D.2}$$

$$\hat{A}_1 = \left(\frac{\hat{\mu}_{\rm S}}{\hat{\Phi}^4}\right)_{,r} + \hat{C}\frac{\hat{\mu}_{\rm S}}{\hat{\Phi}^4}\,, \tag{D.3}$$

$$\hat{A}_2 = \left(\frac{\hat{\mu}_{\rm S}}{r^2\hat{\Phi}^4}\right)_{,\theta} + 3\cot(\theta)\frac{\hat{\mu}_{\rm S}}{r^2\hat{\Phi}^4}\,, \tag{D.4}$$

and

$$\hat{C} = \frac{\hat{\alpha}_{,r}}{\hat{\alpha}} + 10\frac{\hat{\Phi}_{,r}}{\hat{\Phi}} + \frac{4}{r}\,. \tag{D.5}$$

Assuming a harmonic time dependence $\xi^{\varphi}(\mathbf{r},t) = \xi^{\varphi}(\mathbf{r})e^{i\omega t}$ and a separation of variables $\xi^{\varphi}(r,\theta) = R(r)\Theta(\theta)$ leads to

$$\begin{aligned}-\omega^2\hat{A}_0 &= \left[\left(\frac{\hat{\mu}_{\rm S}}{r^2\hat{\Phi}^4}\Theta'(\theta)\right)_{,\theta} + 3\cot(\theta)\frac{\hat{\mu}_{\rm S}}{r^2\hat{\Phi}^4}\Theta'(\theta)\right]\frac{1}{\Theta(\theta)} \\ &\quad + \left[\left(\frac{\hat{\mu}_{\rm S}}{\hat{\Phi}^4}R'(r)\right)_{,r} + \hat{C}\frac{\hat{\mu}_{\rm S}}{\hat{\Phi}^4}R'(r)\right]\frac{1}{R(r)}\,, \end{aligned} \tag{D.6}$$

where a prime denotes the derivative with respect to the corresponding variable r or θ. The angular and radial part have to fulfill this equation independently, such that:

$$0 = \Theta''(\theta) + 3\cot\theta\Theta'(\theta) + \lambda_\theta^2\Theta(\theta)\,, \tag{D.7}$$

$$0 = \frac{\hat{\mu}_{\rm S}}{\hat{\Phi}^4}R''(r) + \left[\left(\frac{\hat{\mu}_{\rm S}}{\hat{\Phi}^4}\right)_{,r} + \hat{C}\frac{\hat{\mu}_{\rm S}}{\hat{\Phi}^4}\right]R'(r) + \lambda_r^2 R(r)\,, \tag{D.8}$$

where $\lambda_r^2 = \left(\omega^2 \hat{A}_0 + \lambda_\theta^2\right)$. Both equations are of singular Sturm-Liouville type, and therefore their solutions R_{λ_r} and Θ_{λ_θ} form a complete, orthonormal set $\Xi_i(r,\theta) = R_{\lambda_r}\Theta_{\lambda_\theta}$. The solution of the angular part consists of the angular part of the vector spherical harmonics $\Psi_n(\theta)$, which is related to the Legendre polynomials $P_n(\theta)$ by

$$\Psi_n(\theta) \sim \frac{\partial P_n(\theta)}{\partial \theta}\,. \tag{D.9}$$

The equation to obtain $R(r)$ is solved numerically with a shooting method. Because the eigenfunctions $\Xi_i(r,\theta)$ form a complete set, it is possible to expand any displacement in terms of the former:

$$\xi^\varphi(r,\theta,t) = \sum_i A_i(t)\ \Xi_i(r,\theta)\,, \tag{D.10}$$

where the eigenmode coefficients $A_i(t)$ are given by the inner product

$$\begin{aligned} A_i(t) &= \langle \xi^\varphi(r,\theta,t), \Xi_i(r,\theta)\rangle \\ &= \int_{r_{\rm cc}}^{r_{\rm s}} \xi^\varphi(r,\theta,t)\ \Xi_i(r,\theta) w_\theta w_r dr d\theta\,. \end{aligned} \tag{D.11}$$

Here $r_{\rm s}$ and $r_{\rm cc}$ are the radii of the surface of the star and of the crust-core interface, respectively. The corresponding weighting functions w_r and w_θ are, according to the Sturm-Liouville theory

$$w_\theta = \sin(\theta)^3\,, \tag{D.12}$$

$$w_r = \frac{\alpha(r)^{-1}\Phi(r)^{10}\ r^4\rho(r)h(r)}{\alpha(r_{\rm cc})^{-1}\Phi(r_{\rm cc})^{10}\ r_{\rm cc}^4\rho(r_{\rm cc})h(r_{\rm cc})}\,. \tag{D.13}$$

We calculate the overlap integrals defined in Eq. (D.11) with a fourth-order Simpsons rule algorithm.

The orthogonality of the different crustal modes is checked numerically in Table D.1. The overlap integrals between different l modes increase in magnitude with increasing l, because the finer spatial structure of higher l modes results in larger numerical errors at a given grid resolution than that for low l modes. The strongest numerical violation of orthogonality between different modes occurs for the same l but different n. The same argument as above applies. The much shorter extension of the crust in radial than in θ direction implies that at a given grid resolution the angular structure is better resolved than the radial one.

In Fig. D.1 we show the first five radial eigenfunctions R_{λ_r} for $\lambda_r = \{0,1,2,3,4\}$. The fundamental $n = 0$ is almost constant throughout the crust and should be resolved accurately at very low grid resolution. The $n > 0$ modes have at least one node inside the crust, and hence require finer numerical resolution.

n=0

n	l	2	3	4	5	6
	2	1.0	8×10^{-6}	-1×10^{-5}	2×10^{-5}	-2×10^{-5}
	3	8×10^{-6}	1.0	2×10^{-5}	-3×10^{-5}	3×10^{-5}
0	4	-1×10^{-5}	2×10^{-5}	1.0	4×10^{-5}	-5×10^{-5}
	5	2×10^{-5}	-3×10^{-5}	4×10^{-5}	1.0	6×10^{-5}
	6	-2×10^{-5}	3×10^{-5}	-5×10^{-5}	6×10^{-5}	1.0
	2	-4×10^{-2}	-3×10^{-7}	5×10^{-7}	-7×10^{-7}	9×10^{-7}
	3	-3×10^{-7}	-4×10^{-2}	-8×10^{-7}	1×10^{-6}	-1×10^{-6}
1	4	5×10^{-7}	-8×10^{-7}	-4×10^{-2}	-2×10^{-6}	2×10^{-6}
	5	-7×10^{-7}	1×10^{-6}	-2×10^{-6}	-4×10^{-2}	-3×10^{-6}
	6	9×10^{-7}	-1×10^{-6}	2×10^{-6}	-3×10^{-6}	-4×10^{-2}

n=1

n	l	2	3	4	5	6
	2	1.0	8×10^{-6}	-1×10^{-5}	2×10^{-5}	-2×10^{-5}
	3	8×10^{-6}	1.0	2×10^{-5}	-3×10^{-5}	3×10^{-5}
1	4	-1×10^{-5}	2×10^{-5}	1.0	4×10^{-5}	-5×10^{-5}
	5	2×10^{-5}	-3×10^{-5}	4×10^{-5}	1.0	6×10^{-5}
	6	-2×10^{-5}	3×10^{-5}	-5×10^{-5}	6×10^{-5}	1.0

Table D.1: The overlap integrals of the different crustal modes of the reference model APR+DH 1.4 obtained with a Simpsons rule algorithm. The grid resolution was 150×100 for $[0, r_s] \times [0, \pi]$. The upper (lower) table gives the values for the overlap integrals with $n = 0$ ($n = 1$) modes.

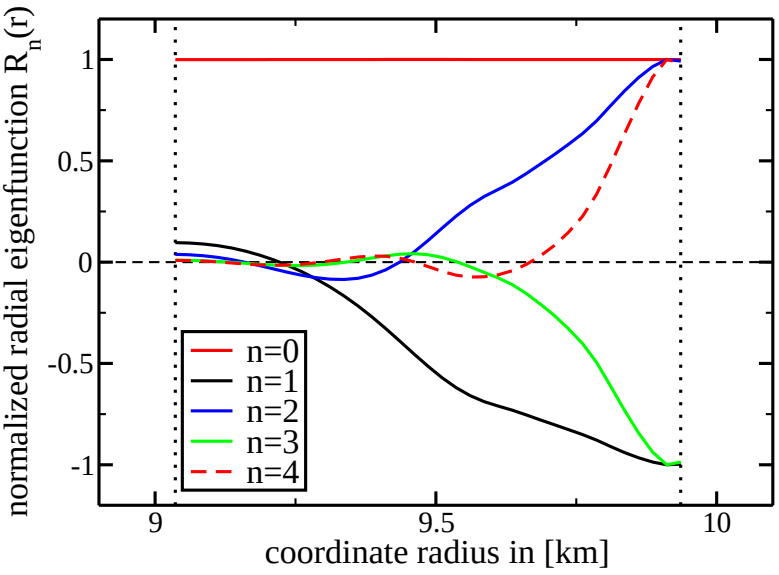

Figure D.1: First five radial eigenfunctions of the crustal shear modes for the model APR+DH 1.4.

E Magnetic field configurations confined in the crust

We follow Aguilera et al. (2008), who give a description of different axisymmetric magnetic field configurations. We neglect the effects of general relativity on the magnetic field and the influence of the magnetic field on the neutron star structure. This should hold, in particular, for fields confined to the crust which contains only few per cent of the total mass. Moreover, we assume that the magnetic field has relaxed to some equilibrium before the crust crystallized. After crystallization the magnetic field is frozen in the crust and, thus, no forces act on the particles. For simplicity we consider purely poloidal fields only.

For axisymmetric fields it is possible to make the following ansatz

$$\mathbf{B}_{\text{poloidal}} = \nabla \times (\mathbf{r} \times \nabla\psi)\,, \tag{E.1}$$

where $\psi = \psi(r, \theta)$ is a scalar whose angular part can be expanded according to

$$\psi(r, \theta) = C \sum_l \frac{P_l(\cos\theta)}{r} S_l(r)\,, \tag{E.2}$$

with C being a normalization constant. The poloidal magnetic field can thus be expressed as

$$B_r = -\frac{B}{2x^2} S_l(x) \frac{1}{\sin\theta} \frac{\partial}{\partial\theta} \left(\sin\theta \frac{\partial}{\partial\theta} P_l(\cos\theta) \right)\,, \tag{E.3}$$

$$B_\theta = \frac{B}{2x} \frac{\partial}{\partial x} S_l(x) \frac{\partial}{\partial\theta} P_l(\cos\theta)\,, \tag{E.4}$$

where $x = r/r_\mathrm{s}$ and B is a constant related to C. For dipolar fields $C = r_\mathrm{s}^2 B/2$. The φ-component of the force-free condition $\nabla \times \mathbf{B} = \mu\mathbf{B}$ (see Chapter 4 for a discussion of force-free fields in the magnetosphere) leads to a Riccati-Bessel equation for $S_l(x)$ (see Aguilera et al., 2008). μ is a parameter related to the currents maintaining the magnetic field. For different l, we have

$$S_l(x) = a_l \mu r_\mathrm{s} x\, j_l(\mu r_\mathrm{s} x) + b_l \mu r_\mathrm{s} x\, n_l(\mu r_\mathrm{s} x)\,, \tag{E.5}$$

where a_l and b_l are parameters, and j_l and n_l are the spherical Bessel functions of first and second kind. The parameters a_l and b_l can be obtained by matching to an exterior

solution of the magnetic field. The spherical Bessel functions used to get the dipolar ($l = 1$), quadrupolar ($l = 2$), and octupolar (l=3) configuration are given by

$$j_1(X) = \frac{\sin X}{X^2} - \frac{\cos X}{X} \tag{E.6}$$

$$j_2(X) = \left(\frac{3}{X^3} - \frac{1}{X}\right)\sin X - \frac{3\cos X}{X^2} \tag{E.7}$$

$$j_3(X) = \left(\frac{15}{X^4} - \frac{6}{X^2}\right)\sin X - \left(\frac{15}{X^3} - \frac{1}{X}\right)\cos X \tag{E.8}$$

$$n_1(X) = -\frac{\cos X}{X^2} - \frac{\sin X}{X} \tag{E.9}$$

$$n_2(X) = \left(-\frac{3}{X^3} + \frac{1}{X}\right)\cos X - -\frac{3\sin X}{X^2} \tag{E.10}$$

$$n_3(X) = \left(-\frac{15}{X^4} + \frac{6}{X^2}\right)\cos X - \left(\frac{15}{X^3} - \frac{1}{X}\right)\sin X \tag{E.11}$$

The function S_l in Eq. E.5 depends on the constants a_l and b_l. For a given l both have to be determined by the boundary conditions for B_r and B_θ at the surface. For a dipolar external field we get

$$a_1 = \cos \mu r_\mathrm{s}\,, \tag{E.12}$$

$$b_1 = \sin \mu r_\mathrm{s}\,, \tag{E.13}$$

while for the quadrupolar external field

$$a_2 = 3\frac{\sin \mu r_\mathrm{s}}{(\mu r_\mathrm{s})^2} - \sin \mu r_\mathrm{s} - 2\frac{\cos \mu r_\mathrm{s}}{(\mu r_\mathrm{s})} + 3\frac{\cos \mu r_\mathrm{s}}{(\mu r_\mathrm{s})^3}\,, \tag{E.14}$$

$$b_2 = -3\frac{\cos \mu r_\mathrm{s}}{(\mu r_\mathrm{s})^2} + \cos \mu r_\mathrm{s} - 2\frac{\sin \mu r_\mathrm{s}}{(\mu r_\mathrm{s})} + 3\frac{\sin \mu r_\mathrm{s}}{(\mu r_\mathrm{s})^3}\,. \tag{E.15}$$

The octupolar field can be matched by

$$a_3 = \cos \mu r_\mathrm{s} - 5\frac{\sin \mu r_\mathrm{s}}{\mu r_\mathrm{s}} - 15\frac{\cos \mu r_\mathrm{s}}{(\mu r_\mathrm{s})^2} + 30\frac{\sin \mu r_\mathrm{s}}{(\mu r_\mathrm{s})^3} + 30\frac{\cos \mu r_\mathrm{s}}{(\mu r_\mathrm{s})^4}\,, \tag{E.16}$$

$$b_3 = \sin \mu r_\mathrm{s} + 5\frac{\cos \mu r_\mathrm{s}}{(\mu r_\mathrm{s})} - 15\frac{\sin \mu r_\mathrm{s}}{(\mu r_\mathrm{s})^2} - 30\frac{\cos \mu r_\mathrm{s}}{(\mu r_\mathrm{s})^3} + 30\frac{\sin \mu r_\mathrm{s}}{(\mu r_\mathrm{s})^4}\,. \tag{E.17}$$

It remains to determine the value of μ. For magnetic fields confined to the crust $B_r = 0$ at the crust-core interface. This translates into a condition for $S_l|_{r_\mathrm{cc}} = 0$, and hence for μ

$$\tan\left[\mu(r_\mathrm{cc} - r_\mathrm{s})\right] - \mu r_\mathrm{s} = 0\,, \tag{E.18}$$

which has to be solved numerically. For the quadrupolar and octupolar configurations the corresponding equations are more complicated and are not given here.

F Orthonormal basis in Schwarzschild geometry

The components of the orthonormal basis in Schwarzschild geometry are given explicitly as follows:

$$\tilde{\mathbf{e}}_r = \alpha \partial_r \,, \tag{F.1}$$

$$\tilde{\mathbf{e}}_\theta = \frac{1}{r} \partial_\theta \,, \tag{F.2}$$

$$\tilde{\mathbf{e}}_\varphi = \frac{1}{r \sin\theta} \partial_\varphi \,. \tag{F.3}$$

The resulting 3-dimensional vector operators are the gradient

$$\tilde{\nabla}\psi = \alpha \psi_{,r} \tilde{\mathbf{e}}_r + \frac{1}{r} \psi_{,\theta} \tilde{\mathbf{e}}_\theta + \frac{1}{r \sin\theta} \psi_{,\varphi} \tilde{\mathbf{e}}_\varphi \,, \tag{F.4}$$

the divergence

$$\begin{aligned} \tilde{\nabla} \cdot \mathbf{B} =& \frac{1}{\sqrt{\gamma}} \left[\left(B_{\tilde{r}} \sqrt{\gamma_{\theta\theta} \gamma_{\varphi\varphi}} \right)_{,r} + \left(B_{\tilde{\theta}} \sqrt{\gamma_{rr} \gamma_{\varphi\varphi}} \right)_{,\theta} + \left(B_{\tilde{\varphi}} \sqrt{\gamma_{rr} \gamma_{\theta\theta}} \right)_{,\varphi} \right] \\ =& \frac{\alpha}{r^2} \left(r^2 B_{\tilde{r}} \right)_{,r} + \frac{1}{r \sin\theta} \left(\sin\theta B_{\tilde{\theta}} \right)_{,\theta} + \frac{1}{r \sin\theta} \left(B_{\tilde{\varphi}} \right)_{,\varphi} \,, \end{aligned} \tag{F.5}$$

and the curl

$$\begin{aligned} \tilde{\nabla} \times \mathbf{B} =& \frac{\tilde{\mathbf{e}}_r \sqrt{\gamma_{rr}}}{\sqrt{\gamma}} \left[\left(\sqrt{\gamma_{\varphi\varphi}} B_{\tilde{\varphi}} \right)_{,\theta} - \left(\sqrt{\gamma_{\theta\theta}} B_{\tilde{\theta}} \right)_{,\varphi} \right] + \frac{\tilde{\mathbf{e}}_\theta \sqrt{\gamma_{\theta\theta}}}{\sqrt{\gamma}} \left[\left(\sqrt{\gamma_{rr}} B_{\tilde{r}} \right)_{,\varphi} - \left(\sqrt{\gamma_{\varphi\varphi}} B_{\tilde{\varphi}} \right)_{,r} \right] \\ &+ \frac{\tilde{\mathbf{e}}_\varphi \sqrt{\gamma_{\varphi\varphi}}}{\sqrt{\gamma}} \left[\left(\sqrt{\gamma_{\theta\theta}} B_{\tilde{\theta}} \right)_{,r} - \left(\sqrt{\gamma_{rr}} B_{\tilde{r}} \right)_{,\theta} \right] \\ =& \frac{\tilde{\mathbf{e}}_r}{r \sin\theta} \left[\left(\sin\theta B_{\tilde{\varphi}} \right)_{,\theta} - \left(B_{\tilde{\theta}} \right)_{,\varphi} \right] + \frac{\tilde{\mathbf{e}}_\theta}{r} \left[\sin^{-1}\theta \left(B_{\tilde{r}} \right)_{,\varphi} - \alpha \left(r B_{\tilde{\varphi}} \right)_{,r} \right] \\ &+ \frac{\tilde{\mathbf{e}}_\varphi}{r} \left[\alpha \left(r B_{\tilde{\theta}} \right)_{,r} - \left(B_{\tilde{r}} \right)_{,\theta} \right] \,. \end{aligned} \tag{F.6}$$

We denote the basis vectors and the vector operators in orthonormal coordinates with the tilde to distinguish them from those in the usual coordinate basis.

G Integration along geodesics

Free falling particles in a curved spacetime follow geodesics. We have given the corresponding geodesic equation in Eq. (2.13). For the numerical integration we begin with the derivatives of the coordinates with respect to the affine parameter λ

$$\frac{dx^\alpha}{d\lambda} = \frac{dt}{d\lambda}\frac{dx^\alpha}{dt}\,, \tag{G.1}$$

and consequently

$$\frac{d^2x^\alpha}{d\lambda^2} = \frac{d^2t}{d\lambda^2}\frac{dx^\alpha}{dt} + \left(\frac{dt}{d\lambda}\right)^2 \frac{d^2x^\alpha}{dt^2}\,. \tag{G.2}$$

With Eq. (2.13) this can be expressed as

$$\frac{d^2x^\alpha}{dt^2} = \left(\Gamma^t_{\beta\gamma}\frac{dx^\alpha}{dt} - \Gamma^\alpha_{\beta\gamma}\right)\frac{dx^\beta}{dt}\frac{dx^\gamma}{dt}\,. \tag{G.3}$$

By defining the momenta $k^\alpha = dx^\alpha/dt$ and the energy $E = dt/d\lambda$ we get

$$\frac{dE}{dt} = -\Gamma^t_{\alpha\beta}k^\alpha k^\beta E\,. \tag{G.4}$$

Thus, Eq. (G.3) can be expressed as follows

$$\frac{dx^\alpha}{dt} = k^a\,, \tag{G.5}$$

$$\frac{dk^\alpha}{dt} = \left(\Gamma^t_{\beta\gamma}k^\alpha - \Gamma^\alpha_{\beta\gamma}\right)k^\beta k^\gamma\,, \tag{G.6}$$

$$\frac{dE}{dt} = -\Gamma^t_{\alpha\beta}k^\alpha k^\beta E\,. \tag{G.7}$$

With $k^t = 1$ these equations explicitly read

$$\begin{aligned}
\frac{dk^r}{dt} &= 2\Gamma^t_{rt}k^r k^r - \Gamma^r_{tt} - \Gamma^r_{rr}k^r k^r - \Gamma^r_{\theta\theta}k^\theta k^\theta - \Gamma^r_{\varphi\varphi}k^\varphi k^\varphi \\
&= 3\frac{\alpha'}{\alpha}k^r k^r - \alpha'\alpha^3 + \alpha^2 r k^\theta k^\theta + \alpha^2 r\sin^2\theta k^\varphi k^\varphi \qquad \text{(G.8)} \\
\frac{dk^\theta}{dt} &= 2\Gamma^t_{rt}k^\theta k^r k^t - 2\Gamma^\theta_{r\theta}k^r k^\theta - \Gamma^\theta_{\varphi\varphi}k^\varphi k^\varphi \\
&= 2\left(\frac{\alpha'}{\alpha} - \frac{1}{r}\right)k^r k^\theta + \sin\theta\cos\theta k^\varphi k^\varphi \qquad \text{(G.9)} \\
\frac{dk^\varphi}{dt} &= 2\Gamma^t_{rt}k^\varphi k^r k^t - 2\Gamma^\varphi_{r\varphi}k^r k^\varphi - 2\Gamma^\varphi_{\theta\varphi}k^\theta k^\varphi \\
&= 2\left(\frac{\alpha'}{\alpha} - \frac{1}{r}\right)k^r k^\varphi - 2\cot\theta k^\theta k^\varphi \qquad \text{(G.10)} \\
\frac{dE}{dt} &= -2\Gamma^t_{rt}k^r k^t E = -2\frac{\alpha'}{\alpha}k^r E \qquad \text{(G.11)}
\end{aligned}$$

These equations are integrated explicitly in time with a Runge-Kutta method. In the above equations we have used the following Christoffel symbols:

$$\begin{aligned}
\Gamma^t_{tr} &= \frac{\alpha'}{\alpha} && \text{(G.12a)} \\
\Gamma^r_{tt} &= \alpha'\alpha^3 && \text{(G.12b)} \\
\Gamma^r_{rr} &= -\frac{\alpha'}{\alpha} && \text{(G.12c)} \\
\Gamma^r_{\theta\theta} &= -\alpha^2 r && \text{(G.12d)} \\
\Gamma^r_{\varphi\varphi} &= -\alpha^2 r\sin^2\theta && \text{(G.12e)} \\
\Gamma^\theta_{r\theta} &= \frac{1}{r} && \text{(G.12f)} \\
\Gamma^\theta_{\varphi\varphi} &= -\sin\theta\cos\theta && \text{(G.12g)} \\
\Gamma^\varphi_{r\varphi} &= \frac{1}{r} && \text{(G.12h)} \\
\Gamma^\varphi_{\theta\varphi} &= \cot\theta && \text{(G.12i)}
\end{aligned}$$

Bibliography

Aguilera, D. N., Pons, J. A., and Miralles, J. A. (2008). 2D Cooling of magnetized neutron stars. A&A, 486:255–271.

Akmal, A., Pandharipande, V. R., and Ravenhall, D. G. (1998). Equation of state of nucleon matter and neutron star structure. Phys. Rev. C, 58:1804–1828.

Alpar, M. A. (2001). On Young Neutron Stars as Propellers and Accretors with Conventional Magnetic Fields. ApJ, 554:1245–1254.

Anile, A. M. (1989). *Relativistic fluids and magneto-fluids : with applications in astrophysics and plasma physics*.

Antón, L., Zanotti, O., Miralles, J. A., Martí, J. M., Ibáñez, J. M., Font, J. A., and Pons, J. A. (2006). Numerical 3+1 General Relativistic Magnetohydrodynamics: A Local Characteristic Approach. ApJ, 637:296–312.

Arnowitt, R., Deser, S., and Misner, C. (1962). *The Dynamics of General Relativity*, chapter 7, pages 227–264. in "Gravitation: an introduction to current research", L.Witten ed. Wiley, New York , and gr-qc/0405109.

Barat, C., Hayles, R. I., Hurley, K., Niel, M., Vedrenne, G., Desai, U., Kurt, V. G., Zenchenko, V. M., and Estulin, I. V. (1983). Fine time structure in the 1979 March 5 gamma ray burst. A&A, 126:400–402.

Baym, G., Pethick, C., and Pines, D. (1969). Superfluidity in Neutron Stars. Nature, 224:673–674.

Beig, R. and Schmidt, B. G. (2003). Relativistic elasticity. *Classical and Quantum Gravity*, 20:889–904.

Beloborodov, A. M. (2009). Untwisting Magnetospheres of Neutron Stars. ApJ, 703:1044–1060.

Beloborodov, A. M. and Thompson, C. (2007). Magnetar corona. Ap&SS, 308:631–639.

Blaes, O., Blandford, R., Goldreich, P., and Madau, P. (1989). Neutron starquake models for gamma-ray bursts. ApJ, 343:839–848.

Bocquet, M., Bonazzola, S., Gourgoulhon, E., and Novak, J. (1995). Rotating neutron star models with a magnetic field. A&A, 301:757–+.

Bonazzola, S., Villain, L., and Bejger, M. (2007). Magnetohydrodynamics of rotating compact stars with spectral methods: description of the algorithm and tests. *Classical and Quantum Gravity*, 24:221–+.

Braithwaite, J. (2009). Axisymmetric magnetic fields in stars: relative strengths of poloidal and toroidal components. MNRAS, 397:763–774.

Braithwaite, J. and Nordlund, Å. (2006). Stable magnetic fields in stellar interiors. A&A, 450:1077–1095.

Braithwaite, J. and Spruit, H. C. (2004). A fossil origin for the magnetic field in A stars and white dwarfs. Nature, 431:819–821.

Braithwaite, J. and Spruit, H. C. (2006). Evolution of the magnetic field in magnetars. A&A, 450:1097–1106.

Canuto, V., Lodenquai, J., and Ruderman, M. (1971). Thomson Scattering in a Strong Magnetic Field. Phys. Rev. D, 3:2303–2308.

Carroll, S. (2004). *Spacetime and Geometry: An Introduction to General Relativity*. Benjamin Cummings.

Carter, B. and Quintana, H. (1972). Foundations of General Relativistic High-Pressure Elasticity Theory. *Royal Society of London Proceedings Series A*, 331:57–83.

Carter, B. and Samuelsson, L. (2006a). Relativistic mechanics of neutron superfluid in (magneto)elastic star crust. *Classical and Quantum Gravity*, 23:5367–5388.

Carter, B. and Samuelsson, L. (2006b). Relativistic mechanics of neutron superfluid in (magneto)elastic star crust. *Classical and Quantum Gravity*, 23:5367–5388.

Cerdá-Durán, P. (2010). Numerical viscosity in hydrodynamics simulations in general relativity. *Classical and Quantum Gravity*, 27(20):205012–+.

Cerdá-Durán, P., Font, J. A., Antón, L., and Müller, E. (2008). A new general relativistic magnetohydrodynamics code for dynamical spacetimes. A&A, 492:937–953.

Cerdá-Durán, P., Stergioulas, N., and Font, J. A. (2009). Alfvén QPOs in magnetars in the anelastic approximation. MNRAS, 397:1607–1620.

Chamel, N. and Haensel, P. (2008). Physics of neutron star crusts. *Living Reviews in Relativity*, 11(10).

Chandrasekhar, S. (1970). Solutions of Two Problems in the Theory of Gravitational Radiation. *Physical Review Letters*, 24:611–615.

Chatterjee, P., Hernquist, L., and Narayan, R. (2000). An Accretion Model for Anomalous X-Ray Pulsars. ApJ, 534:373–379.

Choquet-Bruhat, Y. (21952). Thorme d'existence pour certains systmes d'quations aux drives partielles non linaires,. *Acta Mathematica*, 88:141–225.

Ciolfi, R., Ferrari, V., Gualtieri, L., and Pons, J. A. (2009). Relativistic models of magnetars: the twisted torus magnetic field configuration. MNRAS, 397:913–924.

Ciolfi, R., Lander, S. K., Manca, G. M., and Rezzolla, L. (2011). Instability-driven Evolution of Poloidal Magnetic Fields in Relativistic Stars. ApJ, 736:L6+.

Colaiuda, A., Beyer, H., and Kokkotas, K. D. (2009). On the quasi-periodic oscillations in magnetars. MNRAS, 396:1441–1448.

Colaiuda, A. and Kokkotas, K. D. (2011). Magnetar oscillations in the presence of a crust. MNRAS, 414:3014–3022.

Daugherty, J. K. and Ventura, J. (1978). Absorption of radiation by electrons in intense magnetic fields. Phys. Rev. D, 18:1053–1067.

Demorest, P. B., Pennucci, T., Ransom, S. M., Roberts, M. S. E., and Hessels, J. W. T. (2010). A two-solar-mass neutron star measured using Shapiro delay. Nature, 467:1081–1083.

Dimmelmeier, H., Font, J. A., and Müller, E. (2002a). Relativistic simulations of rotational core collapse I. Methods, initial models, and code tests. A&A, 388:917–935.

Dimmelmeier, H., Font, J. A., and Müller, E. (2002b). Relativistic simulations of rotational core collapse II. Collapse dynamics and gravitational radiation. A&A, 393:523–542.

Dimmelmeier, H., Novak, J., Font, J. A., Ibáñez, J. M., and Müller, E. (2005). Combining spectral and shock-capturing methods: A new numerical approach for 3D relativistic core collapse simulations. Phys. Rev. D, 71(6):064023–+.

Douchin, F. and Haensel, P. (2001). A unified equation of state of dense matter and neutron star structure. A&A, 380:151–167.

Duncan, R. C. (1998). Global Seismic Oscillations in Soft Gamma Repeaters. ApJ, 498:L45.

Duncan, R. C. (2002). Nature, nurture or not sure ? a debate about SGRs and AXPs. Mem. Soc. Astron. Italiana, 73:534–541.

Duncan, R. C. and Thompson, C. (1992). Formation of very strongly magnetized neutron stars - Implications for gamma-ray bursts. ApJ, 392:L9–L13.

El-Mezeini, A. M. and Ibrahim, A. I. (2010). Discovery of Quasi-periodic Oscillations in the Recurrent Burst Emission from SGR 1806-20. ApJ, 721:L121–L125.

Evans, C. R. and Hawley, J. F. (1988). Simulation of magnetohydrodynamic flows - A constrained transport method. ApJ, 332:659–677.

Fernández, R. and Davis, S. W. (2011). The X-ray Polarization Signature of Quiescent Magnetars: Effect of Magnetospheric Scattering and Vacuum Polarization. ApJ, 730:131–+.

Fernández, R. and Thompson, C. (2007). Resonant Cyclotron Scattering in Three Dimensions and the Quiescent Nonthermal X-ray Emission of Magnetars. ApJ, 660:615–640.

Feroci, M., Caliandro, G. A., Massaro, E., Mereghetti, S., and Woods, P. M. (2004). Broadband X-Ray Spectra of Short Bursts from SGR 1900+14. ApJ, 612:408–413.

Ferrario, L. and Wickramasinghe, D. (2006). Modelling of isolated radio pulsars and magnetars on the fossil field hypothesis. MNRAS, 367:1323–1328.

Flowers, E. and Ruderman, M. A. (1977). Evolution of pulsar magnetic fields. ApJ, 215:302–310.

Font, J. A. (2008). Numerical hydrodynamics and magnetohydrodynamics in general relativity. *Living Reviews in Relativity*, 11(7).

Friedman, J. L. and Schutz, B. F. (1978). Secular instability of rotating Newtonian stars. ApJ, 222:281–296.

Gabler, M., Cerdá-Durán, P., Font, J., Müller, E., and Stergioulas, N. (2010). Magneto-elastic torsional oscillations of magnetars. *Journal of Physics Conference Series*, 283(1):012013.

Gabler, M., Cerdá Durán, P., Font, J. A., Müller, E., and Stergioulas, N. (2011). Magneto-elastic oscillations and the damping of crustal shear modes in magnetars. MNRAS, 410:L37–L41.

Gabler, M., Sperhake, U., and Andersson, N. (2009). Nonlinear radial oscillations of neutron stars. Phys. Rev. D, 80(6):064012–+.

Glampedakis, K. and Andersson, N. (2006). Ekman layer damping of r modes revisited. MNRAS, 371:1311–1321.

Glampedakis, K., Samuelsson, L., and Andersson, N. (2006). Elastic or magnetic? A toy model for global magnetar oscillations with implications for quasi-periodic oscillations during flares. MNRAS, 371:L74–L77.

Goldreich, P. and Julian, W. H. (1969). Pulsar Electrodynamics. ApJ, 157:869–+.

Goldreich, P. and Reisenegger, A. (1992). Magnetic field decay in isolated neutron stars. ApJ, 395:250–258.

Gourgoulhon, E. (2007). 3+1 formalism and bases of numerical relativity. *Lectures given at the General Relativity Trimester held in the Institut Henri Poincare (Paris, Sept.-Dec. 2006) and at the VII Mexican School on Gravitation and Mathematical Physics (Playa del Carmen, Mexico, 26. Nov. - 2 Dec. 2006), arXiv:gr-qc/0703035v1.*

Guver, T., Gogus, E., and Ozel, F. (2011). A Magnetar Strength Surface Magnetic Field for the Slowly Spinning Down SGR 0418+5729. *ArXiv e-prints.*

Hambaryan, V., Neuhäuser, R., and Kokkotas, K. D. (2011). Bayesian timing analysis of giant flare of SGR 180620 by RXTE PCA. A&A, 528:A45+.

Herold, H. (1979). Compton and Thomson scattering in strong magnetic fields. Phys. Rev. D, 19:2868–2875.

Horvath, J. E. (2007). What do exotic equations of state have to offer? Ap&SS, 308:431–434.

Isenberg, J. A. (2008). Waveless Approximation Theories of Gravity. *International Journal of Modern Physics D*, 17:265–273.

Israel, G. L., Belloni, T., Stella, L., Rephaeli, Y., Gruber, D. E., Casella, P., Dall'Osso, S., Rea, N., Persic, M., and Rothschild, R. E. (2005). The Discovery of Rapid X-Ray Oscillations in the Tail of the SGR 1806-20 Hyperflare. ApJ, 628:L53–L56.

Jackson, J. D. (1975). *Classical electrodynamics*. New York: Wiley, 2nd edition.

Karlovini, M. and Samuelsson, L. (2003). Elastic stars in general relativity: I. Foundations and equilibrium models. *Classical and Quantum Gravity*, 20:3613–3648.

Karlovini, M. and Samuelsson, L. (2004). Elastic stars in general relativity: Iii. stiff ultrarigid exact solutions. *Classical and Quantum Gravity*, 21:4531–4548.

Karlovini, M. and Samuelsson, L. (2007). Elastic stars in general relativity: IV. Axial perturbations. *Classical and Quantum Gravity*, 24:3171–3189.

Karlovini, M., Samuelsson, L., and Zarroug, M. (2004). Elastic stars in general relativity: Ii. radial perturbations. *Classical and Quantum Gravity*, 21:1559–1581.

Kiuchi, K., Yoshida, S., and Shibata, M. (2011). Nonaxisymmetric instabilities of neutron star with toroidal magnetic fields. A&A, 532:A30+.

Kokkotas, K. and Schmidt, B. (1999). Quasi-Normal Modes of Stars and Black Holes. *Living Reviews in Relativity*, 2:2–+.

Kurganov, A. and Tadmor, E. (2000). New High-Resolution Central Schemes for Nonlinear Conservation Laws and Convection-Diffusion Equations. *Journal of Computational Physics*, 160:241–282.

Landau, L. D. and Lifshitz, E. M. (1981). *Quantum Mechanics Non-Relativistic Theory*. Butterworth-Heinemann, 3rd edition.

Landau, L. D. and Lifshitz, E. M. (1986). *Theory of Elasticity*. Butterworth-Heinemann, 3rd edition.

Lander, S. K. and Jones, D. I. (2009). Magnetic fields in axisymmetric neutron stars. MNRAS, 395:2162–2176.

Lander, S. K. and Jones, D. I. (2011). Oscillations and instabilities in neutron stars with poloidal magnetic fields. MNRAS, 412:1730–1740.

Lander, S. K., Jones, D. I., and Passamonti, A. (2010). Oscillations of rotating magnetized neutron stars with purely toroidal magnetic fields. MNRAS, 405:318–328.

Lasky, P. D., Zink, B., Kokkotas, K. D., and Glampedakis, K. (2011). Hydromagnetic Instabilities in Relativistic Neutron Stars. ApJ, 735:L20+.

Lattimer, J. M. and Prakash, M. (2005). Ultimate Energy Density of Observable Cold Baryonic Matter. *Physical Review Letters*, 94(11):111101–+.

Lattimer, J. M. and Prakash, M. (2007). Neutron star observations: Prognosis for equation of state constraints. Phys. Rep., 442:109–165.

Lee, U. (2007). Axisymmetric oscillations of magnetic neutron stars. MNRAS, 374:1015–1029.

Lee, U. (2008). Axisymmetric toroidal modes of magnetized neutron stars. MNRAS, 385:2069–2079.

Leveque, R. J. (2002). *Finite-Volume Methods for Hyperbolic Problems*. Cambridge University Press, Cambridge.

Levin, Y. (2006). QPOs during magnetar flares are not driven by mechanical normal modes of the crust. MNRAS, 368:L35–L38.

Levin, Y. (2007). On the theory of magnetar QPOs. MNRAS, 377:159–167.

Lichnerowicz, A. (1944). L' integration des équations de la gravitation relativiste et le problème des n corps. *J.Math.Pures et Appl.*, 23:37–63.

Lyutikov, M. and Gavriil, F. P. (2006). Resonant cyclotron scattering and Comptonization in neutron star magnetospheres. MNRAS, 368:690–706.

MacDonald, D. and Thorne, K. S. (1982). Black-hole electrodynamics - an absolute-space/universal-time formulation. MNRAS, 198:345–382.

Malheiro, M., Rueda, J. A., and Ruffini, R. (2011). SGRs and AXPs: Massive Rotating White Dwarfs versus Magnetars. *ArXiv e-prints*.

Markey, P. and Tayler, R. J. (1973). The adiabatic stability of stars containing magneticfields-II. Poloidal fields. MNRAS, 163:77–+.

Marsden, D., Lingenfelter, R. E., Rothschild, R. E., and Higdon, J. C. (2001). Nature versus Nurture: The Origin of Soft Gamma-Ray Repeaters and Anomalous X-Ray Pulsars. ApJ, 550:397–409.

Martí, J. M. and Müller, E. (2003). Numerical hydrodynamics in special relativity. *Living Reviews in Relativity*, 6(7).

Mazets, E. P., Golentskii, S. V., Ilinskii, V. N., Aptekar, R. L., and Guryan, I. A. (1979). Observations of a flaring X-ray pulsar in Dorado. Nature, 282:587–589.

McDermott, P. N., van Horn, H. M., and Hansen, C. J. (1988). Nonradial oscillations of neutron stars. ApJ, 325:725–748.

Mereghetti, S. (2008). The strongest cosmic magnets: soft gamma-ray repeaters and anomalous X-ray pulsars. A&A Rev., 15:225–287.

Messios, N., Papadopoulos, D. B., and Stergioulas, N. (2001). Torsional oscillations of magnetized relativistic stars. MNRAS, 328:1161–1168.

Mignani, R. P. (2011). Optical, ultraviolet, and infrared observations of isolated neutron stars. *Advances in Space Research*, 47:1281–1293.

Mihalas, D. (1978). *Stelalr Atmospheres*. W.H. Freeman & Co.

Misner, C., Thorne, K., and Wheeler, J. (1973). *Gravitation*. W.H. Freeman.

Negele, J. W. and Vautherin, D. (1973). Neutron star matter at sub-nuclear densities. *Nuclear Physics A*, 207:298–320.

Nobili, L., Turolla, R., and Zane, S. (2008a). X-ray spectra from magnetar candidates - I. Monte Carlo simulations in the non-relativistic regime. MNRAS, 386:1527–1542.

Nobili, L., Turolla, R., and Zane, S. (2008b). X-ray spectra from magnetar candidates - II. Resonant cross-sections for electron-photon scattering in the relativistic regime. MNRAS, 389:989–1000.

Oppenheimer, J. and Volkoff, G. (1939). On massive neutron cores. *Phys.Rev. 55*, pages 374–381.

Özel, F., Güver, T., and Psaltis, D. (2009). The Mass and Radius of the Neutron Star in EXO 1745-248. ApJ, 693:1775–1779.

Özel, F. and Psaltis, D. (2009). Reconstructing the neutron-star equation of state from astrophysical measurements. Phys. Rev. D, 80(10):103003–+.

Paerels, F. (1997). Pressure Broadening of Absorption Lines in Neutron Star Atmospheres and Prospects for Measuring Neutron Star Masses and Radii. ApJ, 476:L47+.

Page, D., Prakash, M., Lattimer, J. M., and Steiner, A. W. (2011). Rapid Cooling of the Neutron Star in Cassiopeia A Triggered by Neutron Superfluidity in Dense Matter. *Physical Review Letters*, 106(8):081101–+.

Page, D. and Reddy, S. (2006). Dense Matter in Compact Stars: Theoretical Developments and Observational Constraints. *Annual Review of Nuclear and Particle Science*, 56:327–374.

Pandharipande, V. R. and Smith, R. A. (1975). Nuclear matter calculations with mean scalar fields. *Physics Letters B*, 59:15–18.

Papadopoulos, D. and Esposito, F. P. (1982). Relativistic hydromagnetic wave propagation and instability in an anisotropic universe. ApJ, 257:10–16.

Passamonti, A. and Andersson, N. (2011). Towards real neutron star seismology: Accounting for elasticity and superfluidity. *ArXiv e-prints*.

Pavan, L., Turolla, R., Zane, S., and Nobili, L. (2009). Topology of magnetars external field - I. Axially symmetric fields. MNRAS, 395:753–763.

Perna, R. and Pons, J. A. (2011). A Unified Model of the Magnetar and Radio Pulsar Bursting Phenomenology. ApJ, 727:L51+.

Piro, A. L. (2005). Shear Waves and Giant-Flare Oscillations from Soft Gamma-Ray Repeaters. ApJ, 634:L153–L156.

Rea, N. and Esposito, P. (2011). Magnetar outbursts: an observational review. In D. F. Torres & N. Rea, editor, *High-Energy Emission from Pulsars and their Systems*, pages 247–+.

Rea, N., Esposito, P., Turolla, R., Israel, G. L., Zane, S., Stella, L., Mereghetti, S., Tiengo, A., Götz, D., Göğüş, E., and Kouveliotou, C. (2010). A Low-Magnetic-Field Soft Gamma Repeater. *Science*, 330:944–.

Rea, N., Zane, S., Turolla, R., Lyutikov, M., and Götz, D. (2008). Resonant Cyclotron Scattering in Magnetars' Emission. ApJ, 686:1245–1260.

Roumeliotis, G., Sturrock, P. A., and Antiochos, S. K. (1994). A Numerical Study of the Sudden Eruption of Sheared Magnetic Fields. ApJ, 423:847–+.

Samuelsson, L. and Andersson, N. (2007). Neutron star asteroseismology. Axial crust oscillations in the Cowling approximation. MNRAS, 374:256–268.

Schumaker, B. L. and Thorne, K. S. (1983). Torsional oscillations of neutron stars. MNRAS, 203:457–489.

Shaisultanov, R. and Eichler, D. (2009). What Magnetar Seismology Can Teach Us About Magnetic Fields. ApJ, 702:L23–L26.

Shternin, P. S., Yakovlev, D. G., Heinke, C. O., Ho, W. C. G., and Patnaude, D. J. (2011). Cooling neutron star in the Cassiopeia A supernova remnant: evidence for superfluidity in the core. MNRAS, 412:L108–L112.

Sotani, H., Colaiuda, A., and Kokkotas, K. D. (2008a). Constraints on the magnetic field geometry of magnetars. MNRAS, 385:2161–2165.

Sotani, H., Kokkotas, K. D., and Stergioulas, N. (2007). Torsional oscillations of relativistic stars with dipole magnetic fields. MNRAS, 375:261–277.

Sotani, H., Kokkotas, K. D., and Stergioulas, N. (2008b). Alfvén quasi-periodic oscillations in magnetars. MNRAS, 385:L5–L9.

Steiner, A. W., Lattimer, J. M., and Brown, E. F. (2010). The Equation of State from Observed Masses and Radii of Neutron Stars. ApJ, 722:33–54.

Steiner, A. W. and Watts, A. L. (2009). Constraints on Neutron Star Crusts from Oscillations in Giant Flares. *Physical Review Letters*, 103(18):181101–+.

Stergioulas, N. (1998). Rotating Stars in Relativity. *Living Reviews in Relativity*, 1:8–+.

Strohmayer, T., van Horn, H. M., Ogata, S., Iyetomi, H., and Ichimaru, S. (1991). The shear modulus of the neutron star crust and nonradial oscillations of neutron stars. ApJ, 375:679–686.

Strohmayer, T. E. and Watts, A. L. (2005). Discovery of Fast X-Ray Oscillations during the 1998 Giant Flare from SGR 1900+14. ApJ, 632:L111–L114.

Strohmayer, T. E. and Watts, A. L. (2006). The 2004 Hyperflare from SGR 1806-20: Further Evidence for Global Torsional Vibrations. ApJ, 653:593–601.

Tayler, R. J. (1973). The adiabatic stability of stars containing magnetic fields-I.Toroidal fields. MNRAS, 161:365–+.

Thompson, C. and Duncan, R. C. (1995). The soft gamma repeaters as very strongly magnetized neutron stars - I. Radiative mechanism for outbursts. MNRAS, 275:255–300.

Thompson, C. and Duncan, R. C. (1996). The Soft Gamma Repeaters as Very Strongly Magnetized Neutron Stars. II. Quiescent Neutrino, X-Ray, and Alfven Wave Emission. ApJ, 473:322–+.

Thompson, C. and Duncan, R. C. (2001). The Giant Flare of 1998 August 27 from SGR 1900+14. II. Radiative Mechanism and Physical Constraints on the Source. ApJ, 561:980–1005.

Thompson, C., Duncan, R. C., Woods, P. M., Kouveliotou, C., Finger, M. H., and van Paradijs, J. (2000). Physical Mechanisms for the Variable Spin-down and Light Curve of SGR 1900+14. ApJ, 543:340–350.

Thompson, C., Lyutikov, M., and Kulkarni, S. R. (2002). Electrodynamics of Magnetars: Implications for the Persistent X-Ray Emission and Spin-down of the Soft Gamma Repeaters and Anomalous X-Ray Pulsars. ApJ, 574:332–355.

Timokhin, A. N., Eichler, D., and Lyubarsky, Y. (2008). On the Nature of Quasi-periodic Oscillations in the Tail of Soft Gamma Repeater Giant Flares. ApJ, 680:1398–1404.

Tolman, R. (1939). Static solutions of einstein's field equations for spheres of fluids. *Phys.Rev. 55*, pages 364–373.

Toro, E. F. (1999). *Riemann Solvers and Numerical Methods for Fluid Dynamics*. Springer Verlag, Berlin.

Turolla, R., Zane, S., Pons, J. A., Esposito, P., and Rea, N. (2011). Is SGR 0418+5729 indeed a waning magnetar ? *ArXiv e-prints*.

Uzdensky, D. A. (2004). Force-Free Magnetosphere of an Accretion Disk-Black Hole System. I. Schwarzschild Geometry. ApJ, 603:652–662.

Valori, G., Kliem, B., and Keppens, R. (2005). Extrapolation of a nonlinear force-free field containing a highly twisted magnetic loop. A&A, 433:335–347.

van der Klis, M. (2006). *Rapid X-ray Variability*, pages 39–112.

van Hoven, M. and Levin, Y. (2011). Magnetar oscillations - I. Strongly coupled dynamics of the crust and the core. MNRAS, 410:1036–1051.

van Paradijs, J. and Lewin, W. H. G. (1987). Constraints on the mass-radius relation for the neutron star in the X-ray burst source 4U/MXB 1820-30 located in the globular cluster NGC 6624. A&A, 172:L20–L22.

Ventura, J. (1979). Scattering of light in a strongly magnetized plasma. Phys. Rev. D, 19:1684–1695.

Viganò, D., Pons, J. A., and Miralles, J. A. (2011). Force-free twisted magnetospheres of neutron stars. *ArXiv e-prints*.

Wald, R. (1984). *General Relativity*. University of Chicago Press.

Watts, A. L. and Strohmayer, T. E. (2006). Detection with RHESSI of High-Frequency X-Ray Oscillations in the Tailof the 2004 Hyperflare from SGR 1806-20. ApJ, 637:L117–L120.

Watts, A. L. and Strohmayer, T. E. (2007). Neutron star oscillations and QPOs during magnetar flares. *Advances in Space Research*, 40:1446–1452.

Wilson, J. R., Mathews, G. J., and Marronetti, P. (1996). Relativistic numerical model for close neutron-star binaries. Phys. Rev. D, 54:1317–1331.

Wolfson, R. (1995). Shear-induced opening of the coronal magnetic field. ApJ, 443:810–817.

Wright, G. A. E. (1973). Pinch instabilities in magnetic stars. MNRAS, 162:339–+.

Xu, R. (2007). AXPs/SGRs: Magnetars or quark-stars? *Advances in Space Research*, 40:1453–1459.

Xu, R. X., Tao, D. J., and Yang, Y. (2006). The superflares of soft γ-ray repeaters: giant quakes in solid quark stars? MNRAS, 373:L85–L89.

Yang, W. H., Sturrock, P. A., and Antiochos, S. K. (1986). Force-free magnetic fields - The magneto-frictional method. ApJ, 309:383–391.

York, Jr., J. W. (1979). Kinematics and dynamics of general relativity. In Smarr, L. L., editor, *Sources of Gravitational Radiation*, pages 83–126.

Zane, S., Rea, N., Turolla, R., and Nobili, L. (2009). X-ray spectra from magnetar candidates - III. Fitting SGR/AXP soft X-ray emission with non-relativistic Monte Carlo models. MNRAS, 398:1403–1413.

Parts of this work have been published in scientific Journals or are in the process of publication:

1. Gabler, M., Cerdá-Durán, P., Stergioulas, N., Font, J. A. and Müller, E. (2011). Magneto-elastic oscillations of neutron stars with dipolar magnetic fields arXiv:astro-ph.HR/1109.6233

2. Gabler, M., Cerdá-Durán, P., Font, J. A., Müller, E., and Stergioulas, N. (2011). Magneto-elastic oscillations and the damping of crustal shear modes in magnetars MNRAS, 410:L37-L41.

3. Gabler, M., Cerdá-Durán, P., Font, J., Müller, E., and Stergioulas, N. (2010). Magneto-elastic torsional oscillations of magnetars *Journal of Physics Conference Series*, 283(1):012013.

Acknowledgment

To conclude I would like to express my gratitude to all the people without whose support this thesis never could have been completed successfully.

I thank Ewald Müller and the Max-Planck society for having enabled to conduct the research presented in this thesis at the Max-Planck-Institute for Astrophysics. In particular, I thank my Ph.D. supervisor Ewald Müller for the freedom to visit J. A. Font in Valencia and N. Stergioulas in Thessaloniki, for his scientific guidance and for carefully reading this manuscript.

This thesis was supported by a IKYDA-project between the Max-Planck-Institute for Astrophysics and the Aristotle University of Thessaloniki and an individual DAAD stipend for a long-term visit to the Aristotle University of Thessaloniki. During this long-term visit, several shorter meetings, and many telephone conferences Nikolaos Stergioulas has contributed significantly to the successful completion of this thesis by guiding my research, proposing alternative explanations and discussing the results carefully. I am further grateful for the kind hospitality I have received during the stay in Thessaloniki by Nikolaos Stergioulas and Kimon Zagkouris.

For a second long-term visit I would like to thank José A. Font from the University of Valencia for his kind hospitality. It was a pleasure to work in Valencia and this work has benefited substantially from the discussions during my visit and from the many telephone conferences with José A. Font. Most of the computations have been performed at the *Servicio de Informática de la Universidad de Valencia*.

Special thanks go to Pablo Cerdá-Durán, who collaborated closely on the project of this thesis. I am grateful for all the time he spend on introducing the CoCoNuT/ MCoCoA code to me and for helping me with any programming problems. I cannot count the hours we discussed very fruitfully. Pablo always provided ideas and useful suggestions to solve problems or to improve this work. I could not have completed this thesis without him.

I further would like to thank my colleagues, roommates and friends at the institute, who have supported this thesis by reading parts of the manuscript, sharing experiences, discussing and creating a very productive working atmosphere: Andreas Bauswein, Isabel Cordero-Carrion, Philipp Edelmann, Stephan Hachinger, Henrik Junklewitz, Markus Kromer, Thomas Mädler, Pedro Montero, Tomasz Rembiasz and many others.

During this thesis I was happy to get support from the CompStar community which allowed me to attend a number of schools and conferences, and to come into contact with many scientists in all over Europe.

Schließlich möchte ich auch meinen Eltern Rosemarie und Stephan danken, die mich nicht nur während der letzten drei Jahre immer unterstützt haben.

Renata, minha amada esposa, obrigado pelo seu apoio ao longo dos últimos três anos. Eu sou muito grato que você apoiou todos os meus planos, mesmo que minha tese tem tomado muito de nosso tempo. Eu te amo.